

MARCH 2024

AJNR

VOLUME 45 • PP 249–360

# AJNR

## AMERICAN JOURNAL OF NEURORADIOLOGY

Official Journal ASNR • ASFNR • ASHNR • ASPNR • ASSR  
MARCH 2024 | VOLUME 45 | NUMBER 3 | WWW.AJNR.ORG

THE JOURNAL OF DIAGNOSTIC AND INTERVENTIONAL NEURORADIOLOGY

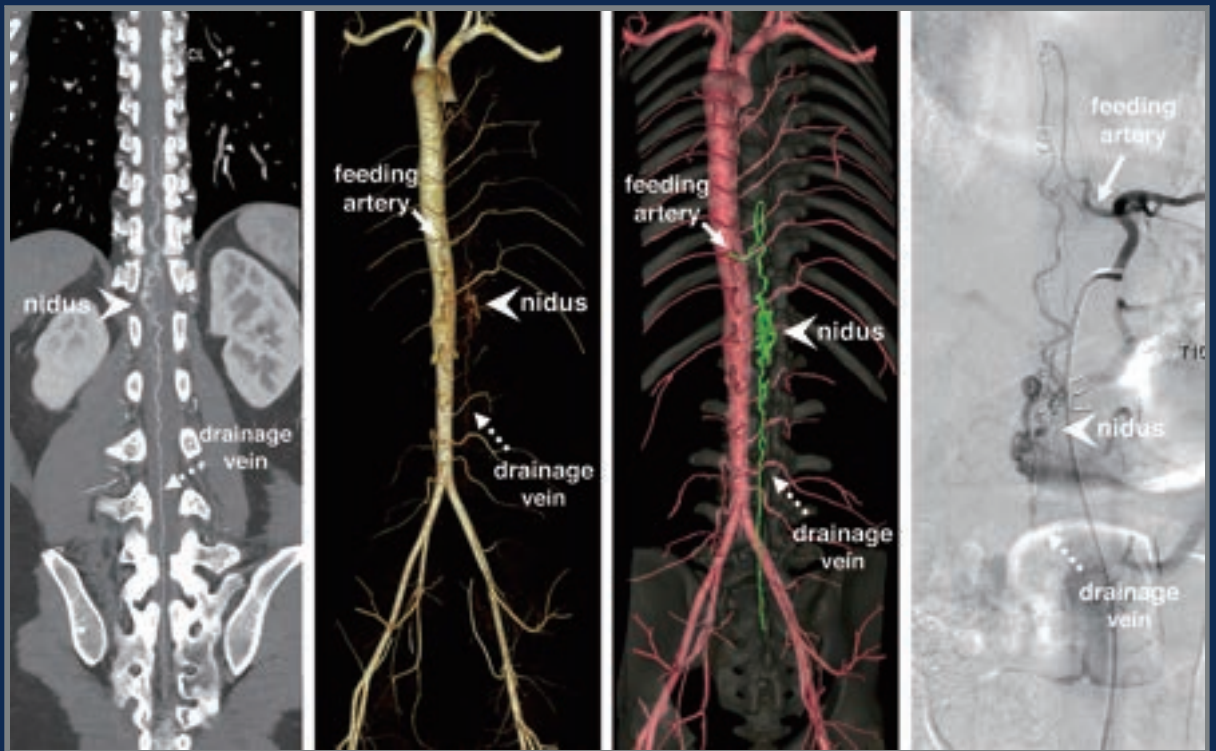
Opportunities and challenges for young professionals in neuroradiology

Multiphase VWI to differentiate culprit atherosclerotic plaque

Deep learning to synthesize contrast-enhanced MR images

MR neurography correlation to histology vs neurosensory testing

Collateral vessels in pediatric anterior circulation ischemic stroke



# FRED™ X™

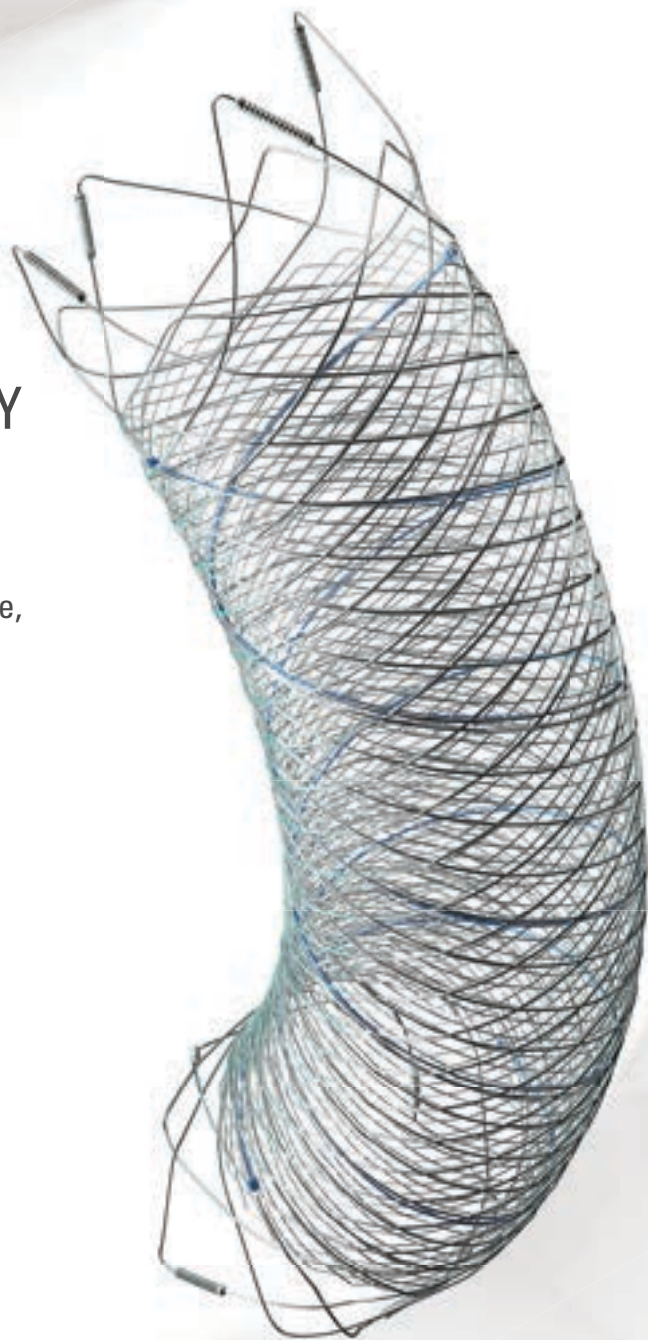
## Flow Diverter Stent

### THE NEXT ADVANCEMENT IN FLOW DIVERSION TECHNOLOGY

The FRED™ X Flow Diverter features the same precise placement and immediate opening of the FRED™ Device, now with X Technology. X Technology is a covalently bonded, nanoscale surface treatment, designed to:

- **REDUCE MATERIAL THROMBOGENICITY<sup>1</sup>**
- **MAINTAIN NATURAL VESSEL HEALING RESPONSE<sup>2,3,4</sup>**
- **IMPROVE DEVICE DELIVERABILITY AND RESHEATHING<sup>1</sup>**

The only FDA PMA approved portfolio with a 0.021" delivery system for smaller device sizes, and no distal lead wire.



For more information, contact your local MicroVention sales representative or visit our website. [www.microvention.com](http://www.microvention.com)



<sup>\*</sup> Data is derived from in vivo and ex vitro testing and may not be representative of clinical performance.

<sup>1</sup> Data on file

<sup>2</sup> Tanaka M et al. Design of biocompatible and biodegradable polymers based on intermediate water concept. Polymer Journal. 2015;47:114-121.

<sup>3</sup> Tanaka M et al. Blood compatible aspects of poly(2-methoxyethylacrylate) (PMEA) – relationship between protein adsorption and platelet adhesion on PMEA surface. Biomaterials. 2000;21:1471-1481.

<sup>4</sup> Schiel L et al. X Coating™: A new biopassive polymer coating. Canadian Perfusion Canadienne. June 2001;11(2):9.

**Indications for Use:** The FRED X System is indicated for use in the internal carotid artery from the petrous segment to the terminus for the endovascular treatment of adult patients (22 years of age or older) with wide-necked (neck width 4 mm or dome-to-neck ratio < 2) saccular or fusiform intracranial aneurysms arising from a parent vessel with a diameter 2.0 mm and 5.0 mm.

**Rx Only:** Federal (United States) law restricts this device to sale by or on the order of a physician. For Healthcare professionals intended use only.

MICROVENTION, FRED and HEADWAY are registered trademarks of MicroVention, Inc. in the United States and other jurisdictions. Stylized X is a trademark of MicroVention, Inc. © 2022 MicroVention, Inc. MM1222 US 03/22

# WEB™ 17

Aneurysm Embolization System

# LOWER PROFILE



## NEW SIZES



## MORE ACCESS OPTIONS



#### INDICATIONS FOR USE:

The WEB Aneurysm Embolization System is intended for the endovascular embolization of ruptured and unruptured intracranial aneurysms and other neurovascular abnormalities such as arteriovenous fistulae (AVF). The WEB Aneurysm Embolization System is also intended for vascular occlusion of blood vessels within the neurovascular system to permanently obstruct blood flow to an aneurysm or other vascular malformation.

#### POTENTIAL COMPLICATIONS:

Potential complications include but are not limited to the following: hematoma at the site of entry, aneurysm rupture, emboli, vessel perforation, parent artery occlusion, hemorrhage, ischemia, vasospasm, clot formation, device migration or misplacement, premature or difficult device detachment, non-detachment, incomplete aneurysm filling, revascularization, post-embolization syndrome, and neurological deficits including stroke and death. For complete indications, potential complications, warnings, precautions, and instructions, see instructions for use (IFU provided with the device).

VIA 21, 27, 33 - The VIA Microcatheter is intended for the introduction of interventional devices (such as the WEB device/stents/flow diverters) and infusion of diagnostic agents (such as contrast media) into the neuro, peripheral, and coronary vasculature.

VIA 17, 17 Preshaped - The VIA Microcatheter is intended for the introduction of interventional devices (such as the WEB device/stents/flow diverters) and infusion of diagnostic agents (such as contrast media) into the neuro, peripheral, and coronary vasculature.

The VIA Microcatheter is contraindicated for use with liquid embolic materials, such as n-butyl 2-cyanoacrylate or ethylene vinyl alcohol & DMSO (dimethyl sulfoxide).

The device should only be used by physicians who have undergone training in all aspects of the WEB Aneurysm Embolization System procedure as prescribed by the manufacturer.

RX Only: Federal law restricts this device to sale by or on the order of a physician.

For healthcare professional intended use only.



MicroVention Worldwide  
Innovat® Center PH +1.714.247.8000

35 Enterprise  
Aliso Viejo, CA 92656 USA  
MicroVention UK Limited  
MicroVention Europe, S.A.R.L.  
MicroVention Deutschland GmbH  
Website  
PH +44 (0) 191 258 6777  
PH +33 (1) 39 21 77 46  
PH +49 211 210 798-0  
microvention.com



WEB™ and VIA™ are registered trademarks  
of Sequent Medical, Inc. in the United States.

©2021 MicroVention, Inc. MM1184 WW 11/2021

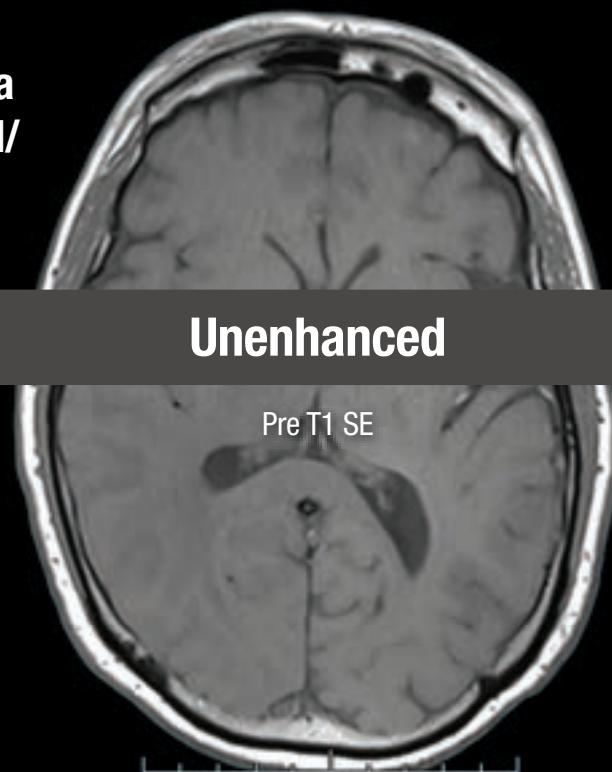


# THIS IS HALF Gd\*

**\*Effective contrast enhancement at half the gadolinium dose (0.05 mmol/kg) vs a macrocyclic GBCA at a dose of 0.1 mmol/kg in approved indications in the U.S.<sup>1-6†</sup>**

  
**Vueway®**  
(gadopiclenol) injection  
485.1 mg/mL

**NO COMPROMISE IN MRI FROM BRACCO,  
YOUR TRUSTED PARTNER**



<sup>†</sup>Phase III CNS Study Design (Study GDX-44-010): Intra-individual, crossover comparison of 0.05 mmol/kg VUEWAY (gadopiclenol) injection vs. 0.1 mmol/kg Gadavist® in MRI of the CNS. Patients with known or suspected CNS lesions. Three primary visualization endpoints (lesion border delineation, lesion internal morphology, degree of contrast enhancement). The CNS study included 256 patients with known or highly suspected CNS lesion(s) with a mean age of 57 years (range: 18-84 years), and 53% female patients.

Please see Brief Summary of Prescribing Information including Boxed Warning on adjacent page.

## **VUEWAY® (gadopiclenol) solution for injection**

### **Indications**

VUEWAY injection is indicated in adults and children aged 2 years and older for use with magnetic resonance imaging (MRI) to detect and visualize lesions with abnormal vascularity in:

- the central nervous system (brain, spine and surrounding tissues),
- the body (head and neck, thorax, abdomen, pelvis, and musculoskeletal system).

### **IMPORTANT SAFETY INFORMATION**

#### **WARNING: NEPHROGENIC SYSTEMIC FIBROSIS (NSF)**

**Gadolinium-based contrast agents (GBCAs) increase the risk for NSF among patients with impaired elimination of the drugs. Avoid use of GBCAs in these patients unless the diagnostic information is essential and not available with non-contrasted MRI or other modalities. NSF may result in fatal or debilitating fibrosis affecting the skin, muscle and internal organs.**

- **The risk for NSF appears highest among patients with:**
  - Chronic, severe kidney disease (GFR < 30 mL/min/1.73 m<sup>2</sup>), or
  - Acute kidney injury.

- **Screen patients for acute kidney injury and other conditions that may reduce renal function. For patients at risk for chronically reduced renal function (e.g. age > 60 years, hypertension, diabetes), estimate the glomerular filtration rate (GFR) through laboratory testing.**
- **For patients at highest risk for NSF, do not exceed the recommended VUEWAY dose and allow a sufficient period of time for elimination of the drug from the body prior to any re-administration.**

### **Contraindications**

VUEWAY injection is contraindicated in patients with history of hypersensitivity reactions to VUEWAY.

### **Warnings**

Risk of **nephrogenic systemic fibrosis** is increased in patients using GBCA agents that have impaired elimination of the drugs, with the highest risk in patients with chronic, severe kidney disease as well as patients with acute kidney injury. Avoid use of GBCAs among these patients unless the diagnostic information is essential and not available with non-contrast MRI or other modalities.

**Hypersensitivity reactions**, including serious hypersensitivity reactions, could occur during use or shortly following VUEWAY administration. Assess all patients for any history of a reaction to contrast media, bronchial asthma and/or allergic disorders, administer VUEWAY only in



LIFE FROM INSIDE

65-year-old man – 3.0 T Siemens  
Brain metastasis from lung adenocarcinoma<sup>7</sup>

SE = Spin Echo. These are representative images from reference studies; individual results may vary.

**Gadopicleenol** 0.05 mmol/kg

Post T1 SE

**Gadobutrol** 0.1 mmol/kg

Post T1 SE

situations where trained personnel and therapies are promptly available for the treatment of hypersensitivity reactions, and observe patients for signs and symptoms of hypersensitivity reactions after administration.

**Gadolinium retention** can be for months or years in several organs after administration. The highest concentrations (nanomoles per gram of tissue) have been identified in the bone, followed by other organs (brain, skin, kidney, liver and spleen). Minimize repetitive GBCA imaging studies, particularly closely spaced studies, when possible.

**Acute kidney injury** requiring dialysis has occurred with the use of GBCAs in patients with chronically reduced renal function. The risk of acute kidney injury may increase with increasing dose of the contrast agent.

Ensure catheter and venous patency before injecting as **extravasation** may occur, and cause tissue irritation.

VUEWAY may **impair the visualization of lesions** seen on non-contrast MRI. Therefore, caution should be exercised when VUEWAY MRI scans are interpreted without a companion non-contrast MRI scan.

The most common adverse reactions (incidence  $\geq 0.5\%$ ) are injection site pain (0.7%), and headache (0.7%).

**You are encouraged to report negative side effects of prescription drugs to the FDA. Visit [www.fda.gov/medwatch](http://www.fda.gov/medwatch) or call 1-800-FDA-1088.**

**Please see BRIEF SUMMARY of Prescribing Information for VUEWAY, including BOXED WARNING on Nephrogenic Systemic Fibrosis.**

Manufactured for Bracco Diagnostics Inc. by Liebel-Flarsheim Company LLC - Raleigh, NC, USA 27616.

VUEWAY is a trademark of Bracco Imaging S.p.A.

All other trademarks and registered trademarks are the property of their respective owners.

**References:** 1. VUEWAY® (gadopicleenol) solution for injection, 485.1 mg/mL Full Prescribing Information and Patient Medication Guide. Monroe Twp., NJ: Bracco Diagnostics Inc.; September 2022. 2. Robic C, Port M, Rousseaux O, et al. Physicochemical and pharmacokinetic profiles of gadopicleenol: a new macrocyclic gadolinium chelate with high T1 relaxivity. *Invest Radiol.* 2019 Aug;54:475-484. 3. GADAVIST® (gadobutrol) Injection. Full Prescribing Information. Bayer HealthCare Pharmaceuticals Inc. Whippany, NJ; April 2022. 4. DOTAREM® (gadoterate meglumine) Injection. Full Prescribing Information. Guerbet LLC. Princeton, NJ; April 2022. 5. CLARISCAN™ (gadoterate meglumine) injection for intravenous use. Full Prescribing Information. GE Healthcare. Chicago, IL; February 2020. 6. ProHance® (Gadoteridol) Injection, 279.3 mg/mL Full Prescribing Information and Patient Medication Guide. Monroe Twp., NJ: Bracco Diagnostics Inc.; June 2022. 7. Loevner LA, Kolumban B, Hutóczki G, et al. Efficacy and safety of gadopicleenol for contrast-enhanced MRI of the central nervous system: the PICTURE randomized clinical trial. *Invest Radiol.* 2023 May;58(5):307-313.

Bracco Diagnostics Inc.  
259 Prospect Plains Road, Building H  
Monroe Township, NJ 08831 USA  
Phone: 609-514-2200  
Toll-Free: 1-877-272-2269 (U.S. only)  
Fax: 609-514-2446

© 2023 Bracco Diagnostics Inc.  
All Rights Reserved. US-VW-2300022 08/23



VISIT  
[VUEWAY.COM](http://VUEWAY.COM)  
FOR MORE  
INFORMATION

# Vueway™ (gadopicleenol) injection, for intravenous use

**BRIEF SUMMARY: Please see package insert of full prescribing information.**

## WARNING: NEPHROGENIC SYSTEMIC FIBROSIS (NSF)

Gadolinium-based contrast agents (GBCAs) increase the risk for NSF among patients with impaired elimination of the drugs. Avoid use of GBCAs in these patients unless the diagnostic information is essential and not available with non-contrast MRI or other modalities. NSF may result in fatal or debilitating fibrosis affecting the skin, muscle and internal organs.

- The risk for NSF appears highest among patients with:
  - Chronic, severe kidney disease (GFR < 30 mL/min/1.73 m<sup>2</sup>), or
  - Acute kidney injury.
- Screen patients for acute kidney injury and other conditions that may reduce renal function. For patients at risk for chronically reduced renal function (e.g. age > 60 years, hypertension, diabetes), estimate the glomerular filtration rate (GFR) through laboratory testing.
- For patients at highest risk for NSF, do not exceed the recommended Vueway dose and allow a sufficient period of time for elimination of the drug from the body prior to any re-administration [see Warnings and Precautions (5.1) in the full Prescribing Information].

## INDICATIONS AND USAGE

Vueway™ (gadopiclenol) is a gadolinium-based contrast agent indicated in adult and pediatric patients aged 2 years and older for use with magnetic resonance imaging (MRI) to detect and visualize lesions with abnormal vascularity in:

- the central nervous system (brain, spine, and associated tissues),
- the body (head and neck, thorax, abdomen, pelvis, and musculoskeletal system).

## CONTRAINDICATIONS

Vueway is contraindicated in patients with history of hypersensitivity reactions to gadopicleenol.

## WARNINGS AND PRECAUTIONS

**Nephrogenic Systemic Fibrosis** Gadolinium-based contrast agents (GBCAs) increase the risk for nephrogenic systemic fibrosis (NSF) among patients with impaired elimination of the drugs. Avoid use of GBCAs among these patients unless the diagnostic information is essential and not available with non-contrast MRI or other modalities. The GBCA-associated NSF risk appears highest for patients with chronic, severe kidney disease (GFR < 30 mL/min/1.73 m<sup>2</sup>) as well as patients with acute kidney injury. The risk appears lower for patients with chronic, moderate kidney disease (GFR 30-59 mL/min/1.73 m<sup>2</sup>) and little, if any, for patients with chronic, mild kidney disease (GFR 60-89 mL/min/1.73 m<sup>2</sup>). NSF may result in fatal or debilitating fibrosis affecting the skin, muscle, and internal organs. Report any diagnosis of NSF following Vueway administration to Bracco Diagnostics Inc. (1-800-257-5181) or FDA (1-800-FDA-1088 or [www.fda.gov/medwatch](http://www.fda.gov/medwatch)).

Screen patients for acute kidney injury and other conditions that may reduce renal function. Features of acute kidney injury consist of rapid (over hours to days) and usually reversible decrease in kidney function, commonly in the setting of surgery, severe infection, injury or drug-induced kidney toxicity. Serum creatinine levels and estimated GFR may not reliably assess renal function in the setting of acute kidney injury. For patients at risk for chronically reduced renal function (e.g., age > 60 years, diabetes mellitus or chronic hypertension), estimate the GFR through laboratory testing.

Among the factors that may increase the risk for NSF are repeated or higher than recommended doses of a GBCA and the degree of renal impairment at the time of exposure. Record the specific GBCA and the dose administered to a patient. For patients at highest risk for NSF, do not exceed the recommended Vueway dose and allow a sufficient period of time for elimination of the drug prior to re-administration. For patients receiving hemodialysis, physicians may consider the prompt initiation of hemodialysis following the administration of a GBCA in order to enhance the contrast agent's elimination [see Use in Specific Populations (8.6) and Clinical Pharmacology (12.3) in the full Prescribing Information]. The usefulness of hemodialysis in the prevention of NSF is unknown.

**Hypersensitivity Reactions** With GBCAs, serious hypersensitivity reactions have occurred. In most cases, initial symptoms occurred within minutes of GBCA administration and resolved with prompt emergency treatment.

- Before Vueway administration, assess all patients for any history of a reaction to contrast media, bronchial asthma and/or allergic disorders. These patients may have an increased risk for a hypersensitivity reaction to Vueway.
- Vueway is contraindicated in patients with history of hypersensitivity reactions to Vueway [see Contraindications (4) in the full Prescribing Information].
- Administer Vueway only in situations where trained personnel and therapies are promptly available for the treatment of hypersensitivity reactions, including personnel trained in resuscitation.
- During and following Vueway administration, observe patients for signs and symptoms of hypersensitivity reactions.

**Gadolinium Retention** Gadolinium is retained for months or years in several organs. The highest concentrations (nanomoles per gram of tissue) have been identified in the bone, followed by other organs (e.g. brain, skin, kidney, liver, and spleen). The duration of retention also varies by tissue and is longest in bone. Linear GBCAs cause more retention than macrocyclic GBCAs. At equivalent doses, gadolinium retention varies among the linear agents with gadodiamide causing greater retention than other linear agents such as gadoxetate disodium, and gadobenate dimeglumine. Retention is lowest and similar

among the macrocyclic GBCAs such as gadoterate meglumine, gadobutrol, gadoteridol, and gadopicleenol.

Consequences of gadolinium retention in the brain have not been established. Pathologic and clinical consequences of GBCA administration and retention in skin and other organs have been established in patients with impaired renal function [see Warnings and Precautions (5.1) in the full Prescribing Information]. There are rare reports of pathologic skin changes in patients with normal renal function. Adverse events involving multiple organ systems have been reported in patients with normal renal function without an established causal link to gadolinium.

While clinical consequences of gadolinium retention have not been established in patients with normal renal function, certain patients might be at higher risk. These include patients requiring multiple lifetime doses, pregnant and pediatric patients, and patients with inflammatory conditions. Consider the retention characteristics of the agent when choosing a GBCA for these patients. Minimize repetitive GBCA imaging studies, particularly closely spaced studies, when possible.

**Acute Kidney Injury** In patients with chronically reduced renal function, acute kidney injury requiring dialysis has occurred with the use of GBCAs. The risk of acute kidney injury may increase with increasing dose of the contrast agent. Do not exceed the recommended dose.

**Extravasation and Injection Site Reactions** Injection site reactions such as injection site pain have been reported in the clinical studies with Vueway [see Adverse Reactions (6.1) in the full Prescribing Information]. Extravasation during Vueway administration may result in tissue irritation [see Nonclinical Toxicology (13.2) in the full Prescribing Information]. Ensure catheter and venous patency before the injection of Vueway.

**Interference with Visualization of Lesions Visible with Non-Contrast MRI** As with any GBCA, Vueway may impair the visualization of lesions seen on non-contrast MRI. Therefore, caution should be exercised when Vueway MRI scans are interpreted without a companion non-contrast MRI scan.

## ADVERSE REACTIONS

The following serious adverse reactions are discussed elsewhere in labeling:

- Nephrogenic Systemic Fibrosis [see Warnings and Precautions (5.1) in the full Prescribing Information]
- Hypersensitivity Reactions [see Contraindications (4) and Warnings and Precautions (5.2) in the full Prescribing Information]

**Clinical Trials Experience** Because clinical trials are conducted under widely varying conditions, adverse reaction rates observed in the clinical trials of a drug cannot be directly compared to rates in the clinical trials of another drug and may not reflect the rates observed in clinical practice.

The safety of Vueway was evaluated in 1,047 patients who received Vueway at doses ranging from 0.025 mmol/kg (one half the recommended dose) to 0.3 mmol/kg (six times the recommended dose). A total of 708 patients received the recommended dose of 0.05 mmol/kg. Among patients who received the recommended dose, the average age was 51 years (range 2 years to 88 years) and 56% were female. The ethnic distribution was 79% White, 10% Asian, 7% American Indian or Alaska native, 2% Black, and 2% patients of other or unspecified ethnic groups.

Overall, approximately 4.7% of subjects receiving the labeled dose reported one or more adverse reactions.

Table 1 lists adverse reactions that occurred in > 0.2% of patients who received 0.05 mmol/kg Vueway.

TABLE 1. ADVERSE REACTIONS REPORTED IN > 0.2% OF PATIENTS RECEIVING VUEWAY IN CLINICAL TRIALS	
Adverse Reaction	Vueway 0.05 mmol/kg (n=708) (%)
Injection site pain	0.7
Headache	0.7
Nausea	0.4
Injection site warmth	0.4
Injection site coldness	0.3
Dizziness	0.3
Local swelling	0.3

Adverse reactions that occurred with a frequency < 0.2% in patients who received 0.05 mmol/kg Vueway included: maculopapular rash, vomiting, worsened renal impairment, feeling hot, pyrexia, oral paresthesia, dysgeusia, diarrhea, pruritus, allergic dermatitis, erythema, injection site paresthesia, Cystatin C increase, and blood creatinine increase.

## Adverse Reactions in Pediatric Patients

One study with a single dose of Vueway (0.05 mmol/kg) was conducted in 80 pediatric patients aged 2 years to 17 years, including 60 patients who underwent a central nervous system (CNS) MRI and 20 patients who underwent a body MRI. One adverse reaction (maculopapular rash of moderate severity) in one patient (1.3%) was reported in the CNS cohort.

## USE IN SPECIFIC POPULATIONS

**Pregnancy Risk Summary** There are no available data on Vueway use in pregnant women to evaluate for a drug-associated risk of major birth defects, miscarriage or other adverse maternal or fetal outcomes. GBCAs cross the human placenta and result in fetal exposure and gadolinium retention. The available human data on GBCA exposure during pregnancy and adverse fetal outcomes are limited and inconclusive (see Data). In animal reproduction studies, there were no adverse developmental effects observed in rats or rabbits with intravenous administration of Vueway during organogenesis (see Data). Because of the potential risks of gadolinium to the fetus, use Vueway only if imaging is essential during pregnancy and cannot be delayed. The estimated background risk of major birth defects and miscarriage for the indicated population(s) are unknown. All pregnancies have a background risk of birth defect, loss, or other adverse outcomes. In the U.S. general population, the estimated background risk of major birth defects and miscarriage in clinically recognized pregnancies is 2% to 4% and 15% to 20% respectively. Data Human Data Contrast enhancement is visualized in the placenta and fetal tissues after maternal GBCA administration. Cohort studies and case reports on exposure to GBCAs during pregnancy have not reported a clear association between GBCAs and adverse effects in the exposed neonates. However, a retrospective cohort study comparing pregnant women who had a GBCA MRI to pregnant women who did not have an MRI reported a higher occurrence of stillbirths and neonatal deaths in the group receiving GBCA MRI. Limitations of this study include a lack of comparison with non-contrast MRI and lack of information about the maternal indication for MRI. Overall, these data preclude

a reliable evaluation of the potential risk of adverse fetal outcomes with the use of GBCAs in pregnancy.

**Animal Data Gadolinium Retention:** GBCAs administered to pregnant non-human primates (0.1 mmol/kg on gestational days 85 and 135) result in measurable gadolinium concentration in the offspring in bone, brain, skin, liver, kidney, and spleen for at least 7 months. GBCAs administered to pregnant mice (2 mmol/kg daily on gestational days 16 through 19) result in measurable gadolinium concentrations in the pups in bone, brain, kidney, liver, blood, muscle, and spleen at one-month postnatal age.

**Reproductive Toxicology:** Animal reproduction studies conducted with gadopicleenol showed some signs of maternal toxicity in rats at 10 mmol/kg and rabbits at 5 mmol/kg (corresponding to 52 times and 57 times the recommended human dose, respectively). This maternal toxicity was characterized in both species by swelling, decreased activity, and lower gestation weight gain and food consumption.

No effect on embryo-fetal development was observed in rats at 10 mmol/kg (corresponding to 52 times the recommended human dose). In rabbits, a lower mean fetal body weight was observed at 5 mmol/kg (corresponding to 57 times the recommended human dose) and this was attributed as a consequence of the lower gestation weight gain.

**Lactation Risk Summary** There are no data on the presence of gadopicleenol in human milk, the effects on the breastfed infant, or the effects on milk production. However, published lactation data on other GBCAs indicate that 0.01% to 0.04% of the maternal gadolinium dose is excreted in breast milk. Additionally, there is limited GBCA gastrointestinal absorption in the breast-fed infant. Gadopicleenol is present in rat milk. When a drug is present in animal milk, it is likely that the drug will be present in human milk (see Data). The developmental and health benefits of breastfeeding should be considered along with the mother's clinical need for Vueway and any potential adverse effects on the breastfed infant from Vueway or from the underlying maternal condition. Data In lactating rats receiving single intravenous injection of [<sup>147</sup>Gd]-gadopiclenol, 0.3% and 0.2% of the total administered radioactivity was transferred to the pups via maternal milk at 6 hours and 24 hours after administration, respectively. Furthermore, in nursing rat pups, oral absorption of gadopicleenol was 3.6%.

**Pediatric Use** The safety and effectiveness of Vueway for use with MRI to detect and visualize lesions with abnormal vascularity in the CNS (brain, spine, and associated tissues), and the body (head and neck, thorax, abdomen, pelvis, and musculoskeletal system) have been established in pediatric patients aged 2 years and older.

Use of Vueway in this age group is supported by evidence from adequate and well-controlled studies in adults with additional pharmacokinetic and safety data from an open-label, uncontrolled, multicenter, single dose study of Vueway (0.05 mmol/kg) in 80 pediatric patients aged 2 to 17 years. The 80 patients consisted of 60 patients who underwent a CNS MRI and 20 patients who underwent a body MRI [see Adverse Reactions (6.1) and Clinical Pharmacology (12.3) in the full Prescribing Information].

The safety and effectiveness of Vueway have not been established in pediatric patients younger than 2 years of age.

**Geriatric Use** Of the total number of Vueway-treated patients in clinical studies, 270 (26%) patients were 65 years of age and over, while 62 (6%) patients were 75 years of age and over. No overall differences in safety or efficacy were observed between these subjects and younger subjects.

This drug is known to be substantially excreted by the kidney, and the risk of adverse reactions to this drug may be greater in patients with impaired renal function. Because elderly patients are more likely to have decreased renal function, it may be useful to monitor renal function.

**Renal Impairment** In patients with renal impairment, the exposure of gadopicleenol is increased compared to patients with normal renal function. This may increase the risk of adverse reactions such as nephrogenic systemic fibrosis (NSF). Avoid use of GBCAs among these patients unless the diagnostic information is essential and not available with non-contrast MRI or other modalities. No dose adjustment of Vueway is recommended for patients with renal impairment. Vueway can be removed from the body by hemodialysis [see Warnings and Precautions (5.1, 5.3, 5.4) and Clinical Pharmacology (12.3) in the full Prescribing Information].

## OVERDOSAGE

Among subjects who received a single 0.3 mmol/kg intravenous dose of gadopicleenol (6 times the recommended dose of Vueway), headache and nausea were the most frequently reported adverse reactions. Gadopicleenol can be removed from the body by hemodialysis [see Clinical Pharmacology (12.3) in the full Prescribing Information].

**PATIENT COUNSELING INFORMATION** Advise the patient to read the FDA-approved patient labeling (Medication Guide).

**Nephrogenic Systemic Fibrosis** Inform the patient that Vueway may increase the risk for NSF among patients with impaired elimination of the drugs and that NSF may result in fatal or debilitating fibrosis affecting the skin, muscle and internal organs.

Instruct the patients to contact their physician if they develop signs or symptoms of NSF following Vueway administration, such as burning, itching, swelling, scaling, hardening and tightening of the skin; red or dark patches on the skin; stiffness in joints with trouble moving, bending or straightening the arms, hands, legs or feet; pain in the hip bones or ribs; or muscle weakness [see Warnings and Precautions (5.1) in the full Prescribing Information].

**Gadolinium Retention** Advise patients that gadolinium is retained for months or years in brain, bone, skin, and other organs following Vueway administration even in patients with normal renal function. The clinical consequences of retention are unknown. Retention depends on multiple factors and is greater following administration of linear GBCAs than following administration of macrocyclic GBCAs [see Warnings and Precautions (5.3) in the full Prescribing Information].

**Injection Site Reactions** Inform the patient that Vueway may cause reactions along the venous injection site, such as mild and transient burning or pain or feeling of warmth or coldness at the injection site [see Warnings and Precautions (5.5) in the full Prescribing Information].

**Pregnancy** Advise pregnant women of the potential risk of fetal exposure to Vueway [see Use in Specific Populations (8.1) in the full Prescribing Information].

## Rx only

US Patent No. 10,973,934  
Manufactured for Bracco Diagnostics Inc. by Liebel-Flarsheim Company LLC  
- Raleigh, NC, USA 27616.  
Toll Free: 1-877-272-2269 (U.S. only)  
Revised November 2022



# The ASNR Career Center

**The Go-To Job Site for Neuroradiology Employers and Job Seekers**

***For Job Seekers***

- Access to an expanded network of jobs via the National Healthcare Career Network
- Confidential resume posting
- Professional online profile

***For Employers***

- Employer resources to help you recruit top talent
- Multiple pricing options, including free Fellowship listings
- Resume search

**Start here: [careers.asnr.org](https://careers.asnr.org)**



**I am a global citizen.  
I am patient-centered care.  
I am an academic neuroradiologist.  
I am a researcher.  
I am a life-long learner.  
I am determined.  
I am curious.  
I am a collaborative team player.  
I am a volunteer.  
I am ASNR.**

**Don't miss out on the tools, resources and relationships you've come to rely on. Log in and renew your ASNR membership today! [www.asnr.org](http://www.asnr.org)**



## **Simplify** the MOC Process



## **Manage** your CME Credits Online

# **CMEgateway.org**

### **Available to Members of Participating Societies**

American Board of Radiology (ABR)  
American College of Radiology (ACR)  
American Roentgen Ray Society (ARRS)  
American Society of Neuroradiology (ASNR)  
Commission on Accreditation of Medical  
Physics Educational Programs, Inc. (CAMPEP)  
Radiological Society of North America (RSNA)  
Society of Interventional Radiology (SIR)  
SNM  
The Society for Pediatric Radiology (SPR)

### **It's Easy and Free!**

Log on to CME Gateway to:

- View or print reports of your CME credits from multiple societies from a single access point.
- Print an aggregated report or certificate from each participating organization.
- Link to SAMs and other tools to help with maintenance of certification.

### **American Board of Radiology (ABR) participation!**

By activating ABR in your organizational profile, your MOC-fulfilling CME and SAM credits can be transferred to your own personalized database on the ABR Web site.

### **Sign Up Today!**

go to [CMEgateway.org](http://CMEgateway.org)

# AJNR *go green*

***AJNR* urges American Society of Neuroradiology members to reduce their environmental footprint by voluntarily suspending their print subscription.**

The savings in paper, printing, transportation, and postage directly fund new electronic enhancements and expanded content.

The digital edition of *AJNR* presents the print version in its entirety, along with extra features including:

- Publication Preview
- Case Collection
- Podcasts
- The *AJNR* News Digest
- The *AJNR* Blog

It also reaches subscribers much faster than print. An electronic table of contents will be sent directly to your mailbox to notify you as soon as it publishes.

Readers can search, reference, and bookmark current and archived content 24 hours a day on [www.ajnr.org](http://www.ajnr.org).

ASNR members who wish to opt out of print can do so by using the *AJNR* Go Green link on the *AJNR* Website (<http://www.ajnr.org/content/subscriber-help-and-services>). Just type your name in the email form to stop print and spare our ecosystem.



JOIN US!

ASNR24

LAS VEGAS  
MAY 18-22, 2024

CELEBRATING NEURORADIOLOGISTS



Join us at ASNR24 where we plan on **Celebrating Neuroradiologists** and showcasing and celebrating our field's many accomplishments. Both in-person and on-demand registration options are available, allowing you to attend the Annual Meeting the way that works best for you!

**Early Bird Registration ends April 15! Register now and save:**  
**[www.asnr.org/annualmeeting](http://www.asnr.org/annualmeeting)**

---

#### ASNR24 will feature:

- Symposium on *Neuroradiology: The New Frontier*, including sessions on VR/AI, photon counting, psychiatric disease, brain tumor imaging, health policy issues and genetic therapies for neurologic diseases.
- Sessions feature emerging topics, neuroradiology essentials, policy and practice updates, and discussions with international and industry colleagues. Many sessions this year will also feature case presentations, panel discussions, and audience response polling.
- Approximately 200 podium presentations and 500 ePosters and Educational Exhibits on the latest advancements in research, technology, policy and practice innovations for neuroradiology.
- Social and fun community connection experiences, including the Presidential Gala and a Neuro Networking Reception by the pool
- Special sessions and social events for community and specialty groups, including Spine, Head and Neck, Healthcare, Pediatrics, Functional, AI, Interventional, Young Professionals, New Retirees, Fellowship Directors, International Affiliates, and many more.

#### ASNR24 Host Hotel and Conference Location

Caesars Palace  
3570 S Las Vegas Blvd.  
Las Vegas, NV 89109

Play, dine and unwind like royalty at Caesars Palace Las Vegas, the remarkable, palatial center-strip resort. After a day of learning and networking, enjoy being just steps away from a variety of activities, ranging from world-class shopping and dining to outdoor adventures and shows. For ease and convenience, book in the ASNR hotel room block.



#### Accreditation Statement

The American Society of Neuroradiology is accredited by the Accreditation Council for Continuing Medical Education (ACCME) to provide continuing medical education for physicians and takes responsibility for the content, quality and scientific integrity of this CME activity.

The American Society of Neuroradiology designates this live activity for a maximum of 27.25 AMA PRA Category 1 Credits™. Physicians should claim only the credit commensurate with the extent of their participation in the activity. The American Society of Neuroradiology designates this enduring material for a maximum of 62.25 AMA PRA Category 1 Credits™. Physicians should claim only the credit commensurate with the extent of their participation in the activity.

---

Visit **[www.asnr.org/annualmeeting](http://www.asnr.org/annualmeeting)** for complete details and to register.



# AJNR

## AMERICAN JOURNAL OF NEURORADIOLOGY


MARCH 2024  
VOLUME 45  
NUMBER 3  
WWW.AJNR.ORG

Publication Preview at [www.ajnr.org](http://www.ajnr.org) features articles released in advance of print.  
Visit [www.ajnrblog.org](http://www.ajnrblog.org) to comment on AJNR content and chat with colleagues.

### EDITORIAL

- 249 **Streamlining the Manuscript Submission Process at the *American Journal of Neuroradiology*: Paving the Way for Efficiency and Reducing Hurdles for Authors** *Max Wintermark*

### REVIEW ARTICLE

-  250 **Patient Engagement in Neuroradiology: A Narrative Review and Case Studies** *Nadja Kadom, et al.*








HEALTH POLICIES/QUALITY  
IMPROVEMENT/  
EVIDENCE-BASED  
NEUROIMAGING

### STATE OF PRACTICE

-  256 **Young Professionals in Neuroradiology: Opportunities, Challenges, and Future Directions** *Anna V. Trofimova, et al.*

HEALTH POLICIES/QUALITY  
IMPROVEMENT/  
EVIDENCE-BASED  
NEUROIMAGING

### GENERAL CONTENTS

-  262 **Delayed Enhancement of Intracranial Atherosclerotic Plaque Can Better Differentiate Culprit Lesions: A Multiphase Contrast-Enhanced Vessel Wall MRI Study** *Beibei Sun, et al.*
-  271 **Development of Collateral Vessels after Anterior Circulation Large Vessel Occlusion in Pediatric Arterial Ischemic Stroke Relates to Stroke Etiology: A Longitudinal Study** *Manoëlle Kossorotoff, et al.*
-  277 **Reducing False-Positives in CT Perfusion Infarct Core Segmentation Using Contralateral Local Normalization** *Alexander Rau, et al.*
-  284 **CTA Supplemented by CTP Increases Interrater Reliability and Endovascular Treatment Use in Patients with Aneurysmal SAH** *Christian Heitkamp, et al.*
-  291 **Prevalence of “Ghost Infarct Core” after Endovascular Thrombectomy** *Johanna M. Ospel, et al.*
-  296 **Effect of Clot Burden Score on Safety and Efficacy of Intravenous Alteplase Prior to Mechanical Thrombectomy in Acute Ischemic Stroke: A Subgroup Analysis of a Randomized Phase 3 Trial** *Zifu Li, et al.*
-  302 **MR-Guided Focused Ultrasound Thalamotomy in the Setting of Aneurysm Clip** *Henrik Odéen, et al.*

NEUROVASCULAR/  
STROKE IMAGING

NEUROVASCULAR/  
STROKE IMAGING

NEUROVASCULAR/  
STROKE IMAGING












NEUROVASCULAR/  
STROKE IMAGING

NEUROVASCULAR/  
STROKE IMAGING

NEUROVASCULAR/  
STROKE IMAGING

NEUROINTERVENTION

AJNR (Am J Neuroradiol ISSN 0195–6108) is a journal published monthly, owned and published by the American Society of Neuroradiology (ASNR), 820 Jorie Boulevard, Oak Brook, IL 60523. Annual dues for the ASNR include approximately 19% for a journal subscription. The journal is printed by Intellicor Communications, 330 Eden Road, Lancaster, PA 17601; Periodicals postage paid at Oak Brook, IL and additional mailing offices. Printed in the U.S.A. POSTMASTER: Please send address changes to American Journal of Neuroradiology, P.O. Box 3000, Denville, NJ 07834, U.S.A. Subscription rates: nonmember \$475 (\$560 foreign) print and online, \$320 online only; institutions \$550 (\$625 foreign) print and basic online, \$1080 (\$1160 foreign) print and extended online, \$380 online only (basic), \$825 online only (extended); single copies are \$35 each (\$40 foreign). Indexed by PubMed/MEDLINE, BIOSIS Previews, Current Contents (Clinical Medicine and Life Sciences), EMBASE, Google Scholar, HighWire Press, Q-Sensei, RefSeek, Science Citation Index, SCI Expanded, ReadCube, and Semantic Scholar. Copyright © American Society of Neuroradiology.

-  305 **Dynamic Changes in Long-Standing Multiple Sclerosis Revealed by Longitudinal Structural Network Analysis Using Diffusion Tensor Imaging** *Hui-Qin Zhang, et al.*
-   312 **Synthesizing Contrast-Enhanced MR Images from Noncontrast MR Images Using Deep Learning** *Gowtham Murugesan, et al.*
-  320 **Imaging Biomarker for Early-Stage Alzheimer Disease: Utility of Hippocampal Histogram Analysis of Diffusion Metrics** *Hiroto Takahashi, et al.*
-    328 **Prediction of Surgical Outcomes in Normal Pressure Hydrocephalus by MR Elastography** *Pragatl Karki, et al.*
-  335 **Efficacy of MR Neurography of Peripheral Trigeminal Nerves: Correlation of Sunderland Grade versus Neurosensory Testing** *Shuda Xia, et al.*
-  342 **Diagnostic Performance of Dynamic Contrast-Enhanced 3T MR Imaging for Characterization of Orbital Lesions: Validation in a Large Prospective Study** *Emma O'Shaughnessy, et al.*
-   351 **Application of Spinal Subtraction and Bone Background Fusion CTA in the Accurate Diagnosis and Evaluation of Spinal Vascular Malformations** *Xuehan Hu, et al.*
- 358 **Multinodular and Vacuolating Neuronal Tumor-like Lesion of the Spinal Cord: Two Case Reports** *Joris Schollaert, et al.*

ULTRA-HIGH-FIELD MRI/  
IMAGING OF EPILEPSY/  
DEMYELINATING DISEASES/  
INFLAMMATION/INFECTION

ARTIFICIAL  
INTELLIGENCE

NEURODEGENERATIVE  
DISORDER IMAGING

NEURODEGENERATIVE  
DISORDER IMAGING

HEAD AND NECK  
IMAGING

HEAD AND NECK  
IMAGING

SPINE IMAGING AND  
SPINE IMAGE-GUIDED  
INTERVENTIONS

SPINE IMAGING AND  
SPINE IMAGE-GUIDED  
INTERVENTIONS

#### BOOK REVIEWS *R.M. Quencer, Section Editor*

Please visit [www.ajnrblog.org](http://www.ajnrblog.org) to read and comment on Book Reviews.



In this study by Hu et al, clinically prevalent spinal artery CTA postprocessing techniques were used to achieve precise visualization and localization of spinal vascular malformations using 3D-volume rendering. Spinal CTA images (multiplanar reconstruction CTA [A], routine bone subtraction CTA [B], spinal subtraction and bone background fusion CTA [C], and digital subtraction angiography [D]) demonstrate crucial parts of the spinal arteriovenous malformation, including nidus (arrowhead), feeding artery (solid arrow), and drainage vein (dotted arrow).



Indicates Editor's Choices selection



Indicates Fellows' Journal Club selection



Indicates open access to non-subscribers at [www.ajnr.org](http://www.ajnr.org)



Indicates article with supplemental online data



Indicates article with supplemental online video



Evidence-Based Medicine Level 1



Evidence-Based Medicine Level 2



# AMERICAN JOURNAL OF NEURORADIOLOGY

Official Journal:

American Society of Neuroradiology  
American Society of Functional Neuroradiology  
American Society of Head and Neck Radiology  
American Society of Pediatric Neuroradiology  
American Society of Spine Radiology

MARCH 2024 • VOLUME 45 • NUMBER 3 • WWW.AJNR.ORG

## EDITOR-IN-CHIEF

**Max Wintermark, MD, MAS, FASFN, FICIS**

*Frank T. McGraw Memorial Chair in the Study of Cancer  
Professor and Chair of Neuroradiology  
The University of Texas MD Anderson Center*

## DEPUTY EDITOR

**Lubdhra M. Shah, MD, MS**

Professor of Radiology and Director of Spine Imaging  
Department of Radiology and Imaging Sciences  
University of Utah

## SPECIAL ADVISORS TO THE EDITOR-IN-CHIEF

**Mauricio Castillo, MD, FACR**

MA Mauro Distinguished Professor of Radiology  
University of North Carolina-Chapel Hill

**Robert Quencer, MD**

Professor Emeritus  
Department of Radiology  
University of Miami

## ARTIFICIAL INTELLIGENCE

### Senior Editor

**Reza Forghani, MD, PhD**

Professor of Radiology & Artificial Intelligence  
Vice Chair of AI  
Director, Radiomics & Augmented Intelligence Laboratory (RAIL)  
Department of Radiology  
University of Florida College of Medicine

### Associate Editors

**Andreas Rauschecker, MD, PhD**

Assistant Professor-in-Residence  
Co-Executive Director and Clinical Director,  
Center for Intelligent Imaging (ci<sup>2</sup>)  
Department of Radiology & Biomedical Imaging  
University of California, San Francisco

**Sam (Seyedmehdi) Payabvash, MD**

Assistant Professor of Radiology  
Yale School of Medicine  
Connecticut

## BRAIN TUMOR IMAGING

### Senior Editor

**Ben Ellingson, PhD**

Professor and Director of MRI Research  
Director, UCLA Brain Tumor Imaging Laboratory  
Department of Radiological Sciences  
David Geffen School of Medicine  
University of California, Los Angeles

### Associate Editors

**Ali Nabavizadeh, MD**

Assistant Professor of Radiology  
Division of Neuroradiology  
University of Pennsylvania

**Mark S. Shiroishi, MD, MS, FASFN**

Assistant Professor, Division of Neuroradiology,  
Department of Radiology  
Director of Neuro-Oncology Imaging - USC Brain Tumor Center  
Chief of Pediatric Neuroradiology - Los Angeles General Medical Center  
Affiliated Faculty - USC Imaging Genetics Center  
Mark and Mary Stevens Neuroimaging and Informatics Institute  
Keck School of Medicine of USC  
University of Southern California

## EMERGENCY NEURORADIOLOGY

### Senior Editor

**Karen Buch, MD**

Assistant Professor of Radiology  
Massachusetts General Hospital

### Associate Editors

**Melissa A. Davis, MD, MBA**

Vice Chair of Medical Informatics  
Associate Professor  
Department of Radiology and Biomedical Imaging  
Yale School of Medicine  
Connecticut

**Jason Talbott, MD, PhD**

Associate Professor, Neuroradiology Section  
Department of Radiology and Biomedical Imaging  
University of California, San Francisco and  
Zuckerberg San Francisco General Hospital

## HEAD AND NECK IMAGING

### Senior Editor

**Amy Juliano, MD**

Associate Professor of Radiology  
Massachusetts Eye and Ear  
Harvard Medical School

### Associate Editors

**Burce Ozgen, MD**

Clinical Professor of Radiology  
University of Illinois at Chicago

**David Zander, MD**

Assistant Professor, Radiology  
University of Colorado School of Medicine

## HEALTH POLICIES/QUALITY IMPROVEMENT/ EVIDENCE-BASED NEUROIMAGING

### Senior Editor

**Nadja Kadom, MD, FACR, FAAP**

Professor, Department of Radiology and Imaging Sciences  
Emory University School of Medicine  
Pediatric Neuroradiologist, Department of Radiology  
Children's Healthcare of Atlanta

## Associate Editors

**Melissa M. Chen, MD**

Associate Professor,  
Department of Neuroradiology, Division of Diagnostic Imaging  
The University of Texas MD Anderson Center

**Ajay Malhotra, MBBS, MD, MMM**

Professor of Radiology and Biomedical Imaging and Neurosurgery  
Yale School of Medicine  
Connecticut

## MOLECULAR NEUROIMAGING/NUCLEAR MEDICINE

### Senior Editor

**Ana M. Franceschi, MD, PhD**

Associate Professor of Radiology  
Donald and Barbara Zucker School of Medicine at Hofstra/Northwell  
The Feinstein Institutes for Medical Research  
Neuro-PET Imaging  
Lenox Hill Hospital  
New York

### Associate Editors

**Nadya Pyatigorskaya, MD, PhD**

Neuroradiology Department, Pitié-Salpêtrière Hospital  
Researcher, Brain Institute (ICM)  
France

**Marc Daniel Benayoun, PhD, MD**

Assistant Professor of Radiology  
Co-Section Head of Nuclear Medicine  
Medical Director of Nuclear Medicine and PET  
Vice Chair of Radiation Drug Research Committee  
Atrium Wake Forest Health  
North Carolina

## NEURODEGENERATIVE DISORDER IMAGING

### Senior Editor

**Gloria Chiang, MD**

Associate Professor, Co-Director of the Brain Health Imaging Institute  
Department of Radiology  
Weill Cornell Medicine/NewYork-Presbyterian Hospital

### Associate Editors

**Fang Frank Yu, MD**

Assistant Professor of Radiology  
Division of Neuroradiology, Department of Radiology  
Advanced Imaging Research Center  
University of Texas Southwestern Medical Center

**Priya Rajagopalan, MBBS, MPH**

Assistant Professor of Radiology, Division of  
Neuroradiology  
Associate Program Director, Neuroradiology  
Fellowship  
Medical Director, Center for Image Acquisition  
Mark and Mary Stevens Neuroimaging and  
Informatics Institute  
Keck School of Medicine, University of Southern  
California

**NEUROIMAGING PHYSICS/FUNCTIONAL  
NEUROIMAGING/CT AND MRI TECHNOLOGY****Senior Editor****Hongyu An, DSc**

Professor, Mallinckrodt Institute of Radiology  
Neurology, Biomedical Engineering, Electrical and  
Systems Engineering, Division of Biology and  
Biomedical Sciences  
Director, Biomedical Magnetic Resonance Center  
Associate Director, Center for Clinical Imaging Research  
Washington University in St. Louis

**Associate Editors****Timothy J. Carroll, PhD**

Professor, Department of Radiology  
University of Chicago

**Hugo de Jong, PhD**

Professor of Medical Physics Radiology and  
Nuclear Medicine  
UMC Utrecht  
the Netherlands

**NEUROINTERVENTION****Senior Editor****Steven Hetts, MD, FACP**

Co-Chief, NeuroEndovascular Surgery Service Line  
Chief of Interventional Neuroradiology, Mission  
Bay Hospitals  
Professor of Radiology, Biomedical Imaging, and  
Neurological Surgery  
University of California, San Francisco

**Associate Editors****Kristine Blackham, MD**

Associate Professor  
Diagnostic and Interventional Neuroradiology  
Clinic for Radiology and Nuclear Medicine  
University Hospital of Basel

**Maksim Shapiro, MD**

Clinical Associate Professor  
Departments of Radiology, Neurosurgery, and  
Neurology  
Division of Neurointerventional Radiology  
NYU Langone Health and Bellevue NYCH +  
Hospitals  
New York

**NEUROPSYCHIATRIC IMAGING****Senior Editor****Jody Tanabe, MD**

Professor  
Chief of Neuroradiology  
University of Colorado-Anschutz Medical Campus

**Associate Editors****John-Paul J. Yu, MD, PhD**

Assistant Professor of Radiology, Psychiatry, and  
Biomedical Engineering  
University of Wisconsin School of Medicine and  
Public Health

**J. Eric Schmitt, MD, PhD**

Assistant Professor of Radiology and Psychiatry  
Division of Neuroradiology  
Perelman School of Medicine, University of  
Pennsylvania

**NEUROVASCULAR/STROKE IMAGING****Senior Editor****Ajay Gupta, MD, MS**

Professor and Chair, Department of Radiology  
Columbia University  
New York

**Associate Editors****Shalini Amukotuwa, MB BS, PhD,  
FRANZCR**

Head of Neuroradiology and Director of MRI,  
Monash Health  
Associate Professor of Radiology, Monash University  
Australia

**Mahmud Mossa-Basha, MD**

Professor of Radiology, Neurology and Electrical  
Engineering  
Vice Chair of Clinical Research and Clinical  
Transformation  
Co-Director of the Research Vascular Imaging Lab  
University of Washington School of Medicine

**PEDIATRIC NEUROIMAGING****Senior Editor****Caroline D. Robson, MBChB**

Division Chief & Endowed Chair, Neuroradiology  
Director, Head & Neck Imaging  
Department of Radiology  
Department of Otolaryngology  
Boston Children's Hospital  
Harvard Medical School

**Associate Editors****Anna Trofimova, MD, PhD**

Assistant Professor, Radiology and Imaging  
Sciences, Emory University  
Pediatric Neuroradiologist, Children's Healthcare  
of Atlanta

**Matthew Whitehead, MD**

Department of Radiology, Division of  
Neuroradiology  
Children's Hospital of Philadelphia  
Associate Professor of Radiology  
Perelman School of Medicine, University of  
Pennsylvania

**SPINE IMAGING AND SPINE IMAGE-GUIDED  
INTERVENTIONS****Senior Editor****J. Levi Chazen, MD**

Associate Professor, Neuroradiology  
Director, Spine Imaging  
Hospital for Special Surgery  
Weill Cornell Medicine  
New York

**Associate Editors****Jennifer McCarty, MD**

UTHealth Houston

**Vinil Shah, MD**

Associate Professor of Radiology Neuroradiology  
Division Chief  
University of California, San Francisco

**ULTRA-HIGH-FIELD MRI/IMAGING OF  
EPILEPSY/DEMYELINATING DISEASES/  
INFLAMMATION/INFECTION****Senior Editor****Erik Middlebrooks, MD**

Professor of Radiology  
Mayo Clinic Florida

**Associate Editors****Susie Y. Huang, MD, PhD**

Associate Professor of Radiology, Harvard  
Medical School  
Associate Chair, Faculty Affairs, Department of  
Radiology  
Director of Translational Neuro MR Imaging &  
Connectomics, Athinoula A. Martinos Center for  
Biomedical Imaging  
Massachusetts General Hospital

**Girish Bathla, MD, FRCR**

Associate Professor, Neuroradiology  
Mayo Clinic  
Minnesota

**OUTREACH AND EDUCATION****Senior Editor****Lea Alhilali, MD**

Radiology Partners, HonorHealth Research  
Institute  
Arizona

**DIGITAL MEDIA AND ENGAGEMENT****Senior Editor****Kevin Hsu, MD**

Clinical Assistant Professor  
Department of Radiology  
NYU Grossman School of Medicine  
New York

**Case Collection Editors****Matylda Machnowska, BMedSc, MD,  
FRCSC, ABR**

Assistant Professor of Radiology, University of  
Toronto  
Neuroradiologist, Sunnybrook Health Sciences  
Centre

**Anvita Pauranik, MD**

Clinical Assistant Professor of Radiology  
BC Children's Hospital  
University of British Columbia

**Sandy Cheng-Yu Chen, MD**

Chair, Translational Imaging Research Center  
Taipei Medical University Hospital  
Vice President of Taipei Medical University

**Social Media Editor****Kimberly Seifert, MD, MS**

Stanford University  
California

**Assistant Social Media Editors****Ani Hoxha, MD**

Mother Theresa UHC  
Albania

**Maxwell Opoku, MD**

Novosibirsk State Research University  
Russia



#### Podcast Editor

##### **Kevin Hiatt, MD**

Assistant Professor, Radiology  
Wake Forest University School of Medicine  
North Carolina

#### Deputy Podcast Editor

##### **George K. Vilanilam, MD**

PGY5 Resident Physician, Department of Radiology  
University of Arkansas for Medical Sciences

#### STATISTICS

##### Senior Editor

##### **Bryan A. Comstock, MS**

Senior Biostatistician, Department of Biostatistics  
University of Washington

#### EDITORIAL FELLOWS

##### **Alexandre Boutet, MD, PhD**

Neuroradiologist  
Joint Department of Medical Imaging  
University of Toronto

##### **Nicholas S. Cho, MD/PhD Candidate**

University of California, Los Angeles

##### **Burak Berksu Ozkara, MD**

Research Fellow  
Department of Neuroradiology  
The University of Texas MD Anderson Center

#### BOOK REVIEW EDITOR

##### **Robert Quencer, MD**

Professor Emeritus  
Department of Radiology  
University of Miami

---

*Founding Editor*  
**Juan M. Taveras**

*Editors Emeriti*  
Mauricio Castillo, Robert I. Grossman,  
Michael S. Huckman, Robert M. Quencer,  
Jeffrey S. Ross

---

*Managing Editor*  
**Karen Halm**  
*Assistant Managing Editor*  
**Laura Wilhelm**  
*Executive Director, ASNR*  
**Mary Beth Hepp**

## Streamlining the Manuscript Submission Process at the *American Journal of Neuroradiology*: Paving the Way for Efficiency and Reducing Hurdles for Authors

Max Wintermark, Editor-in-Chief

**T**he *American Journal of Neuroradiology* (AJNR) has recently introduced a revamped submission process with the objective of improving efficiency, clarity, and expediting the dissemination of groundbreaking research within our field. One of the key features of this overhaul is the introduction of manuscript-specific submission templates, offering a more streamlined and standardized approach for authors.

For the initial submission of their manuscript, authors are strongly encouraged to use the initial submission template available on the AJNR website. This template, characterized by its simplicity, is crafted to ensure the coherent presentation of essential information necessary for the initial review. Incorporated within the template are clear instructions for authors, contributing to a user-friendly experience. The initial submission template is versatile and allows authors the flexibility of reusing the same docu-

ment for submission to another journal in the event of rejection from the AJNR, reflecting our commitment to prioritizing authors' efficiency and convenience.

On acceptance or assignment for revision, authors are directed to use revision templates tailored to their specific manuscript types. The adoption of these templates is not merely a procedural formality; rather, it serves as a catalyst for expediting the publication process because these templates can be easily converted into preprints that can be released promptly to the AJNR subscribers.

Authors are asked to disclose potential conflicts at the outset to ensure a transparent review process. However, the completion of more time-consuming disclosure forms is deferred until after manuscript acceptance or during the revision stage. This approach is designed to optimize authors' time, minimizing unnecessary tasks and focusing on specific requirements only when necessary.

In conclusion, AJNR's refined submission process underscores a commitment to transparency, efficiency, and the prompt dissemination of high-quality research in neuroradiology. The introduction of tailored submission templates not only simplifies the submission process for authors but also accelerates the journey of research from acceptance to publication. As the landscape of academic publishing evolves, AJNR's proactive measures position it at the forefront of facilitating a seamless and author-friendly publication experience.

# Patient Engagement in Neuroradiology: A Narrative Review and Case Studies

 Nadja Kadom,  Zofia M. Lasiecka,  Alexander J. Nemeth,  Jeffrey B. Rykken,  Yvonne W. Lui, and  David Seidenwurm



## ABSTRACT

**SUMMARY:** The field of patient engagement in radiology is evolving and offers ample opportunities for neuroradiologists to become involved. The patient journey can serve as a model that inspires patient engagement initiatives. The patient journey in radiology may be viewed in 5 stages: 1) awareness that an imaging test is needed, 2) considering having a specific imaging test, 3) access to imaging, 4) imaging service delivery, and 5) ongoing care. Here, we describe patient engagement opportunities based on literature review and paired with case studies by practicing neuroradiologists.

**ABBREVIATION:** OOPC = out-of-pocket cost

Patient engagement refers to the desire by, and capability of, patients to actively participate in their own health care journey, in a way uniquely appropriate to the individual, through collaboration with a care provider or health care institution, with the aim of improving health outcomes and enhancing the overall patient experience.<sup>1</sup> The idea of patient engagement emphasizes treating patients as active participants in their health care rather than passive recipients of medical advice. Neuroradiologists play a crucial role in patient care, and understanding patient engagement can substantially impact the way we interact with and provide care to our patients.

When adapted to neuroradiology practice, patient engagement includes giving access to the information and resources patients need to make decisions related to neuroimaging studies. This can include explaining the purpose, benefits, and potential risks of a particular imaging test or procedure to patients, addressing their concerns, and ensuring they have a clear understanding of the results and their implications. Fundamental principles in patient engagement comprise empowering patients to ask questions and express their preferences, recognizing that

patients have unique perspectives and knowledge about their own bodies, and allowing them to let their personal circumstances influence their health care choices.<sup>2</sup> By embracing patient engagement, neuroradiologists can create a patient-centered approach to care that can improve patient satisfaction, compliance with recommended treatments, and overall health outcomes.<sup>3</sup>

Here, we performed a narrative review of patient engagement opportunities in diagnostic neuroradiology or radiology by using a patient journey framework (Online Supplemental Data).<sup>4</sup> Additionally, members of the ASNR Quality, Safety, and Value Committee provided examples of initiatives from their own practices. Patient engagement is still a “young” movement in health care; because of a paucity of neuroradiology-specific examples in the published literature, some relevant adaptations were made from radiology in general or from medicine at large.

## The Patient Journey Framework


A simple and intuitive way to identify opportunities for patient engagement comes with patient journey mapping, where patients describe in sequence each step, point of contact, and each experience along their care journey.<sup>4</sup> Patient journey mapping is a visual representation of the patient’s points of engagement with the health care system as a linear path. This can be used as a tool to identify opportunities for improvement, for example, how radiology could meet a patient’s needs at each stage of this journey (Online Supplemental Data).


In general, there are 5 steps in this journey that have been described in medicine, which can be summarized as Awareness, Consideration, Access, Service Delivery, and Ongoing Care<sup>4</sup> and which we adapted to radiology. The journey starts with the patient’s Awareness that they need medical care, and it usually

Received September 20, 2023; accepted after revision September 20.

From the Emory University School of Medicine (N.K.), Children’s Healthcare of Atlanta, Atlanta, Georgia; Emory University School of Medicine (Z.M.L.), Atlanta, Georgia; Northwestern University, Feinberg School of Medicine, Northwestern Memorial Hospital (A.J.N.), Chicago, Illinois; University of Minnesota (M-Health) (J.B.R.), Minneapolis, Minnesota; New York University, Grossman School of Medicine (Y.W.L.), New York, New York; and Sutter Health (D.S.), Sacramento, California.

Please address correspondence to Nadja Kadom, MD, Department of Radiology, 1405 Clifton Rd NE, Atlanta, GA 30322; e-mail: nkadom@emory.edu; @nkpiano

 Indicates open access to non-subscribers at [www.ajnr.org](http://www.ajnr.org)

 Indicates article with online supplemental data.

<http://dx.doi.org/10.3174/ajnr.A8077>

involves information gathering through online searches, review sites, marketing campaigns, networking, and community involvement. During the Consideration stage, patients decide whether a health system can meet their needs by contemplating factors, such as referrals, coverage and benefits, recommendations, access, and ratings and reviews. Once decided, the Access stage refers to scheduling and preparing for a visit with a health care professional or service, which entails a variety of communications as part of the scheduling and patient acquisition process, as well as any information regarding getting to the location and how to prepare for the visit. The following Service Delivery stage extends from checking in to checking out, and includes admission, discharge, and billing. The final stage is Ongoing Care with a goal of attaining and maintaining wellness and/or continued care management. Here, we adapt these journey stages to radiology as follows: 1) awareness that an imaging test is needed, 2) considering having a specific imaging test, 3) access to imaging, 4) imaging service delivery, and 5) ongoing care (Online Supplemental Data).

### **Patient Engagement in Neuroradiology/Radiology**

In the following, we present a narrative review of patient engagement in neuroradiology by using the patient journey (Online Supplemental Data). When available, the content was enriched by case studies in neuroradiology that may not be available in the published literature and that highlight successes and barriers.

#### **Stage 1: Awareness**

**Definition.** Patient awareness of needing medical imaging involves information gathering (eg, online searches, review sites, marketing campaigns, networking, community involvement).<sup>4</sup>

**Narrative Review.** At this stage of the patient's journey, the key intervention to improve engagement is communication with the purpose of education, for example, through written information or through visuals, such as infographics or videos. Educational materials for patients become relevant and may change in content depending on the stage of the patient's journey.

Based on research in medicine, during the Awareness stage, patients mostly look for information on commercial websites (.com) (~70%), followed by using a search engine (~10%), or searching academically affiliated sites (.edu) (~10%) and government-sponsored websites (.gov) (5%).<sup>5</sup> Nonprofit organizations (.org) were not an important source of information.<sup>5</sup> The main issue with seeking information from commercial sites is that it can be challenging to differentiate useful health information from marketing and promotional materials. Accordingly, patients experienced higher levels of frustration when using search engines, and search engines required more effort, as well as raised concerns regarding the content quality.<sup>5</sup>

RadiologyInfo.org is a patient-facing website that is accessible at no charge and sponsored by the Radiological Society of North America and the American College of Radiology. The site explains various imaging modalities, including CT and MR imaging, and mentions specialties like mammography, women's and men's imaging, nuclear medicine, and radiation therapy, but does not explain other radiology subspecialties, such as neuroradiology. Among the conditions that are addressed on the site are

several neuroradiology entities, such as carotid artery stenosis, dementia, epilepsy, head and neck cancer, head injury, headache, parathyroid disease, and stroke. Entering the search terms "neuroradiology" or "neuroimaging," however, yields no results for patients who may have heard these terms and are looking for more information. RadiologyInfo.org has undergone revisions to improve language levels, but language levels remain very high, both for the English and Spanish language versions.<sup>6,7</sup>

ImageGently.org is mostly geared toward radiologists and promotes decreasing patient exposure to ionizing radiation, especially in children. ImageGentlyParents.org, while having its own website, contains currently very limited information for parents. It offers an option for submitting inquiries, but it is unclear who these messages are being sent to and what type of response to expect.

The American Society of Neuroradiology has dedicated a web page to patient information ([www.asnr.org/patientinfo](http://www.asnr.org/patientinfo)) and represents a great opportunity for neuroradiologists to become involved and collaborate with patients on adding meaningful and patient-centered content. Such efforts could alleviate patients' online search frustrations and offer curated and reliable content.<sup>5</sup> Linking neuroradiology-specific information to larger efforts, such as RadiologyInfo.org, could potentially increase the traffic on this website. Ideally, commercial patient-facing websites should promote content that was generated and/or curated by radiologists and neuroradiologists. Overall, this represents a great opportunity for neuroradiologists to develop content and enhance the field's visibility and value to patients.

There were no case studies for this section.

#### **Stage 2: Consideration**

**Definition.** Patients decide whether having an imaging test can meet their needs; involves weighing factors, for example, referrals, insurance coverage/out-of-pocket cost (OOPC), recommendations, access, ratings, and reviews.<sup>4</sup>

**Narrative Review.** To aid with the decision whether an imaging test would be useful, clinicians can use Clinical Decision Support systems. These systems typically relate to a specific clinical scenario, are evidence-based, and are intended to increase the appropriateness of imaging utilization.<sup>8</sup> Informed patients, however, may choose not to follow the recommendations that arise from the use of evidence-based guidelines because those do not incorporate patients' personal preferences.<sup>9</sup> Shared decision-making has evolved as an approach where clinical providers enable patients to make decisions that take into consideration both the clinical and scientific evidence, as well as the patient's personal context, goals, values, and preferences for health care.<sup>9</sup> Shared decision-making occurs continually along the patient journey, and radiology plays a role in deciding whether an imaging test is the best choice, which imaging test is most appropriate, and what to do with the imaging results. Patient decision aids can be used to convey scientific evidence, list trade-offs, and to elucidate patient preferences when deciding whether imaging is the best choice, such as for lung cancer screening.<sup>10</sup> There is currently a scarcity of patient-decision aids for imaging decisions, which represents a huge opportunity for neuroradiologists to get involved.



Patients often select providers that have been suggested to them by another health professional, and they may use comparative information when there is a specific health outcome they have in mind, or when they do not trust in their health provider.<sup>11</sup> Patients consider the following characteristics when choosing a provider: Availability under the existing insurance plan, accessible in a convenient location, affiliated with an academic center, certified/qualified physicians and staff, friendly and understanding communication style, provides updates, and more.<sup>11</sup>

An example of a publicly available site that offers comparable information on health care providers is Medicare's Care Compare,<sup>12</sup> and rankings performed by specific organizations, such as U.S. News or Leapfrog's Safety Grade. Of note, none of these sources include imaging services quality metrics in their scoring and ranking systems. Medicare's tool permits searching for and comparing radiologists on a limited number of features, such as distance from the patient, telehealth services, specialties, board certification, education and training, affiliations, etc. While accreditation status of an imaging facility may be a publicly available indicator of service quality, there is currently no list of features or metrics that could be used to better define and measure neuroradiology services quality.

Another opportunity for patient engagement at this stage lies with providing information regarding billing and OOPC. Starting in January 2021, the Centers for Medicare and Medicaid Services required that hospitals provide clear and accessible information regarding pricing for items and services.<sup>13</sup> Radiology practices can offer patient-friendly price transparency tools to estimate personalized OOPC, which patients may perceive as a benefit.<sup>14</sup> Of note, these estimates may vary over time and can be inaccurate.<sup>14</sup> For example, patients from the same insurance company can each have different OOPCs, and those insurance contracts change over time. An important aspect of offering price transparency tools is to couple access with explanations of differences in service when paying more.<sup>15</sup> For example, patients with severe back pain listed among services and features that they would pay more for: improved imaging results accuracy, an imaging facility that was recommended by the provider, or a facility with a higher online star rating.<sup>15</sup> As neuroradiologists, we are aware that patients who pay more do not necessarily receive higher quality care. There is an opportunity to engage patients in jointly defining quality indicators and jointly raising awareness of neuroradiology service quality metrics that are worth paying more for.

A case study *A Patient Decision Aid (PDA) for Imaging Pediatric Headache* has been added for this section (Online Supplemental Data).

### Stage 3: Access

**Definition.** Scheduling and preparing for an imaging test; involves communications (eg, scheduling), patient acquisition process, directions to the imaging location, and test preparation.<sup>4</sup>

**Narrative Review.** Allowing patients to book their own appointments increases patient engagement, as indicated by a reduction in the number of missed appointments.<sup>16</sup> Self-scheduling also allows patients to schedule appointments so that relatives can join them.<sup>17</sup> While many radiology practices offer online scheduling

for patients, many academic imaging centers that use centralized scheduling have difficulty in offering this service to their patients.<sup>18</sup> There is a huge opportunity to advocate for patient self-scheduling in neuroradiology, understanding that this may require elaborate algorithms to help patients schedule the examination on a scanner in the system that is best suited to deliver the image quality required for their clinical indication, for example, ability to perform functional MR imaging before neurosurgical interventions or perfusion imaging for patients with brain tumors. Commercial applications are evolving.<sup>19</sup> Patients may want to reach out to the imaging facility with questions ahead of their appointment, which could be addressed by offering a number to call or by giving access to a blog site that shows answers to frequently asked questions.<sup>20</sup> Of note, offering self-scheduling can create disparities for patients, which could be mitigated by pairing this service with efforts of facilitating portal use for all patient populations.<sup>21</sup>

At this stage in the patient journey, it would be appropriate to provide patients with information regarding items to bring to the appointment, patient preparation instructions, an explanation of the check-in process, navigation and wayfinding, and checklists before CT and MR imaging examinations.<sup>22</sup> Such information can easily be shared through electronic patient portals, mobile applications, or websites.<sup>21</sup>

The concept of helping patients prepare for an imaging study may differ between radiologists and patients. Radiologists naturally focus on preparing patients to assure the images can be acquired without complications and will be of diagnostic quality. Examples include limiting PO intake before a fluoroscopy examination of the upper gastrointestinal tract or advising patients not to use deodorant before a mammogram. Patient-centered preparation, on the other hand, may include explanations of the imaging modality and technique, and any discomfort or risks associated with it, such as lying on a hard MR imaging table for a prolonged period, exposure to ionizing radiation in CT, need for sedation in MR imaging, physical effects of IV contrast injections, and risks associated with a variety of IV contrast agents. Patients may feel uncomfortable thinking they have to undress for an examination and an explanation on why, how, and where to undress can help alleviate anxiety ahead of time. Infographics and leaflets can be effective in providing patients with the information they seek at an accessible language level and are typically reinforced by visuals.<sup>22,23</sup> Virtual reality applications have also proved useful, particularly in preparing patients for MR imaging scans.<sup>24</sup>

Wayfinding can be improved by sharing maps and images of sites, parking options, and entrances before the appointment.<sup>22</sup> It is important to include patients in the process of developing these materials, to assure they meet patients' needs.<sup>22</sup> Neuroradiologists could examine their patients' ability to find imaging sites and advocate for more effective wayfinding design, which may include wayfinding kiosks or apps in addition to design features that include color coding, landmarks, room and elevator labeling, and signage.<sup>25</sup>

A case study *Our Pediatric Radiology Website* has been added for this section (Online Supplemental Data).

#### **Stage 4: Service**

**Definition.** Having the imaging test; involves participation (eg, checking in), following instructions, enduring discomfort, discharge, billing.<sup>4</sup>

**Narrative Review.** Delays can be avoided if patients are informed ahead of time what information they will need upon check-in. Facilitated by the COVID-19 pandemic, some imaging practices continue to offer remote check-in to their patients,<sup>26</sup> which can conceivably save time and create a sense of privacy. Of note, the check-in process provides an opportunity to let patients know about access to patient portals.<sup>20,27</sup>

Patients are generally motivated to cooperate with instructions for successful image acquisitions unless they cannot physically comply. There is a paucity of scripts that could help radiology technologists and nurses communicate to patients how they can cooperate.<sup>28</sup> Neuroradiologists could collaborate with technologists, nurses, and patients to develop scripts to let patients know how they can cooperate for neuroimaging studies. Communication and establishing rapport with patients are fundamental for managing patient distress, discomfort, or anxiety.<sup>29</sup> Patients may experience various discomforts, such as having to undress, needle sticks, and contrast effects, as well as uncomfortable positioning during image acquisitions. For neuroradiology, discomfort is mostly related to MR imaging, less so to CT imaging on modern scanners.<sup>30</sup> Simple interventions to decrease discomfort in MR imaging include shorter scanning protocols and audiovisual distraction with goggles and/or headphones.<sup>31</sup>

Before discharging the patient after the images have been acquired, there is an opportunity to give patients a preliminary report, or there may be a necessity to manage patients with critical findings immediately. While discussing preliminary results with patients is still not common practice in radiology, it was shown to be feasible in academic settings, such as head and neck cancer imaging, and is appreciated by patients.<sup>32,33</sup> Interestingly, patients may only appreciate the service after they have experienced it.<sup>33</sup> Decades of negative stereotypes about radiologists, such as radiologists avoiding patient contact, being antisocial, and focused on lifestyle or money rather than patient care<sup>34</sup> have slowed the adoption of direct communications with patients. In a European practice model, results communication directly to patients resulted in highly relevant changes to the radiology report in one-third of cases.<sup>35</sup> Interestingly, radiologists who did not offer direct communication with patients were viewed by patients as being less competent.<sup>35</sup> In the United States, there is currently no established reimbursement model for diagnostic radiology consultations with patients that could drive broader adoption of this service.

On occasion, critical findings may be uncovered on an outpatient imaging examination and may necessitate immediate action. For example, a brain tumor may be found on outpatient imaging for headaches or seizures. The technologist may alert the radiologist to such a finding to facilitate modifying the imaging protocol, such as adding IV contrast and/or potentially adding spine imaging. The changes in the imaging protocol may alert the patient that something unusual has occurred which can cause increased anxiety and questions. Radiologists may be

asked to explain the situation to the patient and should be prepared to do so.

Radiologists should be trained in explaining imaging findings.<sup>36,37</sup> The American College of Radiology provides a free Communication Curriculum for patient communications that can be used by any radiologist, practicing or in training.<sup>38</sup> Key concepts in communicating with patients include a supportive environment, ability to establish rapport, ability to open a discussion, ability to elicit more information, ability to understand the patient's and family's preferences, ability to share information at the patient's literacy level, providing accurate information, being empathetic, and providing closure.<sup>36,39</sup>

When all is said and done, it may not be clear to patients what will happen next. At the time of discharging patients from the imaging facility additional information can be provided, such as instructions on how to access results, which is of immediate interest to most patients.<sup>40</sup> In addition, discharge information to engage patients may include options for contacting a radiologist, a reminder to follow-up with the referring provider, an invitation to provide feedback regarding the services in a survey, or instructions on how to exit the facility. Patients who had a contrast reaction may be given documentation of the contrast that was administered, the type of reaction that was observed, and how it was treated, so they can make future decisions regarding the risks of repeat IV contrast administrations. Similarly, there may be follow-up instructions for patients with contrast extravasations.

Three case studies have been added for this section: *Reading Room in Brain Tumor Clinic* (Online Supplemental Data), *A Companion Case of Embedded Reading Rooms: One Stop Shop* (Online Supplemental Data), and *Bad News Bear Program* (Online Supplemental Data).

#### **Stage 5: Ongoing Care**

**Definition.** Dealing with imaging results (eg, deciding next steps in care, dealing with a diagnosis and with unexpected actionable findings, dealing with diagnostic uncertainty).<sup>4</sup>

**Narrative Review.** The radiology results can play an important role in the patient's ongoing care, such as anxiety relief when a severe diagnosis is excluded, informing further management when a diagnosis is established, indicating and coordinating the use of additional resources to arrive at a diagnosis, and providing information regarding prognosis for an established diagnosis.

Normal imaging results are valuable for diagnoses that lack specific diagnostic criteria and require exclusion of other entities, such as hypertensive encephalopathy.<sup>41</sup> Additionally, in adult headache patients, normal imaging results can decrease patient anxiety and lower cost by reducing downstream utilization of health care services.<sup>42</sup> Radiologists have an opportunity to use the word "normal" rather than more obscure verbiage ("negative") to make it easy for patients to understand this type of result.<sup>43</sup>

When a diagnosis is established through radiology findings, it is important that patients can understand what this finding means to make decisions regarding next steps. The Joint Commission's National Patient Safety Goals state that patients make better health care decisions when they understand their personal health data.<sup>44</sup> Radiology results are always documented

and communicated in writing. The key tenets for patient engagement entail making radiology written reports both accessible and understandable to patients.<sup>30</sup> To improve patients' ability to comprehend radiology reports, a variety of interventions can be used, such as lay summaries,<sup>45</sup> Generative Pretrained Transformer translations,<sup>46</sup> or multimedia reports that link to lexica and explanatory images.<sup>47</sup> Interestingly, 82% of patients preferred receiving the detailed report rather than a lay summary, particularly for abnormal results.<sup>48</sup> In addition, radiologists could make themselves available to patients if there are questions, for example, by adding their phone number to the report or offering virtual consultations.<sup>49,50</sup>

There remain concerns regarding patients' reactions to reports when there is a finding, such as increased anxiety. While a few cases of suicide in response to devastating radiology results have been reported, patients prefer getting access to results even when it increases their anxiety.<sup>51</sup>

Patients are increasingly viewing radiology reports via patient portals, but portals are far from being used by all patients, which likely reflects a variety of disparities based on race, primary language, insurance status, and other factors.<sup>52</sup> A set of "Universal Precautions" has been proposed to improve communication and participation for all patients regardless of health literacy.<sup>52</sup> These precautions contain 18 actions that promote the development of effective patient-centered communications.<sup>52</sup> Besides forming a team and working with patients on the development of communications, additional advice includes offering actionable content, by using intuitive design, tailoring messages to specific patient needs, and much more.<sup>52</sup>

An evolving area for patient engagement in radiology pertains to follow-up recommendations for actionable incidental findings. Radiologists are using direct patient notifications to increase adherence to follow-up recommendations, which could be as low as 52%.<sup>53,54</sup> The impact of direct notification of the patient on follow-up adherence may be low in systems with an existing reliable process for notifying providers of recommended follow-up.<sup>55,56</sup> There is currently not enough scientific evidence exploring other patient engagement benefits from direct notifications, such as building trust and loyalty, which represents a research opportunity for neuroradiologists.

Two case studies have been added for this section: *Video Reporting* (Online Supplemental Data) and *Actionable Incidental Findings Notifications to Patients* (Online Supplemental Data).

## CONCLUSIONS

The vision for neuroradiology is to cultivate patient engagement and transform the traditional practice model into a collaborative effort that creates an empowered patient journey. Neuroradiologists can demonstrate commitment to this vision through initiatives that promote transparent communication, accessible information, and shared decision-making for patients. This vision is grounded in collaboration between patients, neuroradiologists, and health care providers to align products and services with patients' needs and preferences. By valuing patient perspectives, neuroradiologists can inspire a new era of collaboration in health care.

Disclosure forms provided by the authors are available with the full text and PDF of this article at [www.ajnr.org](http://www.ajnr.org).

## REFERENCES

- Higgins T, Larson E, Schnall R. **Unraveling the meaning of patient engagement: a concept analysis.** *Patient Educ Couns* 2017;100:30–36 CrossRef Medline
- Detmer D, Singleton P, Macleod A, et al. **The informed patient: study report.** 2003
- Hibbard JH, Greene J. **What the evidence shows about patient activation: better health outcomes and care experiences; fewer data on costs.** *Health Aff (Millwood)* 2013;32:207–14 CrossRef Medline
- Joseph AL, Kushniruk AW, Borycki EM. **Patient journey mapping: current practices, challenges and future opportunities in health-care.** *Knowledge Manage e-learning* 2020;12:387
- LaValley SA, Kiviniemi MT, Gage-Bouchard EA. **Where people look for online health information.** *Health Info Libr J* 2017;34:146–55 CrossRef Medline
- Bange M, Huh E, Novin SA, et al. **Readability of patient education materials from RadiologyInfo.org: has there been progress over the past 5 years?** *AJR Am J Roentgenol* 2019;213:875–79 CrossRef Medline
- Novin SA, Huh EH, Bange MG, et al. **Readability of Spanish-language patient education materials from RadiologyInfo.org.** *J Am Coll Radiol* 2019;16:1108–13 CrossRef Medline
- Zygmunt ME, Ikuta I, Nguyen XV, et al. **Clinical decision support: impact on appropriate imaging utilization.** *Acad Radiol* 2023;30:1433–40 CrossRef Medline
- Montori VM, Brito JP, Murad MH. **The optimal practice of evidence-based medicine: incorporating patient preferences in practice guidelines.** *JAMA* 2013;310:2503–04 CrossRef Medline
- Agency for Healthcare Research and Quality. **Is lung cancer screening right for me?** <https://effectivehealthcare.ahrq.gov/sites/default/files/wysiwyg/lung-cancer-screening-decision-aid.pdf>. Accessed June 24, 2023
- Victoor A, Delnoij DM, Friele RD, et al. **Determinants of patient choice of healthcare providers: a scoping review.** *BMC Health Serv Res* 2012;12:272 CrossRef Medline
- Medicare. **Care compare.** <https://www.medicare.gov/care-compare/>. Accessed June 25, 2023
- Centers for Medicare and Medicaid Services. **Hospital price transparency.** <https://www.cms.gov/hospital-price-transparency#:~:text=Starting%20January%201%2C%202021%2C%20each,with%20all%20items%20and%20services>. Accessed July 11, 2023
- Sadigh G, Carlos RC. **Price transparency in radiology: challenges and opportunities to improve.** *AJR Am J Roentgenol* 2021;217:1243–44 CrossRef Medline
- Manik R, Carlos RC, Duszak R Jr, et al. **Costs versus quality in imaging examination decisions.** *J Am Coll Radiol* 2022;19:450–59 CrossRef Medline
- Dusheiko M, Gravelle H. **Choosing and booking and attending? Impact of an electronic booking system on outpatient referrals and non-attendances.** *Health Econ* 2018;27:357–71 CrossRef Medline
- Kruuse-Jensen K, Madsen KS, Bruun DM, et al. **Do outpatients with cancer and their relatives want to use an online booking system to book the appointment and radiographer for their CT examination? A small-scale study in Denmark.** *Radiography (Lond)* 2022;28:174–79 CrossRef Medline
- Itri JN. **Patient-centered radiology.** *Radiographics* 2015;35:1835–46 CrossRef Medline
- Hamilton-Basich M. **openDoctor to deliver radiology digital front door experience.** *AXIS Imaging News*. March 9, 2021.
- Towbin AJ, O'Connor T, Perry LA, et al. **Using informatics to engage patients.** *Pediatr Radiol* 2020;50:1514–24 CrossRef Medline
- Ganeshan S, Pierce L, Mourad M, et al. **Impact of patient portal-based self-scheduling of diagnostic imaging studies on health disparities.** *J Am Med Inform Assoc* 2022;29:2096–100 CrossRef Medline

22. Wahab SA, Wahab RA, Butcher B, et al. **Humanizing radiology appointment education to improve patient experience.** *J Am Coll Radiol* 2022;19:647–51 CrossRef Medline
23. Ginat DT, Christoforidis G. **A printed information leaflet about MRI and radiologists improves neuroradiology patient health literacy.** *Neuroradiol J* 2018;31:609–13 CrossRef Medline
24. Ashmore J, Di Pietro J, Williams K, et al. **A free virtual reality experience to prepare pediatric patients for magnetic resonance imaging: cross-sectional questionnaire study.** *JMIR Pediatr Parent* 2019;2:e11684 CrossRef
25. Harper C, Jefferies S, Crosser A, et al. **Exploring hospital wayfinding systems: touchscreen kiosks, apps and environmental cues.** In: *Proceedings of the International Symposium on Human Factors and Ergonomics in Health Care* (Vol. 8, No. 1, pp. 172–175), 2019. Los Angeles: SAGE CrossRef
26. RadNet. **Virtual Check-iN.** <https://www.radnet.com/community-radiology/remote-check-in>. Accessed July 11, 2023
27. Vincoff NS, Barish MA, Grimaldi G. **The patient-friendly radiology report: history, evolution, challenges and opportunities.** *Clin Imaging* 2022;89:128–35 CrossRef Medline
28. Bankier AA, O'Donnell CR, Boisselle PM. **Quality initiatives. Respiratory instructions for CT examinations of the lungs: a hands-on guide.** *Radiographics* 2008;28:919–31 CrossRef Medline
29. Lang EV. **Managing distress, discomfort, and anxiety in imaging.** *Radiol Manage* 2011;33:55–58 Medline
30. Niehoff JH, Heuser A, Michael AE, et al. **Patient comfort in modern computed tomography: what really counts.** *Tomography* 2022;8:1401–12 CrossRef Medline
31. Oztek MA, Brunnquell CL, Hoff MN, et al. **Practical considerations for radiologists in implementing a patient-friendly MRI experience.** *Top Magn Reson Imaging* 2020;29:181–86 CrossRef Medline
32. Pahade J, Couto C, Davis RB, et al. **Reviewing imaging examination results with a radiologist immediately after study completion: patient preferences and assessment of feasibility in an academic department.** *AJR Am J Roentgenol* 2012;199:844–51 CrossRef Medline
33. Mohan SK, Hudgins PA, Patel MR, et al. **Making time for patients: positive impact of direct patient reporting.** *AJR Am J Roentgenol* 2018;210:W12–17 CrossRef Medline
34. Grimm LJ, Fish LJ, Carrico CW, et al. **Radiology stereotypes, application barriers, and hospital integration: a mixed-methods study of medical student perceptions of radiology.** *Acad Radiol* 2022;29:1108–15 CrossRef Medline
35. Gutzeit A, Sartoretti E, Reisinger C, et al. **Direct communication between radiologists and patients improves the quality of imaging reports.** *Eur Radiol* 2021;31:8725–32 CrossRef Medline
36. Rockall AG, Justich C, Helbich T, et al. **Patient communication in radiology: moving up the agenda.** *Eur J Radiol* 2022;155:110464 CrossRef Medline
37. Harvey JA, Cohen MA, Brenin DR, et al. **Breaking bad news: a primer for radiologists in breast imaging.** *J Am Coll Radiol* 2007;4:800–08 CrossRef Medline
38. American College of Radiology. **Communication curriculum.** <https://www.acr.org/Member-Resources/rfs/learning/Communication-for-Radiology-Residents>. Accessed July 12, 2023
39. Brown SD, Rider EA, Jamieson K, et al. **Development of a standardized Kalamazoo communication skills assessment tool for radiologists: validation, multisource reliability, and lessons learned.** *AJR Am J Roentgenol* 2017;209:351–57 CrossRef Medline
40. Koney N, Roudenko A, Ro M, et al. **Patients want to meet with imaging experts.** *J Am Coll Radiol* 2016;13:465–70 CrossRef Medline
41. Potter T, Schaefer TJ. **Hypertensive Encephalopathy.** Treasure Island, FL: StatPearls. <https://www.ncbi.nlm.nih.gov/books/NBK554499>. Accessed July 12, 2023
42. Howard L, Wessely S, Leese M, et al. **Are investigations anxiolytic or anxiogenic? A randomised controlled trial of neuroimaging to provide reassurance in chronic daily headache.** *J Neurol Neurosurg Psychiatry* 2005;76:1558–64 CrossRef Medline
43. Hoang JK. **Avoid jargon terms for normal.** *J Am Coll Radiol* 2015;12:546 CrossRef Medline
44. Mishra VK, Hoyt RE, Wolver SE, et al. **Qualitative and quantitative analysis of patients' perceptions of the patient portal experience with OpenNotes.** *Appl Clin Inform* 2019;10:10–18 CrossRef Medline
45. American College of Radiology Data Science Institute. **Patient Friendly Report Summary.** <https://www.acrdsi.org/DSI-Services/Define-AI/Use-Cases/Automated-Patient-Friendly-Report-Summary>. Accessed June 24, 2023
46. Lyu Q, Tan J, Zapadka ME, et al. **Translating radiology reports into plain language using ChatGPT and GPT-4 with prompt learning: results, limitations, and potential.** *Vis Comput Ind Biomed Art* 2023;6:9 CrossRef Medline
47. Folio LR, Machado LB, Dwyer AJ. **Multimedia-enhanced radiology reports: concept, components, and challenges.** *Radiographics* 2018;38:462–82 CrossRef Medline
48. Mangano MD, Rahman A, Choy G, et al. **Radiologists' role in the communication of imaging examination results to patients: perceptions and preferences of patients.** *AJR Am J Roentgenol* 2014;203:1034–39 CrossRef Medline
49. Kemp J, Gannuch G, Kornbluth C, et al. **Radiologists include contact telephone number in reports: experience with patient interaction.** *AJR Am J Roentgenol* 2020;215:673–78 CrossRef Medline
50. Panagides JC, Achuck E, Daye D. **Synchronous virtual patient consultations in radiology.** *AJR Am J Roentgenol* 2022;219:164–65 CrossRef Medline
51. Kadom N, Tamasi S, Vey BL, et al. **Info-RADS: adding a message for patients in radiology reports.** *J Am Coll Radiol* 2021;18:128–32 CrossRef Medline
52. Smith B, Magnani JW. **New technologies, new disparities: the intersection of electronic health and digital health literacy.** *Int J Cardiol* 2019;292:280–82 CrossRef Medline
53. Mabotuwana T, Hall CS, Hombal V, et al. **Automated tracking of follow-up imaging recommendations.** *AJR Am J Roentgenol* 2019;212:1287–94 CrossRef Medline
54. Mannix J, LaVoye J, Wasserman M, et al. **Notification system for overdue radiology recommendations improves rates of follow-up and diagnosis.** *AJR Am J Roentgenol* 2021;217:515–20 CrossRef Medline
55. Mattay GS, Mittl GS, Zafar HM, et al. **Early impact of Pennsylvania Act 112 on follow-up of abnormal imaging findings.** *J Am Coll Radiol* 2020;17:1676–83 CrossRef Medline
56. Loftus R, Kadom N, Wandtke B. **Impact of early direct patient notification on follow-up completion for non-urgent actionable incidental radiology findings.** *J Am Coll Radiol* 2023 Oct 9:S1546–1440 (23)00758–55

# Young Professionals in Neuroradiology: Opportunities, Challenges, and Future Directions

Anna V. Trofimova, Yi Li, Parisa Mazaheri, Arun Krishnan, Seyedmehdi Payabvash, Manon Kappelhof, and Judith A. Gadde

## ABSTRACT

**SUMMARY:** The Young Professionals Committee of the American Society of Neuroradiology identifies and serves the interests of young professionals in neuroradiology, defined as those still in training or within 5 years of its completion. Being a young professional is an exciting, dynamic, and demanding stage of one's professional career. As the landscape of neuroradiology practice changes, new opportunities and challenges occur for those in the early stage of their career. It is important to recognize and support the needs of young professionals because an investment in their professional development is an investment in the future of our specialty. In this article, we aimed to address the most notable developments relevant to current and future young professionals in neuroradiology as well as highlight the work done by the Young Professionals Committee of the American Society of Neuroradiology in serving the needs of these young professionals, focusing on early neuroradiology engagement, flexible work arrangements, private practice, social media, artificial intelligence, and international collaborations.

**ABBREVIATIONS:** AI = artificial intelligence; ASNR = American Society of Neuroradiology; YPC = Young Professionals Committee

The Young Professionals Committee (YPC) of the American Society of Neuroradiology (ASNR) identifies and serves the interests of young professionals in neuroradiology, defined as those still in training or within 5 years of its completion. The 2023–2024 YPC has brought together 46 volunteers from different backgrounds, training and career stages, geographic locations, and practice settings to share their unique perspectives on serving the needs and supporting the professional development of young professionals in neuroradiology nationwide and outside the United States. Being in training and transitioning into practice as a junior practitioner are relatively short-but-demanding stages of one's professional career. Activities pertaining to this stage remain relevant across multiple generations of radiologists, including the excitement and challenges of choosing a first job, solidifying clinical expertise and developing a clinical practice, and establishing an academic niche and/or building a foundation

for future promotion. Some of the opportunities and dilemmas posed before today's young professionals are unique, however, shaped by the current changing socioeconomic and health care environment and by technologic advances and generational changes, adding additional layers of complexity.

In this article, we aimed to address the most notable developments relevant to current and future young professionals in neuroradiology as well as to highlight the work done by the YPC of the ASNR in serving the needs of these young professionals, focusing on early neuroradiology engagement, flexible work arrangements, private practice, social media, artificial intelligence (AI), and international collaborations.

## Significance of Early Engagement in Neuroradiology

With the expansion of academic and private medical centers and rising clinical volumes in neuroradiology, there is an increasing recognition of the importance of recruiting young physicians to our field.<sup>1</sup> Prior research shows that earlier exposure<sup>1,2</sup> and mentorship<sup>3</sup> during medical school, even as early as middle school,<sup>4</sup> influences entry into medicine as well as residency and specialty selection. Subsequent experiences in early radiology residency heavily influence the choice of subspecialty. Most important, mentorship at early stages of medical education also introduces diversity into the field, whereby those who are currently underrepresented are encouraged to engage with neuroradiology, generating a path toward an eventual career choice.<sup>4</sup> A recent survey of Program Directors in Radiology showed that early mentorship

Received July 21, 2023; accepted after revision September 29.

From the Children's Healthcare of Atlanta (A.V.T.), Emory University School of Medicine, Atlanta, Georgia; University of California (Y.L.), San Francisco, California; Mallinckrodt Institute of Radiology (P.M.), Washington University School of Medicine, St. Louis, Missouri; Northside Radiology Associates (A.K.), Atlanta, Georgia; Yale School of Medicine (S.P.), New Haven, Connecticut; Amsterdam University Medical Center (M.K.), University of Amsterdam, Amsterdam, the Netherlands; and Ann & Robert H. Lurie Children's Hospital of Chicago (J.A.G.), Northwestern University Feinberg School of Medicine, Chicago, Illinois.

Please address correspondence to Anna V. Trofimova, MD, PhD, Children's Healthcare of Atlanta, Emory University School of Medicine, 1405 Clifton Rd, Atlanta, GA 30322; e-mail: atrofim@emory.edu; @DrTrofimova

<http://dx.doi.org/10.3174/ajnr.A8147>



was thought to be the most important factor for increasing the recruitment of women and underrepresented-in-medicine students into the field of radiology.<sup>5</sup> In multiple other male-dominated specialties such as surgery, earlier outreach has been shown to decrease the sex gap.<sup>6</sup>

With these factors in mind, the ASNR and YPC recognize that early outreach to high school students, medical students, and junior residents is important for establishing a pipeline of future neuroradiologists from diverse backgrounds. This collective pool of learners will develop into the future leaders of our profession. To introduce medical students to a career in neuroradiology early in their medical education, at the 2023 ASNR Annual Meeting, the YPC hosted 10 medical students from the Chicago area on a tour of the Annual Meeting. These medical students attended oral and poster sessions and engaged with attendees. They were also invited to join the YPC mentoring reception and to meet with residents, fellows, and practicing neuroradiologists, to learn from both the junior and senior members of our society. Additionally, recognizing the importance of early engagement, for the first time, the ASNR sponsored fifteen \$1000 scholarships for medical students who received awards for best abstracts, allowing them to attend and present their research at the 2023 Annual Meeting.

Before the 2023 Annual Meeting in the fall of 2022, the YPC hosted a virtual webinar directed at medical students and residents to introduce these learners to the diversity of career options in neuroradiology. In this webinar, speakers from different geographic and practice settings spoke about how they found their way to the field of neuroradiology and how they chose their practice setup and their subspecialty.

Finally, in an effort to engage with those early in training and to recruit them into neuroradiology, the YPC is expanding its current mentoring program to include medical students and residents. In the current mentorship program, senior faculty mentors are matched with junior faculty mentees from different institutions on the basis of mutual personal, research, and clinical interests. In an expansion of this program, junior faculty can serve as mentors for medical students, residents, and fellows, allowing mentorship and sponsorship across institutions starting at earlier levels of training. This plan will open opportunities for research and collaboration to those at smaller institutions and will expand the reach of engagement in neuroradiology.

Young professionals in the neuroradiology community can actively participate in these efforts by joining the YPC mentorship program, by being matched with trainees around the country. Locally, early career faculty can reach out to underrepresented students and offer shadowing experience in the reading room, as well as mentorship in research and educational projects. Faculty can support and sponsor students' entry into the field of radiology and neuroradiology and grow the ranks of our profession.

### **The Value of Flexible Work Arrangements**

Workplace flexibility is of varying importance across generations, with Millennials (born between 1981 and 1996) and Gen Z (born between 1996 and 2010) placing the highest value on such arrangements. Recent surveys reveal that workplace flexibility is the foremost criterion for new job selection among these age

groups,<sup>7</sup> including young professionals in neuroradiology. This preference is especially important because Millennials will constitute 75% of the workforce by 2025.<sup>8</sup>

Flexible work arrangements remove barriers to career advancement and foster a sense of inclusion among radiologists. Workplace flexibility can be achieved in multiple ways, such as flexitime (flexible work hours within a defined timeframe such as flexible starting and ending times), flexiplace (remote work), a compressed week, and part-time work. At the individual level, flexible arrangements increase radiologists' autonomy and reduce burnout by allowing them to better manage their personal and professional responsibilities. This flexibility is especially important for individuals with more personal responsibilities, particularly women, young radiologists, those in dual-earner households, and individuals with children.<sup>9</sup> Institutions, as well as radiologists, will benefit from the flexibility. At the organizational level, workplace flexibility has been shown to increase productivity, lower costs, improve recruitment and retention of radiologists, increase diversity, and improve job satisfaction.<sup>10</sup>

Limited data are available on the prevalence of flexible work arrangements in radiology. Initially used for after hours or urgent studies, teleradiology services were primarily provided by corporate practices. Especially with the onset of the coronavirus 2019 (COVID-19) pandemic, however, academic institutions have started to embrace fully remote positions. For example, the University of Rochester Medical Center (Rochester, New York) has seen notable adoption of remote positions, with 40% of new faculty hires in 2022 being in fully remote roles. As of April 2023, 12.5% of the clinical faculty at the institution are completely remote and seamlessly integrated into the academic and education mission.<sup>11</sup> According to the 2019 American College of Radiology Commission on Human Resources Workforce Survey, 16% of radiologists worked part-time and 68% of practices had part-time radiologists in 2019.<sup>12</sup>

It is time to re-imagine neuroradiology workspace and workflow along with other industries. As we move forward, we should not only allow but also encourage flexible practices to conform to the preferences of a new generation of practitioners. We must also actively work on biases such as proximity bias, which is the unfair preference and recognition given to employees working on-site based on the false assumption that people are more productive on-site than at home.<sup>13</sup>

A hybrid remote approach, in which radiologists are present on-site for a few days per week and work the remaining days remotely, may be an appropriate intermediate approach. This model offers numerous benefits in both academic and private practice environments, such as expanded access to skilled professionals for remote sites, improved equity and fairness, increased productivity, reduced expenses, added personal flexibility and autonomy, and overall better work experiences for radiologists.

### **Changing the Private Practice Landscape**

One of the strategic goals of the ASNR YPC is to identify the specific needs and career development resources for supporting young professionals in neuroradiology in private practice settings. Neuroradiology, similar to other subspecialties in radiology, is undergoing an evolution in private practice. There is an overall

increased demand for radiology services as the number of examinations continues to grow after the immediate and marked increase in imaging examination volume following the COVID-19 pandemic, known as the post-COVID-19 bounce.<sup>14,15</sup> Additionally, the trend toward increased subspecialization, as well as retirement and burnout, has increased the need for neuroradiologists in private practice.<sup>16</sup> This need is driven by requests of referring clinician specialists, the desire for increased quality, the need for efficiency with ever-larger imaging sets, the increased need to be familiar with advanced technology and how to use it, and the advancement of stroke management with the neuroradiologist serving a key role. All these factors have increased the needs of private practices to employ neuroradiologists.<sup>17-19</sup> The further consolidation of private practices into larger groups has also contributed to the trend of subspecialization from a practical aspect. In many groups, however, some degree of general skills may also be preferred to manage on-call and cross-coverage responsibilities. Smaller private practices are most likely to continue to have opportunities for those who want to practice both general radiology and neuroradiology.

Larger private practice groups allow a larger number of neuroradiologists to share the call pool and coverage for vacation, holidays, and weekends. These features have resulted in an increased demand for neuroradiologists by private practices with a variety of job opportunities. Neuroradiology job seekers have options of traditional on-site, remote, and hybrid work settings to meet the demands of the specific group and the desired lifestyle for the individual radiologist. Many larger practices have 24/7 stroke coverage, which often warrants employment of a team of neuroradiologists to allow complete coverage. Remote work has now become a mainstay of most private practices, and many groups offer remote or hybrid work.<sup>20</sup> The opportunity to choose a lifestyle-based practice also exists, with evening and overnight shifts often offering more vacation than traditional day shifts.

Regarding types of private practices, one can expect a choice of independent private practices; multispecialty private practices, which are often hospital based; and private equity-owned practices with the latter trend considerably increasing.<sup>21-23</sup> Full-time employed, part-time employed, and independent contractor opportunities are currently available and allow radiologists to customize their type of employment setting. The trend toward commoditization of radiology has also led to some practices that allow variable workloads with compensation proportionate to the number of studies read. Overall, private practice offers neuroradiologists flexibility to customize a work setting that is best for their lifestyle.

### ***The Role of Social Media in a Professional Career***

Professional social media use continues to become more prevalent in the radiology community, especially during and following the height of the COVID-19 pandemic. Twitter (now X) continues to be one of the most popular social media platforms in the radiology space. However, other platforms are also being used such as YouTube, Instagram, and TikTok, among others. There are many potential benefits to using social media professionally, including in education, leadership, mentorship/sponsorship,

research, branding, and academic advancement.<sup>24</sup> These are areas that can impact young professionals in their early careers.

The COVID-19 pandemic helped us see the positive effects that social media can have on professional networking and branding. The lack of geographic barriers allows social media to connect people across the world who might not ever cross paths physically. Additionally, social media is traditionally less hierarchical, potentially creating a sense of ease for young professionals to connect with more experienced radiologists. These interactions via social media can, therefore, lead to informal mentorship relationships for young professionals, in addition to the formal mentorship opportunities already available through the ASNR YPC. Professional relationships extending beyond colleagues at our workplace can be especially important when it comes to seeking referees for academic promotion.

The ASNR YPC has used social media to reach young professionals to alert them to opportunities. One specific example is using social media to advertise the dedicated YPC programming at the ASNR Annual Meeting. The free ASNR webinar that are shared via social media, as well as via e-mail, can also be very beneficial for young professionals. ASNR also uses social media to share volunteer opportunities, such as calls for committee or task force members, that can boost a young professional's curriculum vitae and serve as a networking opportunity within the society.

Some of the potential negative aspects of social media use are important to highlight as well. Before starting to use social media professionally, one should investigate any institutional or departmental social media policies, because these are becoming more common. Additionally, online information should always be scrutinized, especially if a peer-reviewed resource is not included, and the reputation of the individual posting the information can also be considered.

An underappreciated potential negative aspect of social media is the impact on the mental health of young professionals, specifically regarding well-being and self-esteem. These negative effects have been demonstrated in children and adolescents previously.<sup>25</sup> Social media is used by some for self-advocacy toward academic advancement, but this sort of self-advocacy is potentially difficult and uncomfortable for others.<sup>26</sup> The number of those using social media for self-advocacy or self-promotion can result in what is known as an "echo chamber" effect, creating groups of like-minded users with a shared narrative.<sup>26, 27</sup> The amount of time spent on social media, either consuming or creating content, also needs to be monitored and regulated by the individual, because it can take time away from other academic and clinical endeavors, as well as personal time.

Finally, while there can be benefits to using social media professionally, participation in social media is not required to succeed as a young professional in radiology, and it has not been well-studied in regard to academic advancement at this time.<sup>26</sup>

### ***The Promise and Pitfalls of Artificial Intelligence***

AI is expected to have a substantial impact on radiology practice in the coming years and to particularly affect the careers of neuroradiologists who are currently in the field or who have recently entered the field. Some of the ways AI is likely to influence the field are the following:

- **Automated analysis:** AI algorithms can process and analyze medical images more quickly and potentially more accurately than humans. This feature can help radiologists detect abnormalities such as tumors, aneurysms, or strokes with higher sensitivity and specificity. AI-based systems can act as powerful diagnostic aids, improving the efficiency and accuracy of interpretation.
- **Workflow optimization:** AI tools can streamline the workflow of radiologists by automating certain tasks. For example, AI algorithms can automatically prioritize urgent cases, flag potential abnormalities for further review, and perform quantitative measurements,<sup>28</sup> saving time and allowing radiologists to focus on more complex and critical cases.<sup>29</sup>
- **Decision support:** AI can provide decision support to radiologists by integrating patient data, clinical history, and imaging findings. By analyzing a wide range of information, AI systems can offer suggestions for diagnosis, treatment planning, and patient management. This support can enhance the decision-making process and help radiologists and neuroradiologists make more informed choices.
- **Precision medicine:** AI can contribute to the development of personalized treatment plans by analyzing imaging data in combination with genomic information and clinical data. AI algorithms can identify imaging biomarkers, predict disease progression, and assess treatment response,<sup>30</sup> facilitating the implementation of precision medicine approaches tailored to individual patients.
- **Quality assurance:** AI algorithms can be used for quality control and standardization of radiologic interpretations. By comparing radiologists' reports with AI-generated assessments, potential discrepancies or errors can be identified. This feedback loop can help improve the accuracy and consistency of radiologic interpretations.
- **Research and education:** AI can aid in the discovery of new imaging biomarkers and patterns that may not be easily discernible to human observers. Additionally, AI-based virtual training platforms can simulate realistic radiology cases, providing a valuable tool for training and continuing education for radiologists.<sup>31</sup>

While AI has great potential, it is not expected to replace radiologists.<sup>32-34</sup> Instead, it is envisioned as a valuable tool that can augment their capabilities, improve efficiency, and enhance patient care in neuroradiology practice.<sup>28</sup> This issue should be specially highlighted and clarified for trainees and medical students because there is a general negative perception regarding the impact of AI on radiology practice.<sup>35</sup> Some of the key points to highlight include the following:

- **Complementary tool:** Computer-assisted diagnosis and AI should be introduced as tools that complement radiologists rather than replace them, by reducing their workload, catching missed findings, and reducing errors.
- **Limitations of AI:** While AI excels at specific, well-defined tasks, it still struggles with many aspects of image interpretation that require human judgment, understanding of clinical context, and integration of information from multiple sources.

- **The human element:** Radiology is not just about interpreting images. It is about communicating results, consulting with other physicians, and integrating imaging findings with clinical information. These "soft skills" are deeply human and difficult for machines to replicate.
- **Continual learning:** Medicine, including radiology, is a continually evolving field. AI models are only as good as the data on which they were trained. Radiologists will always be needed to understand and adapt to new diseases, techniques, and technologies.
- **Validation and regulation:** The process of validating, regulating, and incorporating AI tools into clinical practice is rigorous. These checks and balances ensure that AI is used safely and appropriately.
- **Continuous feedback loop:** The evolution of AI in radiology will require a continuous feedback loop with radiologists. This will involve radiologists training AI, validating its findings, and refining its algorithms.

Finally, a radiologist's or neuroradiologist's training is not just about reading scans; it involves understanding anatomy, pathology, physiology, and clinical medicine at a deep level. This holistic approach to patient care is beyond the current reach of AI.

### ***Bringing the World Together: International Outreach and Collaborations***

Young professionals increasingly recognize the value and significance of international outreach and collaboration in neuroradiology. In the current century, it is easier than ever to communicate and share knowledge with anyone in the world. Technologic advances are spreading to all corners of the Earth in record time. It is the responsibility of science and medicine to use these to advance medical knowledge, clinical practice, and human health globally. Within the field of neuroradiology, the ASNR contributes in multiple ways, including the International Collaborations Committee, the Anne G. Osborn ASNR International Outreach Professor Program, and initiatives conducted by the YPC. For example, the YPC newsletter reaches out 4 times per year to all members worldwide, with information about the events and opportunities of ASNR directed toward young professionals.

For young neuroradiology clinician-scientists, international collaborations can be especially fruitful: Shared projects and research fellowships provide a win-win situation in terms of ideas, resources, knowledge, and network. For randomized controlled trials, international collaborations can improve inclusion speed and generalizability with 1 example being the Canadian Efficacy and Safety of Nerinetide for the Treatment of Acute Ischaemic Stroke (ESCAPE-NA1) trial.<sup>36</sup> In clinical practice, sharing of experiences and knowledge is valuable to improve practice on both sides. This sharing may be useful on a personal scale too: Approximately 12% of practicing radiologists in the United States are foreign medical graduates, and the participation of foreign graduates in radiology training programs increased from 2% to 15% between 2006 and 2020.<sup>37</sup>

At the ASNR Annual Meeting, of almost 2000 in-person and more than 4500 virtual registrations, approximately 5% are international participants. For young professionals, including

international young professionals, workshops and networking events are organized to expand their knowledge and networks. Now that COVID-19-related travel restrictions have ended, we hope that international participation will continue to increase.

## CONCLUSIONS

Being a young professional is an exciting, dynamic, and demanding stage of one's professional career. As the landscape of neuro-radiology practice changes, new opportunities and challenges arise for those in the early stage of their career. The ASNR YPC recognizes the importance of identifying and supporting the needs of young professionals because an investment in their professional development is an investment in the future of our specialty.

**Disclosure forms** provided by the authors are available with the full text and PDF of this article at [www.ajnr.org](http://www.ajnr.org).

## REFERENCES

1. Taylor CS, Weatherly B, Farley EP, et al. **Generating medical student interest in the field of radiology.** *J Am Coll Radiol* 2018;15:340–42 CrossRef Medline
2. Branstetter BF, Faix LE, Humphrey AL, et al. **Preclinical medical student training in radiology: the effect of early exposure.** *AJR Am J Roentgenol* 2007;188:W9–14 CrossRef Medline
3. Vayani OR, Lassner JW, Shehata C, et al. **Using a nationwide virtual radiology student interest group to expand medical students' general awareness, drive greater interest, and achieve uniform national messaging in the field of radiology.** *Acad Radiol* 2023;30:1210–19 CrossRef Medline
4. Abraham P, Chatterjee T, Flores EJ, et al. **An upstream reparative justice framework for improving diversity in radiology.** *J Am Coll Radiol* 2023;20:652–66 CrossRef Medline
5. Musa A, Afify O, Al-Hihi M, et al. **Views of diagnostic radiology residency program directors regarding methods to increase female and under-represented in medicine residents: a cross-sectional study.** *Acad Radiol* 2023;30:541–47 CrossRef Medline
6. Abelson JS, Chartrand G, Moo TA, et al. **The climb to break the glass ceiling in surgery: trends in women progressing from medical school to surgical training and academic leadership from 1994 to 2015.** *Am J Surg* 2016;212:566–72.e1 CrossRef Medline
7. Deloitte. **Deloitte's Gen Z and Millennial Survey reveals two generations striving for balance and advocating for change.** May 18, 2022. <https://www.deloitte.com/global/en/about/press-room/deloittes-gen-z-and-millennial-survey-reveals-two-generations-striving-for-balance-and-advocating-for-change.html>. Accessed May 27, 2023
8. Timmes M. **Council Post. Millennials And Gen Z: Now Is The Time To Reshape Businesses To Harness Their Power.** *Forbes*. June 27, 2022. <https://www.forbes.com/sites/forbescoachescouncil/2022/06/27/millennials-and-gen-z-now-is-the-time-to-reshape-businesses-to-harness-their-power/?sh=7af9b48a5c98>. Accessed May 27, 2023
9. Mazaheri P, Hawk KE, Ledermann EJ, et al. **Flexible work arrangements and their impact on women in radiology: RSNA 2021 panel discussion summary sponsored by AAWR and more.** *Clin Imaging* 2023;94:56–61 CrossRef Medline
10. Golden L. **Flexible Work Schedules: What Are We Trading Off to Get Them?** *Monthly Labor Review* March 2001;50–67. <https://www.bls.gov/opub/mlr/2001/03/art3full.pdf>. Accessed May 27, 2023
11. Oppenheimer DC, Harvey JA. **Remote radiology: point-enhance efficiency, promote work-life balance, and ameliorate staffing issues.** *AJR Am J Roentgenol* 2023;221:17–18 CrossRef Medline
12. Bender CE, Bansal S, Wolfman D, et al. **2019 ACR Commission on Human Resources Workforce Survey.** *J Am Coll Radiol* 2020;17:673–75 CrossRef Medline
13. Tsipursky G. **What Is Proximity Bias and How Can Managers Prevent It?** *Harv Bus Rev*. October 4, 2022. <https://hbr.org/2022/10/what-is-proximity-bias-and-how-can-managers-prevent-it>. Accessed May 27, 2023
14. Baginski S. **2022 Radiologist Job Market Update: High volume, high pay and a search for high quality of life.** *Radiology Business*. May 25, 2022. <https://radiologybusiness.com/sponsored/1065/vrad/topics/healthcare-management/healthcare-staffing/2022-radiologist-job-market>. Accessed July 3, 2023
15. Naidich JJ, Boltyenkov A, Wang JJ, et al. **Recovery of outpatient imaging utilization during the first wave of the COVID-19 pandemic.** *Clin Imaging* 2021;80:277–82 CrossRef Medline
16. Fleishon HB. **The Radiology Labor Shortage.** *ACR Bulletin*. February 10, 2022. <https://www.acr.org/Practice-Management-Quality-Informatics/ACR-Bulletin/Articles/March-2022/The-Radiology-Labor-Shortage>. Accessed July 3, 2023
17. Rosenkrantz AB, Hughes DR, Duszak R. **Increasing subspecialization of the national radiologist workforce.** *J Am Coll Radiol* 2020;17:812–18 CrossRef Medline
18. Lindgren EA, Patel MD, Wu Q, et al. **The clinical impact of subspecialized radiologist reinterpretation of abdominal imaging studies, with analysis of the types and relative frequency of interpretation discrepancies.** *Abdom Imaging* 2014;39:1119–26 CrossRef Medline
19. Christensen EW, Pelzl CE, Hemingway J, et al. **Drivers of ischemic stroke hospital cost trends among older adults in the United States.** *J Am Coll Radiol* 2023;20:411–21 CrossRef Medline
20. Neitzel E, vanSonnenberg E, Markovich D, et al. **The new normal or a return to normal: nationwide remote radiology reading practices after two years of the COVID-19 pandemic.** *J Am Coll Radiol* 2023;20:804–08 CrossRef Medline
21. Stempniak M. **'Startling Shift': 70% of physicians employed by private equity firms or other corporate entities.** *Radiology Business*. July 15, 2021. <https://radiologybusiness.com/topics/healthcare-management/healthcare-economics/physicians-employed-private-equity-corporate>. Accessed July 3, 2023
22. Hanson PS. **Private Practice Trends in the US: Will Increasing Competitiveness Weaken the Profession?** *HealthManagement*. 2009;9. <https://healthmanagement.org/c/imaging/issuearticle/private-practice-trends-in-the-us-will-increasing-competitiveness-weaken-the-profession>. Accessed July 3, 2023
23. Hula N. **The Top 3 Trends Shaping the Future of Imaging.** *Advisory Board*. <https://www.advisory.com/blog/2022/07/imaging-trends>. Accessed July 3, 2023
24. Spieler B, Ballard DH, Mazaheri P, et al. **Social media in radiology: overview and usefulness of online professional #SoMe Profiles.** *Acad Radiol* 2021;28:526–39 CrossRef Medline
25. Richards D, Caldwell PH, Go H. **Impact of social media on the health of children and young people.** *J Paediatr Child Health* 2015;51:1152–57 CrossRef Medline
26. Ayyala RS. **Harms in encouraging social media use for individual academic advancement.** *AJR Am J Roentgenol* 2023;220:606–07 CrossRef Medline
27. Cinelli M, De Francisci Morales G, Galeazzi A, et al. **The echo chamber effect on social media.** *Proc Natl Acad Sci U S A* 2021;118: e2023301118 CrossRef Medline
28. Cohen RY, Sodickson AD. **An orchestration platform that puts radiologists in the driver's seat of AI innovation: a methodological approach.** *J Digit Imaging* 2023;36:700–14 CrossRef Medline
29. Weikert T, Litt HI, Moore WH, et al. **Reduction in radiologist interpretation time of serial CT and MR imaging findings with deep learning identification of relevant priors, series and finding locations.** *Acad Radiol* 2023;30:2269–79 CrossRef Medline
30. Aboian M, Bousabarah K, Kazarian E, et al. **Clinical implementation of artificial intelligence in neuroradiology with development of a novel workflow-efficient picture archiving and communication system-based automated brain tumor segmentation and radiomic feature extraction.** *Front Neurosci* 2022;16:860208 CrossRef Medline

31. Shiang T, Garwood E, DeBenedictis CM. **Artificial intelligence-based decision support system (AI-DSS) implementation in radiology residency: introducing residents to AI in the clinical setting.** *Clin Imaging* 2022;92:32–37 CrossRef Medline
32. Langlotz CP. **Will artificial intelligence replace radiologists?** *Radiol Artif Intell* 2019;1:e190058 CrossRef Medline
33. Goyal M, McDonough R. **Eudaimonia and the future radiologist.** *Acad Radiol* 2022;29:909–13 CrossRef Medline
34. Khosravi P, Schweitzer M. **Artificial intelligence in neuroradiology: a scoping review of some ethical challenges.** *Front Radiol* 2023;3:1149461 CrossRef Medline
35. Park CJ, Yi PH, Siegel EL. **Medical student perspectives on the impact of artificial intelligence on the practice of medicine.** *Curr Probl Diagn Radiol* 2021;50:614–19 CrossRef Medline
36. Hill MD, Goyal M, Menon BK, et al; ESCAPE-NA1 Investigators. **Efficacy and safety of nerinetide for the treatment of acute ischaemic stroke (ESCAPE-NA1): a multicentre, double-blind, randomised controlled trial.** *Lancet* 2020;395:878–87 CrossRef Medline
37. Huda F, Rozenshtein A, Bedi H. **The American Board of Radiology's alternate pathway for diagnostic radiology: what the programs and the applicants need to know.** *Acad Radiol* 2022;29:465–68 CrossRef Medline



# Delayed Enhancement of Intracranial Atherosclerotic Plaque Can Better Differentiate Culprit Lesions: A Multiphase Contrast-Enhanced Vessel Wall MRI Study

Beibei Sun, Lingling Wang, Xiao Li, Jin Zhang, Jianjian Zhang, Jiaqi Tian, Mahmud Mossa-Basha, Jianrong Xu, Yan Zhou, Huilin Zhao, and Chengcheng Zhu



## ABSTRACT

**BACKGROUND AND PURPOSE:** Intracranial plaque enhancement (IPE) identified by contrast-enhanced vessel wall MR imaging (VW-MR imaging) is an emerging marker of plaque instability related to stroke risk, but there was no standardized timing for postcontrast acquisition. We aim to explore the optimal postcontrast timing by using multiphase contrast-enhanced VW-MR imaging and to test its performance in differentiating culprit and nonculprit lesions.

**MATERIALS AND METHODS:** Patients with acute ischemic stroke due to intracranial plaque were prospectively recruited to undergo VW-MR imaging with 1 precontrast phase and 4 consecutive postcontrast phases (9 minutes and 13 seconds for each phase). The signal intensity (SI) values of the CSF and intracranial plaque were measured on 1 precontrast and 4 postcontrast phases to determine the intracranial plaque enhancement index (PEI). The dynamic changes of the PEI were compared between culprit and nonculprit plaques on the postcontrast acquisitions.

**RESULTS:** Thirty patients with acute stroke (aged  $59 \pm 10$  years, 18 [60%] men) with 113 intracranial plaques were included. The average PEI of all intracranial plaques significantly increased (up to 14%) over the 4 phases. There was significantly increased PEI over the 4 phases for culprit plaques (an average increase of 23%), but this was not observed for nonculprit plaques. For differentiating culprit and nonculprit plaques, we observed that the performance of IPE in the second postcontrast phase (cutoff = 0.83, AUC = 0.829 [0.746–0.893]) exhibited superior accuracy when compared with PEI in the first postcontrast phase (cutoff = 0.48; AUC = 0.768 [0.680–0.843]) ( $P = .022$ ).

**CONCLUSIONS:** A 9-minute delay of postcontrast acquisition can maximize plaque enhancement and better differentiate between culprit and nonculprit plaques. In addition, culprit and nonculprit plaques have different enhancement temporal patterns, which should be evaluated in future studies.

**ABBREVIATIONS:** AUC = area under the curve; ICC = intraclass correlation coefficient; ICAD = intracranial atherosclerosis disease; IPE = intracranial plaque enhancement; PEI = plaque enhancement index; PI = pituitary infundibulum; ROC = receiver operating characteristic; SD = standard deviation; VW = vessel wall

Intracranial atherosclerosis disease (ICAD) is one of the leading causes of ischemic stroke worldwide.<sup>1–3</sup> The development of 3D contrast-enhanced vessel wall MR imaging (VW-MR imaging) has improved the evaluation of ICAD by characterizing intracranial plaque features qualitatively and quantitatively.<sup>4–7</sup> Intracranial

plaque enhancement (IPE), a marker of plaque inflammation, is one of the major high-risk plaque features associated with ischemic stroke.<sup>8,9</sup> Strong enhancement is associated with recent ischemic events,<sup>10,11</sup> and it can predict stroke recurrence.<sup>12–15</sup>

However, there is no standard imaging and analysis method by which to quantify IPE. Most studies evaluated intracranial plaque enhancement via qualitative grading (grade 0: none; grade I: higher than normal wall but less than pituitary infundibulum (PI); grade II: similar to or higher than PI).<sup>10,16–18</sup> Despite its ease of use by radiologists, qualitative grading lacks quantitative information, and reproducibility (interrater) is only moderate ( $\kappa = 0.75$  to

Received May 29, 2023; accepted after revision December 5.

From the Department of Radiology, Ren Ji Hospital (B.S., L.W., X.L., Jin Zhang, Jianjian Zhang, J.T., J.X., Y.Z., H.Z.), and College of Health Science and Technology (B.S., L.W., X.L., Jin Zhang, Jianjian Zhang, J.T., J.X., Y.Z., H.Z.), Shanghai Jiao Tong University School of Medicine, Shanghai, China; and Department of Radiology (M.M., C.Z.), University of Washington, Seattle, Washington.

Beibei Sun and Lingling Wang contributed equally to this work and are co-first authors.

This study was supported by the National Natural Science Foundation of China (grants 82271942, 82171279, 82302181), Science and Technology Commission of Shanghai Municipality Explorer project (22TS1400600), Shanghai Municipal Population and Family Planning Commission (20204Y0091), Shanghai Municipal Public Health Excellent Young Talents Training Program (GWVI-11.2-YQ50), and Renji Hospital Shanghai Jiao Tong University School of Medicine (2019NYB5ZX01). Chengcheng Zhu was supported by United States National Institute of Health (NIH) grants R01HL162743 and R00HL136883.

Please address correspondence to Huilin Zhao, Department of Radiology, Ren Ji Hospital, Shanghai Jiao Tong University School of Medicine, 160 Pujian Rd, Shanghai 200127, China; e-mail: huilinzhaol3@163.com

Indicates article with online supplemental data.

<http://dx.doi.org/10.3174/ajnr.A8132>

0.83).<sup>10,17,19</sup> Quantitative enhancement is a preferred approach and has been used in many recent studies.<sup>20–23</sup> Additionally, in previous studies, the timing of postcontrast VW-MR imaging after contrast injection either varied, ranging from 0 to 20 minutes,<sup>10,13,24–26</sup> or was unreported.<sup>27</sup> A dynamic enhancement study indicated that intracranial atherosclerosis enhancement might change over time.<sup>28</sup> Thus, it is important to optimize the timing to maximize lesion enhancement for the identification of high-risk lesions and to standardize the protocol for future multicenter studies.

The purposes of this study are as follows: 1) identify the ideal postcontrast timing for enhancing the visualization of IPE by using multiphase contrast-enhanced VW-MR imaging and 2) explore the suitable postcontrast timing for distinguishing between culprit and nonculprit lesions.

## MATERIALS AND METHODS

### Study Population

Informed consent was obtained from all participants, and all protocols were approved by the institutional review board. Consecutive patients with acute ischemic stroke (within 4 weeks of symptoms) due to intracranial atherosclerotic plaque were prospectively recruited between March 2020 and March 2021, and they underwent full-head 3D contrast-enhanced VW-MR imaging. The inclusion criteria for this study were: 1) patients with intracranial arterial stenosis detected on MR angiography, CT angiography, or digital subtraction angiography; 2) ischemic infarct confirmed by DWI within 4 weeks; and 3) stroke etiology determined to be intracranial artery stenosis via the identification of intracranial artery plaque on 3D VW-MR imaging. The exclusion criteria were: 1) intracranial artery occlusion; 2) a high risk of carotid artery-to-artery embolism: the coexistence of >50% stenosis or unstable plaques (the presence of at least 3 of the following features: calcification, hemorrhage, superficial irregularity, and being lipid-rich) of the ipsilateral extracranial carotid artery having been detected via imaging (sonography, MR angiography, CT angiography, or digital subtraction angiography); 3) complex aortic arch plaques confirmed by CT angiography (plaque with complex composition or ulcerated or thickness  $\geq 4$  mm)<sup>29</sup>; 4) evidence of cardioembolic source ischemic stroke (recent myocardial infarction within 3 weeks, atrial fibrillation or flutter, evidence of cardiac or valvular thrombus on echocardiography or other imaging); 5) clinical evidence of the presence of vasculopathy, other than atherosclerosis (eg, vasculitis, reversible cerebral vasoconstriction syndrome, or other vasospastic processes, Moyamoya disease, or dissection); 6) degraded image quality of 3D VW-MR imaging that limited the accurate delineation of the artery boundaries for quantitative analysis; and 7) subsequent scans were abandoned if any stage of the postcontrast phases had an unsatisfactory image quality. Participants' data, including vascular risk factors such as age, sex, body mass index, hypertension, diabetes, dyslipidemia, and current smoking, were extracted from an institutional database.

### 3D VW-MR Imaging Protocol

VW-MR imaging was performed on a 3T MR scanner (Prisma, Siemens) by using a 64-channel phased-array neurovascular coil. The imaging protocol included 3D time-of-flight MR angiography

as well as 1 precontrast and 4 postcontrast enhanced T1-weighted 3D sampling perfection with application-optimized contrasts by using different flip-angle evolutions (SPACE; Siemens) acquisitions. The 3D time-of-flight MR angiography used the following parameters: TR/TE, 21.0/3.69 ms; number of slices, 48; flip angle, 16°; field of view, 220 × 195 mm<sup>2</sup>; voxel size, 0.6 mm<sup>3</sup>; acquisition matrix, 384 × 345; slabs, 5; and scan time, 6 minutes and 2 seconds. This was followed by precontrast T1-weighted SPACE with the following parameters: sagittal imaging orientation; TR/TE, 1000/15 ms; number of slices, 240; field of view, 193 × 193 mm<sup>2</sup>; voxel size, 0.6 mm<sup>3</sup>; acquisition matrix, 320 × 320; slabs, 1; and scan time, 9 minutes and 13 seconds. Motion-sensitized driven equilibrium was used to suppress the signal of slow flow with a 500 mTms<sup>2</sup>/m gradient in the x-y-z directions in order to enhance the visualization of the vessel wall.<sup>30</sup> Four consecutive phases of postcontrast T1-SPACE were acquired after a gadolinium-based contrast (Magnevist) injection (0.1 mmol/kg at a rate of 1.5 mL/s). Four postcontrast phases were consecutively scanned immediately after the injection of the contrast agent without any time intervals in between. These phases were initiated at the following time intervals after the contrast injection: 0 minutes for the first phase, 9 minutes and 13 seconds for the second phase, 18 minutes and 26 seconds for the third phase, and 27 minutes and 39 seconds for the fourth phase. The total scan time of the 4 postcontrast phases was 36 minutes and 52 seconds.

### Image Analysis

Three neuroradiologists (B.S., L.W., and X.L., each with 6 years of experience in neurovascular imaging), blinded to clinical information, each independently reviewed VW-MR imaging studies on PACS software (Carestream Health, Version 11.4.0.0179), and performed qualitative and quantitative measurements. Discrepancies were resolved through a consensus discussion with a fourth radiologist (H.Z., with 12 years of experience in neurovascular imaging). An image quality rating was assigned by using a 3-point scale, where 1 = poor [low SNR and obscured vessel wall or lumen boundaries], 2 = marginal (passable SNR with a few motions or blood artifacts, distinguishable vessel wall, but partially obscured vessel lumen and wall boundaries), and 3 = good (high SNR without artifacts, clearly displaying vessel lumen boundary and wall).<sup>31</sup> The MR data sets with image quality ratings of 1 were excluded from further analyses. Intracranial atherosclerotic plaques were identified by using a previously reported definition (the presence of focal wall thickening<sup>10</sup> on both precontrast and postcontrast VW-MR imaging. The raters identified all plaques involving the arterial branches of the circle of Willis, including the C4–7 segment of the internal carotid artery, the A1–2 segment of the anterior cerebral artery, the M1–2 segment of the middle cerebral artery, the V4 segment of the vertebral artery, the P1–2 segment of the posterior cerebral artery, and the basilar artery.

The culprit plaque was defined as 1) the only lesion within the vascular territory of the stroke or 2) the most stenotic lesion when multiple plaques were present upstream of the stroke territory.<sup>10</sup> We have identified a total of 30 culprit plaques, with 24 falling into category A (representing the sole lesion within the

vascular territory of the stroke) and 6 falling into the less common category B (in which multiple plaques were present upstream of the stroke territory). For these 6 category B plaques, detailed information on their location, enhancement grade, and stenosis grade are provided in the Online Supplemental Data. All 6 of the category B culprit plaques have the highest stenosis degree as well as the highest enhancement degree. There was no plaque that had a high enhancement but a low degree of stenosis. In addition, we have excluded patients presenting with the scenario in which the most stenotic plaque exhibits lower enhancement and a less stenotic plaque displays strong enhancement, as this situation can pose challenges in defining the culprit plaque.

The plaque enhancement grade was classified into 3 grades on the postcontrast T1-SPACE images by using previously published criteria:<sup>10,32</sup> grade 0, no enhancement, defined as the signal intensity of the plaque being similar to that of the adjacent normal vessel wall; grade I, mild enhancement, defined as the signal intensity of the plaque being lower than that of the pituitary infundibulum but higher than that of the adjacent normal vessel wall; and grade II, obvious enhancement, defined as the signal intensity of the plaque being similar to or greater than that of the pituitary infundibulum. Though a quantitative analysis method is preferred to qualitative grading, we still performed grading in this study to identify the potential changes of grades when the post-contrast scans were acquired at different times, and such grading was widely used in previous clinical studies.

Quantitative plaque enhancement was analyzed by using the plaque enhancement index (PEI).

$$PEI = \frac{\frac{SI_{\text{plaque-post}}}{SI_{\text{CSF-post}}} - \frac{SI_{\text{plaque-pre}}}{SI_{\text{CSF-pre}}}}{\frac{SI_{\text{plaque-pre}}}{SI_{\text{CSF-pre}}}}$$

where “pre” indicates precontrast enhanced images and “post” indicates postcontrast enhanced images. The SI of plaque was measured on a section orthogonal to the course of the parent artery with images that were magnified 6-fold on the image viewer. Three ROIs were placed over the target lesion, on the section with the most conspicuous lesion enhancement and on the adjacent section in each direction on the first postcontrast phase images. The PEI was calculated by the mean SI of the ROIs from the 3 slices. The reference structure CSF expected to normalize PEI was also measured (an ROI of 10 mm<sup>2</sup> drawn on the frontal horn of the right lateral ventricle). It needs to be mentioned that few patients changed position during the scanning process. So, we did not register the precontrast and 4 phases of postcontrast images in the same patient, but the measurement of the ROIs of the reference object and plaque was copied between the precontrast and 4 phases of postcontrast images (automatic align). Then, the position was manually adjusted, which ensured that the ROIs’ positions and sizes in the pre contrast and 4 phases of postcontrast images were consistent. The ROI of the intracranial plaque and CSF were all manually segmented by using medical imaging viewer software (Vue PACS Livewire, Carestream).

Within this study cohort, 20 plaques (10 culprit plaques and 10 nonculprit plaques) in 10 cases were randomly selected. A

quantitative analysis was independently performed by 2 radiologists (B.S. and L.W., each with 6 years of experience in neurovascular imaging). A qualitative analysis was performed by 3 radiologists (B.S., L.W., and X.L., each with 6 years of experience in neurovascular imaging). One reviewer (L.W.) independently reevaluated the same 20 plaques 2 months after the initial evaluation for an intrarater agreement analysis.

## Statistics

All analyses were performed by using the SPSS software package (version 23.0). Continuous data are presented as mean ± standard deviation (SD). All variables were tested for normal and homogeneous variance by using the Shapiro-Wilk normality test and Levene test, respectively. Categorical variables were recorded as frequencies and percentages. Multiple paired *t* tests were conducted after a 1-way repeated-measures ANOVA to assess differences among the 4 postcontrast phases. To address the issue of multiple comparisons and the nonindependence of plaques within the same subjects, we first applied the Bonferroni correction to control the family error rate and maintain overall significance levels. Second, to account for the nonindependence of plaques within the same subjects, we utilized a mixed-effects model repeated measures ANOVA for multiple comparisons. Interobserver and intraobserver agreement were calculated with the Kendall W or Cohen  $\kappa$  value for the categorical data and the intraclass correlation coefficient (ICC) for the continuous data. A value of Kendall W, Cohen  $\kappa$  or ICC of >0.80 indicated excellent agreement. All tests were 2-tailed, and *P* values of <.05 were considered to be indicative of a statistically significant result. A 1-way repeated measures design with a sample of 60 subjects (30 patients for each group), measured at 4 time points, achieved a 0.15 effect size and 95% power to detect differences among the PEI means by using a Geisser-Greenhouse corrected *F* test at a .05 significance level. The standard deviation across subjects at the same time point was assumed to be 0.515. The pattern of the covariance matrix is to have all correlations equal with a correlation of 0.7 between the first and second time point PEI measurements. These calculations were conducted by using PASS 2023 Power Analysis and Sample Size Software (2023) (NCSS). The result showed that a minimum sample size of 30 was needed in each group. Accordingly, we planned to include 30 participants in this prospective study. The receiver-operating characteristic (ROC) curves to differentiate between culprit and nonculprit lesions were plotted for 4 postcontrast phases, and the area under the curve (AUC) values were calculated. We utilized the DeLong test to compare the ROC curves between postcontrast phases. This test calculates a test statistic (*z*) and its corresponding *P* value based on paired ROC curves and the standardized area differences between them. Additionally, to determine the optimal cutoff value used to estimate sensitivity and specificity, we conducted a comprehensive analysis by maximizing the Youden index derived from the ROC curve.

## RESULTS

### Patient Demographics and Intracranial Plaque Characteristics

From March 2020 to March 2021, 62 participants were recruited to undergo 3D VW-MR imaging. Thirty-two participants were

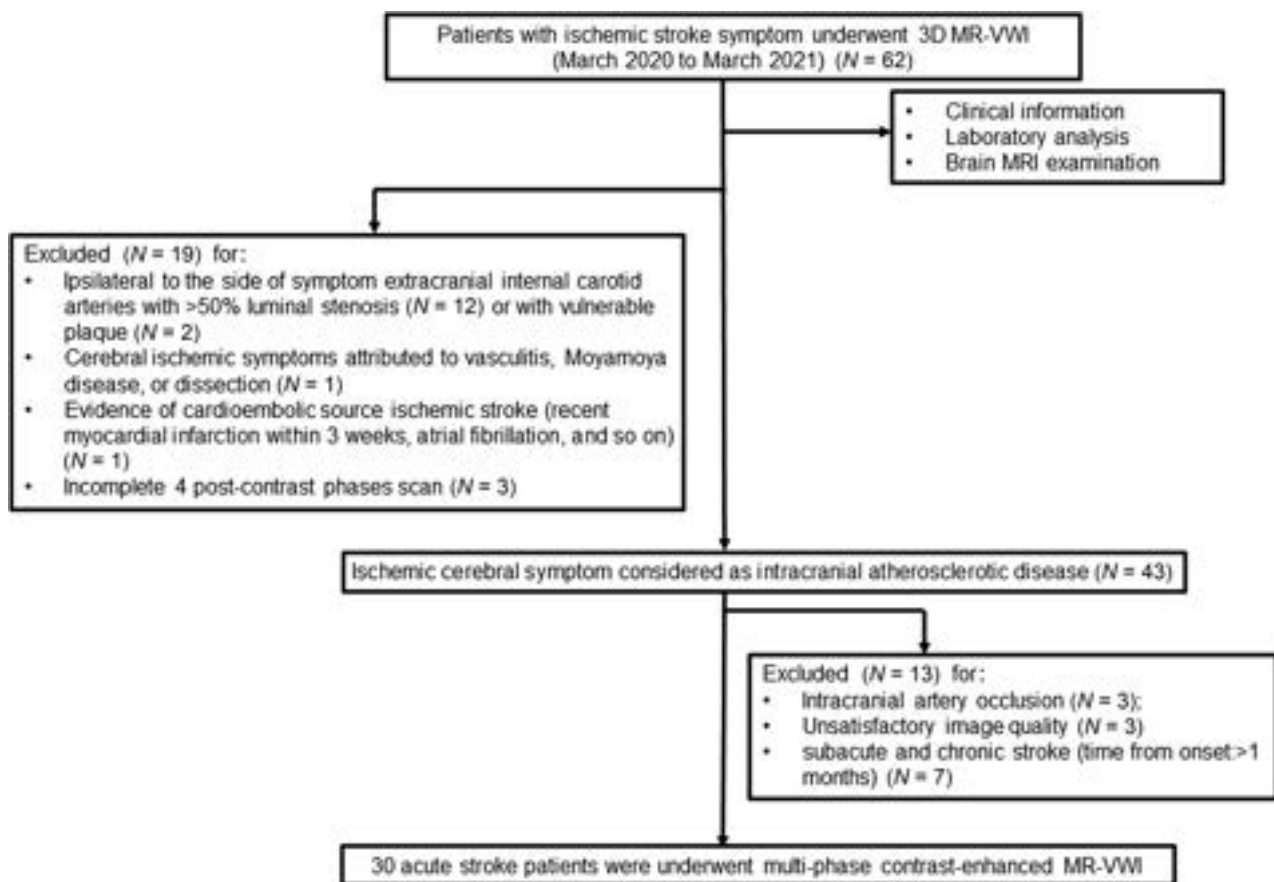


FIG 1. Patient selection flow chart.

**Table 1: Demographic and intracranial plaque characteristics of 30 patients with acute stroke**

Patient Demographics	Mean $\pm$ SD or Median (IQR) or n (%)
Age (years)	59.0 $\pm$ 9.7
Body mass index (kg/cm <sup>2</sup> )	24.6 $\pm$ 2.9
Sex (male)	18 (60.0%)
Hypertension	21 (70.0%)
Diabetes	11 (36.7%)
Dyslipidemia	6 (20.0%)
Current smoking	5 (16.7%)
Plaque location	
Internal carotid artery (C4–7)	25 (22.1%)
Middle cerebral artery	34 (30.1%)
Anterior cerebral artery	6 (5.3%)
Basilar artery	17 (15.0%)
Vertebral artery	21 (18.6%)
Posterior cerebral artery	10 (8.9%)
Plaque stenosis (%)	
30% $\leq$ stenosis < 50% (grade I)	74 (65.5%)
50% $\leq$ stenosis < 70% (grade II)	15 (13.3%)
Stenosis $\geq$ 70% (grade III)	24 (21.2%)
Plaque numbers (n)	3.0 (2.0–6.0)

excluded because of 1) intracranial artery occlusion ( $n = 3$ ); 2) the coexistence of ipsilateral extracranial carotid atherosclerosis with  $>50\%$  stenosis ( $n = 12$ ) or unstable features ( $n = 2$ ); 3) evidence of cardioembolic source ischemic stroke ( $n = 1$ ); 4) the presence of nonatherosclerotic intracranial vasculopathy ( $n = 1$ ); 5) insufficient image quality ( $n = 3$ ); 6) a stroke  $>1$  month since

onset ( $n = 7$ ); and 7) having an incomplete set of 4 postcontrast phase scans ( $n = 3$ ). The flow chart is summarized in Fig 1. Finally, a total of 30 patients with 113 plaques were included (aged  $59 \pm 10$  years, 18 [60.0%] men). The median plaque number for the group of patients is 3.0 [interquartile range, [2.0–6.0]]. The demographic and intracranial plaque characteristics are summarized in Table 1.

#### Dynamic Changes of Quantitative Enhancement of Culprit and Nonculprit Plaques

The PEI of all intracranial plaques significantly increased (on average 14.1%) over time after the contrast injection, from  $0.64 \pm 0.49$  at the first postcontrast phase to  $0.73 \pm 0.51$  at the fourth postcontrast phase ( $P = .033$ ). For the culprit plaque, the PEI significantly increased 22.1% with time after the contrast injection, from  $1.02 \pm 0.53$  at the first postcontrast phase to  $1.20 \pm 0.49$  at the fourth postcontrast phase ( $P = .034$ ). There were no significant differences between the second and third, second and fourth, or third and fourth postcontrast phases in either the all intracranial plaques or the culprit plaques. In addition, the nonculprit plaques showed no significant differences among the 4 postcontrast phases ( $P = .450$ ) (Fig 2 and Table 2). Two examples of patients with culprit and nonculprit plaques are demonstrated in Fig 3.

The ROC curves for distinguishing between culprit and nonculprit plaques are graphically represented in Fig 4, and a detailed summary of the AUC values can be found in Table 3. Specifically,



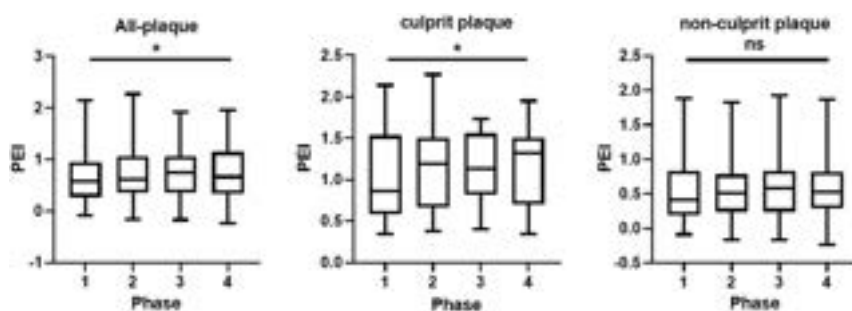


**FIG 2.** Plaque enhancement index (PEI; the mean signal intensity of plaque normalized by CSF) change of culprit and nonculprit plaques over time. The boxes were drawn with the median (line in the box) as well as the 25<sup>th</sup> and 75<sup>th</sup> percentiles. The bars above and below the box are the maximum and minimum values of the PEI, respectively. The PEI values of all intracranial plaques and culprit plaques increase over the 4 phases ( $P = .033$ ,  $P = .034$ , respectively). The PEI values of the nonculprit plaques show no significant differences among the 4 postcontrast phases ( $P = .450$ ). \*,  $P < .05$ ; ns, not significant.

**Table 2: Plaque enhancement index change of culprit and nonculprit plaques over time**

Phase	PEI		
	All Plaques (n = 113) <sup>a</sup>	Nonculprit Plaque (n = 83) <sup>a</sup>	Culprit Plaque (n = 30) <sup>b</sup>
1st	0.66 ± 0.51	0.54 ± 0.44	1.02 ± 0.53
2nd	0.72 ± 0.52	0.55 ± 0.42	1.17 ± 0.50
3rd	0.73 ± 0.47	0.58 ± 0.39	1.16 ± 0.41
4th	0.76 ± 0.53	0.60 ± 0.44	1.20 ± 0.49
$P^c$	.033	.450	.034
$P$ 1st versus 2nd	.014	.578	.007
$P$ 1st versus 3rd	.049	.446	.057
$P$ 1st versus 4th	.029	.401	.035
$P$ 2nd versus 3rd	.879	.640	.869
$P$ 2nd versus 4th	.502	.572	.680
$P$ 3rd versus 4th	.458	.771	.477

<sup>a</sup> A mixed-effects model repeated measures ANOVA for continuous variables was used to analyze the differences between all 4 postcontrast phases in all plaque groups and the nonculprit plaque group.

<sup>b</sup> A 1-way repeated-measures ANOVA for continuous variables was used to analyze the differences between the 4 postcontrast phases in the culprit plaque group. This was followed by a pair-wise comparison post hoc analysis using Bonferroni correction to compare the differences between the PEI values of each 2 contrast phases.

<sup>c</sup>  $P$  values of the comparisons of the 4 postcontrast phases.

the AUC values for PEI in the 4 postcontrast phases were 0.768 (0.680–0.843), 0.829 (0.746–0.893), 0.840 (0.759–0.902), and 0.812 (0.727–0.879), respectively.

The cutoff values of PEI in the 4 postcontrast phases were 0.48 (sensitivity = 59.0%, specificity = 86.7%), 0.83 (sensitivity = 80.7%, specificity = 70.0%), 0.95 (sensitivity = 83.1%, specificity = 70.0%), and 0.98 (sensitivity = 84.3%, specificity = 70.0%), respectively. In addition, the AUC for PEI in the second postcontrast phases was higher than that observed for PEI in the first postcontrast phases ( $P = .022$ ) to detect culprit plaques, but no differences were found between the other postcontrast phases (Table 4).

### Dynamic Changes of Qualitative Enhancement of Culprit and Nonculprit Plaques

As shown in the Online Supplemental Data, during the 4 postcontrast enhanced phases, the grade II percentage of culprit plaques was higher than that of the nonculprit plaques, and the grade 0 and grade I percentages of culprit plaques were both lower than those of the nonculprit plaques. As shown in the first postcontrast phase, there were 16 (14.2%)

grade 0, 69 (61.1%) grade I, and 28 (24.7%) grade II plaques. Over time, the degree of enhancement increased over subsequent phases. The grade II plaques significantly increased from 28 (24.7%) to 54 (47.8%) ( $P < .05$ ), whereas the grade 0 (from 14.2% to 6.2%) and grade I (from 61.1% to 46.0%) plaques showed a decreasing trend ( $P > .05$ ). In addition, the enhancement grade changed a lot during the 4 postcontrast enhanced phases in the culprit and nonculprit plaques ( $P = .020$  and  $P = .006$ , respectively). The percentage of grade II tended to increase during the 4 postcontrast enhanced phases in the culprit and nonculprit plaques, whereas the percentages of grade I and grade 0 gradually decreased during the 4 postcontrast enhanced phases.

The enhancement grades of 42 (37.2%) plaques in 17 (56.7%) patients changed during the 4 postcontrast phases (Online Supplemental Data). 30% of the culprit plaques from 9 patients showed an enhancement grade change from grade I to grade II. Similarly, in the nonculprit plaque group, 39.8% of the plaques from 18 patients exhibited an enhancement grade change.

The ability of the enhancement grade to differentiate between culprit and nonculprit plaques did not show a significant difference among the 4 postcontrast enhanced phases (Online Supplemental Data).

### 3D VW-MR Imaging Measurement Reproducibility

The interrater and intrarater reproducibility data are summarized in the Online Supplemental Data. There was excellent interrater and intrarater agreement for all measurements (all Kendall  $\kappa$  and ICC values were greater than 0.80).

### DISCUSSION

In this study, we attempt to standardize the postcontrast timing for evaluating intracranial vessel wall enhancement by using multiphase contrast-enhanced VW-MR imaging. We found that 1) a 9-minute delay in postcontrast acquisition proved to be beneficial for enhancing plaque visibility and enhancing the differentiation between culprit and nonculprit plaques and 2) culprit and nonculprit plaques exhibit unique enhancement patterns over time, which is a facet deserving of exploration in future research. Such results highlight the importance of the standardization of imaging protocols and possibly explain the large variability of previous studies due to inconsistent postcontrast timing. Our study



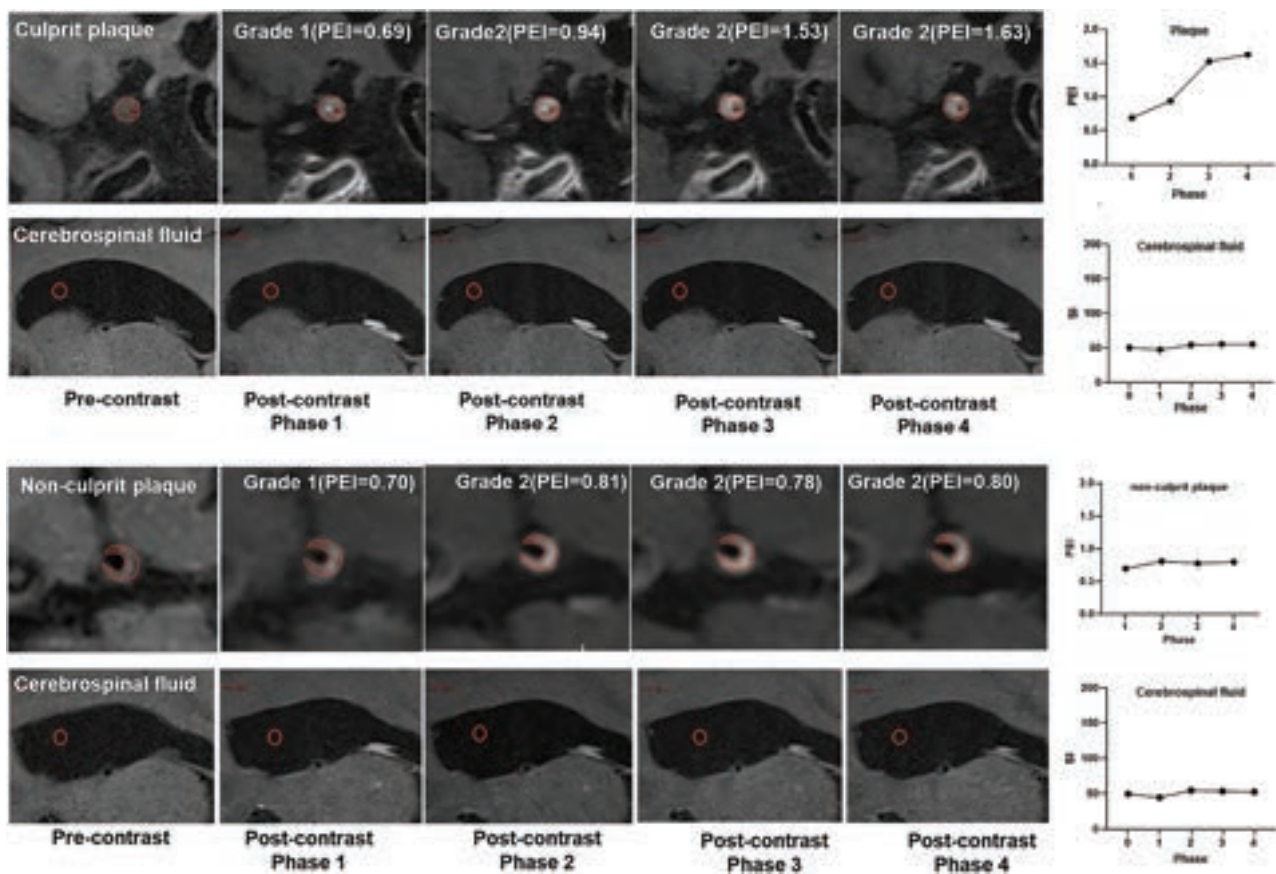


**FIG 3.** Cases of the culprit and nonculprit plaque signal intensity change during the 4 postcontrast phases.

provides an important reference for the design of future multicenter studies targeting intracranial plaques on VW-MR imaging and stroke risk. The 9-minute delay could also be considered for utilization in other postcontrast sequences as a part of the clinical stroke imaging protocol, potentially without extending the overall duration of the MR imaging examination.

The time interval of postcontrast VW-MR imaging after contrast administration was inconsistent in previous studies, ranging from 0–20 minutes (or was unreported in many studies). Skarpathiotakis et al<sup>26</sup> obtained postcontrast images immediately after contrast administration, whereas Qiao et al<sup>10</sup> acquired postcontrast images 5 minutes after contrast injection. Song et al<sup>13</sup> obtained postcontrast images within 10 minutes after the administration of contrast injection, whereas Vakil et al<sup>25</sup> performed postcontrast T1-weighted imaging within 20 minutes of contrast injection. Because of the large variation of these previous studies, the enhancement measurements were not interchangeable. De Havenon et al<sup>33</sup> retrospectively examined the impact of time intervals between contrast administration and postcontrast VW-MR imaging (range from 0 to 40 min) on the enhancement of 35 intracranial plaques in 35 patients with acute ischemic stroke and found that a longer duration after contrast injection was associated with increased plaque enhancement. However, each patient had only 1 postcontrast acquisition with variable postcontrast timing, and the effects of interpatient differences could not be ruled out. Stroke severity, stroke acuity at the time of imaging, and other factors could lead to different plaque enhancement.

Our prospective study had a more rigorous design through the use of Multiphase postcontrast VW-MR imaging in the same patient.

Our study also found that by prolonging the time interval between contrast administration and postcontrast VW-MR imaging to at least 9 minutes, the plaque enhancement index increased. After the injection of the gadolinium contrast agent, the contrast goes into the plaque in one of two possible ways: 1) via the vasa vasorum<sup>9</sup> (neovasculature) in the adventitia of the artery and 2) via direct penetration from the surface of the plaque. By either way, it needs a few minutes or longer to reach the peak concentration. Such a phenomenon is also present in other diseases. For example, in cardiac MR imaging examinations, late gadolinium enhancement is widely used to detect myocardium scars. Delayed contrast-enhanced scans with CT or MR are also the standard clinical imaging protocol for adrenal glands and tumors.<sup>34</sup> We also noticed that increasing the delay time to 18 minutes or longer will not further increase the enhancement. Thus, the delay of 9 minutes is the best option without excessively increasing the scan time. We also found that delayed enhancement could better distinguish between culprit and nonculprit plaques. This was because the culprit plaques had different enhancement curves than did the nonculprit plaques. The culprit plaques had increased PEI levels and then stayed at a high PEI level. The nonculprit plaques did not have a significant increase in PEI, even when acquired with a long delay. The reason may be that culprit plaques had rich vasa vasorum and high permeability,

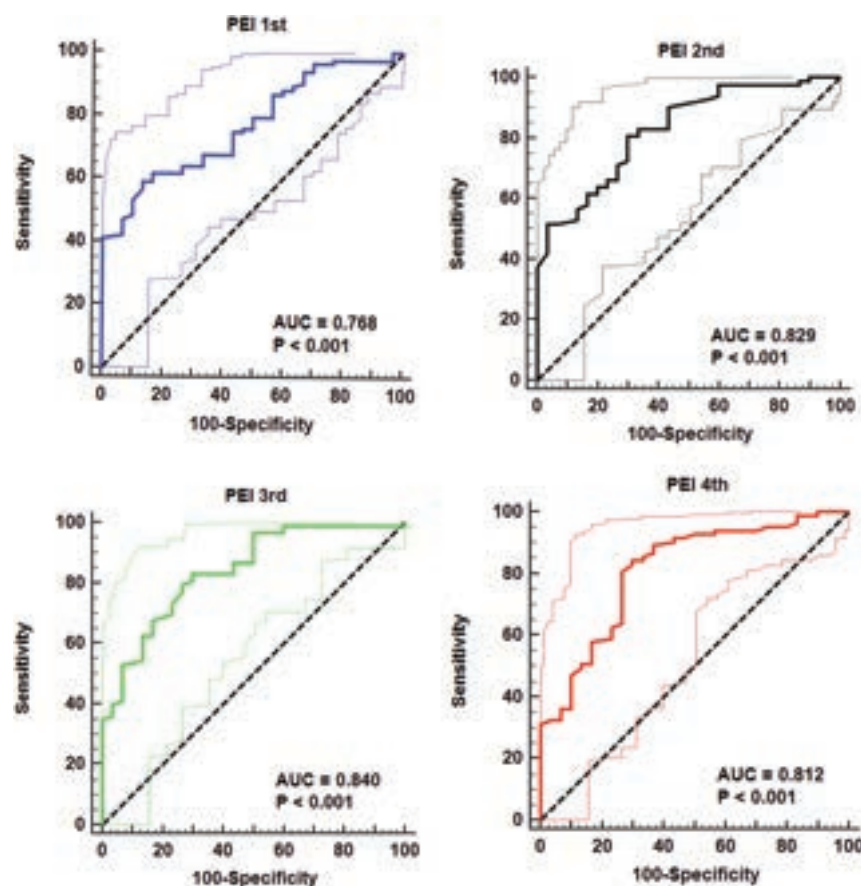


**FIG 4.** The ROC of the plaque enhancement index in the 4 contrast-enhanced phases for differentiating between culprit and nonculprit plaques.

**Table 3: Plaque enhancement index in different contrast-enhanced phases to differentiate between culprit and nonculprit plaques**

Variables	AUC (95% CI)	Sensitivity/Specificity	Cutoff	P Value
PEI 1st	0.768 (0.680–0.843)	59.0%/86.7%	0.48	<.001
PEI 2nd	0.829 (0.746–0.893)	80.7%/70.0%	0.83	<.001
PEI 3rd	0.840 (0.759–0.902)	83.1%/70.0%	0.95	<.001
PEI 4th	0.812 (0.727–0.879)	84.3%/70.0%	0.98	<.001

**Table 4: Comparison of ROC curves of PEI to differentiate between culprit and nonculprit plaques between 4 postcontrast phases**

Variables	Difference between AUC area	95% CI	z statistic	P Value
PEI 1st versus PEI 2nd	0.060 ± 0.026	0.009–0.112	2.293	.022
PEI 1st versus PEI 3rd	0.071 ± 0.039	–0.005–0.148	1.824	.068
PEI 1st versus PEI 4th	0.043 ± 0.038	–0.032–0.118	1.131	.258
PEI 2nd versus PEI 3rd	0.011 ± 0.025	–0.038–0.060	0.444	.657
PEI 2nd versus PEI 4th	0.017 ± 0.027	–0.036–0.070	0.628	.530
PEI 3rd versus PEI 4th	0.028 ± 0.024	–0.020–0.076	1.151	.249

whereas the nonculprit plaques lacked such high-risk features. It is noteworthy that researchers such as Qiao et al<sup>10</sup> have successfully employed a 5-minute delay in their studies, as exemplified in their work published in *Radiology*. This raises the possibility that a 5-minute delay might be adequate for distinguishing between culprit and nonculprit plaques. It is essential to highlight that the main focus of our study was not only to distinguish between plaque types but also to understand how intracranial plaque enhancement changes over time. The 9-minute delay recommended in clinical practice may not be realistic. The need for dynamic contrast-enhanced scans<sup>28</sup> with high temporal

resolution is recognized to guide us toward achieving better results with shorter delay times. However, the study design involves longitudinal/multiphase postcontrast acquisition in the same patient, and the findings above suggest that our study remains relevant. Our study serves as an initial exploration of a trend, albeit within a small sample. It underscores the need for further research with larger sample sizes and an improved study design to complement and refine these initial findings.

In addition, we observed significant changes in the enhancement grade between culprit and nonculprit plaques at 4 enhancement periods, with 42 (37.2%) plaques in 17 (56.7%)

patients displaying changes during the 4 postcontrast phases (Online Supplemental Data). The enhancement grade of 30% of the culprit plaques in 9 patients changed from grade I to grade II. Similarly, in the nonculprit plaque group, 39.8% of plaques from 18 patients showed enhanced grade changes. Our findings demonstrated that the enhancement grade is not fixed but dynamically changing, with some grade I plaques transitioning to grade II and vice versa over time. The possible reason for the above phenomenon is that the pituitary infundibulum (the reference used to assess enhancement grade) also changes over time. We have also found that there is no statistically significant difference in the differentiation ability of enhancement grades between culprit and nonculprit plaques across the 4 postcontrast phases. These findings suggest that enhancement grades alone may not provide a strong discriminatory capability to distinguish between these plaque types. Different from our study, Kwee et al<sup>35</sup> investigated intracranial atherosclerotic plaques in patients at 140 days poststroke and found differences in the evolution of culprit and nonculprit plaques. They demonstrated that the contrast enhancement grade of intracranial atherosclerotic plaques can persist for months after an ischemic event. The culprit plaques showed the highest baseline enhancement grade more frequently and were more likely to remain at grade II, whereas the nonculprit plaques were more likely to show a decline in enhancement grade at follow-up.

In our study, we focused on determining the optimal postcontrast timing for differentiating between culprit and nonculprit plaques. We conducted longitudinal/multiphase postcontrast vessel wall MR imaging to evaluate how the enhancement of intracranial plaques changes over time within relatively shorter imaging intervals (0, 9, 18, and 27 minutes after the contrast injection). Our findings are based on a different approach that is aimed at understanding how plaque enhancement changes in acute ischemic stroke phases (within 4 weeks of symptoms) following contrast administration. Kwee et al's<sup>35</sup> study examined patients at a much later time point (140 days poststroke) and offered insights into the plaque changes that occur in the post-stroke period, shedding light on the longer-term implications. In contrast, our study aimed to determine the optimal timing for clinical imaging in the acute phase, which has value in the diagnosis and management of patients with acute ischemic stroke. We provided insights into an early dynamic of plaque enhancement, specifically within an hour of contrast injection. The above findings suggest that the enhancement effects vary at different periods. Further validation in chronic patients is needed.

This study had several limitations. First, the 9-minute delay used in our study may not be realistic in clinical practice. As imaging technology advances, shorter scan times can provide more detailed temporal resolution, which is crucial for capturing subtle changes in plaque enhancement. Second, this was a single-center study that used only 1 scan protocol (3D SPACE) with 1 vendor (Siemens) and 1 contrast agent (Magnevist at 0.1 mmol/kg). Multicenter studies across multiple scan protocols and multiple platforms will be needed to confirm our results. Third, the difference in enhancement behavior between culprit and nonculprit plaques may depend on the arterial input (which may vary between subjects). However, postcontrast

images were acquired a few minutes after the injection (about 9 minutes). By this time, the contrast agent has been evenly distributed into the blood. Finally, our study has a limited sample size, and some nonculprit plaques came from the same patients. To ensure robust and unbiased statistics, we used correction methods. A larger-scale study is needed to validate the findings and extend the current research.

## CONCLUSIONS

A 9-minute delay of postcontrast acquisition can maximize plaque enhancement and better differentiate between culprit and nonculprit plaques. In addition, culprit and nonculprit plaques have different enhancement temporal patterns, which should be evaluated in future studies.

**Disclosure forms** provided by the authors are available with the full text and PDF of this article at [www.ajnr.org](http://www.ajnr.org).

## REFERENCES

1. Arenillas JF. **Intracranial atherosclerosis: current concepts.** *Stroke* 2011;42:S20–3 CrossRef Medline
2. White H, Boden-Albala B, Wang C, et al. **Ischemic stroke subtype incidence among whites, blacks, and Hispanics: the Northern Manhattan Study.** *Circulation* 2005;111:1327–31 CrossRef Medline
3. Wong KS, Huang YN, Gao S, et al. **Intracranial stenosis in Chinese patients with acute stroke.** *Neurology* 1998;50:812–13 CrossRef Medline
4. de Havenon A, Mossa-Basha M, Shah L, et al. **High-resolution vessel wall MRI for the evaluation of intracranial atherosclerotic disease.** *Neuroradiology* 2017;59:1193–202 CrossRef Medline
5. Mossa-Basha M, Alexander M, Gaddikeri S, et al. **Vessel wall imaging for intracranial vascular disease evaluation.** *J Neurointerv Surg* 2016;8:1154–59 CrossRef Medline
6. Alexander MD, de Havenon A, Kim SE, et al. **Assessment of quantitative methods for enhancement measurement on vessel wall magnetic resonance imaging evaluation of intracranial atherosclerosis.** *Neuroradiology* 2019;61:643–50 CrossRef Medline
7. Dieleman N, Yang W, Abrigo JM, et al. **Magnetic resonance imaging of plaque morphology, burden, and distribution in patients with symptomatic middle cerebral artery stenosis.** *Stroke* 2016;47:1797–802 CrossRef Medline
8. Gorelick PB, Wong KS, Bae HJ, et al. **Large artery intracranial occlusive disease: a large worldwide burden but a relatively neglected frontier.** *Stroke* 2008;39:2396–99 CrossRef Medline
9. Portanova A, Hakakian N, Mikulis DJ, et al. **Intracranial vasa vasorum: insights and implications for imaging.** *Radiology* 2013;267:667–79 CrossRef Medline
10. Qiao Y, Zeiler SR, Mirbagheri S, et al. **Intracranial plaque enhancement in patients with cerebrovascular events on high-spatial-resolution MR images.** *Radiology* 2014;271:534–42 CrossRef Medline
11. Wang E, Shao S, Li S, et al. **A high-resolution MRI study of the relationship between plaque enhancement and ischemic stroke events in patients with intracranial atherosclerotic stenosis.** *Front Neurol* 2018;9:1154 CrossRef Medline
12. Kim JM, Jung KH, Sohn CH, et al. **Intracranial plaque enhancement from high resolution vessel wall magnetic resonance imaging predicts stroke recurrence.** *Int J Stroke* 2016;11:171–79 CrossRef Medline
13. Song X, Zhao X, Liebeskind DS, et al. **Incremental value of plaque enhancement in predicting stroke recurrence in symptomatic intracranial atherosclerosis.** *Neuroradiology* 2020;62:1123–31 CrossRef Medline
14. Yang D, Liu J, Yao W, et al. **The MRI enhancement ratio and plaque steepness may be more accurate for predicting recurrent ischemic**

- cerebrovascular events in patients with intracranial atherosclerosis. *Eur Radiology* 2022;32:7004–13 CrossRef Medline
15. Xu C, Qin J, Yu J, et al. Association of plaque enhancement on vessel wall MRI and the phosphodiesterase 4D variant with stroke recurrence in patients with symptomatic intracranial atherosclerosis. *Neuroradiology* 2022;64:1781–94 CrossRef Medline
  16. van der Kolk AG, Zwanenburg JJ, Brundel M, et al. Intracranial vessel wall imaging at 7.0-T MRI. *Stroke* 2011;42:2478–84 CrossRef Medline
  17. Lu SS, Ge S, Su CQ, et al. MRI of plaque characteristics and relationship with downstream perfusion and cerebral infarction in patients with symptomatic middle cerebral artery stenosis. *J Magn Reson Imaging* 2018;48:66–73 CrossRef Medline
  18. Li X, Sun B, Wang L, et al. Association of type 2 diabetes mellitus and glycemic control with intracranial plaque characteristics in patients with acute ischemic stroke. *J Magn Reson Imaging* 2021;54:655–66 CrossRef Medline
  19. Song JW, Pavlou A, Burke MP, et al. Imaging endpoints of intracranial atherosclerosis using vessel wall MR imaging: a systematic review. *Neuroradiology* 2021;63:847–56 CrossRef Medline
  20. Shi Z, Li J, Zhao M, et al. Quantitative histogram analysis on intracranial atherosclerotic plaques: a high-resolution magnetic resonance imaging study. *Stroke* 2020;51:2161–69 CrossRef Medline
  21. Wu G, Wang H, Zhao C, et al. Large culprit plaque and more intracranial plaques are associated with recurrent stroke: a case-control study using vessel wall imaging. *AJNR Am J Neuroradiol* 2022;43:207–15 CrossRef Medline
  22. Ran Y, Wang Y, Zhu M, et al. Higher plaque burden of middle cerebral artery is associated with recurrent ischemic stroke: a quantitative magnetic resonance imaging study. *Stroke* 2020;51:659–62 CrossRef Medline
  23. Sun B, Wang L, Li X, et al. Intracranial atherosclerotic plaque characteristics and burden associated with recurrent acute stroke: a 3D quantitative vessel wall MRI study. *Front Aging Neurosci* 2021;13:706544 CrossRef Medline
  24. Wu F, Ma Q, Song H, et al. Differential features of culprit intracranial atherosclerotic lesions: a whole-brain vessel wall imaging study in patients with acute ischemic stroke. *J Am Heart Assoc* 2018;7:e009705
  25. Vakil P, Vranic J, Hurley MC, et al. T1 gadolinium enhancement of intracranial atherosclerotic plaques associated with symptomatic ischemic presentations. *AJNR Am J Neuroradiol* 2013;34:2252–58 CrossRef Medline
  26. Skarpathiotakis M, Mandell DM, Swartz RH, et al. Intracranial atherosclerotic plaque enhancement in patients with ischemic stroke. *AJNR Am J Neuroradiol* 2013;34:299–304 CrossRef Medline
  27. Wang W, Yang Q, Li D, et al. Incremental value of plaque enhancement in patients with moderate or severe basilar artery stenosis: 3.0 T high-resolution magnetic resonance study. *Biomed Res Int* 2017;2017:4281629 CrossRef Medline
  28. Vakil P, Elmokadem AH, Syed FH, et al. Quantifying intracranial plaque permeability with dynamic contrast-enhanced MRI: a pilot study. *AJNR Am J Neuroradiol* 2017;38:243–49 CrossRef Medline
  29. Ntaios G, Pearce LA, Meseguer E, et al. Aortic arch atherosclerosis in patients with embolic stroke of undetermined source: an exploratory analysis of the NAVIGATE ESUS trial. *Stroke* 2019;50:3184–90 CrossRef Medline
  30. Wang J, Yarnykh VL, Yuan C. Enhanced image quality in black-blood MRI using the improved motion-sensitized driven-equilibrium (iMSDE) sequence. *J Magn Reson Imaging* 2010;31:1256–63 CrossRef Medline
  31. Wang J, Zhang S, Lu J, et al. High-resolution MR for follow-up of intracranial steno-occlusive disease treated by endovascular treatment. *Front Neurol* 2021;12:706645 CrossRef Medline
  32. Hartman JB, Watase H, Sun J, et al. Intracranial aneurysms at higher clinical risk for rupture demonstrate increased wall enhancement and thinning on multicontrast 3D vessel wall MRI. *Br J Radiology* 2019;92:20180950 CrossRef Medline
  33. de Havenon A, Muhina HJ, Parker DL, et al. Effect of time elapsed since gadolinium administration on atherosclerotic plaque enhancement in clinical vessel wall MR imaging studies. *AJNR Am J Neuroradiol* 2019;40:1709–11 CrossRef Medline
  34. Szolar DH, Korobkin M, Reittner P, et al. Adrenocortical carcinomas and adrenal pheochromocytomas: mass and enhancement loss evaluation at delayed contrast-enhanced CT. *Radiology* 2005;234:479–85 CrossRef Medline
  35. Kwee RM, Qiao Y, Liu L, et al. Temporal course and implications of intracranial atherosclerotic plaque enhancement on high-resolution vessel wall MRI. *Neuroradiology* 2019;61:651–57 CrossRef Medline



# Development of Collateral Vessels after Anterior Circulation Large Vessel Occlusion in Pediatric Arterial Ischemic Stroke Relates to Stroke Etiology: A Longitudinal Study

Manoëlle Kossorotoff, David Grévent, Charles-Joris Roux, and Francis Brunelle



## ABSTRACT

**BACKGROUND AND PURPOSE:** The characteristics of large vessel occlusion (LVO) in the acute phase of pediatric arterial ischemic stroke and their natural history according to stroke etiology are poorly explored. This study aimed at describing the prevalence and the radiological evolution of LVO in pediatric AIS.

**MATERIALS AND METHODS:** This single-center retrospective study included consecutive non-neonate children with acute arterial ischemic stroke, intracranial proximal LVO in the anterior circulation (MCA, anterior cerebral artery, and/or ICA), and clinical and imaging follow-up for at least 18 months, during a 9-year period.

**RESULTS:** Intracranial LVO was observed in 24.8% of patients with anterior circulation arterial ischemic stroke and adequate follow-up ( $n = 26/105$ ), with a median age of 4.2 years (IQR 0.8–9), sex ratio 1.16. The main stroke etiology associated with LVO was unilateral focal cerebral arteriopathy ( $n = 12$ , 46%). During follow-up, a specific pattern of unilateral poststroke anastomotic bridge was observed in 8/26 patients, with the poststroke development of nonperforating collaterals forming a bridge in bypass of the LVO site with visible distal flow, within a median delay of 11 months. The development of unilateral poststroke anastomotic bridge was only observed in patients with unilateral focal cerebral arteriopathy. No patient with this pattern experienced stroke recurrence or further progressive vascular modifications.

**CONCLUSIONS:** After stroke, the development of unilateral poststroke anastomotic bridge is specifically observed in children with focal cerebral arteriopathy, appearing in the first year after stroke. This clinical-radiologic pattern was not associated with stroke recurrence or arterial worsening, differentiating it from progressive intracranial arteriopathy, such as Moyamoya angiopathy.

**ABBREVIATIONS:** ACA = anterior cerebral artery; AIS = arterial ischemic stroke; FCA = focal cerebral arteriopathy; IQR = interquartile range; LVO = large vessel occlusion; MMA = Moyamoya angiopathy; MT = mechanical thrombectomy; PCA = posterior cerebral artery; U-PS = unilateral post stroke

Stroke in children is a rare but devastating event, with long-lasting developmental consequences affecting the child's and family's lives. Large vessel occlusion (LVO) is observed in 20%–25% of pediatric arterial ischemic stroke (AIS)<sup>1,2</sup> and there is growing evidence for the use of mechanical thrombectomy in this setting to improve long-term outcomes.<sup>3–9</sup> However, there is still some debate concerning the importance of including stroke etiology in the decision-making process, as focal cerebral arteriopathy (FCA)

seems to be associated with an increased rate of re-occlusion after mechanical thrombectomy.<sup>8</sup> Indeed, the specificities of LVO according to stroke etiology in children and the angiographic natural history of pediatric LVO have not been reported so far. This study explored LVO characteristics in pediatric AIS according to stroke etiology, specifically addressing radiologic and clinical outcomes with and without recanalization treatments, focusing on poststroke collateral vessel development.

Received August 18, 2023; accepted after revision December 1.

From the French Center for Pediatric Stroke (M.K., C.-J.R.), Paris, France; Pediatric Neurology Department (M.K.) and Pediatric Radiology Department (D.G., C.-J.R., F.B.), APHP University Hospital Necker-Enfants Malades, Paris, France; and INSERM U1266 (M.K.), Paris, France.

Please address correspondence to Manoëlle Kossorotoff, MD, PhD, French Center for Pediatric Stroke, Pediatric Neurology Department, University Hospital Necker-Enfants Malades, APHP, 149 rue de Sèvres, 75015 Paris, France; e-mail: manoelle.kossorotoff@aphp.fr



Indicates article with online supplemental data.

<http://dx.doi.org/10.3174/ajnr.A8114>

## MATERIALS AND METHODS

This study is a retrospective analysis of the prospectively maintained single-center database of pediatric AIS in the Necker-Enfants Malades University Hospital, Paris, France. Patients were included if they fulfilled the following criteria: 1) non-neonate pediatric patients (28 days – 17 years old) presenting with AIS in the anterior circulation between January 1, 2010, and December 31, 2018; 2) large vessel occlusion in the intracranial anterior circulation, eg, proximal middle cerebral artery (MCA, M1, and/or M2



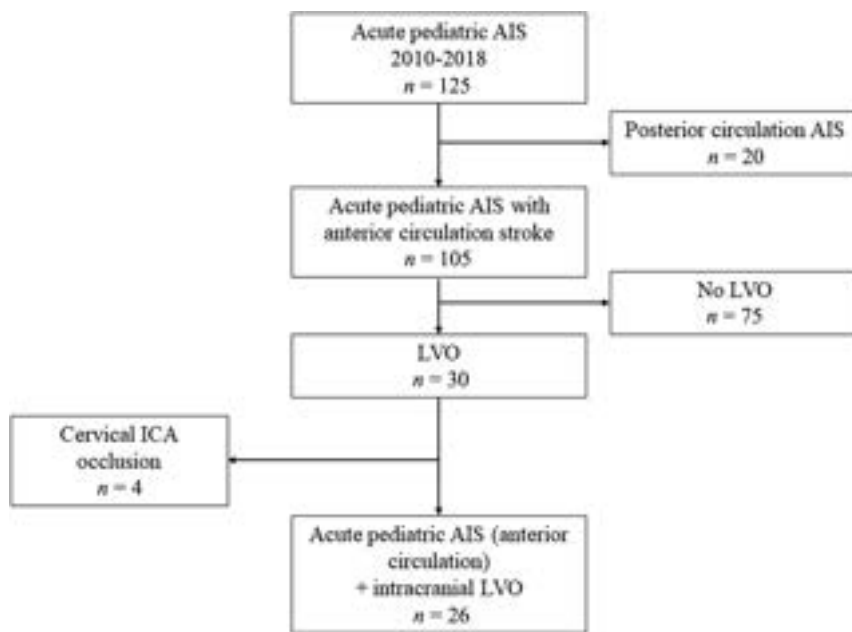


**FIG 1.** Study flow chart.

segments) and/or the proximal anterior cerebral artery (ACA, A1 segment) and/or the terminal portion of the ICA observed on imaging at the acute phase; and 3) available clinical, parenchymal, and vascular imaging follow-up for at least 18 months. Clinical and demographic data, medical history, and etiological work-up results were extracted from the local database. Imaging data (MR, CT, MRA, CTA) were centrally reviewed. Stroke characteristics and vascular findings at the acute phase and during follow-up were recorded. Stroke recurrence was defined as persistent new focal deficit associated with a new ischemic lesion on MR imaging after initial stroke. Early vessel reocclusion without new ischemic lesion, or TIA were not considered as a stroke recurrence. Retained stroke etiology was determined according to the CASCADE classification for pediatric stroke (Online Supplemental Data).<sup>10</sup>

Because of the small sample, data were expressed in median and interquartile range (IQR). Comparisons of values between subgroups used nonparametric tests, eg, Wilcoxon rank sum test. Participants' legal guardians provided consent for the anonymized use of data.

## RESULTS

### Prevalence of Anterior Circulation LVO

During the inclusion period, 105 patients aged 28 days to 17 years old had both an AIS in the anterior circulation territories and available clinical and imaging follow-up for at least 18 months. Among them, intracranial LVO was observed in 26 patients (24.8%), 14 boys and 12 girls, with a median age of 4.2 years old (IQR, 0.8–9) (Fig 1).

### Characteristics of LVO and Stroke at the Acute Phase

LVO was determined on TOF-MRA for all patients, including 2 patients who had both MRA and CTA at the acute phase. Intracranial LVO was unilateral in 25/26 patients, more frequent

on the left side ( $n = 16$ , right side  $n = 9$ ,  $P = .019$ ). The most frequent site of occlusion was the proximal MCA ( $n = 25$ , M1 segment  $n = 16$ , M2 segment  $n = 9$ ) and 9/26 patients had a large occlusion involving several arterial segments. LVO was associated with stenosis of other intracranial arteries in 8/26 patients (homolateral  $n = 7$ , contralateral  $n = 1$ ). Brain infarction involved deep MCA territory ( $n = 20$ ), superficial MCA territory ( $n = 21$ ), and/or ACA territory ( $n = 3$ ). Most patients (17/26) had no previous medical history. The other patients had a cardiac condition (malformative shunting cardiopathy  $n = 3$ , cardiac failure with extracorporeal membrane oxygenation support  $n = 1$ ), sickle cell anemia ( $n = 1$ ), leukemia ( $n = 1$ ), systemic disease (FARSA deficiency,<sup>11</sup>  $n = 1$ ), or recent benign head trauma ( $n = 1$ ). A significant proportion of

patients ( $n = 10/26$ , 38%) received a hyperacute recanalization treatment, including mechanical thrombectomy ( $n = 3$ ). Final etiological diagnosis of AIS according to the Childhood AIS Standardized Classification And Diagnostic Evaluation (CASCADE) classification showed a predominance of intracranial arteriopathy ( $n = 15/26$ ). Retained etiologies were the following: unilateral FCA ( $n = 12$ , 46%, all of FCA-i [infectious/inflammatory] type), bilateral cerebral arteriopathy of childhood ( $n = 3$ , 11%), cervical/aortic arteriopathy ( $n = 3$ , 11%), cardioembolic ( $n = 7$ , 27%), hematologic/thrombotic ( $n = 1$ , 4%). Patients with FCA were younger than patients with other stroke causes (median age 1.93 versus 6.33 years old,  $P = .06$ ) (Online Supplemental Data).

### Clinical and Angiographic Outcomes

Median follow-up duration was 31 months (IQR 18–38), with a median 4 arterial imaging procedures per patient during the study period (8 CTA angio-CTs, 111 MRAs). The ratio of patients with vessel patency (complete patency or residual stenosis) slightly increased over time on poststroke serial imaging: 50% in the 12 patients re-imaged  $\leq 48$  hrs after stroke diagnosis/treatment ( $n = 6$ , of which 4 had received IV r-tPA and 1 IV r-tPA and mechanical thrombectomy), 58% in the 24 patients imaged at 1–3 months after stroke, and 62.5% in the 24 patients imaged at 12–18 months after stroke. A stroke recurrence was noted in 6/26 patients (23%) during follow-up, whose stroke etiologies according to CASCADE classification were cardio-embolic ( $n = 3$ ), aortic/cervical arteriopathy ( $n = 1$ ), bilateral cerebral arteriopathy of childhood/Moyamoya angiopathy (MMA) ( $n = 1$ ), and hematologic/thrombotic ( $n = 1$ ).

### Poststroke Development of Collateral Vessels

During follow-up, collateral vessels originating from the occluded/stenotic arterial segment were observed in 11/26

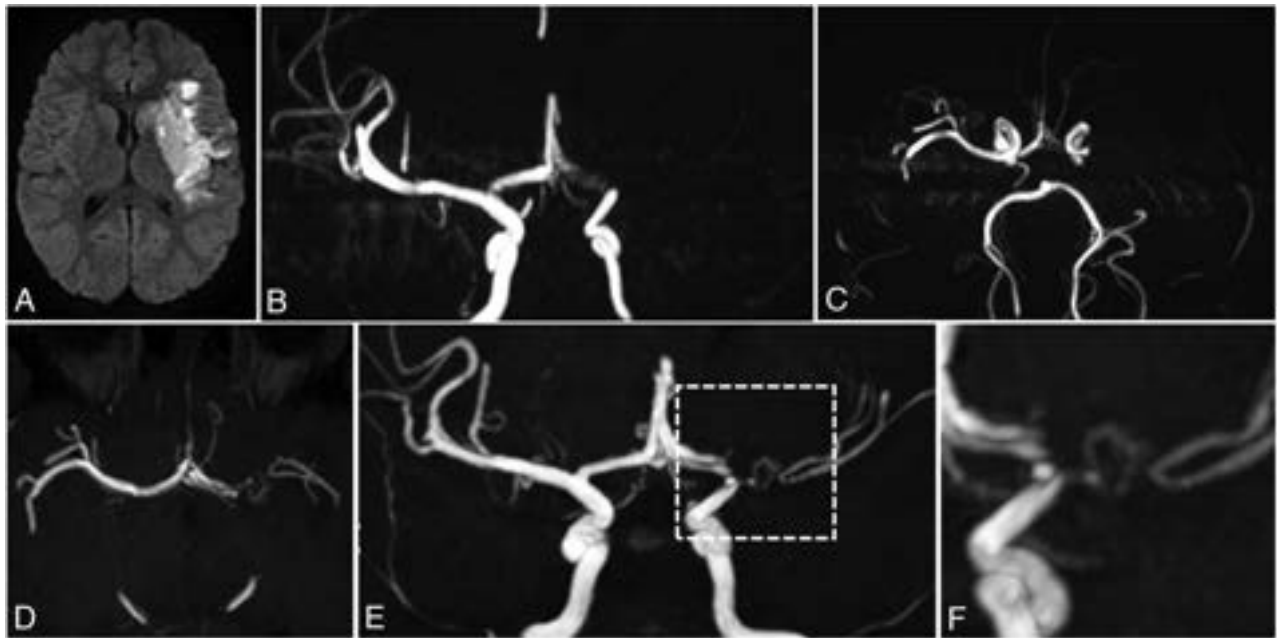


**FIG 2.** U-PS anastomotic bridge development in a patient with AIS and LVO, and unilateral FCA. Upper panel: acute phase MR imaging, showing recent MCA infarction with DWI hypersignal (A), with proximal left MCA occlusion and left A1 stenosis on the time-of-flight MRA, coronal view MIP 15 mm (B) and axial view MIP 10 mm (C). No collateral is visible at the acute phase. Lower panel: MR imaging 12 months after stroke occurrence. Time-of-flight MRA shows strictly unilateral left anomalies. Axial view (D) shows a reverted to normal left A1 segment and a persisting steno-occlusive M1 lesion, favoring the diagnosis of FCA. E, Coronal view shows a U-PS anastomotic bridge bypassing the M1 occlusion, with distal visible flow. F, Closer view of the U-PS anastomotic bridge illustrates the collaterals direction, parallel to the main MCA trunk, without perforating lenticulostriate collaterals.

patients. Collateral vessels were already present on the acute phase imaging in 2 patients, fulfilling the diagnostic criteria for MMA.<sup>12</sup> For 9 patients without observed collaterals at the acute phase, a progressive development of such vessels was noted during follow-up (Online Supplemental Data). One patient with bilateral intracranial arteriopathy developed further bilateral collaterals and had a MMA diagnosis. The 8 patients with initial strictly unilateral intracranial artery involvement who developed further homolateral collaterals displayed remarkable common temporal and anatomic characteristics. These collateral vessels had a typical pattern forming a bridge in bypass of the residual stenosis or occlusion, starting upstream from the arterial stenosis/occlusion, spanning over the stenotic/occluded zone, and connecting downstream with the main arterial trunk with visible distal flow. They did not display a perforating lenticulostriate route, but they were parallel to the main trunk of the originating artery (MCA  $n=7$  and/or ACA  $n=3$ ) though distinct from it. They were thin and sometimes serpiginous, without draining veins. This specific aspect was thus labeled unilateral poststroke (U-PS) anastomotic bridge (Fig 2). Median development delay of U-PS anastomotic bridge was 11 months (IQR 5–12). After the development of this U-PS anastomotic bridge, the vascular aspects of the circle of Willis and of the U-PS anastomotic bridge itself were stable over the rest of the follow-up period (Fig 3). Of note, no patient with U-PS anastomotic bridge had stroke recurrence during follow-up.

Interestingly, the development of U-PS anastomotic bridge was only observed in patients with unilateral FCA as a stroke cause ( $n=8/8$ ). In patients with unilateral FCA and LVO, 8/12

(66.7%) developed U-PS anastomotic bridge. U-PS anastomotic bridge development was not associated with age at stroke onset, stroke location, severity, or management, including recanalization treatments (Online Supplemental Data). Furthermore, U-PS anastomotic bridge development was not different in patients with FCA with persisting LVO and in patients with FCA with vessel patency evaluated at 3 months after stroke ( $n=3/5$  versus  $n=5/7$ , not significant).

The 3 patients with bilateral collaterals had a very different course. They had bilateral cerebral arteriopathy, and 2 of them had visible collaterals at stroke onset imaging, with a perforating lenticulostriate route, consistent with Moyamoya network. One patient developed poststroke collaterals associating both Moyamoya network and U-PS anastomotic bridge. These patients met the diagnostic criteria for MMA. Two had arterial worsening after stroke and 1 experienced a stroke recurrence during follow-up.

## DISCUSSION

This study addressing anterior circulation LVO in pediatric AIS (excluding neonates) provides novel data concerning a specific radiologic evolution pattern of intracranial LVO in children relating to stroke etiology.

In our series, intracranial LVO was observed in 24.6% of children with acute anterior circulation AIS. Though our study focused only on anterior circulation LVO, these findings are in line with the reported prevalence of LVO in childhood stroke of 23.5% in a retrospective population-based cohort study by Bhatia et al<sup>2</sup> and 22.4% in a single-center retrospective study by Bonnet et al.<sup>1</sup>

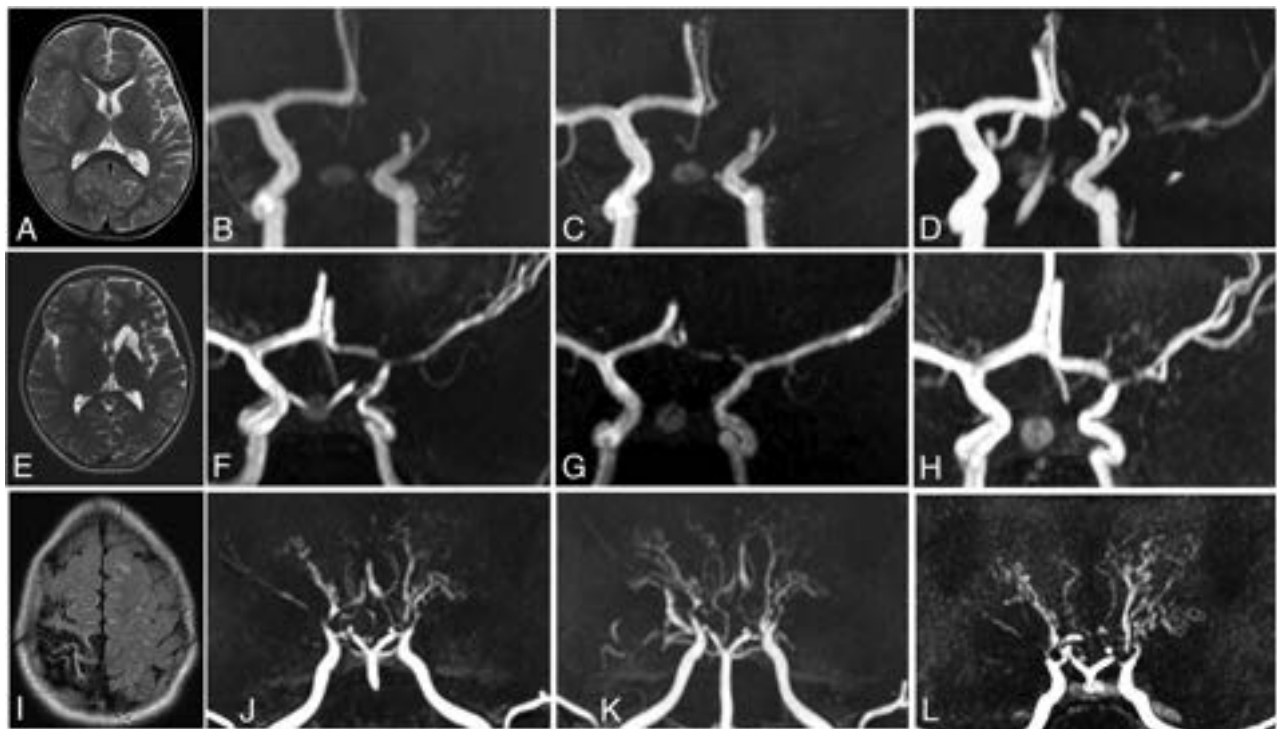






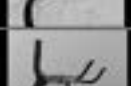
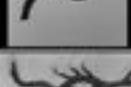
**FIG 3.** Patterns of angiographic evolution in patients with FCA and U-PS anastomotic bridge development, compared with Moyamoya angiopathy. *Upper panel:* Patient with left superficial MCA infarction (A, MRI axial T2) and FCA. Angiographic evolution (3D time-of-flight MRA) with persisting occlusion 6 and 12 months after stroke (B and C), and U-PS anastomotic bridge in bypass of the occluded M1 segment with visible downstream MCA segments (D). *Middle panel:* Patient with left deep and superficial MCA infarction (E, MRI axial T2) and FCA. Angiographic evolution (3D time-of-flight MRA) with initial M1 occlusion (F). Partial improvement of MCA 6 months after stroke (G), with the observation of U-PS anastomotic bridge 12 months after stroke (H). *Lower panel:* Patient with right superficial MCA infarction (I, MRI axial T2) and Moyamoya angiopathy. Angiographic evolution (3D time-of-flight MRA) with bilateral steno-occlusive lesions of the terminal ICAs, MCAs, and ACAs (J). Bilateral perforating collaterals, present at stroke onset (I) and developing over time with a classical puff of smoke appearance. Progression of the arteriopathy with disappearance of MCAs and ACAs 6 and 24 months after stroke (K and L).

Concerning angiographic outcomes, we described a specific pattern of U-PS anastomotic bridge, characterized by the development in the first year after stroke of a collateral network forming a bridge in bypass of the residual stenosis or occlusion, with visible distal flow in the still or formerly occluded main arterial trunk, in patients without visible collaterals at the acute phase. This pattern is specific as it does not meet the criteria for other described approaching vascular patterns (Fig 4).

First, as collaterals were not present at stroke onset, this precludes congenital variations or anomaly, such as fenestration, duplication, aplastic or twig-like artery aspects. In these congenital variations, the regression of anastomoses from the embryonic primitive mesh of intracranial arterial networks did not occur, leading to the persistence of remnants of embryologic development.<sup>13-16</sup> They are sometimes reported as a potential risk factor for ischemic or hemorrhagic stroke.<sup>17,18</sup> Of note, no such variation was observed in our patients. Second, as U-PS anastomotic bridge developed after LVO, a specific intracranial arterial compensatory mechanism of downstream chronic ischemia can be hypothesized. Indeed, a similar compensatory mechanism has been described in cervical or systemic arteries, occurring during the embryonic phase, or acquired hypoxic conditions. Cervical carotid rete mirabile is an embryonic compensatory phenomenon, visible as a meshwork of multiple, freely intercommunicating arterioles fed by external carotid artery branches, which

reconstitute the absent or hypoplastic segments of the internal carotid artery. It may be bilateral and associated with other vascular aspects (aorta malformation, posterior circulation rete mirabile) or a general condition (pseudoxanthoma elasticum).<sup>19-22</sup> It may represent a risk factor for ischemic or hemorrhagic cerebrovascular diseases.<sup>23</sup> Postocclusive neovascularization has been described in systemic arteries, in which vasa vasorum, adventitial vessels form plexus in the wall of large blood vessels, with a mainly nutritive role; development would be stimulated by local subacute hypoxic conditions (atherosclerosis, diabetes, vasculitis, etc), figuring a phenomenon of compensatory neovascularization. This has been notably reported in coronary arteries, aorta, and cervical internal carotid artery occlusion.<sup>24-26</sup> To our knowledge, these mechanisms have not been reported affecting the circle of Willis, except in a handful of case reports.<sup>27</sup> The existence of intracranial vasa vasorum has been debated, and they are suggested to be present only in the proximal parts of MCA, ACA, and intracranial ICA.<sup>28-30</sup> U-PS anastomotic bridge could thus represent a similar mechanism of postocclusive neovascularization, with the development of intracranial vasa vasorum located in the proximal segments of the circle of Willis arteries.

Interestingly, not every patient with LVO developed U-PS anastomotic bridge. No association with age at stroke onset or duration of vessel occlusion was found. U-PS anastomotic bridge development was strongly associated with stroke etiology: this

	Location	Typically affected vessels	Vascular network location / orientation	Unilateral or bilateral	Other affected arterial segments, association	Progressive ?	Schematic figure
<b>ACQUIRED CONDITIONS</b>							
U-PS anastomotic bridge	Intracranial	MCA, I-ICA, ACA	External to the artery main trunk / Bridge in by-pass of stenosis or occlusion	unilateral	Contiguous segments (MCA, I-ICA, ACA)	Non progressive	
Moyamoya angiopathy	Intracranial	I-ICA, MCA, ACA	External to the artery main trunk / Direction perpendicular from MCA main axis (perforating lenticulostriate collaterals)	mostly bilateral	May be associated with extracranial vascular anomalies when syndromic (MFS, ACTA2, etc.)	Progressive	
Post-occlusive vasa vasorum neovascularization	Systemic arteries	Coronary arteries, aorta, cervical ICA	Within the vessel wall of the occluded artery / Parallel with the artery main trunk	nd	Associated with atherosclerosis, diabetes, vasculitis	Non progressive	
<b>CONGENITAL CONDITIONS / VARIATIONS</b>							
Rete mirabile	Cervical, intracavernous ICA	ICA branches feeding the cervical or cavernous ICA, VA/BA	External to the ICA main trunk but close to it / Parallel with the artery main axis, in by-pass of hypoplastic artery (typically ICA-ICA by-pass)	bilateral	VA/BA, associated with other vascular malformations (aorta). Reported association with pseudoxanthoma elasticum	Non progressive	
Twiglike MCA	Intracranial	M2 segment of MCA	In place of MCA main trunk: persistent fetal network of the primitive MCA	unilateral	Associated with congenital variation or anomaly of the Circle of Willis	Non progressive	
Fenestration	Intracranial	Anterior communicating artery, proximal BA, Less frequent in MCA (M1 segment) and ACA	In place of the artery main trunk: double channel, No collaterals	mostly unilateral	Associated with congenital variation or anomaly of the Circle of Willis. Aneurysm development at the site of fenestration	Non progressive	

**FIG 4.** Distinctive features of U-PS anastomotic bridge compared with vascular patterns with close appearance. (i)-ICA = (intracranial)-internal carotid artery; ECA = external carotid artery; VA = vertebral artery; BA = basilar artery. Illustration is from Lin et al<sup>22</sup> for rete mirabile. Drawings by F.B. and M.K., with courtesy.

pattern was only observed in patients with unilateral FCA, and 66% of children with FCA and LVO developed U-PS anastomotic bridge. This suggests that, rather than a nonspecific mode of vascular healing after local ischemic changes related to LVO, it could be related to subacute local conditions and modifications associated with FCA, for instance, subacute hypoxia and/or vessel wall inflammation, stimulating angiogenic factors.<sup>30,31</sup>

Finally, it seems important to differentiate this vascular aspect from Moyamoya Angiopathy MMA. MMA is a progressive steno-occlusive disease involving the distal internal cerebral artery and its bifurcation, and the adjacent proximal ACA and MCA. It often shows bilateral, symmetric, or asymmetric segmental stenoses of the involved arteries. Stenoses are associated with several types of developing compensatory vessels: basal collateral vessels, leptomeningeal collaterals, and anastomotic internal-external carotid systems collaterals. Basal collaterals are abnormally dilated lenticulostriate and thalamo-perforating arteries, arising from the MCA to the basal ganglia and thalamus.<sup>12,27,32</sup> Key points differentiate MMA and U-PS anastomotic bridge: 1) in MMA dilated perforating arteries supplying the basal ganglia arise perpendicularly from the MCA trunk, whereas in U-PS anastomotic bridge collaterals go parallel with the MCA main trunk (the difference is well observed on coronal view) (Figs 3 and 4); and 2) MMA is classically bilateral, sometimes asymmetrical but rarely unilateral, whereas U-PS anastomotic bridge is unilateral without contralateral arterial anomaly (stenosis/occlusion). The latter point is of utmost importance as both an aspect of anastomotic bridge and abnormal perforating lenticulostriate (Moyamoya network) may be observed in patients with Moyamoya. It seems important to identify isolated U-PS anastomotic bridge because,

though these patients have developing collaterals, they did not experience any stroke recurrence nor vascular disease progression, contrary to patients with Moyamoya angiopathy. In our study, recurrent strokes only occurred in non-FCA patients. This emphasizes the fact that patients with FCA usually do not experience recurrent stroke regardless of whether they had collaterals or not. Thus, the observation of a U-PS anastomotic bridge after stroke with an isolated strictly unilateral LVO, and no contralateral vascular anomaly should not be considered as a risk for poor outcome or stroke recurrence.

Our study limitations mainly relate to the small sample and to its retrospective nature. Different angiographic imaging modalities may also induce biases: TOF-MRA may over-call occlusion in a stenosis with minimal flow, and 3T MRA may have a better resolution than 1.5T MRA for the anastomotic bridge observation. However, the homogeneous technique in our study may limit the bias for intrasample angiographic comparisons: 25/26 patients had TOF-MRA in the acute phase and during follow-up, mostly on 1.5T scan. Only 1 patient had initial MRA and CTA at 48 h poststroke, but he had a persistent right proximal M2 segment occlusion, which precludes a bias of patency related to imaging technique.

## CONCLUSIONS

LVO represented 24.8% of non-neonatal pediatric AIS in the anterior circulation in our study. A specific pattern of U-PS anastomotic bridge, with unilateral network of collaterals bypassing the affected zone, appearing in the first year after stroke and remaining stable without stroke recurrence, is strongly associated with FCA. Further studies are needed to confirm the association of



U-PS anastomotic bridge with FCA, and to refine differences between unilateral FCA with collaterals and MMA.

## ACKNOWLEDGMENTS

We thank Kim Tran Dong for technical assistance.

Disclosure forms provided by the authors are available with the full text and PDF of this article at [www.ajnr.org](http://www.ajnr.org).

## REFERENCES

- Bonnet W, Dowling MM, Plumb P. Prevalence and natural history of large vessel occlusion in childhood acute ischemic stroke [Abstract P580]. *Stroke* 2021;52:AP580 CrossRef Medline
- Bhatia KD, Briest R, Goetti R, et al. Incidence and natural history of pediatric large vessel occlusion stroke: a population study. *JAMA Neurol* 2022;79:488–97 CrossRef Medline
- Tabone L, Mediamolle N, Bellesme C, et al. Regional pediatric acute stroke protocol: initial experience during 3 years and 13 recanalization treatments in children. *Stroke* 2017;48:2278–81 CrossRef Medline
- Amlie-Lefond C, Wainwright MS. Response by Amlie-Lefond and Wainwright to letter regarding article, 'organizing for acute arterial ischemic stroke in children.' *Stroke* 2020;51:e37 CrossRef Medline
- Bigi S, Dulcey A, Gralla J, et al. Feasibility, safety, and outcome of recanalization treatment in childhood stroke. *Ann Neurol* 2018;83:1125–32 CrossRef Medline
- Chabrier S, Ozanne A, Naggara O, et al. Hyperacute recanalization strategies and childhood stroke in the evidence age. *Stroke* 2021;52:381–84 CrossRef Medline
- Sporns PB, Sträter R, Minnerup J, et al. Feasibility, safety, and outcome of endovascular recanalization in childhood stroke: the Save ChildS Study. *JAMA Neurol* 2020;77:25–34 CrossRef Medline
- Kossorotoff M, Kerleroux B, Boulouis G; KidClot Group, et al. Recanalization treatments for pediatric acute ischemic stroke in France. *JAMA Netw Open* 2022;5:e2231343 CrossRef Medline
- Bhatia KD, Chowdhury S, Andrews I, et al. Association between thrombectomy and functional outcomes in pediatric patients with acute ischemic stroke from large vessel occlusion. *JAMA Neurol* 2023;80:910–18 CrossRef Medline
- Bernard TJ, Manco-Johnson MJ, Lo W, et al. Towards a consensus-based classification of childhood arterial ischemic stroke. *Stroke* 2012;43:371–77 CrossRef Medline
- Charbit-Henrion F, Goguyer-Deschaumes R, Borensztajn K, et al. Systemic inflammatory syndrome in children with FARSA deficiency. *Clin Genet* 2022;101:552–58 CrossRef Medline
- Kuroda S, Houkin K. Moyamoya disease: current concepts and future perspectives. *Lancet Neurol* 2008;7:1056–66 CrossRef Medline
- Menshawi K, Mohr JP, Gutierrez J. A functional perspective on the embryology and anatomy of the cerebral blood supply. *J Stroke* 2015;17:144–58 CrossRef Medline
- Seo BS, Lee YS, Lee HG, et al. Clinical and radiological features of patients with aplastic or twiglike middle cerebral arteries. *Neurosurgery* 2012;70:1472–80; discussion 1480 CrossRef Medline
- Liu HM, Lai DM, Tu YK, et al. Aneurysms in twig-like middle cerebral artery. *Cerebrovasc Dis* 2005;20:1–5 CrossRef Medline
- Gailloud P, Albayram S, Fasel JH, et al. Angiographic and embryologic considerations in five cases of middle cerebral artery fenestration. *AJNR Am J Neuroradiol* 2002;23:585–87 Medline
- Berry AD, Kepes JJ, Wetzel MD. Segmental duplication of the basilar artery with thrombosis. *Stroke* 1988;19:256–60 CrossRef Medline
- Kloska SP, Schlegel PM, Sträter R, et al. Causality of pediatric brainstem infarction and basilar artery fenestration? *Pediatr Neurol* 2006;35:436–38 CrossRef Medline
- Mondel PK, Saraf R, Limaye US. Rete mirabile associated with pial arteriovenous fistula: imaging features with literature review. *J Neurointerv Surg* 2017;9:e36 CrossRef Medline
- Fuwa I. A pediatric case of carotid rete mirabile. *Stroke* 1994;25:1268–70 CrossRef Medline
- Araki Y, Imai S, Saitoh A, et al. A case of carotid rete mirabile associated with pseudoxanthoma elasticum: a case report. *No To Shinkei* 1986;38:495–500 Medline
- Lin E, Linfante I, Dabus G. Unilateral rete mirabile as a result of segmental agenesis of the ascending petrous segment of the internal carotid artery: embryology, differential diagnosis and clinical implications. *Interv Neuroradiol* 2013;19:73–77 CrossRef Medline
- Paschoal EH, Yamaki VN, Júnior FMP, et al. Carotid rete mirabile associated with subarachnoid hemorrhage from intracranial aneurysm: a case report and systematic review. *Interv Neuroradiol* 2015;21:55–60 CrossRef Medline
- Srivatsa SS, Edwards WD, Boos CM, et al. Histologic correlates of angiographic chronic total coronary artery occlusions: influence of occlusion duration on neovascular channel patterns and intimal plaque composition. *J Am Coll Cardiol* 1997;29:955–63 CrossRef Medline
- Martin MA, Marotta TR. Vasa vasorum: another cause of the carotid string sign. *AJNR Am J Neuroradiol* 1999;20:259–62 Medline
- Kemény V, Droste DW, Nabavi DG, et al. Collateralization of an occluded internal carotid artery via a vasa vasorum. *Stroke* 1998;29:521–23 CrossRef Medline
- Muthusami P, Krings T, Raybaud C, et al. Intracranial artery to artery spontaneous revascularization in a child. *Childs Nerv Syst* 2017;33:2035–38 CrossRef Medline
- Aydin F. Do human intracranial arteries lack vasa vasorum? A comparative immunohistochemical study of intracranial and systemic arteries. *Acta Neuropathol* 1998;96:22–28 CrossRef Medline
- Connolly ES Jr, Huang J, Goldman JE, et al. Immunohistochemical detection of intracranial vasa vasorum: a human autopsy study. *Neurosurgery* 1996;38:789–93 CrossRef Medline
- Portanova A, Hakakian N, Mikulis DJ, et al. Intracranial vasa vasorum: insights and implications for imaging. *Radiology* 2013;267:667–79 CrossRef Medline
- Fullerton HJ, Stence N, Hills NK; VIPS Investigators, et al. Focal cerebral arteriopathy of childhood: novel severity score and natural history. *Stroke* 2018;49:2590–96 CrossRef Medline
- Brozici M, van der Zwan A, Hillen B. Anatomy and functionality of leptomeningeal anastomoses: a review. *Stroke* 2003;34:2750–62 CrossRef Medline



# Reducing False-Positives in CT Perfusion Infarct Core Segmentation Using Contralateral Local Normalization

Alexander Rau, Marco Reisert, Christian A. Taschner, Theo Demerath, Samer Elsheikh, Benedikt Frank, Martin Köhrmann, Horst Urbach, and Elias Kellner



## ABSTRACT

**BACKGROUND AND PURPOSE:** The established global threshold of rCBF <30% for infarct core segmentation can lead to false-positives, as it does not account for the differences in blood flow between GM and WM and patient-individual factors, such as microangiopathy. To mitigate this problem, we suggest normalizing each voxel not only with a global reference value (ie, the median value of normally perfused tissue) but also with its local contralateral counterpart.

**MATERIALS AND METHODS:** We retrospectively enrolled 2830 CTP scans with suspected ischemic stroke, of which 335 showed obvious signs of microangiopathy. In addition to the conventional, global normalization, a local normalization was performed by dividing the rCBF maps with their mirrored and smoothed counterpart, which sets each voxel value in relation to the contralateral counterpart, intrinsically accounting for GM and WM differences and symmetric patient individual microangiopathy. Maps were visually assessed and core volumes were calculated for both methods.

**RESULTS:** Cases with obvious microangiopathy showed a strong reduction in false-positives by using local normalization (mean 14.7 mL versus mean 3.7 mL in cases with and without microangiopathy). On average, core volumes were slightly smaller, indicating an improved segmentation that was more robust against naturally low blood flow values in the deep WM.

**CONCLUSIONS:** The proposed method of local normalization can reduce overestimation of the infarct core, especially in the deep WM and in cases with obvious microangiopathy. False-positives in CTP infarct core segmentation might lead to less-than-optimal therapy decisions when not correctly interpreted. The proposed method might help mitigate this problem.

**ABBREVIATIONS:** MA = microangiopathic alteration; NoMA = no microangiopathic alteration; rCBF = relative CBF; rCBV = relative CBV;  $T_{\max}$  = maximum of the residue function

In most centers, indication for therapy of acute stroke is based on multimodal CT imaging protocols that comprise noncontrast CT, CTA, and CTP imaging.<sup>1</sup> CTP is a powerful tool in stroke imaging with proved high accuracy for the detection of ischemic lesions and the delineation of irreversibly damaged tissue (the so-called infarct core) and the penumbra that represents tissue potentially salvageable if reperfused. CTP was successfully employed as a selection criterion for endovascular therapy in 2 important trials, showing benefit for patients with limited-size-

predicted infarct core and substantial salvageable brain tissue.<sup>2,3</sup> Therefore, current stroke guidelines require CTP in patients with extended and unclear time windows.<sup>4</sup> Despite recent studies on thrombectomy in patients presenting with large ischemic core,<sup>5,6</sup> estimation of the infarct core by CTP is of central importance for patient selection in the prolonged time window.<sup>2,4</sup>

To approximate the infarct core and the penumbra, metrics based on the perfusion bolus dynamics are calculated and compared between ischemic and healthy tissue.<sup>7</sup> In detail, the time to peak of the contrast agent bolus ( $T_{\max}$ ; ie, the maximum of the residue function) is employed to assess a delay in perfusion. The  $T_{\max}$  is given in absolute units of seconds, and the typically used threshold of  $T_{\max} > 6$  seconds represents a relevant delay.<sup>8</sup> The CBF, on the other hand, cannot be easily quantified and is therefore typically normalized to a reference value. Typically, as reference, the median value of the hemisphere contralateral to the stroke side or the median CBF of the patient's normally perfused tissue identified as  $T_{\max} \leq 4$  seconds is used. The infarct core is obtained by thresholding this normalized relative map with rCBF <30%.<sup>1,9</sup>

Received October 7, 2023; accepted after revision November 20.

From the Departments of Neuroradiology (A.R., C.A.T., T.D., S.E., H.U.), Diagnostic and Interventional Radiology (A.R.), Stereotactic and Functional Neurosurgery (M.R.), and Medical Physics (M.R., E.K.), Medical Center—University of Freiburg, Faculty of Medicine, University of Freiburg, Freiburg, Germany; and Department of Neurology and Center for Translational Neuro- and Behavioral Sciences (B.F., M.K.), University Hospital Essen, Essen, Germany.

Please address correspondence to Elias Kellner, Breisacher Str 64, 79106, Freiburg, Germany; e-mail: elias.kellner@uniklinik-freiburg.de



Indicates article with online supplemental data.

<http://dx.doi.org/10.3174/ajnr.A8111>

This “global” normalization approach can easily be implemented and standardized but is potentially hampered by several factors: It does not account for the differences in perfusion dynamics in GM and WM<sup>10-12</sup> and patient-individual characteristics, such as microangiopathic WM alterations.<sup>13</sup> Especially the latter constitutes a major challenge in the calculation of perfusion values as the WM gliotic tissue shows a delayed and reduced perfusion already without acute vessel occlusion present.<sup>11,12,14</sup> Whereas in general, overestimation of ischemic core volume is uncommon,<sup>15</sup> these and other limitations can lead to false-positives in CTP infarct core segmentation<sup>16-18</sup> and thus to misleading therapy decisions when not correctly interpreted.<sup>19</sup>

To overcome this technical challenge and account for microangiopathy as an important co-pathology in the context of cerebrovascular disease, we propose a dual approach. In addition to normalizing CBF values in each voxel with a global reference value, we suggest an additional normalization with local regions from the contralateral counterpart when calculating relative perfusion metrics. This comprehensive method accounts for both global and local factors, enhancing the accuracy of the analysis.

## MATERIALS AND METHODS

### Participants

For this retrospective study, we included patients who received neuroimaging, including CTP due to a suspected stroke between 2014 and 2021. For data management and image processing, all images were exported and anonymized to a local instance of the imaging platform NORA ([www.nora-imaging.org](http://www.nora-imaging.org)). We excluded all patients with nonischemic lesions, such as tumors or hemorrhages. Image data were individually assessed for quality and patients with substantial image artifacts (ie, due to movement) were excluded from further analysis. Image data and patient records were assessed for the presence of microangiopathic brain damage.<sup>20</sup> We identified patients with relevant WM microangiopathic alterations (MA, eg, Fazekas >1) and assigned them to the MA group, whereas patients without relevant WM lesions (Fazekas 0 and 1) were assigned to the NoMA group. To accomplish this, an experienced neuroradiologist evaluated noncontrast CT data in 5-mm axial reconstructions by using a soft kernel. Furthermore, we excluded cases with old and bilateral infarctions.

The study was approved by the Institutional Review Board (Ethics Committee–University of Freiburg; EK 20/1047) and carried out in accordance with the Declaration of Helsinki and its later amendments. Due to the retrospective nature of this study, the need for written informed consent was waived.

### CT Imaging

CT scans were performed on a 128–detector row (Somatom Definition Flash; Siemens) or a 64–detector row multidetector CT scanner (Somatom Definition 64 AS; Siemens). CTP series were acquired in the axial scan mode with the following protocols for the Somatom Definition Flash: 80 kV, 180 mAs, collimation =  $16 \times 1.2$  mm, no gantry tilt, tube rotation time = 0.3 seconds, toggle technique (5 blocks  $\times$  0.3 = 1.5 seconds), z-coverage = 100 mm, section thickness = 5 mm, increment = 5 mm, 27 series every 1.5 seconds = 42 seconds scan time

(effective temporal resolution in the middle of the plane = 1.5 seconds, in the periphery = 2.6 seconds) after intravenous (16–18 G) injection of 40 mL of Imeron 400 (iopamidol; Bracco) + 30 mL of sodium chloride (NaCl) at a flow rate of 6 mL/seconds.

The parameters for Somatom Definition 64 AS were as follows: 80 kV, 180 mAs, collimation =  $32 \times 1.2$  mm, no gantry tilt, tube rotation time = 0.3 seconds, toggle technique (5 blocks  $\times$  0.3 seconds = 1.5 seconds), z-coverage = 90 mm, section thickness = 5 mm, increment = 3 mm, 30 series every 1.5 seconds = 45 seconds scan time (effective temporal resolution in the middle of the plane = 1.5 seconds, in the periphery = 2.6 seconds) after intravenous (16–18 G) injection of 40 mL of Imeron 400 + 30 mL of NaCl at a flow rate of 6 mL/seconds.

### Calculation of Perfusion Values

Perfusion scans were analyzed by using a research version of the software package VEOcore (VEObrian, [www.veobrain.com](http://www.veobrain.com)). The software provides fully automated processing of perfusion scans, including motion correction, denoising, deconvolution by using Tikhonov regularization, and automated quality control. The output of the software is perfusion maps of relative CBF (rCBF), relative CBV (rCBV), and  $T_{\max}$ , as well as segmentations of hypoperfusion, core and mismatch, and corresponding volumes in milliliters by using the commonly established thresholds of  $T_{\max} > 6$  seconds for delayed perfusion and rCBF <30% for the infarct core.<sup>2,21,22</sup> Good agreement of VEOcore with other perfusion software has been demonstrated.<sup>23,24</sup>

Our study employed 2 distinct normalization approaches for thresholding the rCBF maps. First, we adopted the conventional well-established global normalization method, wherein each voxel's value is normalized to the average value of the contralateral hemisphere.<sup>9</sup> Mathematically, this normalization is achieved by dividing each voxel's value by a common factor (ie, the median value of normally perfused tissue defined as  $T_{\max} \leq 4$  seconds).<sup>25</sup> It is important to note that this process globally scales the rCBF map but retains the relative differences between voxels.

Additionally, we investigated the feasibility and potential of a more localized normalization approach (a schematic is provided in Fig 1). The concept behind this method is to normalize each voxel not to a global reference value but rather to its corresponding counterpart in the contralateral hemisphere. To achieve this, a transformation is required to map each voxel to its direct counterpart. This was obtained by nonrigid registration of the baseline image of the perfusion scan with a vertically mirrored copy of that image by using SPM12 (Wellcome Trust Center for Neuroimaging). When applying this transformation to the rCBF data array, a mirrored array can be obtained that directly relates each voxel to its contralateral counterpart. Normalization was then accomplished through voxelwise division of the original image (ie, the whole brain CBF map) by the mirrored one. However, several considerations were taken into account. Brain symmetry is rarely perfect, and registration inherently entails some degree of uncertainty. Moreover, division by noisy maps can introduce instabilities. Furthermore, very high flow values in the counterpart, particularly in large vessels, can result in very low values after division, potentially

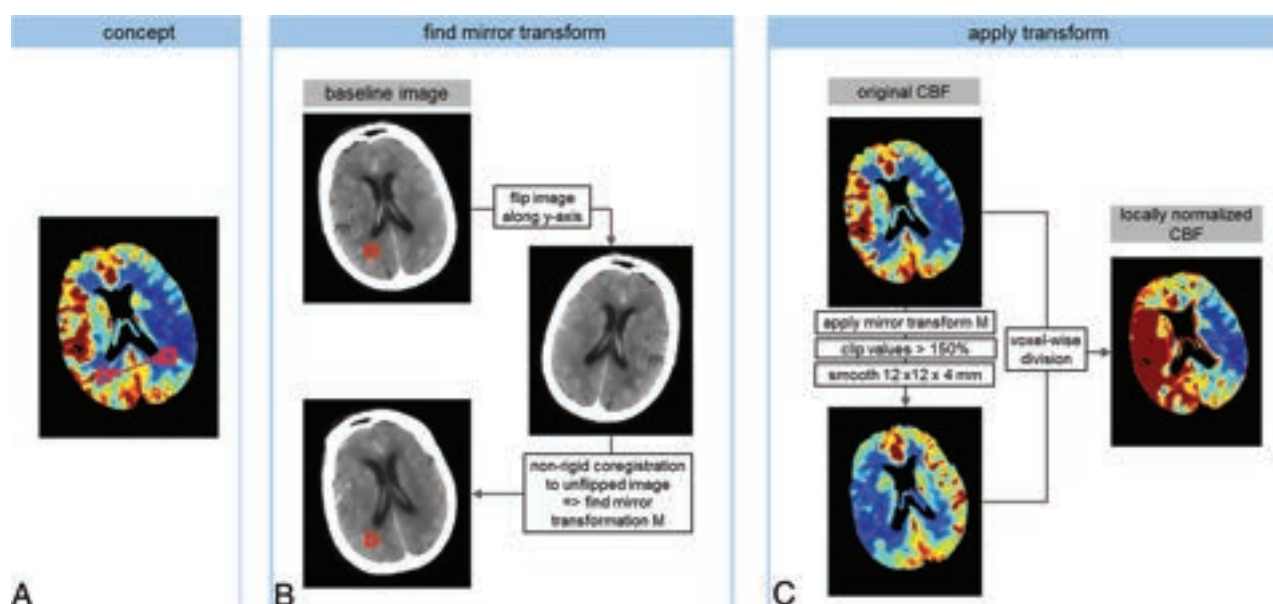


**FIG 1.** Schematic of the workflow for global and local normalization of CT perfusion-derived CBF with subsequent thresholding to 30% to obtain a segmentation of the ischemic core. In the global approach, each voxel is normalized to the entire contralateral hemisphere, whereas in the local approach, a voxel is compared with a local region on the contralateral side. This leads to an equalization between GM and WM and thus a more distinct contrast in the perfusion maps.

#### Patient characteristics

	<i>n</i>	Sex (Female)	Age (yr)	Stroke Evident	Mean Core Volume (mL)	
					Global Normalization	Local Normalization
No microangiopathy	2830	49%	72.6 ± 15.2	1334 (47%)	41.0 ± 46.9	31.4 ± 41.1
Microangiopathy	335	59%	73.5 ± 17.1	175 (52%)	60.3 ± 49.0	33.6 ± 39.3

leading to false-positives. To address these issues, 2 precautionary measures were implemented before division: The mirrored image was clipped, meaning that any value exceeding 150% was capped at 150%, and the mirrored image then underwent smoothing with a Gaussian filter with a sigma of  $12 \times 12 \times 4$  mm.

The local approach allows each voxel's value to be related to a local region of the contralateral hemisphere, inherently accommodating differences between GM and WM<sup>11</sup> and accounting for patient-specific microangiopathic changes, which typically manifest symmetrically.<sup>26</sup> With these locally normalized maps, a threshold of 30% can now be interpreted as 30% relative to a local contralateral region, rather than relative to an averaged reference value.

Finally, for both the globally and locally normalized rCBF maps, a threshold of relative rCBF < 30% was applied. Subsequent morphologic image opening and closing operations were applied to remove speckle noise followed by the calculation of infarct volumes.<sup>27</sup> To avoid false-positives on the healthy hemisphere, segmentations were restricted to the affected hemisphere only, determined as the one with the greater median  $T_{\max}$ .

#### Statistical Analyses

Statistical analyses were performed by using MATLAB (MathWorks). We generated correlation plots for both the NoMA and MA groups. The average changes in infarct volumes when comparing globally and locally normalized rCBF maps for both groups were assessed by relative means by using the linear

regression coefficient and by absolute means by using the mean differences and SDs between both approaches derived from Bland-Altman plots between both approaches.

#### Data Availability

Data and code are available from the authors upon reasonable request and approval by the local ethics committee.

## RESULTS

#### Participants

We retrospectively enrolled 2830 CTP scans of patients with suspected ischemic stroke (52% women, mean age  $73 \pm 15$  years), of which 335 showed obvious signs of microangiopathy corresponding to the MA group. While age did not significantly differ between the MA and NoMA groups ( $P = .2$ ), significantly more women had MA ( $P < .001$ ). Further information is provided in the Table.

#### Perfusion Values before and after Local Normalization

Correlation and Bland-Altman plots of the calculated core volumes by using both approaches are presented in Figure 2. On average, all volumes were reduced upon applying the local normalization approach. These reductions were significantly higher in the MA group (mean difference  $-14.7$  mL, SD 14.6 mL, regression slope 0.62) and less pronounced in the NoMA group (mean difference  $-3.7$  mL, SD 6.7 mL, regression slope 0.82) ( $P < .001$ ). Visual assessment of the MA group perfusion maps revealed in particular

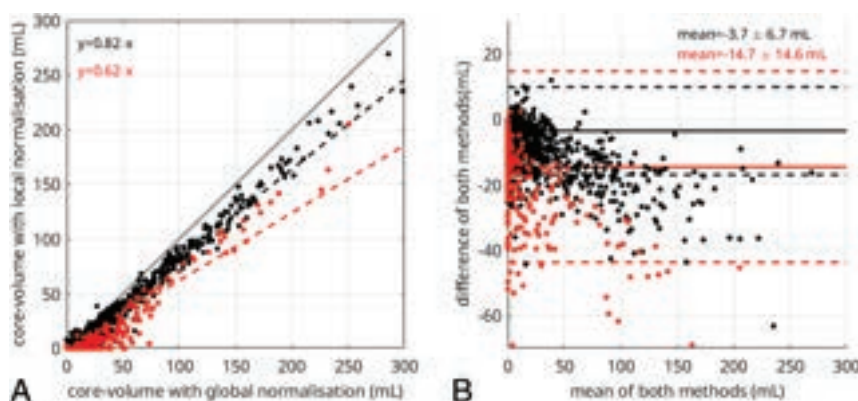


**FIG 2.** Correlation plot (A) and Bland-Altman plot (B) comparing core volumes derived with global and local normalization for the NoMa and MA groups (black and red, respectively). Dashed lines indicate linear regression in the correlation plot, and 2 SDs in the Bland-Altman plot.

a considerable reduction of positively scored voxels in the deep WM. Figures 3 and 4 show exemplary comparisons for both NoMa and MA cases.

## DISCUSSION

The proposed method of local normalization can significantly reduce the extent of false-positive voxels in infarct core segmentation, especially in the deep WM and in cases with obvious microangiopathy.

This is of considerable relevance for the application of CTP in clinical routine as perfusion imaging is an increasingly utilized component in the workup and management of patients with acute ischemic stroke, as the decision to use recanalizing therapy frequently relies on CTP results.<sup>4</sup> False-positive voxels in perfusion imaging-derived calculations can thus erroneously influence therapy decisions.

Our data suggest that especially microangiopathic changes in the deep WM constitute a relevant influence on the calculation of infarct core volumes. In the context of cerebrovascular disease, microangiopathic changes are a frequent co-pathology in patients with vascular disease,<sup>28</sup> so a correction of false-positive values caused by microangiopathy might be relevant in the presence of small vessel disease. This is corroborated by the fact that we noted a substantially higher reduction of core volumes in cases with microangiopathy versus without. Moreover, visual inspection of cases with small vessel disease revealed that the proposed correction method mainly removed false-positives in the deep WM, which is supported by the case in Figure 4.

However, in patients without obvious microangiopathy, the local normalization approach also resulted in a reduction of infarct volumes of  $\sim 3.7$  mL, or 18% on average. Again, this was attributed to WM regions, where the blood flow is naturally lower compared with the GM.<sup>10,11,29-32</sup> In contrast to the global normalization, the introduced local approach allowed for a more distinct calculation of the perfusion in the GM and WM, thus leading to fewer voxels identified as ischemic upon applying the threshold of  $rCBF < 30\%$ . Whether such voxels truly are false-positives, or whether the threshold of  $rCBF < 30\%$  needs to be adapted to better delineate the ischemic tissue and

avoid underestimation requires evaluation in future studies, including follow-up imaging.

Previously, the term “ghost infarct core” was introduced to characterize instances of false-positives in infarct core segmentation,<sup>16</sup> and several underlying factors, such as poor collaterals, have been suggested.<sup>17-19</sup> In our study, we have identified and analyzed an additional factor that warrants consideration.

Novel infarct segmentation techniques leveraging deep learning are rapidly advancing.<sup>33-37</sup> These techniques not only perform with sufficient precision but also allow for a more multi-

parametric approach by simultaneously taking information from different raw data and derived features into account. Furthermore, some methods are able to account for contralateral asymmetries through innovative data augmentation methods, such as vertical image flipping.<sup>33</sup> Against this, we perceive our local normalization approach not as a competitor to deep learning but rather as a potentially valuable contribution to both conventional and deep learning-based postprocessing. It is important to recognize that the effectiveness of deep learning substantially hinges on preprocessing steps and the judicious selection of appropriate training data sets, and our work offers insights that can potentially aid in refining deep learning models in both aspects.

In principle, differential GM and WM perfusion or microangiopathic damage may not only impact  $rCBF$ , but also  $T_{max}$ .<sup>13</sup> However, because  $T_{max}$  is directly quantified in units of seconds and thus does not require normalization, and GM versus WM differences are less pronounced in  $T_{max}$ ,<sup>11</sup> we did not consider a local normalization for  $T_{max}$  in the context of this study.

For  $rCBV$  evaluation, on the other hand, a local contralateral normalization might also offer benefits regarding visual and quantitative scoring of collateralization, as illustrated in the Online Supplemental Data for exemplary cases. A more detailed analysis of  $rCBV$  was beyond the scope of the present study and might be part of future research.

A general limitation of our work is the fact that we do not have a consistent reference standard, for example, an MR imaging examination as close in time as possible or a follow-up MR imaging indicating the final infarct volume. Also, an underlying assumption of our approach is that microangiopathic changes are largely symmetrical, which may not be true in rare cases. Another limitation is associated with the “healthy” hemisphere. In cases involving old or bilateral infarctions, this might lead to biased results (Online Supplemental Data). This issue is also pertinent in the global approach, but more pronounced when using local normalizations. It is crucial in such instances to cross-reference with the globally normalized maps for a more comprehensive assessment. Moreover, the local normalization approach induced a rather unusual impression of the  $rCBF$  maps and might hamper the assessment of the “healthy” hemisphere as visible in the



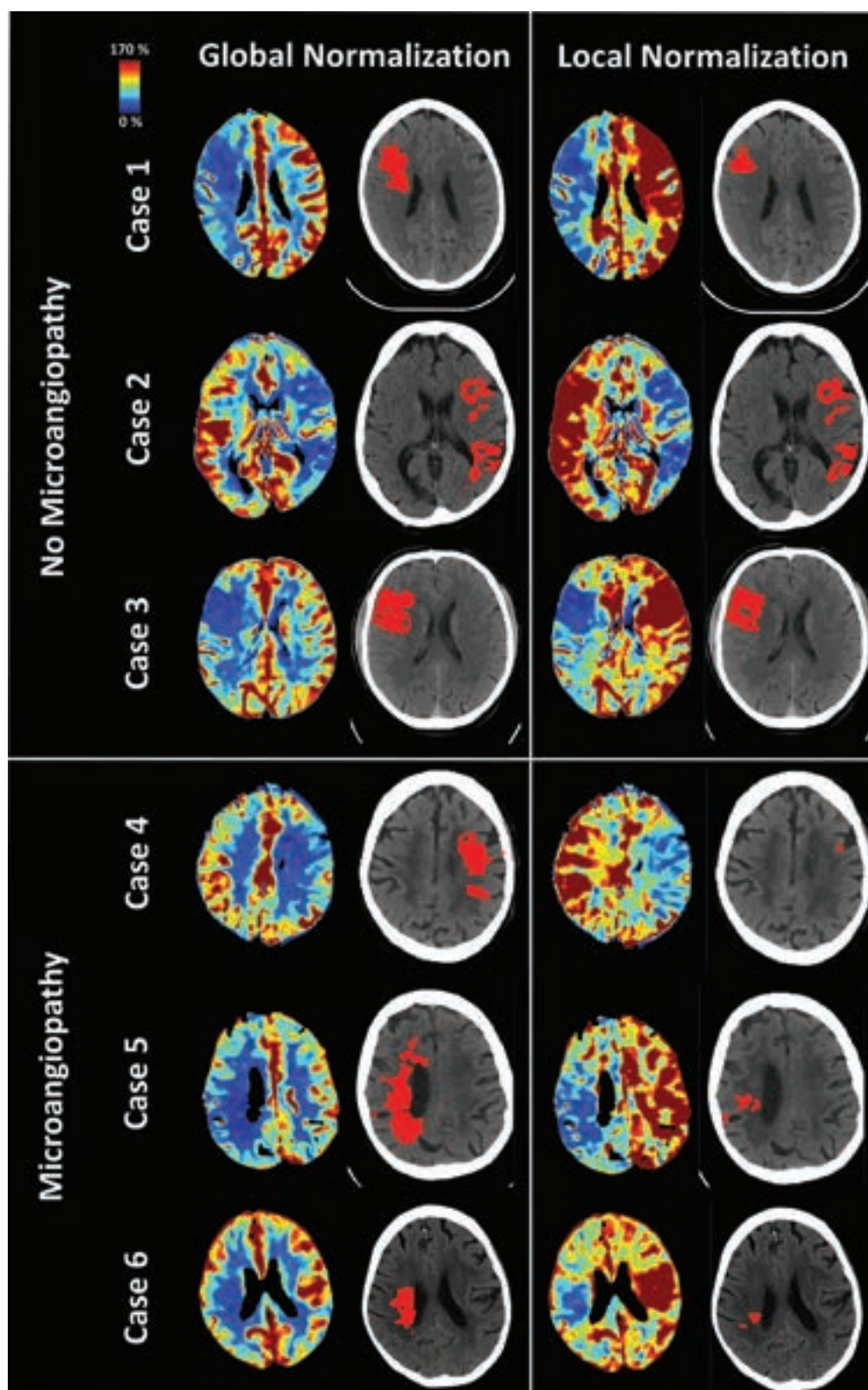


**FIG 3.** Comparison of global (*left*) and local (*right*) normalization for CBF maps and threshold-based ischemic core segmentations in 3 cases without and with WM small vessel disease.

exemplary cases in which the image impression is more of a mirrored picture of the ischemic hemisphere and does not allow for an intrahemispheric assessment of rCBF values. Hence, the

proposed approach of a local contralateral normalization must not replace the conventional rCBF calculation but rather supplement it in cases with suspected false-positives (eg, due to severe



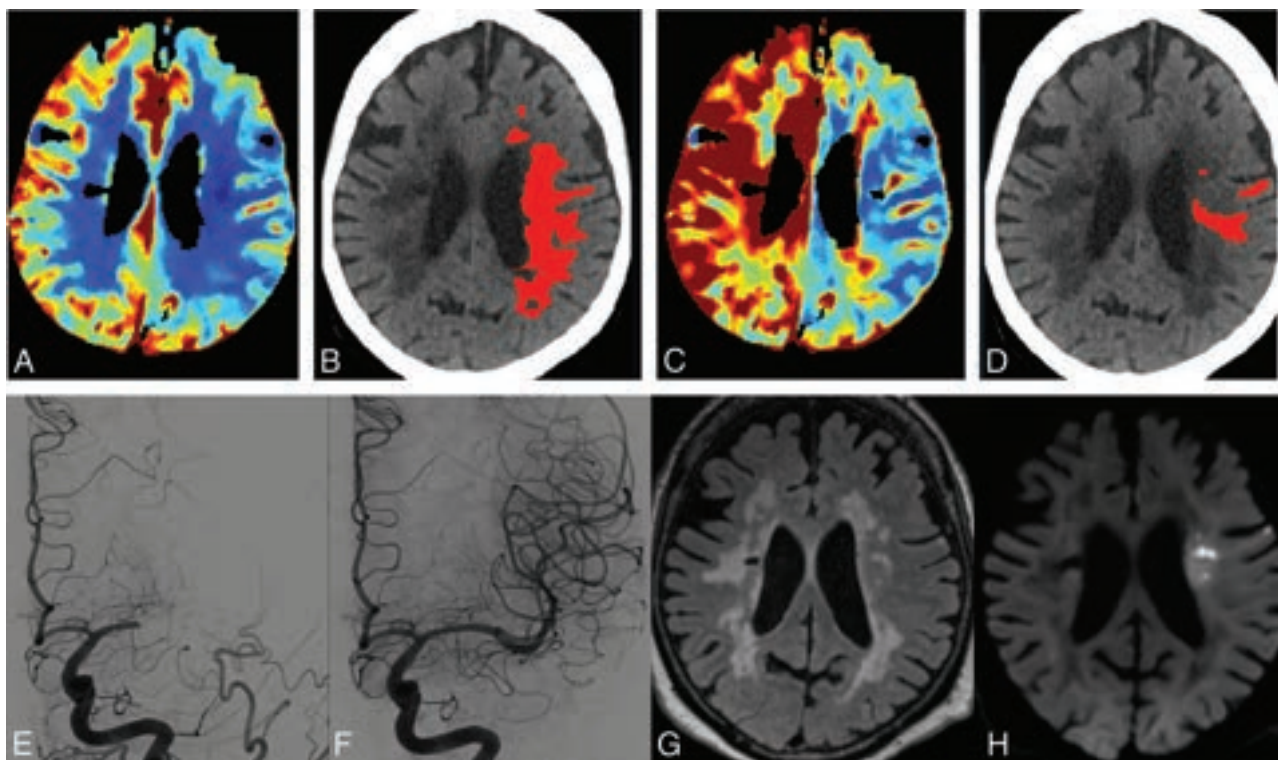


**FIG 4.** Image data of an 83-year-old woman 5 hours after onset of a left MCA occlusion. CTP with global contralateral normalization (A) suggested an infarct core involving the centrum semiovale (B). In contrast, CTP with local contralateral normalization (C) did not display the deep WM as infarct core (D). The MI segment was recanalized following one thrombectomy maneuver by using a 4 × 40 mm Solitaire stent (E, F). Follow-up MR imaging shows distinct microangiopathy (G, FLAIR), but only scattered subacute centrum semiovale infarct (H, DWI).

microangiopathy). Additionally, our results should raise attention to the potential impact of microangiopathy on rCBF values.

## CONCLUSIONS

A local normalization of CTP parameters in addition to the global normalization might reduce false-positives in CTP infarct core segmentation that could potentially lead to suboptimal therapy decisions.

Disclosure forms provided by the authors are available with the full text and PDF of this article at [www.ajnr.org](http://www.ajnr.org).

## REFERENCES

- Demeestere J, Wouters A, Christensen S, et al. **Review of perfusion imaging in acute ischemic stroke.** *Stroke* 2020;51:1017–24 CrossRef Medline
- Albers GW, Marks MP, Kemp S, DEFUSE 3 Investigators, et al. **Thrombectomy for stroke at 6 to 16 hours with selection by perfusion imaging.** *N Engl J Med* 2018;378:708–18 CrossRef Medline
- Nogueira RG, Jadhav AP, Haussen DC, DAWN Trial Investigators, et al. **Thrombectomy 6 to 24 hours after stroke with a mismatch between deficit and infarct.** *N Engl J Med* 2018;378:11–21 CrossRef Medline
- Powers WJ, Rabinstein AA, Ackerson T, et al. **Guidelines for the early management of patients with acute ischemic stroke. 2019 Update to the 2018 Guidelines for the Early Management of Acute Ischemic Stroke: a guideline for healthcare professionals from the American Heart Association/American Stroke Association.** *Stroke* 2019;50:e344–e418 CrossRef Medline
- Sarraj A, Hassan AE, Abraham MG, SELECT2 Investigators, et al. **Trial of endovascular thrombectomy for large ischemic strokes.** *N Engl J Med* 2023;388:1259–71 CrossRef Medline
- Huo X, Ma G, Tong X, ANGEL-ASPECT Investigators, et al. **Trial of endovascular therapy for acute ischemic stroke with large infarct.** *N Engl J Med* 2023;388:1272–83 CrossRef Medline
- Konstant AA, Goldmakher GV, Lee TY, et al. **Theoretic basis and technical implementations of CT perfusion in acute ischemic stroke: 1. Theoretic basis.** *AJNR Am J Neuroradiol* 2009;30:662–68 CrossRef Medline
- Olivot JM, Mlynash M, Inoue M, DEFUSE 2 Investigators, et al. **Hypoperfusion intensity ratio predicts infarct progression and functional outcome in the DEFUSE 2 cohort.** *Stroke* 2014;45:1018–23 CrossRef Medline
- Campbell BC, Christensen S, Levi CR, et al. **Cerebral blood flow is the optimal CT perfusion parameter for assessing infarct core.** *Stroke* 2011;42:3435–40 CrossRef Medline
- Falcao AL, Reutens DC, Markus R, et al. **The resistance to ischemia of white and gray matter after stroke.** *Ann Neurol* 2004;56:695–701 CrossRef Medline
- Chen C, Bivard A, Lin L, et al. **Thresholds for infarction vary between gray matter and white matter in acute ischemic stroke: a CT perfusion study.** *J Cereb Blood Flow Metab* 2019;39:536–46 CrossRef Medline
- Arakawa S, Wright PM, Koga M, et al. **Ischemic thresholds for gray and white matter: a diffusion and perfusion magnetic resonance study.** *Stroke* 2006;37:1211–16 CrossRef Medline
- Marstrand JR, Garde E, Rostrup E, et al. **Cerebral perfusion and cerebrovascular reactivity are reduced in white matter hyperintensities.** *Stroke* 2002;33:972–76 CrossRef Medline
- Shi Y, Thrippleton MJ, Makin SD, et al. **Cerebral blood flow in small vessel disease: a systematic review and meta-analysis.** *J Cereb Blood Flow Metab* 2016;36:1653–67 CrossRef Medline
- Hoving JW, Marquering HA, Majoie CB, et al. **Volumetric and spatial accuracy of computed tomography perfusion estimated**

- ischemic core volume in patients with acute ischemic stroke. *Stroke* 2018;49:2368–75 CrossRef Medline
16. Boned S, Padroni M, Rubiera M, et al. Admission CT perfusion may overestimate initial infarct core: the ghost infarct core concept. *J Neurointerv Surg* 2017;9:66–69 CrossRef Medline
  17. Martins N, Aires A, Mendez B, et al. Ghost infarct core and admission computed tomography perfusion: redefining the role of neuroimaging in acute ischemic stroke. *Interv Neurol* 2018;7:513–21 CrossRef Medline
  18. Rodrigues GM, Mohammaden MH, Haussen DC, et al. Ghost infarct core following endovascular reperfusion: a risk for computed tomography perfusion misguided selection in stroke. *Int J Stroke* 2021 Nov 19 [Epub ahead of print] CrossRef Medline
  19. Ballout AA, Oh SY, Huang B, et al. Ghost infarct core: a systematic review of the frequency, magnitude, and variables of CT perfusion overestimation. *J Neuroimaging* 2023;33:716–24 CrossRef Medline
  20. Fazekas F, Chawluk JB, Alavi A, et al. MR signal abnormalities at 1.5 T in Alzheimer's dementia and normal aging. *AJR Am J Roentgenol* 1987;149:351–56 CrossRef Medline
  21. Lin L, Bivard A, Krishnamurthy V, et al. Whole-brain CT perfusion to quantify acute ischemic penumbra and core. *Radiology* 2016;279:876–87 CrossRef Medline
  22. Olivot JM, Mlynash M, Thijs VN, et al. Optimal  $T_{max}$  threshold for predicting penumbral tissue in acute stroke. *Stroke* 2009;40:469–75 CrossRef Medline
  23. Psychogios MN, Sporns PB, Ospel J, et al. Automated perfusion calculations vs. visual scoring of collaterals and CBV-ASPECTS: has the machine surpassed the eye? *Clin Neuroradiol* 2021;31:499–506
  24. Kellner E, Urbach H. Machine outputs must be checked. *Clin Neuroradiol* 2021;31:507–08 CrossRef Medline
  25. Amukotuwa S, Straka M, Aksoy D, et al. Cerebral blood flow predicts the infarct core: new insights from contemporaneous diffusion and perfusion imaging. *Stroke* 2019;50:2783–89 CrossRef Medline
  26. Veldsman M, Kindalova P, Husain M, et al. Spatial distribution and cognitive impact of cerebrovascular risk-related white matter hyperintensities. *Neuroimage Clin* 2020;28:102405 CrossRef Medline
  27. Kellner E, Rau A, Demerath T, et al. Contrast bolus interference in a multimodal CT stroke protocol. *AJNR Am J Neuroradiol* 2021;42:1807–14 CrossRef Medline
  28. Georgakis MK, Duering M, Wardlaw JM, et al. WMH and long-term outcomes in ischemic stroke: a systematic review and meta-analysis. *Neurology* 2019;92:e1298–308 CrossRef Medline
  29. Bristow MS, Simon JE, Brown RA, et al. MR perfusion and diffusion in acute ischemic stroke: human gray and white matter have different thresholds for infarction. *J Cereb Blood Flow Metab* 2005;25:1280–87 CrossRef Medline
  30. Schaefer PW, Roccatagliata L, Ledezma C, et al. First-pass quantitative CT perfusion identifies thresholds for salvageable penumbra in acute stroke patients treated with intra-arterial therapy. *AJNR Am J Neuroradiol* 2006;27:20–25 Medline
  31. Eilaghi A, d'Esterre CD, Lee TY, et al. Toward patient-tailored perfusion thresholds for prediction of stroke outcome. *AJNR Am J Neuroradiol* 2014;35:472–77 CrossRef Medline
  32. d'Esterre CD, Boesen ME, Ahn SH, et al. Time-dependent computed tomographic perfusion thresholds for patients with acute ischemic stroke. *Stroke* 2015;46:3390–97 CrossRef Medline
  33. Clèrigues A, Valverde S, Bernal J, et al. Acute ischemic stroke lesion core segmentation in CT perfusion images using fully convolutional neural networks. *Comput Biol Med* 2019;115:103487 CrossRef Medline
  34. Rava RA, Podgorsak AR, Waqas M, et al. Investigation of convolutional neural networks using multiple computed tomography perfusion maps to identify infarct core in acute ischemic stroke patients. *J Med Imaging (Bellingham)* 2021;8:014505 CrossRef Medline
  35. Soltanpour M, Greiner R, Boulanger P, et al. Improvement of automatic ischemic stroke lesion segmentation in CT perfusion maps using a learned deep neural network. *Comput Biol Med* 2021;137:104849 CrossRef Medline
  36. Werdiger F, Parsons MW, Visser M, et al. Machine learning segmentation of core and penumbra from acute stroke CT perfusion data. *Front Neurol* 2023;14:1098562 CrossRef Medline
  37. Shi T, Jiang H, Zheng B. C2MA-Net: cross-modal cross-attention network for acute ischemic stroke lesion segmentation based on CT perfusion scans. *IEEE Trans Biomed Eng* 2022;69:108–18 CrossRef Medline

# CTA Supplemented by CTP Increases Interrater Reliability and Endovascular Treatment Use in Patients with Aneurysmal SAH

Christian Heitkamp, Vincent Geest, Bogdana Tokareva, Laurens Winkelmeier, Tobias D. Faizy, Lukas Meyer, Anna A. Kyselyova, Hanno S. Meyer, Rabea Wentz, Jens Fiehler, Maxim Bester, and Christian Thaler



## ABSTRACT

**BACKGROUND AND PURPOSE:** Cerebral vasospasm is a common complication of aneurysmal SAH and remains a risk factor for delayed cerebral ischemia and poor outcome. The interrater reliability of CTA in combination with CTP has not been sufficiently studied. We aimed to investigate the reliability of CTA alone and in combination with CTP in the detection of cerebral vasospasm and the decision to initiate endovascular treatment.

**MATERIALS AND METHODS:** This is a retrospective single-center study including patients treated for aneurysmal SAH. Inclusion criteria were a baseline CTA and follow-up imaging including CTP due to suspected vasospasm. Three neuroradiologists were asked to grade 15 intracranial arterial segments in 71 cases using a tripartite scale (no, mild <50%, or severe >50% vasospasm). Raters further evaluated whether endovascular treatment should be indicated. The ratings were performed in 2 stages with a minimum interval of 6 weeks. The first rating included only CTA images, whereas the second rating additionally encompassed CTP images. All raters were blinded to any clinical information of the patients.

**RESULTS:** Interrater reliability for per-segment analysis of vessels was highly variable ( $\kappa = 0.16$ – $0.61$ ). We observed a tendency toward higher interrater reliability in proximal vessel segments, except for the ICA. CTP did not improve the reliability for the per-segment analysis. When focusing on senior raters, the addition of CTP images resulted in higher interrater reliability for severe vasospasm ( $\kappa = 0.28$ ; 95% CI, 0.10–0.46 versus  $\kappa = 0.46$ ; 95% CI, 0.26–0.66) and subsequently higher concordance ( $\kappa = 0.23$ ; 95% CI,  $-0.01$ – $0.46$  versus  $\kappa = 0.73$ ; 95% CI, 0.55–0.91) for the decision of whether endovascular treatment was indicated.

**CONCLUSIONS:** CTA alone offers only low interrater reliability in the graduation of cerebral vasospasm. However, using CTA in combination with CTP might help, especially senior neuroradiologists, to increase the interrater reliability to identify severe vasospasm following aneurysmal SAH and to increase the reliability regarding endovascular treatment decisions.

**ABBREVIATIONS:** ACA = anterior cerebral artery; aSAH = aneurysmal SAH; DCI = delayed cerebral ischemia; IQR = interquartile range; TCD = transcranial Doppler sonography

Despite advances in the acute management of aneurysmal SAH (aSAH), cerebral vasospasm is a frequent complication.<sup>1</sup> It remains a risk factor of delayed cerebral ischemia (DCI) and an important predictor of poor outcome.<sup>2</sup> Conservative treatment strategies include induced hypertension, maintaining euvolemia, and oral or intravenously administered calcium

channel blockers to prevent and treat DCI. When conservative treatment strategies fail, the application of an intra-arterial vasodilator or angioplasty of the affected vessel segments has been proposed.<sup>3</sup> DSA is considered the criterion standard to assess cerebral vasospasm.<sup>4</sup> However, DSA is a time-consuming diagnostic technique and can be accompanied by rare-but-severe complications due to its invasive nature.<sup>5</sup> Transcranial Doppler sonography (TCD) is used as a noninvasive screening method to determine patients at risk of cerebral vasospasm. However, this technique is highly operator-dependent, requires a sufficient acoustic window, and has a low sensitivity.<sup>6</sup> Therefore, CTA is widely used to evaluate vessel narrowing in patients after aSAH and to guide further invasive treatment decisions.<sup>3</sup> Unfortunately, it offers only a low sensitivity in detecting cerebral vasospasm, and interrater reliability has been reported to be moderate at best.<sup>7–9</sup> However, the interrater reliability of CTA

Received August 16, 2023; accepted after revision December 2.

From the Departments of Neuroradiology (C.H., V.G., B.T., L.W., T.D.F., L.M., A.A.K., J.F., M.B., C.T.) and Neurosurgery (H.S.M.), University Medical Center Hamburg-Eppendorf, Hamburg, Germany; and Department of Diagnostic and Interventional Radiology (R.W.), Katholisches Marienkrankenhaus, Hamburg, Germany.

M. Bester and C. Thaler contributed equally to this work.

Please address correspondence to Christian Heitkamp, MD, University Medical Center Hamburg-Eppendorf, Martinistrasse 52, 20251 Hamburg, Germany, e-mail: c.heitkamp@uke.de



Indicates article with online supplemental data.

<http://dx.doi.org/10.3174/ajnr.A8110>

in combination with CTP to assess cerebral vasospasm and guide treatment decisions has not been sufficiently studied.<sup>8,10,11</sup>

The aim of this study was to investigate the reliability of CTA alone and in combination with CTP in the detection of cerebral vasospasm and the decision to initiate endovascular treatment. We hypothesized that adding CTP to CTA in the assessment of vasospasm will increase the interrater reliability. In addition, we hypothesized that CTP would be useful in clinical decision-making regarding the need for invasive treatment.

## MATERIALS AND METHODS

### Study Design

This retrospective cohort study was conducted in accordance with the Guidelines for Reporting Reliability and Agreement Studies (GRAAS) (<https://www.equator-network.org/wp-content/uploads/2012/12/GRRAS-checklist-for-reporting-of-studies-of-reliability-and-agreement.pdf>).<sup>12</sup> We conducted a single-center retrospective study at our tertiary stroke center, including all patients treated for aSAH between January 2019 and December 2022. Inclusion criteria for our study were the following: a complete baseline image data set including CTA, suspected vasospasm with follow-up multimodal CT including perfusion imaging, and subsequent DSA with the decision for endovascular treatment.

Imaging data were assessed in 2 stages by 3 neuroradiologists, each with different levels of experience, spanning 3, 9, and 15 years: 1) The first rating contained nonenhanced cranial CT and CTA images at baseline and follow-up imaging. 2) The second rating additionally included CTP images of the same patients. The second rating was performed at least 6 weeks after the first one to minimize recall bias. All raters were blinded to clinical information, the reason for follow-up imaging, and whether all patients received endovascular treatment. The decision to perform endovascular treatment was made by the treating neurointerventionalist. In 8 of 71 cases of vasospasm, the endovascular treatment was performed by raters participating in this study. Clinical data including patient, aneurysm, and treatment characteristics were obtained from medical records. Furthermore, the indication for conducting follow-up CT, along with the time interval between the admission and follow-up CT, was retrieved.

The study was approved by the local ethics committee (Ärztchamber Hamburg, Germany; 2022–300245-WF). All study protocols and procedures were conducted in accordance with the Declaration of Helsinki. Patient consent was not needed due to the retrospective nature of the study.

### Diagnostic Protocol for the Detection of Vasospasm

Daily clinical and TCD assessments were conducted to detect neurologic deterioration or sonographic signs of vasospasm. TCD was performed by trained physicians or technicians, who measured the mean velocity in both the MCA and anterior cerebral artery (ACA) whenever possible. Following the Association of the Scientific Medical Societies in Germany (AWMF; <https://www.ncbi.nlm.nih.gov/pmc/articles/PMC4106509/>) guidelines,<sup>13</sup> the TCD measurements were recorded as the mean velocity (cubic centimeters). Elevated TCD measurements in the MCA were identified by a mean velocity exceeding 140 cm/s or doubling within a 24-hour period. If patients experienced a new

neurologic deficit, deterioration in consciousness, or elevated TCD measurements, multimodal imaging including CTA and CTP was performed. Also refer to the Online Supplemental Data illustrating our local protocol of a diagnostic algorithm for the detection of cerebral vasospasm after aSAH.

### Imaging and Ratings: Classification and Categories

All CT scans were performed on a 256 dual-section scanner (Somatom Definition Flash; Siemens). Details on image acquisition can be found in the Online Supplemental Data. One data set per patient included axial nonenhanced cranial CT images, thin-section axial CTA, and axial, coronal, and sagittal MIP images. In addition, each CTP data set for the second rating contained whole-brain coverage of the perfusion CBF, CBV, MTT, and time-to-maximum. CTP images were automatically processed using syngo.via (Version VB30A\_HF91; Siemens). The imaging data and corresponding DICOM source information were fully anonymized before being provided to the raters in digital format. The raters performed the evaluations using a commercially available DICOM viewer (Horos; Version 3.3.6; Horosproject). According to a previous study,<sup>14</sup> raters were asked to grade vasospasms by visual judgment using a tripartite scale for each vessel separately. The scale included no vasospasm, mild vasospasm <50% narrowing, and severe vasospasm >50% narrowing. The admission CTA was used as a reference when evaluating vasospasm on follow-up CTA.<sup>7,11,15</sup> Arterial segments were predefined as follows: supraclinoid ICA; M1 and M2 segments of the MCA; A1 and A2 segments of the ACA; P1 and P2 segments of the posterior cerebral artery, as well as the basilar artery. Finally, readers were requested to determine whether endovascular treatment was recommended for the patients. Within the framework of the second rating, raters were additionally asked whether perfusion deficits were present.

### Statistical Analysis

Descriptive statistics were performed to display clinical information, including patient, aneurysm, and treatment characteristics as well as the reason for follow-up CT being performed. The normality of data distribution was assessed using Shapiro-Wilk tests. Continuous variables are presented as mean (SD) for normally distributed variables and medians with interquartile ranges (IQR) for non-normally distributed variables. Categorical variables are described as counts and percentages. According to a previous study,<sup>16</sup> a per-patient assessment with dichotomization between no vasospasm and severe vasospasm was calculated if the rater estimated narrowing to be severe for at least 1 of the ICA, M1, M2, A1, A2, P1, P2, or basilar segments. Interrater agreement for dichotomized variables was assessed using the Fleiss  $\kappa$  for all 3 raters and the Cohen  $\kappa$  for the 2 senior raters (M.B. and C.T.) using 95% bias-corrected confidence intervals obtained with 1000 bootstrap resampling. The interrater agreement of each vessel's vasospasm rating was calculated using the Krippendorff  $\alpha$ . Intrarater agreement was assessed using the Cohen  $\kappa$  for dichotomized variables and the Krippendorff  $\alpha$  for the per-segment analysis of each vessel.

An illustration depicting the various statistical tests is included in the Online Supplemental Data. The level of agreement was



**Table 1: Patient baseline, procedural, and outcome characteristics**

Patient Characteristics (n = 46)	
Age (mean)	56.6 (SD, 12.6)
Female sex (No.) (%)	33 (71.7)
Hunt and Hess (median) (IQR)	3 (2–4)
Modified Fisher scale (median) (IQR)	4 (3–4)
Intracerebral hemorrhage (No.) (%)	23 (50.0)
Hypertension (No.) (%)	29 (63.0)
Smoker (No.) (%)	17 (37.0)
Aneurysm characteristics	
Ruptured aneurysm location	
ICA (No.) (%)	16 (34.8)
MCA (No.) (%)	5 (10.9)
ACA (No.) (%)	17 (37.0)
Posterior circulation (No.) (%)	8 (17.4)
Aneurysm size (median) (IQR) (mm)	6.5 (5–8.25)
Patients with multiple aneurysms (No.) (%)	3 (6.5)
Treatment characteristics	
Clip (No.) (%)	8 (17.4)
Endovascular treatment (No.) (%)	38 (82.6)
EVD placement (No.) (%)	36 (78.3)
Patients with 2 instances of vasospasm (No.) (%)	25 (54.3)

**Note:**—EVD indicates external ventricular drain.

**Table 2: Reasons to perform follow-up CT examination (n = 71)**

Reasons	
Only neurologic deterioration (eg, reduced level of consciousness or new focal deficit) (No.) (%)	30/71 (42.3)
Only elevated TCD profiles (No.) (%)	17/71 (23.9)
Neurologic deterioration and elevated TCD profiles (No.) (%)	19/71 (26.8)
Decreased P <sub>bt</sub> O <sub>2</sub> (No.) (%)	1/71 (1.4)
Screening CT (comatose patients without TCD acoustic window) (No.) (%)	4/71 (5.6)

**Note:**—P<sub>bt</sub>O<sub>2</sub> indicates partial pressure of brain tissue oxygen.

**Table 3: Interrater reliability and agreement for the graduation of vasospasm on CT<sup>a</sup>**

	First Rating (CTA)		Second Rating (CTA + CTP)	
	Agreement (%)	Interrater Reliability κ (95% CI)	Agreement (%)	Interrater Reliability κ (95% CI)
Supraclinoid ICA				
Right (n = 68)	87	0.31 (0.12–0.51)	86	0.13 (–0.03–0.28)
Left (n = 70)	89	0.27 (0.07–0.48)	91	0.30 (0.05–0.56)
MCA, M1				
Right (n = 68)	87	0.58 (0.46–0.69)	82	0.43 (0.27–0.60)
Left (n = 67)	87	0.55 (0.39–0.70)	86	0.50 (0.34–0.67)
MCA, M2				
Right (n = 71)	83	0.38 (0.22–0.53)	80	0.25 (0.05–0.45)
Left (n = 71)	82	0.16 (–0.01–0.32)	86	0.32 (0.15–0.49)
ACA, A1				
Right (n = 68)	83	0.50 (0.36–0.64)	75	0.36 (0.20–0.53)
Left (n = 67)	85	0.61 (0.48–0.74)	76	0.36 (0.18–0.55)
ACA, A2				
Right (n = 70)	77	0.37 (0.20–0.53)	70	0.20 (0.06–0.35)
Left (n = 70)	78	0.40 (0.24–0.55)	66	0.12 (–0.03–0.26)
Basilar (n = 70)	93	0.37 (0.19–0.55)	91	0.28 (0.09–0.47)
PCA, P1				
Right (n = 70)	89	0.53 (0.37–0.68)	85	0.13 (–0.02–0.28)
Left (n = 70)	87	0.44 (0.29–0.60)	86	0.18 (0.00–0.35)
PCA, P2				
Right (n = 71)	89	0.36 (0.17–0.55)	89	0.15 (0.05–0.25)
Left (n = 71)	89	0.43 (0.20–0.65)	91	0.21 (0.08–0.34)

**Note:**—PCA indicates posterior cerebral artery.

<sup>a</sup>Vasospasm was graded using a tripartite scale for each vessel separately. The scale included no vasospasm, mild vasospasm <50%, and severe vasospasm >50%. Interrater reliability was calculated using the Krippendorff  $\alpha$ .

interpreted according to Landis and Koch<sup>17</sup> (slight agreement, 0–0.2; fair agreement, 0.21–0.4; moderate agreement, 0.41–0.6; substantial agreement, 0.61–0.8; and almost perfect agreement 0.81–1.0). Significant differences between point estimates or between  $k$  values were considered to exist when 95% confidence intervals did not overlap. The data analysis was conducted using Stata 18.0 (Stata/MP 18.0; StataCorp).

### Data Availability

Data supporting the findings of this study are available from the corresponding author on reasonable request.

### RESULTS

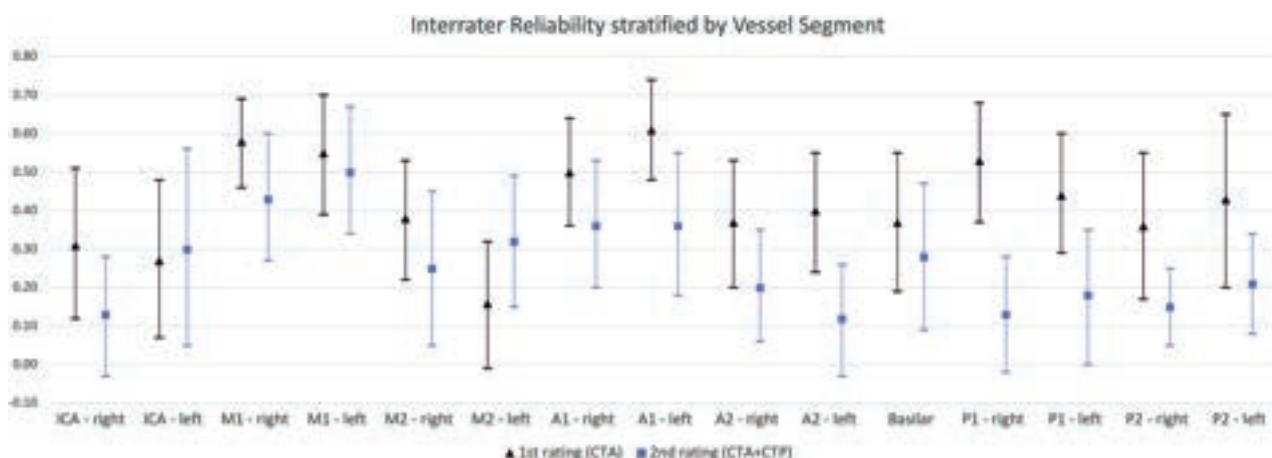
A total of 206 patients were treated for aSAH during our inclusion period. Of those, 47 patients met the inclusion criteria. One patient was excluded from final analysis due to severe imaging artifacts caused by coiling. The final analysis incorporated imaging data from 46 patients, comprising 25 patients who underwent CT imaging more than once. Therefore, a total of 71 CT examinations was assessed. Among the 25 patients who underwent 2 CT examinations, the median time between the first and second CT

was 49 hours (IQR, 26–99 hours). The mean age was 56.6 (SD, 12.6) years, and 71.7% of patients were female. The median Hunt and Hess score was 3 (IQR, 2–4), and the median modified Fisher scale score was 4 (IQR, 3–4). Aneurysms were most frequently located at the ACA (37.0%) and ICA (34.8%). Most aneurysms were treated endovascularly, accounting for 82.6% of all cases. For further information regarding patient, aneurysm, and treatment characteristics refer to Table 1.

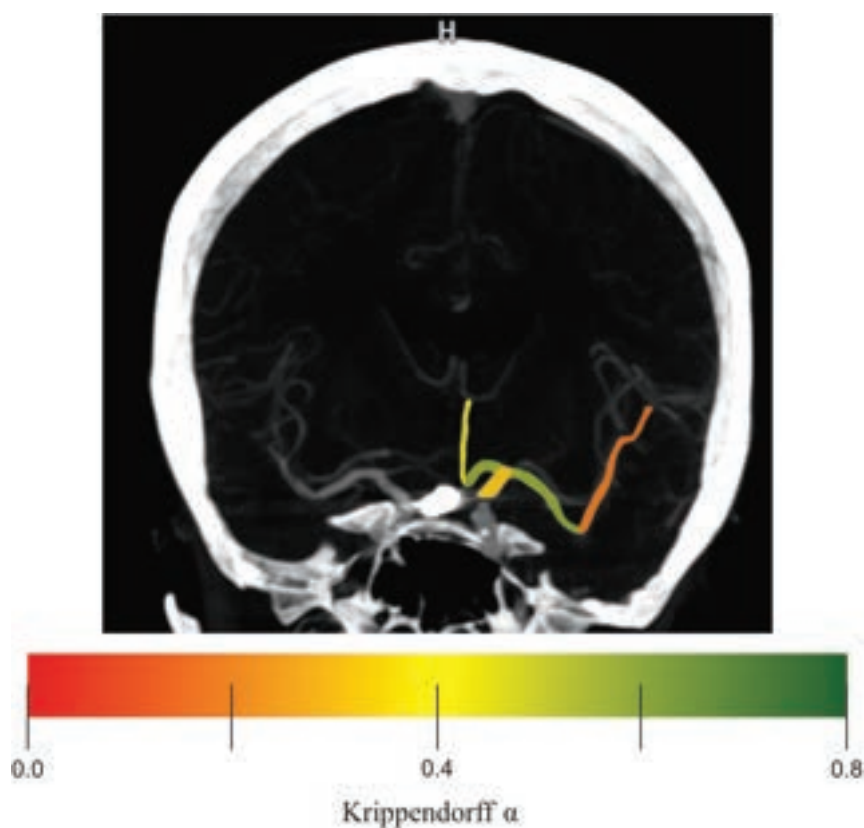
Reasons for suspected vasospasm and subsequent follow-up imaging are shown in Table 2. The median time from ictus to follow-up imaging was 9 days (IQR, 6–11.5 days). The most frequent indication for follow-up imaging was a neurologic deterioration (eg, reduced level of consciousness or a new focal deficit) in 42.3% of all cases. Solely elevated TCD profiles accounted for 23.9%, and neurologic deterioration together with elevated TCD profiles accounted for 26.8% of reasons to perform follow-up CT. Further reasons were screening for vasospasm in comatose patients without a TCD acoustic window (5.7%) and decreased partial pressure of brain tissue oxygen (1.4%). In 22 cases, patients were intubated while receiving follow-up imaging.

Table 3 and Figure 1 provide the distribution of interrater reliability stratified by each vessel segment. The





**FIG 1.** The interrater reliability of first and second ratings (Krippendorff  $\alpha$ ) is stratified by vessel segments. Vasospasm was graded on CTA using a tripartite scale for each vessel separately. The scale included no vasospasm, mild vasospasm  $<50\%$ , and severe vasospasm  $>50\%$ . Krippendorff  $\alpha$  values are displayed by black triangles and blue squares for the first and second ratings, respectively. The black and blue lines indicate the 95% CIs.



**FIG 2.** Illustrative case of a patient without left-hemispheric vasospasm on follow-up imaging. The ICA, A1, and A2 segments of the ACA as well as the M1 and M2 segments of the MCA are highlighted in color. The color graduation indicates the interrater reliability (Krippendorff  $\alpha$ ) for the first rating. The graduation ranges from slight ( $\alpha = .0$ ) to substantial ( $\alpha = .8$ ) agreement. Note that proximal segments accounted for higher interrater reliability except for the ICA.

left A1 segment accounted for the highest interrater reliability with substantial agreement ( $\kappa = 0.61$ ; 95% CI, 0.48–0.74). In general, we observed a tendency toward higher interrater reliability in proximal vessel segments (M1, A1, P1), except for the ICA (Figs 1 and 2). The addition of perfusion maps in the second assessment did

not substantially improve interrater reliability for the individual vessels (Fig 1). In a subsequent analysis, we investigated the interrater reliability for the detection of severe vasospasm in any arterial segment. Interrater reliability was fair for the first ( $\kappa = 0.27$ ; 95% CI, 0.11–0.42) and second ( $\kappa = 0.31$ ; 95% CI, 0.15–0.46) ratings of all raters. Most interesting, there was an increase from fair agreement in the first rating ( $\kappa = 0.28$ ; 95% CI, 0.10–0.46) to moderate agreement in the second rating ( $\kappa = 0.46$ ; 95% CI, 0.26–0.66) when focusing on senior raters. In addition, the restriction to proximal vessels (ICA, A1, M1, P1) further increased point estimates of the interrater reliability of the senior raters from  $\kappa = 0.51$  (95% CI, 0.31–0.72) to  $\kappa = 0.59$  (95% CI, 0.38–0.79) during the 2 assessments.

Regarding the decision about whether endovascular treatment was indicated, the interrater reliability based on CTA alone was fair for all raters ( $\kappa = 0.23$ ; 95% CI, 0.06–0.39) and reached moderate agreement ( $\kappa = 0.47$ ; 95% CI, 0.30–0.64) when adding CTP images for the second assessment. If we took only senior raters into account, interrater reliability increased from fair ( $\kappa = 0.23$ ; 95% CI,  $-0.01$ –0.46) to substantial

( $\kappa = 0.73$ ; 95% CI, 0.55–0.91) across the course of the 2 ratings. Refer to Table 4 for further statistics regarding diagnosis and treatment decisions of vasospasm on CT.

Regarding intrarater agreement, we observed a broad spectrum of agreement among the raters, ranging from slight to

**Table 4: Interrater reliability and agreement regarding graduation and treatment decisions of vasospasm on CT**

	Interrater Reliability and Agreement <sup>a</sup>			
	All Raters (n = 3)		Senior (n = 2)	
	Agreement (%)	Interrater Reliability $\kappa$ (95% CI)	Agreement (%)	Interrater Reliability $\kappa$ (95% CI)
First rating (CTA)				
Detection of severe vasospasm in any arterial segment (>50% narrowing)	63	0.27 (0.11–0.42)	61	0.28 (0.10–0.46)
Endovascular treatment?	62	0.23 (0.06–0.39)	61	0.23 (–0.01–0.46)
Second rating (CTA + CTP)				
Detection of severe vasospasm in any arterial segment (>50% narrowing)	65	0.31 (0.15–0.46)	73	0.46 (0.26–0.66)
Endovascular treatment?	75	0.47 (0.30–0.64)	89	0.73 (0.55–0.91)
Perfusion deficit?	92	0.77 (0.63–0.91)	93	0.82 (0.66–0.97)

<sup>a</sup> Interrater reliability was calculated using the Fleiss  $\kappa$  for all raters and Cohen  $\kappa$  for senior raters.

substantial when focusing on the per-segment analysis of each vessel (Online Supplemental Data) separately. Fair intrarater agreement was observed for all 3 raters (rater 1:  $\kappa$  = 0.22; 95% CI, –0.02–0.47; rater 2:  $\kappa$  = 0.28; 95% CI, 0.06–0.51; rater 3:  $\kappa$  = 0.34; 95% CI, 0.17–0.52) concerning the question of whether to perform endovascular treatment (Online Supplemental Data).

## DISCUSSION

In this single-center retrospective study, we investigated the interrater reliability of CTA alone and in combination with CTP for the detection of cerebral vasospasm after aSAH. Our second objective was to determine the interrater reliability regarding the CT-based decision about whether endovascular treatment was indicated. We observed that the interrater reliability of vasospasm on a vessel segment level was overall very low and highly variable. Higher interrater reliability was observed for proximal vessel segments except for the ICA. CTP did not improve the interrater reliability for the per-segment analysis. However, when focusing on senior neuroradiologists, we found that the addition of CTP images resulted in higher interrater reliability for severe vasospasm and subsequently higher concordance for the decision of whether endovascular treatment was indicated.

To date, most studies focused on the diagnostic accuracy of CTA compared with DSA for the detection of vasospasm.<sup>8,10,15,18</sup> In previous studies, interrater reliability for detecting cerebral vasospasm on CTA alone ranged from moderate to substantial, challenging its sufficiency in diagnosing vasospasm and guiding further treatment decisions.<sup>7,15,18</sup> We also observed low interrater reliability with CTA alone in our study, even when dichotomized for any severe vasospasm. One reason for the low or at least varying interrater agreements might be that there is no consensus on a definition of critical vessel narrowing or a reference standard for evaluating vasospasm, such as whether to use the baseline examination or the contralateral hemisphere as a comparison. For example, Letourneau-Guillon et al<sup>7</sup> found 8 different classification systems with various cutoffs for the evaluation of vasospasm on CTA. Furthermore, the reduction of vessel diameters can be subtle, making it even more challenging when using grading systems with multiple increments. Especially in smaller vessels such as the M2 or A2 segments or even more distal, visual grading becomes more difficult. This issue might explain our observation of higher interrater reliability in proximal vessel segments, except

for the ICA, which is consistent with findings in previous studies.<sup>7,18</sup> Due to the relatively short and tortuous course of the supraclinoid ICA, raters may encounter challenges in establishing a detailed graduation of vasospasm in this vessel. Proximal vessels such as the M1 or the A1 segment typically have a larger diameter and a more extended horizontal course in comparison with their distal counterparts. As a result, it is assumed that changes in these proximal vessel calibers are easier to detect, particularly when contrasted with the inherently narrower calibers observed in distal segments. Therefore, focusing on proximal vessels may be more reliable for clinicians when evaluating vasospasm, but it also highlights the problem of accurately and reliably detecting relevant vasospasm in distal cerebral arteries.

It is not clear which cutoff value of vessel stenosis is most predictive of cerebral ischemia and would necessitate an adjustment of the treatment strategy.<sup>19,20</sup> Thus, we also provided our observers with CTP images because these might indicate hemodynamically relevant vasospasm.<sup>21</sup> We observed substantial agreement for all raters and almost perfect agreement for senior raters in the assessment of perfusion deficits. In contrast to CTA alone, perfusion imaging additionally yields insights into microvascular vasospasm, which may not necessarily affect large- or medium-sized vessels.<sup>22</sup> It has been shown that CTP improves the detection of distal medium- and small-vessel occlusions in patients with embolic stroke,<sup>23</sup> leading to the assumption that it can also enhance the detection of cerebral vasospasm. However, perfusion deficits due to vasospasm are certainly not confined to 1 vascular territory but can be diffuse or only affect the watershed areas between 2 vascular territories.<sup>24</sup> This feature may be an explanation for the relatively low interrater reliability for the per-segment analysis despite additional CTP imaging data, because it can be challenging to assign the perfusion deficit to a distinct vessel segment.

We observed that CTP images increased point estimates regarding the detection of severe vasospasm and, clinically more important, the decision about whether endovascular treatment was indicated. This finding was particularly evident among experienced raters. In previous studies, CTA in combination with CTP has shown high diagnostic accuracy for vasospasm diagnosis, and perfusion deficits have been associated with DCI.<sup>10,25</sup> So far, the role of perfusion imaging to guide treatment decisions in cerebral vasospasm and its benefit as a screening technique on clinical outcome remain unanswered. Perfusion imaging provides

additional information about the blood supply at the tissue level and indicates possible tissue at risk. This information may help observers determine which of the caliber irregularities may be functionally relevant and therefore provides additional information to justify endovascular treatment options, such as intra-arterial administration of spasmolytic drugs or percutaneous transluminal angioplasty. Of note, it must be considered that CTP entails a substantially higher radiation exposure, especially in the case of multiple examinations.

The raters were not given any clinical information such as the presence of new focal neurologic symptoms or TCD elevations. However, information about the patient's clinical status or neurologic deterioration is essential when assessing the risk of focal brain damage in patients with suspected vasospasm and guiding further treatment decisions. The decision to pursue endovascular treatment should be driven by a combination of the patient's clinical and neurologic status as well as imaging findings including DSA.<sup>3</sup> However, patients after aSAH are often sedated or comatose and cannot be evaluated clinically. In this patient cohort, the degree of vasospasm on multimodal CT imaging plays a crucial role in clinical decision-making. Although our study shows that CT screening alone for vasospasm should be used with caution, because interrater reliability for individual vessel segments is low, it may be helpful to focus on proximal vessels and to use perfusion imaging to identify hemodynamically relevant perfusion deficits.

### Limitations

This study has some limitations. Patients were chosen on the basis of the completeness of imaging modalities, possibly introducing selection bias. Furthermore, the generalizability of our findings may be limited because for 25 patients, 2 data sets were included because these patients presented more than once with suspected vasospasm. In addition, our cohort of raters is all from the same institution, and we included only 1 junior rater, restricting the results concerning physicians with limited work experience. In 8 of 71 cases, the endovascular treatment was performed by raters participating in this study. Despite the anonymization of all cases, the raters could have recognized these cases, potentially introducing bias. The heterogeneity of the study cohort was reduced by including only patients who had undergone endovascular treatment, resulting in a scarcity of patients with mild vasospasm. Because the experimental setup of our study differs from the real-life assessment of patients, we can only speculate that responders devoted the necessary time and attention to respond as they would have when evaluating actual patients. Some patients who underwent CT examination were under general anesthesia. Because anesthetic drugs can impact cerebral hemodynamics, their use potentially confounds the interpretability of CTP. Of note, this study focused on the interrater reliability of CTA and CTP in diagnosing vasospasm and the resulting treatment decision. It was not the purpose of this study to investigate the diagnostic accuracy of these 2 modalities, which has been demonstrated previously.<sup>8,10,27</sup> Therefore, we did not compare the CTA and CTP ratings with the DSA.

### CONCLUSIONS

The grading of vasospasm on a per-segment analysis using CTA alone offers only low interrater reliability and is not a sufficient

criterion to guide treatment decisions regarding endovascular therapy. However, perfusion imaging might help experienced neuroradiologists visualize perfusion deficits of presumed vasospastic origin and might improve interrater reliability regarding endovascular treatment decisions.

**Disclosure forms** provided by the authors are available with the full text and PDF of this article at [www.ajnr.org](http://www.ajnr.org).

### REFERENCES

1. Donaldson L, Edington A, Vlok R, et al. **The incidence of cerebral arterial vasospasm following aneurysmal subarachnoid haemorrhage: a systematic review and meta-analysis.** *Neuroradiology* 2022;64:2381–89 CrossRef Medline
2. Harrod CG, Bendok BR, Batjer HH. **Prediction of cerebral vasospasm in patients presenting with aneurysmal subarachnoid hemorrhage: a review.** *Neurosurgery* 2005;56:633 CrossRef Medline
3. Hoh BL, Ko NU, Amin-Hanjani S, et al. **2023 Guideline for the Management of Patients with Aneurysmal Subarachnoid Hemorrhage: a guideline from the American Heart Association/American Stroke Association.** *Stroke* 2023;54:e314–70 CrossRef Medline
4. Francoeur CL, Mayer SA. **Management of delayed cerebral ischemia after subarachnoid hemorrhage.** *Crit Care* 2016;20:277 CrossRef Medline
5. Adami D, Berkefeld J, Platz J, et al. **Complication rate of intraarterial treatment of severe cerebral vasospasm after subarachnoid hemorrhage with nimodipine and percutaneous transluminal balloon angioplasty: worth the risk?** *J Neuroradiol* 2019;46:15–24 CrossRef Medline
6. Gahn G, Gerber J, Hallmeyer S, et al. **Noninvasive assessment of the circle of Willis in cerebral ischemia: the potential of CT angiography and contrast-enhanced transcranial color-coded duplex sonography.** *Cerebrovasc Dis* 1999;9:290–94 CrossRef Medline
7. Letourneau-Guillon L, Farzin B, Darsaut TE, et al. **Reliability of CT angiography in cerebral vasospasm: a systematic review of the literature and an inter- and intraobserver study.** *AJNR Am J Neuroradiol* 2020;41:612–18 CrossRef Medline
8. Allen JW, Praater A, Kallas O, et al. **Diagnostic performance of computed tomography angiography and computed tomography perfusion tissue time-to-maximum in vasospasm following aneurysmal subarachnoid hemorrhage.** *J Am Heart Assoc* 2022;11:e023828 CrossRef Medline
9. Darsaut TE, Keough MB, Chan AM, et al. **Transcranial Doppler velocities and angiographic vasospasm after SAH: a diagnostic accuracy study.** *AJNR Am J Neuroradiol* 2022;43:80–86 CrossRef Medline
10. Greenberg ED, Gold R, Reichman M, et al. **Diagnostic accuracy of CT angiography and CT perfusion for cerebral vasospasm: a meta-analysis.** *AJNR Am J Neuroradiol* 2010;31:1853–60 CrossRef Medline
11. Binaghi S, Colleoni P, Maeder P, et al. **CT angiography and perfusion CT in cerebral vasospasm after subarachnoid hemorrhage.** *AJNR Am J Neuroradiol* 2007;28:750–58 Medline
12. Kottner J, Audigé L, Brorson S, et al. **Guidelines for Reporting Reliability and Agreement Studies (GRRAS) were proposed.** *J Clin Epidemiol* 2011;64:96–106 CrossRef Medline
13. Rabinstein AA, Lanzino G, Wijedicks EF. **Multidisciplinary management and emerging therapeutic strategies in aneurysmal subarachnoid haemorrhage.** *Lancet Neurol* 2010;9:504–19 CrossRef Medline
14. Wintermark M, Ko NU, Smith WE, et al. **Vasospasm after subarachnoid hemorrhage: utility of perfusion CT and CT angiography on diagnosis and management.** *AJNR Am J Neuroradiol* 2006;27:26–34 Medline
15. Shankar JJS, Tan IY, Krings T, et al. **CT angiography for evaluation of cerebral vasospasm following acute subarachnoid haemorrhage.** *Neuroradiology* 2012;54:197–203 CrossRef Medline
16. Darsaut TE, Derksen C, Farzin B, et al. **Reliability of the diagnosis of cerebral vasospasm using catheter cerebral angiography: a**

- systematic review and inter- and intraobserver study. *AJNR Am J Neuroradiol* 2021;42:501–07 CrossRef Medline
17. Landis JR, Koch GG. **The measurement of observer agreement for categorical data.** *Biometrics* 1977;33:159–74 Medline
  18. Chaudhary SR, Ko N, Dillon WP, et al. **Prospective evaluation of multidetector-row CT angiography for the diagnosis of vasospasm following subarachnoid hemorrhage: a comparison with digital subtraction angiography.** *Cerebrovasc Dis* 2008;25:144–50 CrossRef Medline
  19. Budohoski KP, Czosnyka M, Kirkpatrick PJ, et al. **Clinical relevance of cerebral autoregulation following subarachnoid haemorrhage.** *Nat Rev Neurol* 2013;9:152–63 CrossRef Medline
  20. Ohkuma H, Manabe H, Tanaka M, et al. **Impact of cerebral microcirculatory changes on cerebral blood flow during cerebral vasospasm after aneurysmal subarachnoid hemorrhage.** *Stroke* 2000;31:1621–27 CrossRef Medline
  21. Starnoni D, Maduri R, Hajdu SD, et al. **Early perfusion computed tomography scan for prediction of vasospasm and delayed cerebral ischemia after aneurysmal subarachnoid hemorrhage.** *World Neurosurg* 2019;130:e743–52 CrossRef Medline
  22. Greenberg ED, Gobin YP, Riina H, et al. **Role of CT perfusion imaging in the diagnosis and treatment of vasospasm.** *Imaging Med* 2011;3:287–97 CrossRef Medline
  23. Amukotuwa SA, Wu A, Zhou K, et al. **Time-to-maximum of the tissue residue function improves diagnostic performance for detecting distal vessel occlusions on CT angiography.** *AJNR Am J Neuroradiol* 2021;42:65–72 CrossRef Medline
  24. Wazni W, Farooq S, Cox JA, et al. **Use of arterial spin-labeling in patients with aneurysmal sub-arachnoid hemorrhage.** *J Vasc Interv Neurol* 2019;10:10–14 Medline
  25. Cremers CH, Dankbaar JW, Vergouwen MI, et al. **Different CT perfusion algorithms in the detection of delayed cerebral ischemia after aneurysmal subarachnoid hemorrhage.** *Neuroradiology* 2015;57:469–74 CrossRef Medline
  26. Döring K, Mielke D, Moerer O, et al. **Radiation exposure in the acute phase after aneurysmal subarachnoid hemorrhage in the era of CT perfusion.** *Clin Neuroradiol* 2022;32:123–32 CrossRef Medline
  27. Wintermark M, Dillon WP, Smith WS, et al. **Visual grading system for vasospasm based on perfusion CT imaging: comparisons with conventional angiography and quantitative perfusion CT.** *Cerebrovasc Dis* 2008;26:163–70 CrossRef Medline

# Prevalence of “Ghost Infarct Core” after Endovascular Thrombectomy

Johanna M. Ospel, Nathaniel Rex, Leon Rinkel, Nima Kashani, Brian Buck, Jeremy Rempel, Demetrios Sahlas, Michael E. Kelly, Ron Budzik, Michael Tymianski, Michael D. Hill, and Mayank Goyal,  
On behalf of the ESCAPE-NA1 Investigators



## ABSTRACT

**BACKGROUND AND PURPOSE:** Baseline CTP sometimes overestimates the size of the infarct core (“ghost core” phenomenon). We investigated how often CTP overestimates infarct core compared with 24-hour imaging, and aimed to characterize the patient subgroup in whom a ghost core is most likely to occur.

**MATERIALS AND METHODS:** Data are from the randomized controlled ESCAPE-NA1 trial, in which patients with acute ischemic stroke undergoing endovascular treatment were randomized to intravenous tenecteplase or placebo. Patients with available baseline CTP and 24-hour follow-up imaging were included in the analysis. Ghost infarct core was defined as CTP core volume minus 24-hour infarct volume > 10 mL. Clinical characteristics of patients with versus without ghost core were compared. Associations of ghost core and clinical characteristics were assessed by using multivariable logistic regression.

**RESULTS:** A total of 421 of 1105 patients (38.1%) were included in the analysis. Forty-seven (11.2%) had a ghost core > 10 mL, with a median ghost infarct volume of 13.4 mL (interquartile range 7.6–26.8). Young patient age, complete recanalization, short last known well to CT times, and possibly male sex were associated with ghost infarct core.

**CONCLUSIONS:** CTP ghost core occurred in ~1 of 10 patients, indicating that CTP frequently overestimates the infarct core size at baseline, particularly in young patients with complete recanalization and short ischemia duration.

**ABBREVIATIONS:** AIS = acute ischemic stroke; eTICI = expanded TICI; EVT = endovascular treatment; LVO = large vessel occlusion; rCBF = relative CBF

Endovascular treatment (EVT), the current standard of care for acute ischemic stroke (AIS) due to large vessel occlusion (LVO), improves clinical outcomes through reperfusion of ischemic tissue, which stops the progression from ischemia to infarction.<sup>1–5</sup> Based on our current understanding, if the entire ischemic area is irreversibly damaged (ie, there is only infarct “core,” with no penumbra left), EVT is likely to be futile.

Received April 10, 2023; accepted after revision December 1.

From the Departments of Diagnostic Imaging (J.M.O., M.D.H., M.G.) and Clinical Neurosciences (J.M.O., N.R., L.R., M.D.H., M.G.), University of Calgary, Calgary, Alberta, Canada; Department of Diagnostic Imaging (N.R.), Brown University, Providence, Rhode Island; Department of Neurology (L.R.), Amsterdam University Medical Center, Amsterdam, the Netherlands; Department of Neurosurgery (N.K., M.E.K.), University of Saskatchewan, Saskatoon, Saskatchewan, Canada; University of Alberta Hospital (B.B., J.R.), Edmonton, Alberta, Canada; McMaster University (D.S.), Hamilton, Ontario, Canada; Ohio Health (R.B.), Riverside Methodist Hospital, Columbus, Ohio; and NoNO Inc. (M.T.), Toronto, Ontario, Canada.

The ESCAPE-NA1 trial was supported by the Canadian Institutes of Health Research (Grant NCT02930018) and NoNO Inc.

Please address correspondence to Mayank Goyal, MD, PhD, Departments of Radiology and Clinical Neurosciences, University of Calgary, 2500 University Dr NW, Calgary, AB T2N 1N4, Canada; e-mail: mgoyal@ucalgary.ca; @johanna\_ospel; @mayank\_G0; @DCNSNeuro



Indicates article with online supplemental data.

<http://dx.doi.org/10.3174/ajnr.A8113>

Different imaging modalities allow us to estimate the size of the ischemic core; perhaps the most widely used is CTP.<sup>4,6</sup> In CTP, the brain is repeatedly imaged (over 45–90 seconds) after intravenous injection of a bolus of iodinated contrast. These repeated measurements are then used to derive time to maximum, relative CBF (rCBF), and CBV maps. The most commonly used threshold to identify infarct “core” is rCBF < 30%.<sup>3,4,7</sup> Thresholded CTP maps sometimes overestimate the size of the infarct core: a phenomenon that is colloquially known as “ghost core,” occurring in 16%–38% of patients.<sup>8,9</sup> This overestimation of initial infarct size on CTP can cause several problems, including inaccurate outcome prognostication and erroneous treatment decisions.<sup>9</sup> Therefore, it is of interest to quantify the prevalence of the ghost core phenomenon.

In this post hoc analysis of the randomized controlled ESCAPE-NA1 trial, we therefore assessed the prevalence of the ghost core phenomenon and assessed its associations with patient characteristics and clinical outcomes.

## MATERIALS AND METHODS

### Study Sample

This study is a post hoc analysis of the Safety and Efficacy of Tenecteplase in Subjects Undergoing Endovascular Thrombectomy



for Stroke, or ESCAPE-NA1, trial (clinicaltrials.gov: NCT02930018), a double-blind, multicenter randomized controlled trial that evaluated the efficacy of nerinetide in patients with AIS who underwent EVT.<sup>10</sup> Patients were randomly allocated to either receive intravenous nerinetide versus placebo in addition to best medical management. Inclusion criteria were as follows: presence of a LVO, moderate to good collateral circulation, an ASPECTS of 5 or greater, age of at least 18 years, NIHSS of  $>5$ , functional independence before the stroke (Barthel index  $>90$ ), and time since last known well  $<12$  hours. The study was approved by the ethics committee of the University of Calgary and at each participating site. Informed consent was obtained from participants, legally authorized representatives, or via 2-physician consent, depending on national laws and regulations.

### Imaging Acquisition

The ESCAPE-NA1 protocol mandated at minimum a noncontrast head CT and a multiphase CT angiography at baseline and either NCCT or diffusion-weighted MR imaging at 24 hours. Perfusion imaging was performed when part of clinical routine at each respective site, but not mandated by the trial, and therefore only available in a subset of patients. We only included patients with available CT perfusion imaging in the analysis. Perfusion source images, when available, were processed by using RAPID perfusion software version 5.2.2 (iSchemaView) to generate standard rCBF  $<30\%$  volumes.

### Imaging Analysis

All imaging was assessed by a central imaging core lab that was blinded to treatment allocation and clinical outcomes (Online Supplemental Data). Disagreement between 2 readers was solved by a senior neuroradiologist (M.G.; 24 years of experience). Core lab members were blinded to clinical outcomes. During baseline imaging assessment, core lab members were also blinded to 24-hour follow-up imaging. Time intervals between baseline and follow-up imaging readout sessions were  $\geq 4$  weeks.

**Noncontrast CT and CT Angiography.** ASPECTS score was assessed on baseline NCCT. Occlusion location on multiphase CT angiography was reported as either terminal internal carotid artery or M1 segment of the MCA.

**CT Perfusion.** All output DICOMs were converted to NIfTI by using dcm2niix (<http://www.github.com/rordenlab/dcm2niix>), and then underwent automated segmentation by using color-based thresholding in Python version 3.10 (<http://www.python.org>). Segmentation volumes for each threshold were extracted by using 3DSlicer version 5.0.2 (<http://www.slicer.org>). Key Python functions necessary for reproduction of feature extraction and processing are detailed on Github ([https://github.com/naterex23/RAPID\\_Perfusion\\_Processing](https://github.com/naterex23/RAPID_Perfusion_Processing)).

**Angiography.** Expanded TICI score (eTICI) was assessed on the final intracranial DSA run. Successful reperfusion was defined as eTICI 2b–3 (ie,  $>50\%$  reperfusion of the target territory) and near-complete reperfusion as eTICI 2c–3 (ie,  $>90\%$  reperfusion of the target territory).

**24-Hour Imaging.** Final infarct volumes were manually segmented for all patients with follow-up imaging (either NCCT or diffusion-weighted MR imaging) through manual planimetric measurements on axial NCCT or diffusion-weighted MRI follow-up imaging by using the open source software ITK snap (<http://www.itksnap.org>).

### Outcomes of Interest

The primary outcome of this study was CTP ghost core. Because small ghost core volumes could be artificial related to CTP postprocessing or variability in manual infarct segmentations, we opted to define ghost core as ghost core volume  $>10$  mL, that is, final infarct volume at 24 hour – rCBF  $<30\%$  volume at baseline  $< -10$  mL (motivated by a previous publication by Boned et al).<sup>8</sup>

In a secondary analysis, we further assessed the association of ghost core with clinical outcomes, as measured by the mRS at 90 days, which was assessed by blinded assessors who were unaware of the patients' treatment allocation.

### Statistical Analysis

Prevalence of ghost core, patient baseline characteristics, and clinical outcomes in patients with versus without ghost core were described as counts and percentages for categorical variables and median and interquartile ranges for continuous variables. Baseline and treatment characteristics and clinical outcomes were compared between patients with versus without CTP ghost core.

The relationship between ghost infarct core and clinical outcome was modelled in an exploratory approach by using ordinal logistic regression. We adjusted the model for the following pre-specified variables: patient age, baseline NIHSS, alteplase treatment, nerinetide treatment, reperfusion status (final eTICI), and final infarct volume. Furthermore, variables for which associations were seen in univariable analysis were included as adjustment factors. No imputation was performed for missing data because missing data were minimal. The analyses were performed separately for both "any ghost core" and "ghost core  $>10$  mL" as a dependent variable.

All statistical tests were 2-sided and conventional levels of significance ( $\alpha = 0.05$ ) were used for interpretation. All analysis was performed by using Stata 17 (StataCorp).

## RESULTS

Of the 1105 patients enrolled in ESCAPE-NA1, 421 had available CTP and 24-hour follow-up imaging and were included in the analysis. Their baseline characteristics are shown in the Online Supplemental Data. Forty-seven of 421 (11.2%) had a ghost core (defined as ghost core volume  $>10$  mL). The median CTP ghost infarct volume was 13.4 mL (IQR 7.6–26.8) (Fig 1). In the early time window, a ghost core  $>10$  mL was seen in 39/311 (12.5%) patients. In the late time window, a ghost core  $>10$  mL was seen in 8/109 (7.3%) patients. When comparing patients with CT versus MRI 24-hour imaging, a ghost core  $>10$  mL was seen in 23/224 (10.3%) patients with 24-hour CT and 24/197 (12.2%) patients with 24-hour MR imaging ( $P = .540$ ).

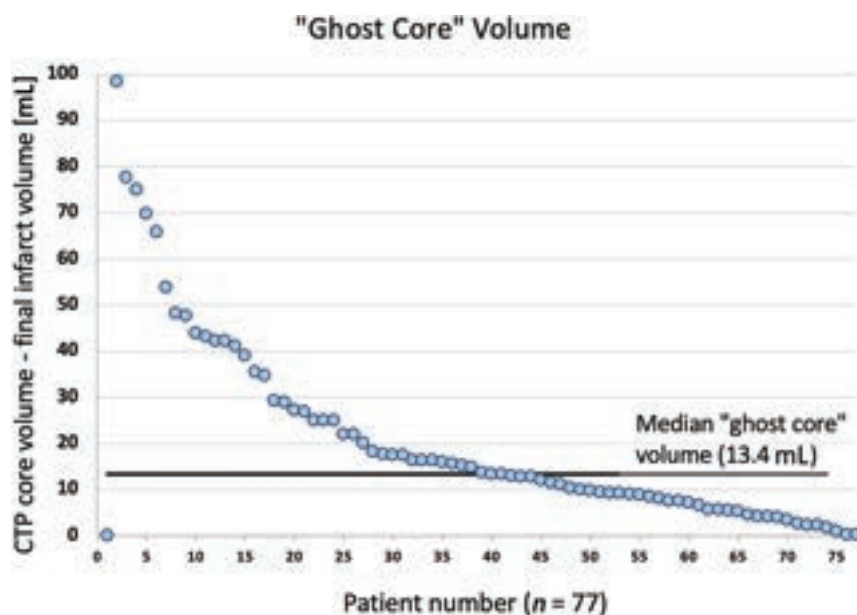


**FIG 1.** “Ghost core” infarct volumes (baseline CTP core volume – 24-hour infarct volume) in the 77 patients who had a baseline CTP rCBF >30% volume that was larger than 24-hour final infarct volume. To be considered a “ghost core” in the current analysis, this difference in volumes had to be >10 mL. Individual patient (blue dot). Median “ghost core” volume was 0.4 mL (black horizontal line).

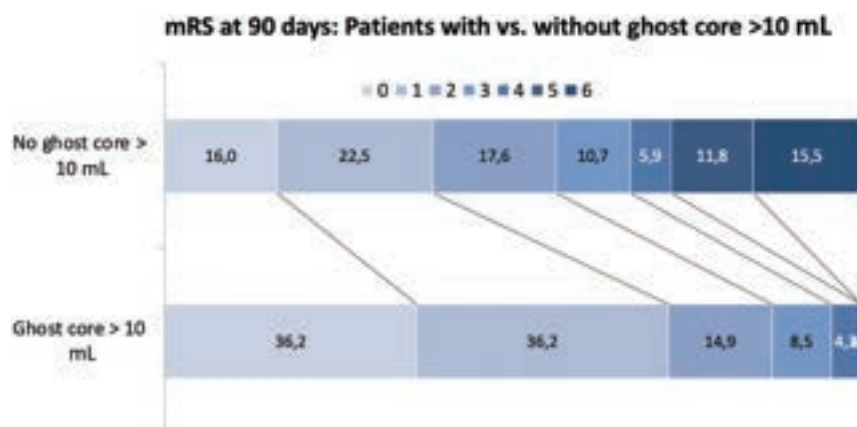


**FIG 2.** mRS at 90 days in patients with and without ghost infarct core >10 mL (ie, CBF <30% infarct core at baseline minus infarct volume at 24 hours >10 mL). mRS categories are shown in ascending order from left to right. Note that 4.3%, 0% and 0% patients achieved mRS 4, 5 and 6 respectively in the lower bar.

### Association of Baseline and Treatment Variables with Ghost Infarct Core

Patients with ghost core were younger, more often male, had better collateral status, a higher proportion of eTICI 2b/3, and shorter last known well-to-CT times (Online Supplemental Data).

In the adjusted analysis, variables that significantly differed between patients with and without ghost core >10 mL were included in a binary logistic regression model with ghost core >10 mL as a dependent variable. Young patient age (adjusted OR 0.83 per 5-year increase [95% CI, 0.74–0.93]), male sex (adjusted OR 1.08 [95% CI, 1.06–4.09]), final eTICI (adjusted OR 1.51 [95% CI, 1.10–2.08]), and last known well-to-CT time (adjusted OR 0.97 per 10-min increase [95% CI, 0.95–0.996]) were associated with ghost core.

### Association of Ghost Infarct Core with Clinical Outcomes

The median mRS in patients with ghost core >10 mL was 1 (IQR 0–2) versus 2 (IQR 1–5) in those without ghost core ( $P < .001$ ) (Fig 2). Forty-one of 47 (87.2%) patients with versus 210/374 (56.2%) patients without ghost core >10 mL achieved a good outcome at 90 days ( $P < .001$ ).

After adjusting for baseline and treatment variables, including final infarct volume, ghost core >10 mL was associated with ordinal mRS (adjusted common OR 0.52 [95% CI 0.28–0.95]).

### DISCUSSION

A ghost core, that is, an overestimation of the infarct size on baseline CTP compared with 24-hour imaging >10 mL, was seen in ~1 of 10 patients. The median ghost core volume was 13 mL. Patients with ghost core were younger, more often male, and had better recanalization status at the end of the EVT procedure and shorter last known well-to-CT times.

Recent randomized controlled trials have shown that EVT is safe and effective even in patients with very large infarcts.<sup>11–13</sup> The implication is that estimating the core infarct by using CTP may not be required for endovascular treatment decision-making. However, it is not yet clear that the benefit of EVT observed in these large core EVT trials will be maintained outside the clinical trial setting, and physicians are often still hesitate to proceed with EVT when a large core is seen on baseline imaging.<sup>14</sup> In some patients, the ghost core phenomenon may be a contributing reason for the observation of benefit in these trials.

Furthermore, current North American and European guidelines recommend perfusion imaging for treatment decision-making in patients with AIS only for patients presenting beyond 6 hours from last known well, but not for those presenting within 6 hours.<sup>2,5</sup> In clinical practice, however, a single stroke imaging protocol is often used for the early and late time window for the sake of simplicity, and this protocol often includes CTP. This means that CTP information is routinely available to physicians in many centers, and therefore invariably taken into account during treatment decision making. CTP overestimation of core volume could influence prognostication, in discussion with family members and possibly result in denial of treatment for a patient who might still benefit from reperfusion.<sup>9</sup> For these reasons, understanding ghost core is essential for the neuroradiologist.

Brain tissue tolerance to ischemia is time-dependent: when ischemia duration is short, much lower cerebral blood flow can be tolerated compared with longer ischemia durations. This was proved as early as 1981, when Jones et al<sup>15</sup> used macaques ischemic stroke models to show that CBF thresholds for infarction were much lower when ischemia duration was short, whereas at longer ischemia durations, infarction already occurred at a higher CBF. This has subsequently been confirmed in human patients with acute ischemic stroke.<sup>16</sup> CTP core thresholds as they are used in clinical practice for AIS imaging today are not time-dependent, and likely represent “average” thresholds that may be accurate in the middle range of ischemia duration. At very short ischemia durations, however, brain tissue can tolerate CBF impairments that are more severe than the commonly used core thresholds.

The current study confirms that the imprecision surrounding the CTP “core” concept is indeed clinically relevant: baseline CTP overestimated infarct volumes compared with 24-hour imaging in >10% of patients, which is roughly similar to previous studies.<sup>8,9</sup> The median ghost core volume was 13 mL; in one-fourth of the patients with ghost core, it exceeded 26 mL. It is not surprising that the use of a single rCBF dichotomy does not adequately delineate infarct core from penumbra, given that ischemia tolerance of brain tissue has been shown to depend on numerous factors, including tissue and cell type,<sup>17</sup> duration of ischemia, and patient age.<sup>18</sup>

The fact that younger patient age was positively associated with ghost infarct core is in line with previous literature, which describes an accelerated ischemic tissue-to-infarct conversion speed in older patients.<sup>18</sup> Furthermore, the age-related decrease in responsivity of the cerebral microvasculature and decrease in cerebral vessel attenuation likely contributes to a reduced recovery potential of ischemic tissue in elderly patients,<sup>19</sup> and may therefore also lead to a reduced prevalence of ghost infarct core.

Previous studies have shown an association of ghost core and poor collateral status.<sup>20</sup> Conversely, we found a significant positive association with better collateral status, but only in the unadjusted analysis. After adjusting for patient baseline factors, no significant association was seen anymore. There are 2 possible explanations for this: first, the ESCAPE-NA1 study included only patients with moderate-to-good collaterals. This preselection of patients may have confounded the results and precluded detection of a significant effect in the multivariable analysis. Second, the decrease in cerebrovascular capacity, and therefore also collateral status, with patient age suggests some degree of multicollinearity of patient age and collateral status. This may be the reason why, after adjusting for patient age, no independent effect of collateral status was observed anymore.

There is robust evidence that ghost core occurs more often in patients with short onset-to-imaging times.<sup>20</sup> Our findings support these previous observations when analyzing the entire patient sample that also included late time window patients. We deliberately refrained from analyzing patient subgroups stratified by ischemia duration due to the relatively small number of patients in these subgroups. Hence, we cannot comment on potential heterogeneity of the effect of onset-to-imaging times within these subgroups.

While the association of ghost core with better recanalization status has been previously described<sup>9</sup> and seems intuitively logical, we do not have a clear explanation for the observed difference in ghost core prevalence between men and women, and suspect that this effect, which was small in magnitude, may have been artificial.

### Limitations

This study has several limitations. First, we batch processed perfusion studies from multiple sites with different sequence acquisition settings and CT machines through the RAPID software algorithm, which has introduced some heterogeneity in our data. Second, we defined CTP infarct core as rCBF <30%, which is the most commonly used threshold, and the results would have looked different if another core threshold had been used. Third, most of the patient population included in this study presented within 6 hours from onset and therefore did not meet guideline-based recommendations for CTP imaging, the latter being restricted to late window patients. Our study included only 109 late window patients, a group that was deemed too small for subgroup analysis, and thus limiting the generalizability of our results to late window patients. However, this simply reflects clinical reality, because CTP was part of the acute stroke imaging protocol in many participating sites, irrespective of the time of patient presentation. Fourth, follow-up infarct volumes were assessed at ~24 hours, but in some patients, but these measurements may not represent final infarct volumes, because infarcts can continue to grow after 24 hours.<sup>21</sup> Fifth, there is a possibility that intravenous thrombolysis treatment may have influenced the occurrence of ghost infarct core in our study and our study was powered to detect such an effect. Lastly, the ESCAPE-NA1 trial had rather stringent eligibility criteria, and our results may therefore not be generalizable to the general EVT population.

### CONCLUSIONS

Baseline CTP overestimated the infarct size in 1 of 10 patients compared with 24-hour imaging, particularly in young patients with complete recanalization and short ischemia duration.

Disclosure forms provided by the authors are available with the full text and PDF of this article at [www.ajnr.org](http://www.ajnr.org).

### REFERENCES

1. Goyal M, Menon BK, van Zwam WH, HERMES Collaborators, et al. **Endovascular thrombectomy after large-vessel ischaemic stroke: a meta-analysis of individual patient data from five randomised trials.** *Lancet* 2016;387:1723–31 CrossRef Medline
2. Powers WJ, Rabinstein AA, Ackerson T, American Heart Association Stroke Council, et al. **2018 guidelines for the early management of patients with acute ischemic stroke: a guideline for healthcare professionals from the American Heart Association/American Stroke Association.** *Stroke* 2018;49:e46–10 CrossRef Medline
3. Albers GW, Marks MP, Kemp S, DEFUSE 3 Investigators, et al. **Thrombectomy for stroke at 6 to 16 hours with selection by perfusion imaging.** *N Engl J Med* 2018;378:708–18 CrossRef Medline
4. Nogueira RG, Jadhav AP, Haussen DC, DAWN Trial Investigators, et al. **Thrombectomy 6 to 24 hours after stroke with a mismatch between deficit and infarct.** *N Engl J Med* 2018;378:11–21 CrossRef Medline

5. Turc G, Bhogal P, Fischer U, et al. **European Stroke Organisation (ESO): European Society for Minimally Invasive Neurological Therapy (ESMINT) Guidelines on Mechanical Thrombectomy in Acute Ischemic Stroke.** *J Neurointerv Surg* 2019;11:535–38 CrossRef Medline
6. Powers WJ, Rabinstein AA, Ackerson T, et al. **Guidelines for the early management of patients with acute ischemic stroke: 2019 Update to the 2018 Guidelines for the Early Management of Acute Ischemic Stroke: a guideline for healthcare professionals from the American Heart Association/American Stroke Association.** *Stroke* 2019;50:e344–e418 CrossRef Medline
7. Campbell BC, Mitchell PJ, Kleinig TJ, EXTEND-IA Investigators, et al. **Endovascular therapy for ischemic stroke with perfusion-imaging selection.** *N Engl J Med* 2015;372:1009–18 CrossRef Medline
8. Boned S, Padroni M, Rubiera M, et al. **Admission CT perfusion may overestimate initial infarct core: the ghost infarct core concept.** *J Neurointerv Surg* 2017;9:66–69 CrossRef Medline
9. Martins N, Aires A, Mendez B, et al. **Ghost infarct core and admission computed tomography perfusion: redefining the role of neuroimaging in acute ischemic stroke.** *Interv Neurol* 2018;7:513–21 CrossRef Medline
10. Hill MD, Goyal M, Menon BK, ESCAPE-NA1 Investigators, et al. **Efficacy and safety of nerinetide for the treatment of acute ischemic stroke (ESCAPE-NA1): a multicentre, double-blind, randomised controlled trial.** *Lancet* 2020;395:878–87 CrossRef Medline
11. Huo X, Ma G, Tong X, et al. **Trial of endovascular therapy for acute ischemic stroke with large infarct.** *N Engl J Med* 2023;388:1272–83 CrossRef Medline
12. Sarraj A, Hassan AE, Abraham MG, SELECT2 Investigators, et al. **Trial of endovascular thrombectomy for large ischemic strokes.** *N Engl J Med* 2023;388:1259–71 CrossRef Medline
13. Yoshimura S, Sakai N, Yamagami H, et al. **Endovascular therapy for acute stroke with a large ischemic region.** *N Engl J Med* 2022;386:1303–13 CrossRef Medline
14. Ospel JM, Singh R, Kashani N, et al. **Endovascular treatment decision making in patients with low baseline ASPECTS: insights from UNMASK EVT, an international multidisciplinary study.** *J Stroke Cerebrovasc Dis* 2020;29:105411 CrossRef Medline
15. Jones TH, Morawetz RB, Crowell RM, et al. **Thresholds of focal cerebral ischemia in awake monkeys.** *J Neurosurg* 1981;54:773–82 CrossRef Medline
16. Rotem SH, Mor S, Chen B, et al. **Infarct core reliability by CT perfusion is a time-dependent phenomenon.** *J Neuroimaging* 2020;30:240–45 CrossRef Medline
17. Nagakane Y, Yamada K, Ohara T, et al. **Preferred involvement of the basal ganglia after lenticulostriate infarction as a possible indicator of different gray and white matter vulnerability.** *Stroke* 2008;39:494–96 CrossRef Medline
18. Ay H, Koroshetz WJ, Vangel M, et al. **Conversion of ischemic brain tissue into infarction increases with age.** *Stroke* 2005;36:2632–36 CrossRef Medline
19. **Changes in neurovascular function in brain microvessels during aging.** *Nature Aging* 2023;3:153–54 CrossRef Medline
20. Ballout AA, Oh SY, Huang B, et al. **Ghost infarct core: a systematic review of the frequency, magnitude, and variables of CT perfusion overestimation.** *J Neuroimaging* 2023;33:716–24 CrossRef Medline
21. Konduri P, Bucker A, Boers A, MR CLEAN Trial Investigators (Multicenter Randomized Clinical Trial of Endovascular Treatment for Acute Ischemic Stroke in the Netherlands), et al. **Risk factors of late lesion growth after acute ischemic stroke treatment.** *Front Neurol* 2022;13:977608 CrossRef Medline

# Effect of Clot Burden Score on Safety and Efficacy of Intravenous Alteplase Prior to Mechanical Thrombectomy in Acute Ischemic Stroke: A Subgroup Analysis of a Randomized Phase 3 Trial

Zifu Li, Yu Zhou, Xiaoxi Zhang, Lei Zhang, Yongwei Zhang, Pengfei Xing, Yongxin Zhang, Qinghai Huang, Qiang Li, Qiao Zuo, Xiaofei Ye, Jianmin Liu, and Pengfei Yang, on behalf of DIRECT-MT Investigators



## ABSTRACT

**BACKGROUND AND PURPOSE:** Whether thrombus burden in acute ischemic stroke modify the effect of intravenous thrombolysis (IVT) before mechanical thrombectomy (MT) remains uncertain. We aim to investigate the treatment effect of stratified clot burden score (CBS) on the efficacy and safety of direct versus bridging MT.

**MATERIALS AND METHODS:** This is an exploratory subgroup analysis of a randomized trial evaluating the effect of CBS on clinical outcome in the DIRECT-MT trial. CBS was divided into 3 groups (0–3, 4–6, and 7–10) based on preoperative CTA, where higher scores indicated a lower clot burden. We report the adjusted common odds ratio for a shift toward better outcomes on the mRS after thrombectomy alone compared with combination treatment by stratified CBS groups.

**RESULTS:** No modification effect of mRS distribution was observed by CBS subgroups (CBS 0–3: adjusted common ratio odds 1.519 [95% CI, 0.928–2.486]; 4–6: 0.924 [0.635–1.345]; 7–10: 1.040 [0.481–2.247]). Patients with CBS 4–6 had a higher rate of early reperfusion (adjusted OR (aOR), 0.3 [95% CI, 0.1–0.9]), final reperfusion (aOR 0.5 [95% CI, 0.3–0.9]), and fewer thrombectomy attempts (aOR 0.4 [95% CI, 0.1–0.7]). Patients with CBS 7–10 had a higher rate of asymptomatic intracranial hemorrhage (14.9% versus 36.8%,  $P = .0197$ ) for bridging MT. No significant difference was observed in other safety outcomes by trichotomized CBS.

**CONCLUSIONS:** The subgroup analysis of DIRECT-MT suggested that thrombus burden did not alter the treatment effect of IVT before MT on functional outcomes in CBS subgroups.

**ABBREVIATIONS:** AIS = acute ischemic stroke; aOR = adjusted OR; acOR = adjusted common odds ratio; CBS = clot burden score; eTICI = expanded TICI; ICH = intracerebral hemorrhage; IVT = intravenous thrombolysis; MT = mechanical thrombectomy

Mechanical thrombectomy (MT) plus intravenous thrombolysis (IVT) has been the standard care for patients who have had acute ischemic stroke (AIS).<sup>1</sup> IVT enhances the probability of early recanalization while carrying the risk of intracerebral hemorrhage. For large thrombus burden, IVT is believed to be less efficient because the rate of recanalization is low for occlusion of proximal large arteries.<sup>2–6</sup> In the meantime, a larger thrombus burden can lead to lower recanalization rates, worse clinical outcomes, and a higher risk of hemorrhagic complications.<sup>4,6,7</sup>

Therefore, IVT may exert a different treatment response to varying thrombus burden.

DIRECT-MT (Direct Intra-arterial Thrombectomy in Order to Revascularize Acute Ischemic Stroke Patients with Large Vessel Occlusion Efficiently in Chinese Tertiary Hospitals Multicenter Randomized Clinical Trial) is a multicenter randomized clinical trial to compare the efficacy of direct MT and bridging MT (MT plus IVT) in eligible patients with acute ischemic stroke, aiming to see whether IVT can be skipped before MT.<sup>8</sup> We hypothesized that thrombus burden may impose a treatment effect on the functional and safety outcomes when applying bridging or direct MT for stratified thrombus burden. Hereby, we sought to examine the effect of stratified clot burden score (CBS 0–3 versus 4–6 versus 7–10) on the clinical outcomes in the subgroup analysis of DIRECT-MT.

## MATERIALS AND METHODS

This is an exploratory analysis of the DIRECT-MT trial, a multicenter randomized clinical trial to determine whether direct MT

Received July 6, 2023; accepted after revision December 4.

From the Neurovascular Center, Changhai Hospital, Naval Medical University, Shanghai, China.

Zifu Li, Yu Zhou, and Xiaoxi Zhang contributed equally to this work.

Please address correspondence to Prof Pengfei Yang, Neurovascular Center, Changhai Hospital, Naval Medical University, Shanghai, China; e-mail: p.yang@vip.163.com



Indicates article with online supplemental data.

<http://dx.doi.org/10.3174/ajnr.A8134>



was noninferior to bridging MT in patients with AIS due to anterior circulation large-vessel occlusion within 4.5 hours after stroke onset. The trial protocol and patient eligibility criteria have been previously published.<sup>8,9</sup> In this secondary analysis, we divided CBS into 3 groups to investigate the treatment effect of CBS on the efficacy and safety of direct MT versus combined thrombolysis with MT.

### **Patients**

The subgroup analysis was conducted within the intention-to-treat population. Patients who received randomization were enrolled in the subgroup analysis. The inclusion criteria for the DIRECT-MT trial included age  $\geq 18$  years, the occlusion of ICA together with the first or proximal segment of the middle cerebral artery on CTA, NIHSS  $\geq 2$ , time window of 4.5 hours applicable to IVT. The exclusion criteria included mRS  $> 2$  or any contraindication to IV alteplase. Patients with missing data of CTA and graded CBS were excluded from the subgroup analysis. The functional outcomes were evaluated by an independent outcome assessment committee. The adverse event was judged by the adverse event committee. Written informed consent was obtained from each patient before randomization. The study protocol was approved by the hospital ethics committee and the research board of participating centers.

### **Stratification of CBS**

CBS is a grading system of reflecting the extent and location of thrombus formation for semiquantitative analysis of thrombus burden for large-vessel occlusion in anterior circulation estimated on CTA.<sup>10</sup> The value of CBS was graded by using the previously described algorithm.<sup>10</sup> The purpose of CBS grading was to qualify the extent of intracranial thrombus, allotting 10 points for the presence of large arteries on CTA. For occlusion of each involved artery, corresponding points were subtracted from the total 10 points. The lower CBS signified a larger thrombus burden. To stratify the CBS rationally, the curve fitting on the relationship of a favorable outcome, mortality, and CBS was validated. After binary logistic regression, we stratified the CBS into 3 subgroups: 0–3, 4–6, and 7–10 (Online Supplemental Data).

### **Outcome Measures**

The radiologic outcomes were evaluated by the DIRECT-MT imaging core lab. All the imaging data were read by 2 independent readers from the core lab who were blinded to treatment allocation and final outcomes. A third reader provided a final adjudication in cases of discrepancies between the 2 readers. The required data regarding the baseline demographics, imaging results, time intervals, and functional and safety outcomes were retrieved from the locked database, and transferred to an independent statistician (X.Y.). The NIHSS was assessed at baseline, thrombectomy after 24 hours, and at 5–7 days or discharge. Early reperfusion before thrombectomy was defined as expanded TICI (eTICI)  $\geq 2a$  on angiogram and successful reperfusion was defined as eTICI  $\geq 2b$ . The clinical outcome was evaluated by means of mRS at 90 days, which was further classified as an excellent functional outcome of mRS 0–1, a favorable outcome of mRS 0–2, and a moderate outcome of

mRS 0–3. Follow-up CT and CTA scanning were performed within 24–72 hours after endovascular treatment. Asymptomatic and symptomatic intracerebral hemorrhages (ICHs) were classified according to the Heidelberg criteria.<sup>11</sup> Procedural complications included any procedural complications, vessel dissection, contrast extravasation, and embolization in a new cerebrovascular territory. Contrast extravasation was defined as contrast leakage on intraprocedural dynamic angiograms.

The primary outcome was to estimate the treatment effect on the functional outcome in patients with stratified CBS by using multivariable ordinal regression to observe the adjusted common ratio odds (acOR) for the shift toward a better functional outcome of the mRS at 90 days for direct MT versus bridging MT. The secondary outcomes included functional and radiologic outcomes. The functional outcomes included the dichotomized mRS at 90 days, Barthel Index 95 or 100 at 90 days, NIHSS after 24 hours, and at 5–7 days or discharge. The radiologic outcomes included early reperfusion before thrombectomy ( $\geq 2a$ ), final reperfusion of eTICI score  $\geq 2b$ , the recanalization rate at 24–72 hours, midline shift, thrombectomy attempts, and the outcome lesion volume on postprocedural CT.

Safety outcomes were death, and asymptomatic and symptomatic ICH, which were classified according to the Heidelberg criteria.<sup>11</sup> Procedural complications included any procedural complications, vessel dissection, contrast extravasation, and embolization in a new cerebrovascular territory. Contrast extravasation was defined as contrast leakage on intraprocedural dynamic angiograms.

### **Statistical Analysis**

Normality of distributions was examined by using histograms and Shapiro–Wilk test. Data are presented as median (interquartile range) or as percentage. The baseline characteristics, functional and safety outcomes were compared by using the adjusted common odds ratio or  $\chi^2$  test for categorical variables, Cochran–Mantel–Haenszel test for stratified categorical data, and Wilcoxon rank-sum test for non-Gaussian distributions by CBS subgroups. Univariate and multivariate regression analyses were performed to observe whether CBS was included as one of the independent prognostic factors that influenced the favorable outcome. The adjusted factors included age, ASPECTS, baseline NIHSS, baseline mRS, time from onset to randomization, collateral score, medical history, CBS, and treatment allocation.

To observe the treatment effect of IVT before MT on the functional outcome by CBS subgroups, multivariable ordinal regression analysis was performed to calculate the acOR for a shift in a direction toward a better functional outcome on the mRS at 90 days. Binary logistic regression was used to calculate the adjusted and unadjusted OR and 95% CIs for secondary outcomes to observe the modification or confounders effect based on CBS stratification, and adjusted and unadjusted relative risk and 95% CI for safety and serious adverse events outcomes. Linear regression was used to calculate adjusted and unadjusted  $\beta$  with 95% CIs for continuous outcomes. Interobserver agreement for trichotomized CBS was measured by using the weighted  $\kappa$  statistic with quadratic weighting.

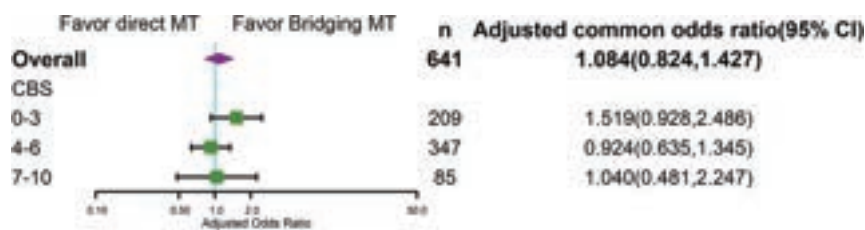


**FIG 1.** Treatment effect for mRS distribution shift on 90 days in trichotomized subgroups.

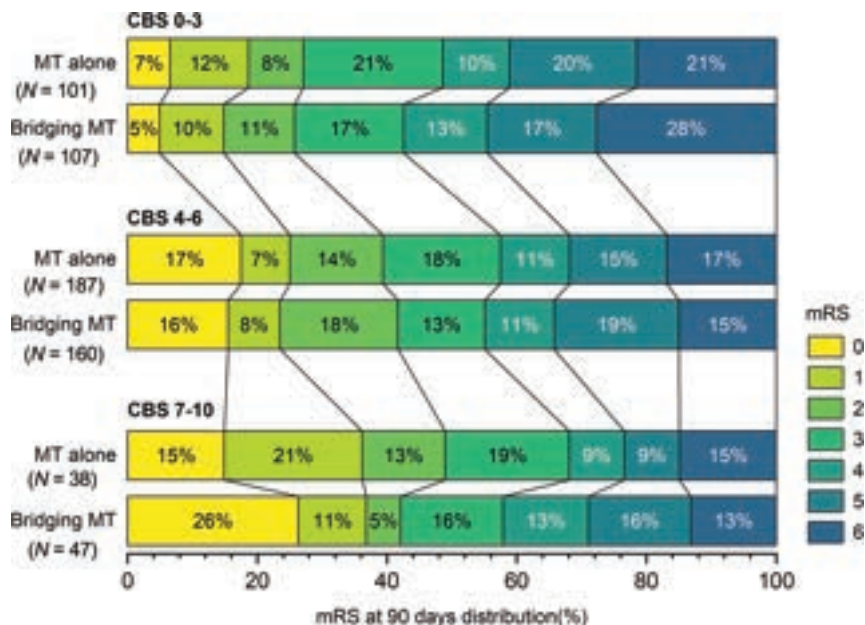


**FIG 2.** Treatment effect for mRS distribution shift on 90 days by treatment group in trichotomized subgroups.

The subgroup analysis was performed by using the SAS version 9.4 (SAS Institute) and R version 4.1.3 software package. A level of  $P < .05$  was accepted as statistically significant.

## RESULTS

The trial profile is shown in the Online Supplemental Data. In the DIRECT-MT trial, 656 patients under randomization, 641 patients were included for subgroup analysis, of whom 315 patients were allocated in direct MT group and 326 patients in bridging MT group. Among the 641 patients, 209 patients had CBS 0-3 (108 [51.7%] in direct MT group versus 101 [48.3%] in bridging MT group, and 347 had CBS 4-6 (direct MT: bridging MT; 160 [46.1%] versus 187 [53.9%]) and 85 had CBS 7-10 (direct MT: bridging MT; 47 [55.3%] versus 38 [44.7%]).

The baseline characteristics of the patients are summarized by CBS subgroups in the Online Supplemental Data. The median time from intravenous alteplase to groin puncture is 27 (interquartile range, 15-39) minutes. No significant difference was observed in the proportion of patients treated with direct or bridging MT between groups. We noticed a longer median time from groin puncture to reperfusion, from randomization to reperfusion, and from stroke onset to reperfusion in patients with lower CBS. However, no significant differences in the median

time from stroke onset to IV alteplase, from stroke onset to reperfusion, or from intravenous alteplase to groin puncture were observed.

Patients with lower CBS had higher NIHSS scores, lower ASPECTS, worse collateral scores (combined grade 0-1, 87.9% of 206 patients with CBS 0-3; 75.3% of 340 patients with CBS 4-6; 61.4% of 83 patients with CBS 7-10), a higher incidence of cardioembolic sources on stroke etiology, a higher proportion of ICA occlusion, and longer time interval from admission to reperfusion, from groin puncture to reperfusion and from randomization to reperfusion (Online Supplemental Data). The time from stroke onset to groin puncture is slightly longer in patients with CBS 4-6. Univariate and multivariate logistic regression analyses showed that CBS was an independent prognostic factor for favorable outcomes (OR, 1.181 [95% CI, 1.064-1.312,  $P = .002$ ]) (Online Supplemental Data).

The outcome of patients was summarized by CBS stratification between 2 groups in the Online Supplemental Data. We noted that patients with lower CBS had a worse degree of overall disability, a lower incidence of excellent, favorable, and moderate functional outcome, Barthel Index 95 or 100 at 90 days, and a higher median

NIHSS after 24 hours and at 5-7 days or discharge. In the meantime, no difference in the rate of early reperfusion before MT and the recanalization rate at 24-72 hours was observed. Patients with lower CBS had a higher successful reperfusion rate (Online Supplemental Data).

The acOR for a better 90-day mRS was 1.5 (95% CI 0.9-2.5) for CBS 0-3, 0.9 (0.6-1.3) for CBS 4-6, and 1.04 (0.5-2.2) for CBS 7-10 in the direct MT group compared with the bridging MT group (Fig 1). There was no significant treatment-by-trichotomized CBS interaction for the ordinal mRS distribution (acOR interaction term relative to CBS 7-10: CBS 0-3, 0.73 [95% CI 0.30-1.81],  $P = .503$ ; CBS 4-6, 1.06 [95% CI 0.45-2.48],  $P = .894$ ) (Fig 2; Online Supplemental Data). No significant difference in the bridging effect was observed for dichotomized mRS, Barthel Index 95 or 100 at 90 days, NIHSS after 24 hours and 5-7 days, or discharge by CBS subgroups.

In the adjusted analysis, patients with CBS 4-6 had a higher rate of early reperfusion (absolute difference 5.76%, adjusted OR (aOR) 0.3 [95% CI, 0.1-0.9]), final reperfusion (absolute difference 8.17%, aOR 0.5 [95% CI, 0.3-0.9]), and less thrombectomy attempts (aOR 0.4 [95% CI, 0.1-0.7]) in bridging MT group than direct MT group for patients with CBS 4-6. With respect to other secondary radiologic outcomes, we noted no

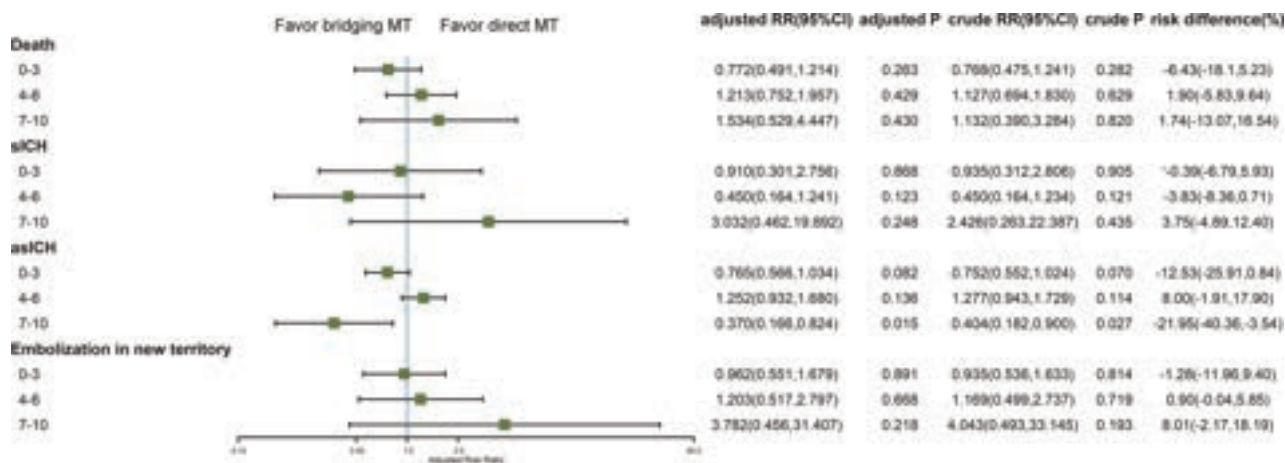


**FIG 3.** Safety outcomes by treatment group in trichotomized subgroups.

significant treatment-by-trichotomized CBS interaction for the recanalization rate at 24–72 h on CTA, midline shift, and outcome lesion volume on CT (Online Supplemental Data).

Patients with lower CBS had higher rates of mortality, asymptomatic ICH, midline shift, any procedural complication, and embolization into a new territory (Online Supplemental Data). We noted no significant difference in symptomatic ICH, vessel dissection, and contrast extravasation between CBS subgroups. With the exception of asymptomatic ICH, we noted no significant treatment-by-trichotomized CBS interaction for any of the other safety outcomes. The asymptomatic rate in the bridging MT group was higher than that in the direct MT group in patients with CBS 7–10 (OR, 0.279 [95% CI, 0.094–0.825],  $P = .0197$ ) (Fig 3; Online Supplemental Data).

The observed agreement for trichotomized CBS was 588 (92%) of 636, yielding a weighted  $\kappa$  of 0.936 (SE 0.012). The concordance correlation coefficient for numeric CBS was 0.941 (95% CI 0.933–0.948).

## DISCUSSION

The subgroup analysis of DIRECT-MT showed that neither modification effect of the treatment strategy of adopting direct or bridging MT nor interaction effect by trichotomized CBS was shown for patients with AIS regarding the overall functional disability. Despite the significantly increased rate of asymptomatic ICH in patients with CBS 7–10, other safety outcomes were not significantly different by CBS subgroups. Thereafter, our results do not support our hypothesis that the degree of clot burden alters the treatment effect of IVT. The clot burden should not alter the physician's decision on whether to use thrombolysis or not.

We found no interaction and modification effect of IVT on the mRS distribution by stratifying thrombus burden. The previous findings showed there was no significant treatment-by-occlusion site interaction for internal carotid artery, M1, and M2.<sup>15,16</sup> In the subgroup analysis, the stratified CBS of 0–3, 4–6, and 7–10 mostly corresponded with the occlusion site of ICA, M1, and M2, respectively. The nonsignificant treatment effect of IVT by CBS stratification may be attributed to several aspects. First, thrombus composition may also pose an important determining effect for

IVT besides thrombus length.<sup>17</sup> Second, the transfer model adopted in the DIRECT-MT is the mothership model. In the model, the working time from intravenous alteplase to groin puncture for IVT was very short, approximately 27 minutes in the DIRECT-MT, leading to inadequate time for alteplase working. Nguyen and Fischer<sup>18</sup> also considered the treatment effect of IVT could not be reflected in the mothership paradigm but drip-and-ship model. For the latter paradigm, the time interval from needle to puncture was significantly longer, and early reperfusion was significantly increased in the drip-and-ship paradigm than in the mothership paradigm.<sup>19,20</sup> Under the drip-and-ship paradigm, patients would potentially benefit from treatment effect of IVT, especially for distal occlusions.

The DIRECT-MT main results showed higher percentages of early reperfusion before MT in the bridging MT group but without statistical significance, and the result was similar to other randomized clinical trials.<sup>9,21,22</sup> On the basis of our prior subgroup analysis, we found that patients with CBS 0–5 had early reperfusion more frequently when they were treated with IVT before MT.<sup>16</sup> Likewise, for patients in the current subgroup analysis, we inferred those patients with CBS 0–3 would also benefit from early reperfusion. However, subgroup analysis showed that early reperfusion occurred more frequently in patients with CBS 4–6 in the bridging MT group, while patients with CBS 0–3 and 7–10 did not achieve this benefit. For patients with CBS 0–3, the occlusion site mostly occurred at the ICA. The proximal occlusion with large thrombus burden had poor response to IVT and could be hardly recanalized.<sup>23–25</sup> This conformed to our anticipation in the clinical practice. In the meantime, patients with CBS 4–6 had a higher rate of early reperfusion, which may be attributed to relatively short thrombus length and thrombus location of M1 segment. Arrarte Terreros et al<sup>24</sup> also reported early recanalization mostly occurred in M1, and more often in M2 after IVT in the drip-and-ship paradigm. Moreover, we failed to observe significant change in early reperfusion in those patients with CBS 7–10 which mainly (79%) occurred at M2. As expected, treatment effect of IVT should be presented with higher recanalization rate for distal occlusions. This may be attributed to the paradigm used in DIRECT-MT. For distal occlusions, adequate time was needed for alteplase to work with the thrombus.<sup>20,23</sup> The nonsignificant

treatment effect of IVT was probably caused by limited time interval from alteplase use to groin puncture to dissolve the thrombus before MT in these patients with CBS 7–10 in the mothership paradigm.

Reperfusion is strongly associated with clinical outcomes in patients with AIS who underwent MT. A higher percentage of final successful reperfusion was observed in the bridging MT group in the main results of DIRECT-MT, though a lack of statistical significance was observed.<sup>9</sup> Bridging MT was associated with higher rates of successful reperfusion and less thrombectomy attempts.<sup>26</sup> In this further subgroup analysis, we found that patients with CBS 4–6 had a significantly higher rate of successful reperfusion and required less thrombectomy attempts in the bridging MT group. The occlusion site of patients with CBS 4–6 was mainly M1, and the thrombus was mostly restricted in the distal M1 or bifurcation. After IVT pretreatment, the size of thrombus was reduced, and the number of thrombectomy passes was less required to retrieve these clots.<sup>26–29</sup>

The main concerns about IVT pretreatment are the hemorrhagic complications. Patients with low CBS had significantly higher rates of mortality, symptomatic or asymptomatic ICH, any procedural complications, and new territory embolization than patients with high CBS. With the exception of asymptomatic ICH, other safety outcomes were comparable in CBS subgroups. Patients with CBS 7–10 had higher incidence of asymptomatic ICH in the bridging MT group, and patients with CBS 0–3 had similar safety outcomes between the two groups. The results did not support our initial assumption that IVT may have a detrimental effect, resulting in a higher rate of symptomatic ICH in patients with a large thrombus burden. In clinical practice, a large dose of unfractionated heparin is conventionally used in the direct MT group while not used in the bridging MT group. The latest evidence showed that periprocedural use of unfractionated heparin was associated with increased risk of symptomatic ICH.<sup>30</sup> The safety outcomes could be confounded by the periprocedural use of unfractionated heparin.

There are several limitations of this subgroup analysis. First, due to post hoc analysis design with relatively small sample size and potential selection bias, the statistical analysis may be underpowered for interaction test between IVT and thrombus burden. In the meantime, the findings in the subgroup analysis were interpreted on the basis of the mothership paradigm implemented in DIRECT-MT, which cannot reflect the treatment effect of IVT in the drip-and-ship paradigm. Therefore, the result of subgroup analysis cannot be overinterpreted, and further randomized controlled trials were warranted for all paradigms.

## CONCLUSIONS

Our findings of the DIRECT-MT trial did not support skipping IVT before MT based on CBS stratification due to the benefit of early reperfusion and comparable safety outcomes in the CBS subgroups. The subgroup analysis showed no modification effect of treatment strategy of using direct or bridging MT for trichotomized CBS subgroups regarding the overall disabilities. Further meta-analysis of randomized controlled trials or cohort studies are warranted to investigate the treatment effect of IVT in all paradigms.

**Disclosure forms** provided by the authors are available with the full text and PDF of this article at [www.ajnr.org](http://www.ajnr.org).

## REFERENCES

- Goyal M, Menon BK, van Zwam WH; HERMES Collaborators, et al. Endovascular thrombectomy after large-vessel ischaemic stroke: a meta-analysis of individual patient data from five randomised trials. *Lancet* 2016;387:1723–31 CrossRef Medline
- Rohan V, Baxa J, Tupy R, et al. Length of occlusion predicts recanalization and outcome after intravenous thrombolysis in middle cerebral artery stroke. *Stroke* 2014;45:2010–17 CrossRef Medline
- Riedel CH, Zimmermann P, Jensen-Kondering U, et al. The importance of size: successful recanalization by intravenous thrombolysis in acute anterior stroke depends on thrombus length. *Stroke* 2011;42:1775–77 CrossRef Medline
- Li G, Wu G, Qin Z, et al. Prognostic value of clot burden score in acute ischemic stroke after reperfusion therapies: a systematic review and meta-analysis. *J Stroke Cerebrovasc Dis* 2019;28:104293 CrossRef Medline
- Legrand L, Naggara O, Turc G, et al. Clot burden score on admission T2\*-MRI predicts recanalization in acute stroke. *Stroke* 2013;44:1878–84 CrossRef Medline
- Yogendrakumar V, Al-Ajlan F, Najm M, et al. Clot burden score and early ischemia predict intracranial hemorrhage following endovascular therapy. *AJNR Am J Neuroradiol* 2019;40:655–60
- Treurniet KM, Yoo AJ, Berkhemer OA; MR CLEAN Investigators, et al. Clot burden score on baseline computerized tomographic angiography and intra-arterial treatment effect in acute ischemic stroke. *Stroke* 2016;47:2972–78 CrossRef Medline
- Yang P, Treurniet KM, Zhang L; DIRECT-MT Investigators, et al. Direct intra-arterial thrombectomy in order to revascularize AIS patients with large vessel occlusion efficiently in Chinese tertiary hospitals: a multicenter randomized clinical trial (DIRECT-MT)-protocol. *Int J Stroke* 2020;15:689–98 CrossRef Medline
- Yang P, Zhang Y, Zhang L; DIRECT-MT Investigators, et al. Endovascular thrombectomy with or without intravenous alteplase in acute stroke. *N Engl J Med* 2020;382:1981–93 CrossRef Medline
- Puetz V, Dzialowski I, Hill MD; Calgary CTA Study Group, et al. Intracranial thrombus extent predicts clinical outcome, final infarct size and hemorrhagic transformation in ischemic stroke: the clot burden score. *Int J Stroke* 2008;3:230–36 CrossRef Medline
- von Kummer R, Broderick JP, Campbell BC, et al. The Heidelberg Bleeding Classification: classification of bleeding events after ischemic stroke and reperfusion therapy. *Stroke* 2015;46:2981–86 CrossRef Medline
- Eilaghi A, Brooks J, d'Este C, et al. Reperfusion is a stronger predictor of good clinical outcome than recanalization in ischemic stroke. *Radiology* 2013;269:240–48 CrossRef Medline
- Derraz I, Pou M, Labreuche J; ASTER and the THRACE Trials Investigators, et al. Clot burden score and collateral status and their impact on functional outcome in acute ischemic stroke. *AJNR Am J Neuroradiol* 2021;42:42–48 CrossRef Medline
- Derraz I, Bourcier R, Soudant M; THRACE Investigators, et al. Does clot burden score on baseline T2\*-MRI impact clinical outcome in acute ischemic stroke treated with mechanical thrombectomy? *J Stroke* 2019;21:91–100 CrossRef Medline
- Zhou Y, Xing P, Li Z; DIRECT-MT Investigators, et al. Effect of occlusion site on the safety and efficacy of intravenous alteplase before endovascular thrombectomy: a prespecified subgroup analysis of DIRECT-MT. *Stroke* 2022;53:7–16 CrossRef Medline
- Zhou Y, Zhang L, Ospel J; DIRECT-MT Investigators, et al. Association of intravenous alteplase, early reperfusion, and clinical outcome in patients with large vessel occlusion stroke: post hoc analysis of the randomized DIRECT-MT trial. *Stroke* 2022;53:1828–36 CrossRef Medline
- Boeckh-Behrens T, Kleine JF, Zimmer C, et al. Thrombus histology suggests cardioembolic cause in cryptogenic stroke. *Stroke* 2016;47:1864–71 CrossRef Medline
- Nguyen TN, Fischer U. Treatment effect of intravenous thrombolysis bridging to mechanical thrombectomy on vessel occlusion site. *Stroke* 2022;53:17–19 CrossRef Medline



19. Gerschenfeld G, Muresan IP, Blanc R, et al. **Two paradigms for endovascular thrombectomy after intravenous thrombolysis for acute ischemic stroke.** *JAMA Neurol* 2017;74:549–56 CrossRef Medline
20. Mueller L, Pult F, Meisterernst J, et al. **Impact of intravenous thrombolysis on recanalization rates in patients with stroke treated with bridging therapy.** *Eur J Neurol* 2017;24:1016–21 CrossRef Medline
21. LeCouffe NE, Kappelhof M, Treurniet KM; MR CLEAN–NO IV Investigators, et al. **A randomized trial of intravenous alteplase before endovascular treatment for stroke.** *N Engl J Med* 2021;385:1833–44 CrossRef Medline
22. Suzuki K, Matsumaru Y, Takeuchi M; SKIP Study Investigators, et al. **Effect of mechanical thrombectomy without vs with intravenous thrombolysis on functional outcome among patients with acute ischemic stroke: the SKIP randomized clinical trial.** *JAMA* 2021;325:244–53 CrossRef Medline
23. Seners P, Turc G, Maier B, et al. **Incidence and predictors of early recanalization after intravenous thrombolysis: a systematic review and meta-analysis.** *Stroke* 2016;47:2409–12 CrossRef Medline
24. Arrarte Terreros N, Bruggeman AA, Swijnenburg IS, et al. **Early recanalization in large-vessel occlusion stroke patients transferred for endovascular treatment.** *J Neurointerv Surg* 2022;14:480–84 CrossRef Medline
25. Menon BK, Al-Ajlan FS, Najm M; INTERSeCT Study Investigators, et al. **Association of clinical, imaging, and thrombus characteristics with recanalization of visible intracranial occlusion in patients with acute ischemic stroke.** *JAMA* 2018;320:1017–26 CrossRef Medline
26. Mistry EA, Mistry AM, Nakawah MO, et al. **Mechanical thrombectomy outcomes with and without intravenous thrombolysis in stroke patients: a meta-analysis.** *Stroke* 2017;48:2450–56 CrossRef Medline
27. Shehabeldin M, Eby B, Wallace AN, et al. **Effect of intravenous thrombolysis on clot survival during mechanical thrombectomy in acute large vessel occlusion strokes.** *Neurosurgery* 2021;89:1027–32 CrossRef Medline
28. Rossi R, Fitzgerald S, Molina S, et al. **The administration of rtPA before mechanical thrombectomy in acute ischemic stroke patients is associated with a significant reduction of the retrieved clot area but it does not influence revascularization outcome.** *J Thromb Thrombolysis* 2021;51:545–51 CrossRef Medline
29. Goyal N, Tsivgoulis G, Pandhi A, et al. **Impact of pretreatment with intravenous thrombolysis on reperfusion status in acute strokes treated with mechanical thrombectomy.** *J Neurointerv Surg* 2019;11:1073–79 CrossRef Medline
30. van der Steen W, van de Graaf RA, Chalos V; MR CLEAN-MED Investigators, et al. **Safety and efficacy of aspirin, unfractionated heparin, both, or neither during endovascular stroke treatment (MR CLEAN-MED): an open-label, multicentre, randomised controlled trial.** *Lancet* 2022;399:1059–69 CrossRef Medline



# MR-Guided Focused Ultrasound Thalamotomy in the Setting of Aneurysm Clip

Henrik Odéen, Lubdha M Shah, Viola Rieke, Dennis L Parker, and Shervin Rahimpour



## ABSTRACT

**SUMMARY:** We report on a 75-year-old woman with a history of right MCA aneurysm clipping and medically refractive right-hand tremor. We successfully performed focused ultrasound thalamotomy of the left ventral intermediate nucleus under MR imaging-guidance at 3T. A thorough pretreatment evaluation of MR thermometry was critical to ensure that adequate precision could be achieved at the intended target. The tremor showed a 75% decrease at 24 hours postprocedure and a 50% decrease at a 3-month follow-up. There were no immediate adverse events.

**ABBREVIATIONS:** MRgFUS = MR-guided focused ultrasound; MRT = MR thermometry; VIM = ventral intermediate nucleus

MR-guided focused ultrasound (MRgFUS) is a stereotactic technique that is increasingly being used for essential tremor and Parkinson-related tremor, in which high-intensity focused ultrasound is used to heat and ablate the thalamic target via precise intraprocedural target localization and the real-time monitoring of thermal dynamics with MR imaging.<sup>1,2</sup> Staged bilateral thalamotomy is a regulatory-approved procedure with a potential for adverse events, including ataxia, dysarthria, and dysphasia.<sup>3-5</sup> However, there is a paucity of literature for MRgFUS in the setting of an intracranial aneurysm clip, which can present challenges with magnetic field inhomogeneity that can render MR thermometry (MRT) unreliable. Here, we present a case of unilateral MRgFUS ventral intermediate nucleus (VIM) thalamotomy for medically refractory tremor in the setting of a contralateral MCA aneurysm clip on a 3T MR imaging scanner. It is shown that a pretreatment MRT study can both aid in evaluating patient-specific MRT performance and result in a safe and efficacious procedure.

## Case

The patient is a 75-year-old, right-handed woman with a history of hypertension, seizure disorder, and aneurysmal subarachnoid hemorrhage treated by MCA clip (Yasargil FE784K, conditional

$B_0 \leq 3T$ ) ligation. The patient presented for a medically refractory right-hand tremor that was diagnosed 10 years prior. The patient had a preprocedural diagnosis of poststroke parkinsonism. The tremor was characterized by a prominent resting and postural tremor (right upper extremity: Clinical Rating Scale for Tremor [CRST]-A 7 [rest 3, postural 3, kinetic 1], CRST-B 11, CRST-C 16). The symptoms, including imbalance, affected her activities of daily living. After discussing the results from the main randomized controlled trial of MRgFUS for essential tremor, including the expected 50% reduction in tremor<sup>6</sup> as well as the risks, benefits, and alternatives, the patient agreed to proceed with MRgFUS of the left VIM.

Before referral to our institution, the patient had a head CT scan done, according to the specifications of the MRgFUS vendor (Insightec). The day before the procedure, diagnostic MR imaging was performed for the structural evaluation and assessment of the degree of susceptibility artifact from the aneurysm clip in the right Sylvian fissure (CT shown in Online Supplemental Data). All MR imaging scans were performed at 3T (Skyra, Siemens). The MR imaging revealed extensive encephalomalacia and gliosis in the right MCA territory from aneurysmal subarachnoid hemorrhage and associated ischemic injury.

On the day of the treatment, the standard MRT protocols were tested with the patient in a focused ultrasonography transducer (Exablate Neuro, Insightec) without the coupling water bath. Before shaving her head or placing the stereotactic frame, the patient's head was stabilized with pads, and imaging was performed with the embedded 2-channel head coils (Insightec). To investigate the homogeneity of the magnetic field and its impact on the MRT in the region of the left VIM target, 30-second duration MRT scans were acquired (8 dynamics). Scans were acquired

Received October 16, 2023; accepted after revision December 4.

From the Departments of Radiology and Imaging Sciences (H.O., L.M.S., V.R., D.L.P.), Neurosurgery (L.M.S., S.R.), and Biomedical Engineering (S.R.), University of Utah, Salt Lake City, Utah.

Grant Support: NIH grants R01EB028316 and R21EB033117.

Please address correspondence to Henrik Odéen, 729 Arapleen Dr, Salt Lake City, UT 84108; e-mail: henrik.odeen@hsc.utah.edu



Indicates article with online supplemental data.

<http://dx.doi.org/10.3174/ajnr.A8109>

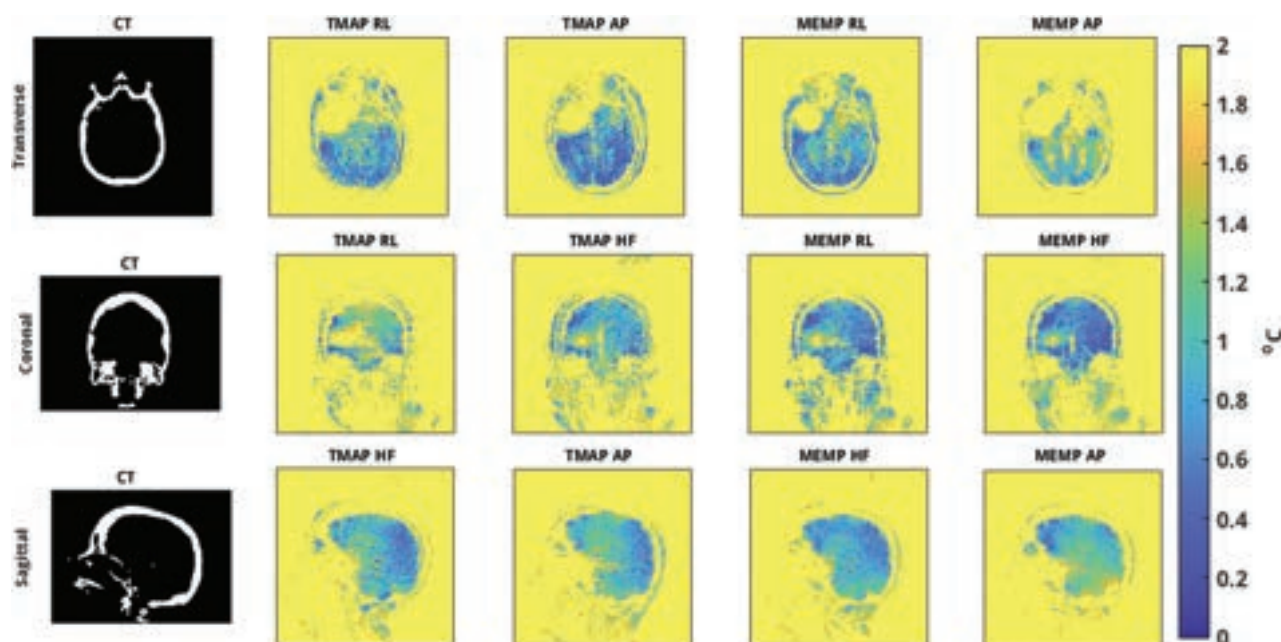


**FIG 1.** CT scan and precision of MRT scans. MRT precision is measured as the standard deviation through time. For all 3 orientations, both phase-encoding directions for both the single-echo and multi-echo MRT sequences are shown. The scans were performed in the Exablate transducer (without the coupling water bath) with a 2-channel radiofrequency receiver coil. The patient's head was stabilized with pads, but no stereotactic frame was used. The scans were performed before the patient's head was shaved.

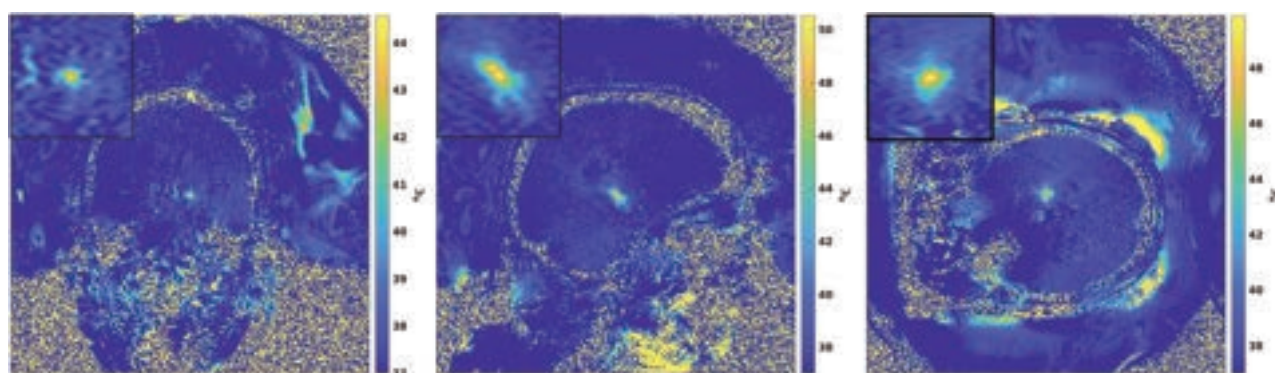


**FIG 2.** MRT of the hottest time point for one heating in each orientation (sonications 2, 7, and 11, respectively, are shown). The inlay in each panel zooms in on a 33 × 33-mm region around the focal spot.

in 3 orthogonal orientations, and for each orientation, both phase-encoding directions were acquired. Scans were performed with vendor-supplied single-echo (TMAP) and multi-echo (MEMP) protocols, for a total of 12 scans (Figure 1). TMAP has a frequency encoding bandwidth of 45 Hz/pixel, whereas MEMP has a bandwidth of 250 Hz/pixel, and hence, less susceptibility to off-resonance effects. For the multi-echo protocol, the echoes were optimally combined by weighting the signal by  $(TE_j \cdot M_j)$ , where TE is the echo time, M is the magnitude image, and  $j = 1:N$  for N echoes.<sup>7</sup> To investigate the precision of the measurement as a function of the spatial location, the standard deviation through time was calculated over each 30-second scan, as shown in Figure 1.

Following the verification of adequate MRT precision in the target area, the patient's head was shaved, secured in a stereotactic head frame, and placed in a cold bath of degassed water. The

patient was placed and secured on the MR imaging scanner table within the Exablate Neuro System (Insightec). After turning off the transducer elements that were interacting with the aneurysm clip, calcifications, etc, 861 of 1024 elements were active (Online Supplemental Data), with a skull attenuation ratio of 0.60. Next, test doses of ultrasonography were delivered while monitoring side effects and tremor reduction (Online Supplemental Data). No side effects were observed during the alignment sonications. During the verification sonications, substantial tremor reduction was not observed in the initially targeted location. Therefore, the target was moved 1 mm posterior and, later, 1.5 mm lateral, given that the patient did not have any sensory changes. The target was moved a total of 4 times, until a tremor reduction was seen with sonications at a temperature of ~49–52°C. A total of 11 sonications with power ranging from 200–952 W, lasting between 11.5–31.4 seconds, and delivering between 2002–22202 J, were performed.

The last 3 sonications were stopped prematurely by the patient because of discomfort, but it was not believed to be related to the aneurysm clip. MRT was successfully acquired during all sonications (Figure 2 and Online Supplemental Data), with a maximum temperature rise of 53.0°C (Online Supplemental Data).

Posttreatment T2-weighted images (axial sampling perfection with application-optimized contrasts by using different flip angle evolution [SPACE sequence; Siemens]) that were acquired immediately posttreatment in 20-channel head coil (Siemens) showed a hyperintense signal at the treatment site (Online Supplemental Data).

## DISCUSSION

Patient-specific factors complicate the MRgFUS treatment of drug refractory tremor. Understanding the technical basis through additional pretreatment scans can aid in the safe performance of the procedure. Successful MRgFUS VIM ablation was achieved with a 75% tremor reduction recorded at 24 hours postprocedure in a patient with an MCA aneurysm clip. A pretreatment MRT study was performed to ensure that satisfactory temperature map quality could be achieved at the intended target. MRT was subsequently successfully acquired in all 3 orthogonal scan planes during the treatment. The pretreatment investigation helped guide which MRT sequence, scan planes, and phase-encoding direction would ultimately be most successful during the treatment. As shown in Figure 1, multi-echo protocols (MEMP), in general, provided better precision than did the single-echo protocol (TMAP) and were therefore used throughout the treatment. The additional preprocedure experiments showed that MRT would be feasible in the thalamus contralateral to the clip, and it was also predicted that MRT would be unreliable in the ipsilateral thalamus. Based on this experience, a pretreatment

scan using the treatment hardware and pulse sequences (especially thermometry) is recommended to evaluate the extent of artifact, based on patient-specific clip type and location.

## CONCLUSIONS

This report demonstrates the feasibility of MRgFUS thalamotomy in a patient with an aneurysm clip. We showed accurate MRT on a 3T scanner by using the multi-echo MRT sequence.

**Disclosure forms** provided by the authors are available with the full text and PDF of this article at [www.ajnr.org](http://www.ajnr.org).

## REFERENCES

1. Jolesz FA, McDannold N. **Current status and future potential of MRI-guided focused ultrasound surgery.** *J Magn Reson Imaging* 2008;27:391–99 CrossRef Medline
2. Moonen CT, Quesson B, Salomir R, et al. **Thermal therapies in interventional MR imaging. Focused ultrasound.** *Neuroimaging Clin N Am* 2001;11:737–47 Medline
3. Sinai A, Nassar M, Eran A, et al. **Magnetic resonance-guided focused ultrasound thalamotomy for essential tremor: a 5-year single-center experience.** *J Neurosurg* 2019;1–8 CrossRef Medline
4. Ito H, Yamamoto K, Fukutake S, et al. **Two-year follow-up results of magnetic resonance imaging-guided focused ultrasound unilateral thalamotomy for medication-refractory essential tremor.** *Intern Med* 2020;59:2481–83 CrossRef Medline
5. Martinez-Fernandez R, Mahendran S, Pineda-Pardo JA, et al. **Bilateral staged magnetic resonance-guided focused ultrasound thalamotomy for the treatment of essential tremor: a case series study.** *J Neurol Neurosurg Psychiatry* 2021;92:927–31 CrossRef Medline
6. Elias WJ, Lipsman N, Ondo WG, et al. **A randomized trial of focused ultrasound thalamotomy for essential tremor.** *N Engl J Med* 2016;375:730–39 CrossRef Medline
7. Odeen H, Parker DL. **Improved MR thermometry for laser interstitial thermotherapy.** *Lasers Surg Med* 2019;51:286–300 CrossRef Medline

# Dynamic Changes in Long-Standing Multiple Sclerosis Revealed by Longitudinal Structural Network Analysis Using Diffusion Tensor Imaging

Hui-Qin Zhang,  Jacky Chi-Yan Lee, Lu Wang, Peng Cao, Koon-Ho Chan, and  Henry Ka-Fung Mak



## ABSTRACT

**BACKGROUND AND PURPOSE:** DTI can be used to derive conventional diffusion measurements, which can measure WM abnormalities in multiple sclerosis. DTI can also be used to construct structural brain networks and derive network measurements. However, few studies have compared their sensitivity in detecting brain alterations, especially in longitudinal studies. Therefore, in this study, we aimed to determine which type of measurement is more sensitive in tracking the dynamic changes over time in MS.

**MATERIALS AND METHODS:** Eighteen patients with MS were recruited at baseline and followed up at 6 and 12 months. All patients underwent MR imaging and clinical evaluation at 3 time points. Diffusion and network measurements were derived, and their brain changes were evaluated.

**RESULTS:** None of the conventional DTI measurements displayed statistically significant changes during the follow-up period; however, the nodal degree, nodal efficiency, and nodal path length of the left middle frontal gyrus and bilateral inferior frontal gyrus, opercular part showed significant longitudinal changes between baseline and at 12 months, respectively.

**CONCLUSIONS:** The nodal degree, nodal efficiency, and nodal path length of the left middle frontal gyrus and bilateral inferior frontal gyrus, opercular part may be used to monitor brain changes over time in MS.

**ABBREVIATIONS:** AD = axial diffusivity; EDSS = Expanded Disability Status Scale; FA = fractional anisotropy; IFGoperc = inferior frontal gyrus, opercular part; MD = mean diffusivity; MFG = middle frontal gyrus; NAWM = normal-appearing WM; ORBsupmed = superior frontal gyrus, medial orbital part; RD = radial diffusivity; SPMS = secondary-progressive MS

Multiple sclerosis is the most prevalent CNS inflammatory demyelinating disease<sup>1</sup> and poses a great threat to the quality of life for patients and their caregivers. DTI, a diffusion model, has frequently been used to explore WM microstructural abnormalities in MS conditions.<sup>2,3</sup> Widely used diffusion measurements include fractional anisotropy (FA), mean diffusivity (MD), axial diffusivity (AD), and radial diffusivity (RD).<sup>4</sup> Microstructural damage can develop in both the lesion area<sup>5</sup> and normal-appearing WM (NAWM)<sup>6</sup> in MS. According to accumulating evidence from current research,<sup>7,8</sup> FA in lesions

often decreases and MD, AD, and RD increase due to demyelination and axonal injury. Similarly, though to a lesser extent, FA in the NAWM also shows a reduction, and MD, AD, and RD are often elevated.<sup>9</sup> However, research on longitudinal microstructural alterations in MS during the follow-up period is limited.

DTI can also be processed by using a network-based approach<sup>10</sup> that maps the topological organization of the brain. Structural networks have provided new insights into the pathologic processes of MS.<sup>11</sup> One of the advantages of graph theory network analysis is that it supports the axonal tension hypothesis,<sup>12</sup> which can reflect the information transfer and neuroplasticity of the brain.<sup>13</sup> The commonly used network measurements are the nodal degree, nodal efficiency, nodal path length, and nodal clustering coefficient.<sup>10</sup> Several recent studies have reported structural DTI network disruption in different subtypes of MS, such as relapsing-remitting MS,<sup>14</sup> secondary-progressive MS (SPMS),<sup>15</sup> and primary-progressive MS,<sup>15</sup> compared with that in healthy controls. For example, Shu et al<sup>16</sup> reported disrupted topological efficiency in MS in terms of reduced global and nodal efficiency compared with those in healthy controls. The clinical relevance of these network measurements has also been reported in previous studies<sup>17,18</sup>; more specifically, Hawkins et

Received August 17, 2023; accepted after revision November 27.

From the Department of Diagnostic Radiology (H.-Q.Z.), National Cancer Center/Cancer Hospital, Chinese Academy of Medical Sciences and Peking Union Medical College, Beijing, China; Department of Diagnostic Radiology (H.-Q.Z., P.C., H.K.-F.M.), Li Ka Shing Faculty of Medicine, Alzheimer's Disease Research Network (H.K.-F.M., K.-H.C.), State Key Laboratory of Brain and Cognitive Sciences (H.K.-F.M.), University of Hong Kong, Hong Kong SAR, China; Department of Medicine (J.C.-Y.L., K.-H.C.), Queen Mary Hospital, Hong Kong SAR, China; and Department of Health Technology and Informatics (L.W.), Hong Kong Polytechnic University, Hong Kong SAR, China.

Please address correspondence to Peng Cao, Department of Diagnostic Radiology, Li Ka Shing Faculty of Medicine, University of Hong Kong, Hong Kong SAR, China; e-mail: caopengl@hku.hk



Indicates article with online supplemental data.

<http://dx.doi.org/10.3174/ajnr.A8115>



al<sup>17</sup> observed that reduced network efficiency could impact multiple cognitive domains in MS, and Welton et al<sup>18</sup> proved that network disruption may serve as a major determinant of cognitive deficits in MS. Charalambous et al<sup>19</sup> proved that structural network disruption measurements could explain disability. However, studies on longitudinal structural DTI network alterations in MS are limited.

Though abundant cross-sectional DTI research on MS focusing on either conventional diffusion measurements or structural network measurements has been published in the past decades, few studies tried to explore whether network measurements or diffusion measurements are more sensitive to detect abnormalities in MS. Research in comparing their sensitivity in longitudinal DTI studies is imperative to probe the brain changes in MS. The conventional diffusion measurements are more vulnerable to the crossing or diverging fibers,<sup>4</sup> while the network measurements may not be, so we hypothesize that the network measures would be superior to capture the brain alterations in MS during the follow-up.

Hence, the main objective of this longitudinal study was to track brain microstructural alterations and brain network changes in MS during a short-term follow-up period of 1 year and then to compare which kind of measurement is more sensitive to capture brain changes over time in MS.

## MATERIALS AND METHODS

### Participants

This longitudinal study was authorized by the local institutional review board, and written informed consent was obtained from all patients. Eighteen patients with MS were recruited for this 1-year longitudinal investigation from the Clinic of the Department of Medicine of the University of Hong Kong from November 2017 to February 2020. All patients with MS were diagnosed according to the latest revised McDonald criteria,<sup>20</sup> and the clinical phenotype classification was based on the latest Lublin criteria.<sup>21</sup> The exclusion criteria were as follows: 1) patients who had claustrophobia or contraindications for MR imaging, 2) patients who had other severe disorders that caused neurologic abnormalities in addition to MS, and 3) patients who were pregnant.

All patients underwent physical examination, neurologic testing, and MR imaging at 3 time points: baseline (t1), at 6 months (t2), and at 12 months (t3). All clinical assessments were performed by the same neurologist during the same week as the MR imaging examinations. The Expanded Disability Status Scale (EDSS) was used to assess physical disability.

### MR Imaging Acquisition

MR imaging was performed at the University Imaging Center by using a 3T scanner (Achieva, Philips Healthcare) with a 32-channel head coil. All participants underwent MR imaging at the 3 time points. The MR imaging protocol included 3D T1-weighted MPRAGE (TR = 6.8 ms, TE = 3.2 ms, TI = 900 ms, matrix = 256 × 256 mm, FOV = 240 × 256 × 204 mm, slice thickness = 1.2 mm), 3D T2-weighted FLAIR (TR = 4800 ms, TE = 266 ms, TI = 1650 ms, matrix = 512 × 512, FOV = 250 × 250 × 184 mm, slice thickness = 0.56 mm), and DTI (TR = 3900 ms, TE = 810 ms, matrix = 80 × 80, FOV = 230 × 90 ×

230 mm, slice thickness = 3 mm). DTI was performed by using a single-shot, spin-echo EPI sequence with a nonzero b-value ( $b = 1,000 \text{ s/mm}^2$ ) along 15 diffusion-encoding gradient directions. Postcontrast (gadolinium) T1WI was acquired at each time point to determine whether the lesions were active or inactive. The total scanning time was 37 min.

### WM Lesion and NAWM Mask

**WM Lesion Segmentation.** 3D T2-weighted FLAIR WM lesions were identified and automatically segmented for each patient at each time point by using the Lesion-Prediction Algorithm<sup>22</sup> implemented in the Lesion Segmentation Toolbox,<sup>23</sup> version 3.0.05, and run in Statistical Parametric Mapping, version 12 (SPM12; <http://www.fil.ion.ucl.ac.uk/spm/>). All produced lesion maps were visually checked and manually corrected to ensure that no errors occurred. The lesion mask that referred to the all voxels of all lesions identified after WM lesion segmentation was also produced.

**Brain Segmentation.** Brain segmentation was carried out by using the Computational Anatomy Toolbox, version 12.6 (CAT12), run with SPM12 implemented in MATLAB R2020a version 9.8.0 (MathWorks). To avoid tissue segmentation bias, lesion-filling was first conducted for MPRAGE images, with the average intensity of surrounding NAWM via “lesion-filling” implemented in Lesion Segmentation Toolbox.<sup>24</sup> Then, the brain was segmented into 3 classes: GM, WM, and CSF, and the WM mask was automatically generated. NAWM masks were obtained by subtracting the lesion mask from the whole WM mask.

### DTI Diffusion Measurements Analysis

DTI data were preprocessed by using the FMRIB Software Library (<http://www.fmrib.ox.ac.uk/fsl>).<sup>25</sup> In the preprocessing steps, the parametric maps (FA, MD, AD, and RD) were derived. The details are provided in the Online Supplemental Data. Then b0 images were transformed into native MPRAGE space.<sup>26</sup> The derived transformation was applied to FA, MD, AD, and RD maps. Then, the measurement values were obtained by using “fslmeans,” part of FMRIB Software Library (<https://fsl.fmrib.ox.ac.uk/fsl/fslwiki/Fslutils>),<sup>25</sup> by using the abovementioned masks.

### Structural WM Network Analysis

**Node definition.** Node and edge were 2 essential components of structural network. Details of the structural WM network analysis are provided in the Online Supplemental Data. Node definition was performed through the following procedures by using SPM12: 1) MPRAGE and b0 first underwent re-origin to make the subsequent co-registration much more accurate; 2) MPRAGE was linearly co-registered to the native b0 image, and the transformation obtained was  $N$ ; 3) MPRAGE was nonlinearly normalized to the ICBM152 T1 template in the standardized Montreal Neurological Institute space. The transformation matrix produced was  $M$ , and the inverse transformation matrix obtained was  $M^{-1}$ ; and 4)  $M^{-1}$  and  $N$  were applied to 90 regions derived from the Automated Anatomical Labeling (<https://omictools.com/aaltool>)<sup>27</sup> atlas in the Montreal Neurological Institute space. Then, the brain was divided into 90 regions in the native diffusion space, which represented the nodes of the brain network.



**Table 1: Demographic and clinical characteristics of MS**

	MS			P Value
	Baseline	6 Months	12 Months	
Sample size	18	18	18	NA
Female:male	13:5	13:5	13:5	NA
Age (yr)	39.11 ± 13.03	39.61 ± 13.03	40.11 ± 13.03	NA
Duration (yr)	12.78 ± 8.53	13.28 ± 8.53	13.78 ± 8.53	NA
EDSS	3.94 ± 2.25	3.94 ± 2.25	4.03 ± 2.18	.633

**Note:**—NA indicates not applicable. The continuous measurements are presented as mean ± standard deviation. EDSS did not show significant changes during the follow-up period. Duration: the time since initial diagnosis of MS.

This node definition method has been adopted in previous research.<sup>16,28,29</sup> The parcellation quality of the b0 image is provided in the Online Supplemental Data.

**WM Tractography.** After preprocessing, DTI was applied to the Diffusion Toolkit<sup>30</sup> for deterministic tractography. For the tractography setting, the Fiber Assignment by Continuous Tracking<sup>31</sup> algorithm was applied; the FA threshold of tracking was set between 0.2 and 1, and the turning angle was 45°, which indicated that if the FA value was <0.2 or the turning angle of the fiber was >45°, the tractography would terminate automatically.<sup>32</sup> These settings have been commonly used in previous studies.<sup>16,29,33,34</sup>

**Edge Definition.** The edges represent the structural connections between 2 separate GM regions. A threshold value of the edge connection was needed to be set to reduce false-positive connections caused by noise and the limitations of tractography. In this study, a threshold of 3 (fiber bundles) was used, which indicated that 2 pair regions were considered connected only if more than 3 fibers existed between them. This threshold value has been commonly used in previous studies.<sup>16,34</sup>

**Network Construction.** The UCLA Multimodal Connectivity package (<https://github.com/jbrown81/umcp>) was used to measure the structural connections between 2 regions. A structural WM network was established for each participant at each time point. Network measurements, including the nodal degree, nodal efficiency, nodal path length, and nodal clustering coefficient, were computed by using the GRaph thEoreTical Network Analysis toolbox (GRETNA).<sup>35</sup>

### Statistical Analysis

All statistical analyses were performed by using SPSS Statistics Version 25 (IBM) and GraphPad Prism version 8.0.0 for Windows (GraphPad Software). Statistical significance was set at  $P < .05$  in all analyses. The normality of the continuous data distribution was tested by using the Shapiro-Wilk test.

Repeated-measures ANCOVA was applied to quantify longitudinal changes in DTI and network measurements assuming normal distribution and equal variance, wherein the measurements served as a within-subject variable, and age and sex were the confounders. The Bonferroni method was used in the subsequent post hoc pair-wise analysis for these variables. Sphericity was a necessity for data distribution in repeated-measures ANCOVA. The Greenhouse-Geisser method was adopted when sphericity could not be satisfied, as determined by the Mauchly

test. When neither normal distribution nor equal variance assumptions were satisfied, the nonparametric Friedman test method was used. The false discovery rate was used to correct for multiple comparisons.

To explore the relationship between these measurements of all brain nodes and EDSS, a series of correlation analyses were first conducted to select the significant regions with EDSS. The left

and right nodes were averaged as 1 node (we did not differentiate between the left and right hemispheres, and the measurement values of the left and right hemispheres of the same node were averaged). All the significant regions, age, and sex together were then put into the stepwise linear model to select the significant predictor of EDSS.

## RESULTS

### Demographic and Clinical Characteristics

All the enrolled 18 patients with MS (15 relapsing-remitting and 3 SPMS) completed the MR imaging scanning and clinical assessment at the 3 time points. The demographic and clinical characteristics of the patients are presented in Table 1. The duration, the time since initial diagnosis of MS, was also provided.

All patients received disease-modifying drugs at the beginning of the study. Two patients with RRMS and 3 patients with SPMS showed worsening during the follow-up period. The details of the patients are presented in Online Supplemental Data. The EDSS scores did not change significantly (Table 1).

### DTI Measurements and Association with EDSS

We observed that FA of lesion was smaller than that of NAWM, while MD, AD, and RD of lesion was larger than that of NAWM across all subjects and time points (Online Supplemental Data). However, all DTI measurements of the lesion and NAWM remained stable over time, as shown in the Online Supplemental Data. There was no significant association among the diffusion measurements of the lesions, NAWM, and EDSS.

### Structural WM Network Measurements

Longitudinal changes in the significant nodal measurements are presented in Figure 1 and the Online Supplemental Data. The nodal degree and nodal efficiency of the left middle frontal gyrus (MFG) and bilateral inferior frontal gyrus, opercular part (IFGoperc) displayed significant decline between t3 and t1; in contrast, the nodal path length of these regions showed a significant increase between t3 and t1. Between t1 and t2 and between t2 and t3, only the region of the left IFGoperc presented significant alterations; that is, the nodal degree and nodal efficiency displayed reduction, whereas the nodal path length showed an increase at t2 compared with those at baseline and at t3 compared with those at t2. In addition, the right superior parietal gyrus exhibited a significant reduction in nodal efficiency between t1 and t2, and between t1 and t3. The nodal clustering coefficients of all the regions remained stable over time (data not shown).

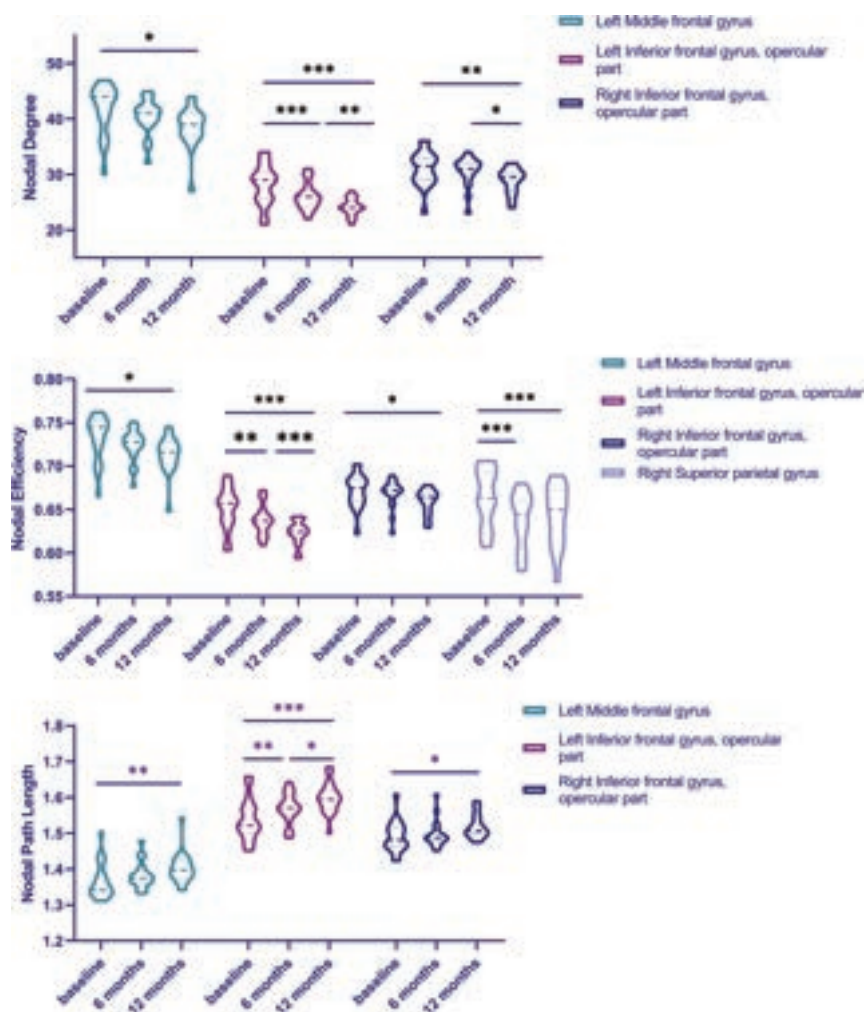


**FIG 1.** Plots of significant nodal network measurements of MS at different time points. \* $P < .05$ ; \*\* $P < .01$ ; \*\*\* $P < .001$ .

### Association between Network Measurements and EDSS

A series of correlations were analyzed to further explore which type of measurement showed a significant association with EDSS. The regions significantly related to EDSS are shown in Figure 2 and the Online Supplemental Data. All selected nodes were entered into the stepwise linear model. Only the nodal path length of the superior frontal gyrus, medial orbital part (ORBsupmed) was selected as a significant predictor for EDSS (Fig 3; Table 2).

## DISCUSSION

In this study, we probed the brain changes in DTI and network measurements over a 1-year follow-up period in 18 patients with MS. The whole lesions (defined as all voxels of all lesions identified after WM lesion segmentation) and NAWM were chosen separately as the ROIs in the conventional diffusion measurement analysis. DTI measurements did not change significantly over the entire study period. While the network measurements showed significant alteration, and their clinical relevance with EDSS was also observed. Based on these findings, we speculated that the network measures may be used to monitor brain changes for MS during follow-up.

### DTI Measurements

Brain changes within 1 year in MS as measured by using DTI remain inconclusive. Some research did not detect significant alterations of diffusion measurement in NAWM or lesions for MS during the 1-year follow-up period.<sup>5,36-38</sup> For example, Ontaneda et al<sup>5</sup> observed that the FA, MD, AD, and RD of NAWM remained stable during the 1-year follow-up period. Our study about diffusion measures can replicate their findings. However, some other studies did report significant progressive microstructural damage during their follow-up period,<sup>39,40</sup> which deviated from our findings. This may be attributed to the lower sample size, different MS subtypes included, analysis methods, or heterogeneous disease-modifying drugs used.

### Structural WM Nodal Network Measurements

We detected topological changes in MS in several frontal brain regions in patients with MS. Compared with baseline, MS showed a significant decrease in the nodal degree and nodal efficiency and significant increase in the nodal path length in the left MFG and bilateral IFGoperc. Reduced nodal efficiency has been reported in previous studies on the MFG and IFGoperc for MS compared with healthy controls.<sup>16</sup>

Our longitudinal studies extended this to a longitudinal period, as these regions exhibited significant changes during the 1-year follow-up period. The pathophysiological changes behind the reduced nodal efficiency may be related to the demyelination and axonal damage, which caused the disconnection between the nodes and eventually induced the lower efficiency of information transfer/communication.<sup>41</sup> Our findings indicate that the nodal degree, nodal efficiency, and nodal path length of the left MFG and bilateral IFGoperc could be used to monitor brain changes over time; moreover, these measurements may be developed as neuroimaging biomarkers to track brain changes in MS, but much more future work is needed. Specifically, the small sample size can be increased in future longitudinal studies, and prospective experiments should be performed. External validation could further verify their clinical values. Due to the small sample size, we could not differentiate between RRMS and SPMS. However, the results were almost stable when we excluded the 3 patients with SPMS (Online Supplemental Data). Another factor that may impact the findings was the disease-modifying treatment. However, we performed the subgroup analysis—the group was divided into 2 subgroups: high-efficiency group (patients who were stable) and low-efficiency group (patients who displayed

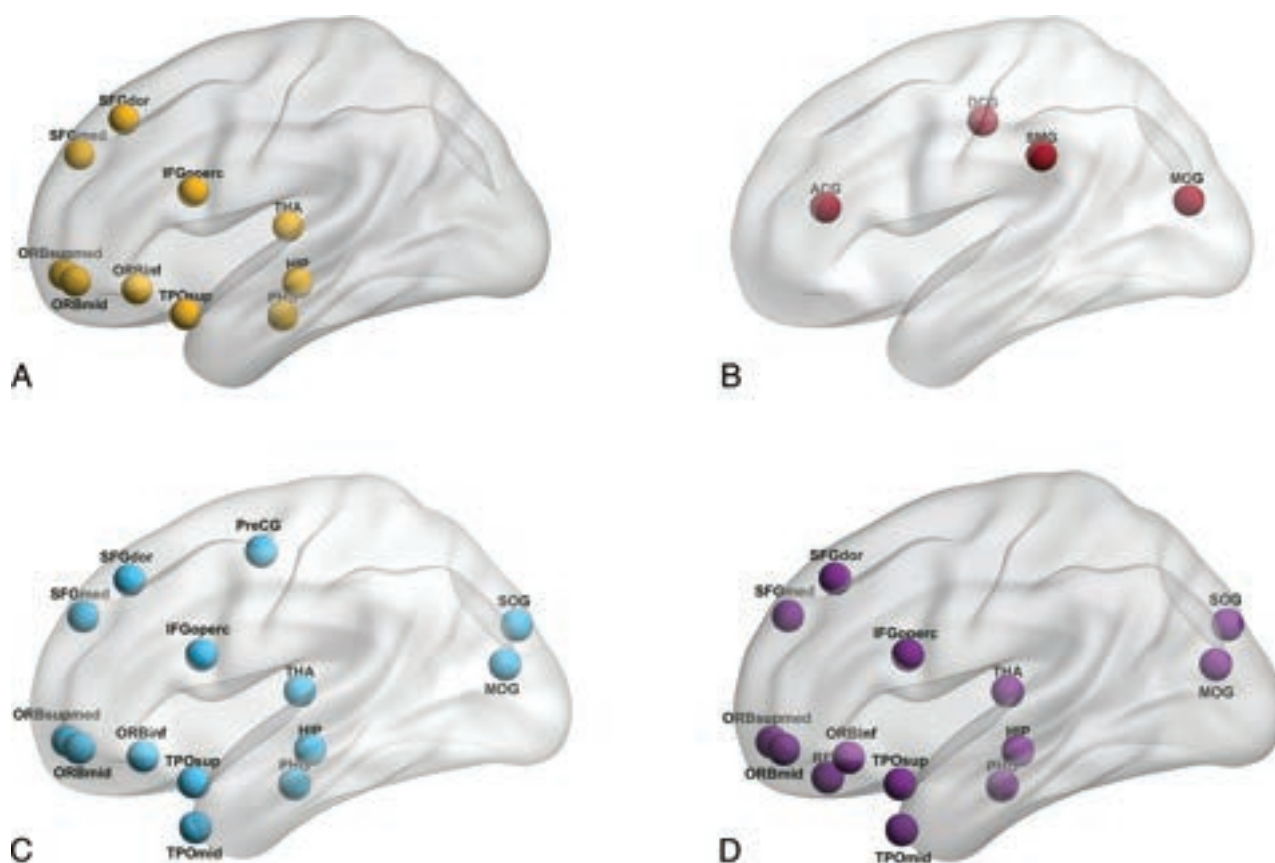


**FIG 2.** Three-dimensional graphs showed regions representing significant association with EDSS. A, Nodal degree. B, Nodal clustering coefficient. C, Nodal efficiency. D, Nodal path length. Brain region corresponding to the anatomical labels can be found in Automated Anatomical Labeling template.

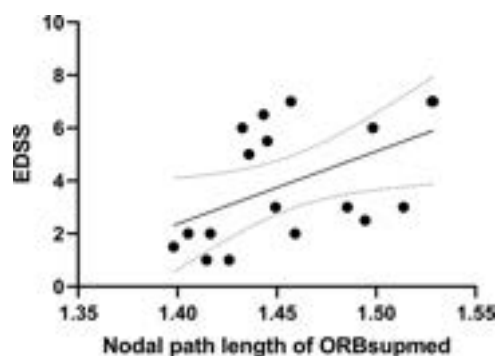


**FIG 3.** Plots of the stepwise linear regression between the nodal path length of superior frontal gyrus, medial orbital part (ORBsupmed), and baseline EDSS.

worsening, including MS02, MS04, MS06, MS07, and MS16). The results are presented in the Online Supplemental Data. We did not detect any significant difference between the 2 subgroups. This suggested that the disease-modifying treatment did not impact the findings.

In our analysis, statistically significant changes were not detected for the diffusion measurements. However, brain structural network measurements showed significant alterations compared with those at baseline. This suggests that conventional diffusion disruption and WM network reorganization may not share identical temporal patterns, indicating that

network measurements could be used to monitor brain changes during follow-up.

#### **Association between Network Measurements and EDSS**

We further explored the relationship between the nodal measurements of all brain regions and EDSS. A multiple linear regression model was established between the nodal path length of ORBsupmed and EDSS, which indicated that it had the potential to be a promising predictor for EDSS. In a longitudinal MS study, Tsagkas et al<sup>42</sup> found that cortical thickness changes in the ORBsupmed region were significantly correlated with EDSS changes during the follow-up period, indicating a relationship between this brain region and EDSS. The underlying cytostructural mechanism may be related to the intralesional axonal loss and the following Wallerian degeneration. This eventually may cause the clinical disability. Similarly, these cytostructural changes may also cause the disconnection between the brain regions and increase the path length needed to information transfer. So, we were allowed to observe a positive relationship between nodal path length of ORBsupmed and EDSS.

#### **Limitations**

Our study still has some limitations. We did not recruit healthy controls; therefore, we could not track longitudinal changes in healthy individuals and were unable to compare the longitudinal differences between patients with MS and healthy controls. Future studies should also recruit healthy controls. Furthermore, our



**Table 2: Selected linear regression model about EDSS**

	Dependent Variable	R <sup>2</sup>	Adjusted R <sup>2</sup>	Regression Coefficient	95% CI	P Value
Model	EDSS(tl)	0.366	0.327	—	—	—
Constant	—	—	—	−46.625	[−81.89, −11.35]	.013
Nodal path length of ORBsupmed	—	—	—	34.231	[10.36, 58.10]	.008

**Note:**—The en dash indicates not applicable.

sample size was relatively small, and our findings may be viewed as preliminary and need confirmation in a larger cohort of MS. However, in this longitudinal study, each patient was examined and assessed 3 times, and the findings could still provide some clinical value.

## CONCLUSIONS

The nodal degree, nodal efficiency, and nodal path length of the left MFG and bilateral IFGoperc may be used to monitor the brain changes over time in MS. The nodal path length of ORBsupmed could be used to evaluate physical disability in patients with MS. These findings together could elevate our understanding of MS.

**Disclosure forms** provided by the authors are available with the full text and PDF of this article at [www.ajnr.org](http://www.ajnr.org).

## REFERENCES

- Reich DS, Lucchinetti CF, Calabresi PA. **Multiple sclerosis.** *N Engl J Med* 2018;378:169–80 CrossRef Medline
- Ge Y, Law M, Grossman RI. **Applications of diffusion tensor MR imaging in multiple sclerosis.** *Ann NY Acad Sci* 2006;1064:202–19 CrossRef Medline
- Inglese M, Bester M. **Diffusion imaging in multiple sclerosis: research and clinical implications.** *NMR Biomed* 2010;23:865–72 CrossRef Medline
- Soares JM, Marques P, Alves V, et al. **A hitchhiker's guide to diffusion tensor imaging.** *Front Neurosci* 2013;7:31 CrossRef Medline
- Ontaneda D, Sakaie K, Lin J, et al. **Identifying the start of multiple sclerosis injury: a serial DTI study.** *J Neuroimaging* 2014;24:569–76 CrossRef Medline
- Huang J, Liu Y, Zhao T, et al. **White matter microstructural alterations in clinically isolated syndrome and multiple sclerosis.** *J Clin Neurosci* 2018;53:27–33 CrossRef Medline
- Klistorner A, Wang C, Yiannikas C, et al. **Evidence of progressive tissue loss in the core of chronic MS lesions: a longitudinal DTI study.** *Neuroimage Clin* 2018;17:1028–35 CrossRef Medline
- Yu FF, Chiang FL, Stephens N, et al. **Characterization of normal-appearing white matter in multiple sclerosis using quantitative susceptibility mapping in conjunction with diffusion tensor imaging.** *Neuroradiology* 2019;61:71–79 CrossRef Medline
- de Kouchkovsky I, Fieremans E, Fleysher L, et al. **Quantification of normal-appearing white matter tract integrity in multiple sclerosis: a diffusion kurtosis imaging study.** *J Neurol* 2016;263:1146–55 CrossRef Medline
- Rubinov M, Sporns O. **Complex network measures of brain connectivity: uses and interpretations.** *Neuroimage* 2010;52:1059–69 CrossRef Medline
- Fleischer V, Radetz A, Ciolac D, et al. **Graph theoretical framework of brain networks in multiple sclerosis: a review of concepts.** *Neuroscience* 2019;403:35–53 CrossRef Medline
- Van Essen DC. **A tension-based theory of morphogenesis and compact wiring in the central nervous system.** *Nature* 1997;385:313–18 CrossRef Medline
- Newman ME. **Modularity and community structure in networks.** *Proc Natl Acad Sci USA* 2006;103:8577–82 CrossRef Medline
- Llufriu S, Martinez-Heras E, Solana E, et al. **Structural networks involved in attention and executive functions in multiple sclerosis.** *Neuroimage Clin* 2017;13:288–96 CrossRef Medline
- Kocevar G, Stamile C, Hannoun S, et al. **Graph theory-based brain connectivity for automatic classification of multiple sclerosis clinical courses.** *Front Neurosci* 2016;10:478 CrossRef Medline
- Shu N, Liu Y, Li K, et al. **Diffusion tensor tractography reveals disrupted topological efficiency in white matter structural networks in multiple sclerosis.** *Cereb Cortex* 2011;21:2565–77 CrossRef Medline
- Hawkins R, Shatil AS, Lee L, et al. **Reduced global efficiency and random network features in patients with relapsing-remitting multiple sclerosis with cognitive impairment.** *AJNR Am J Neuroradiol* 2020;41:449–55 CrossRef Medline
- Welton T, Constantinescu CS, Auer DP, et al. **Graph theoretic analysis of brain connectomics in multiple sclerosis: reliability and relationship with cognition.** *Brain Connect* 2020;10:95–104 CrossRef Medline
- Charalambous T, Tur C, Prados F, et al. **Structural network disruption markers explain disability in multiple sclerosis.** *J Neurol Neurosurg Psychiatry* 2019;90:219–26 CrossRef Medline
- Thompson AJ, Banwell BL, Barkhof F, et al. **Diagnosis of multiple sclerosis: 2017 revisions of the McDonald criteria.** *Lancet Neurol* 2018;17:162–73 CrossRef Medline
- Lublin FD, Coetzee T, Cohen JA, International Advisory Committee on Clinical Trials in MS, et al. **The 2013 clinical course descriptors for multiple sclerosis.** *Neurology* 2020;94:1088–92 CrossRef Medline
- Schmidt P. **Bayesian inference for structured additive regression models for large-scale problems with applications to medical imaging.** Dissertation, LMU München: Faculty of Mathematics, Computer Science and Statistics 2017
- Schmidt P, Gaser C, Arsic M, et al. **An automated tool for detection of FLAIR-hyperintense white-matter lesions in multiple sclerosis.** *Neuroimage* 2012;59:3774–83 CrossRef Medline
- Battaglini M, Jenkinson M, De Stefano N. **Evaluating and reducing the impact of white matter lesions on brain volume measurements.** *Hum Brain Mapp* 2011;33:2062–71 CrossRef Medline
- Smith SM, Jenkinson M, Woolrich MW, et al. **Advances in functional and structural MR image analysis and implementation as FSL.** *Neuroimage* 2004;23 Suppl 1:S208–19 CrossRef Medline
- Jenkinson M, Beckmann CF, Behrens TE, et al. **FSL.** *NeuroImage* 2012;62:782–90 CrossRef Medline
- Tzourio-Mazoyer N, Landeau B, Papathanassiou D, et al. **Automated anatomical labeling of activations in SPM using a macroscopic anatomical parcellation of the MNI MRI single-subject brain.** *Neuroimage* 2002;15:273–89 CrossRef Medline
- Gong G, He Y, Concha L, et al. **Mapping anatomical connectivity patterns of human cerebral cortex using in vivo diffusion tensor imaging tractography.** *Cereb Cortex* 2009;19:524–36 CrossRef Medline
- Liu Y, Duan Y, Dong H, et al. **Disrupted module efficiency of structural and functional brain connectomes in clinically isolated syndrome and multiple sclerosis.** *Front Hum Neurosci* 2018;12:138 CrossRef Medline
- Wang R, Benner T, Sorensen AG, et al. **Diffusion toolkit: a software package for diffusion imaging data processing and tractography.** *Proc Intl Soc Mag Reson Med* 2007;15

31. Mori S, Crain BJ, Chacko VP, et al. **Three-dimensional tracking of axonal projections in the brain by magnetic resonance imaging.** *Ann Neurol* 1999;45:265–69
32. Basser PJ, Pajevic S, Pierpaoli C, et al. **In vivo fiber tractography using DT-MRI data.** *Magn Reson Med* 2000;44:625–32 CrossRef
33. Shu N, Duan Y, Xia M, et al. **Disrupted topological organization of structural and functional brain connectomes in clinically isolated syndrome and multiple sclerosis.** *Sci Rep* 2016;6:29383 CrossRef Medline
34. Xu X, Lau KK, Wong YK, et al. **The effect of the total small vessel disease burden on the structural brain network.** *Sci Rep* 2018;8:7442 CrossRef Medline
35. Wang J, Wang X, Xia M, et al. **GRETN: a graph theoretical network analysis toolbox for imaging connectomics.** *Front Hum Neurosci* 2015;9:386
36. Schneider R, Genc E, Ahlborn C, et al. **Temporal dynamics of diffusion metrics in early multiple sclerosis and clinically isolated syndrome: a 2-year follow-up tract-based spatial statistics study.** *Front Neurol* 2019;10:1165 CrossRef Medline
37. Zivadinov R, Bergsland N, Hagemeier J, et al. **Effect of teriflunomide on gray and white matter brain pathology in multiple sclerosis using volumetric and diffusion-tensor imaging MRI measures.** *J Neurol Sci* 2018;388:175–81 CrossRef Medline
38. Rashid W, Hadjiprocopis A, Davies G, et al. **Longitudinal evaluation of clinically early relapsing-remitting multiple sclerosis with diffusion tensor imaging.** *J Neurol* 2008;255:390–97 CrossRef Medline
39. Toschi N, De Santis S, Granberg T, et al. **Evidence for progressive microstructural damage in early multiple sclerosis by multi-shell diffusion magnetic resonance imaging.** *Neuroscience* 2019;403:27–34 CrossRef Medline
40. Fox RJ, Cronin T, Lin J, et al. **Measuring myelin repair and axonal loss with diffusion tensor imaging.** *AJNR Am J Neuroradiol* 2011;32:85–91 CrossRef Medline
41. Lemus HN, Warrington AE, Rodriguez M. **Multiple sclerosis.** *Neurol Clin* 2018;36:1–11 CrossRef Medline
42. Tsagkas C, Chakravarty MM, Gaetano L, et al. **Longitudinal patterns of cortical thinning in multiple sclerosis.** *Hum Brain Mapp* 2020;41:2198–215 CrossRef Medline



# Synthesizing Contrast-Enhanced MR Images from Noncontrast MR Images Using Deep Learning

Gowtham Murugesan,  Fang F. Yu,  Michael Achilleos,  John DeBevits,  Sahil Nalawade,  Chandan Ganesh,  Ben Wagner,  Ananth J Madhuranthakam, and  Joseph A. Maldjian



## ABSTRACT

**BACKGROUND AND PURPOSE:** Recent developments in deep learning methods offer a potential solution to the need for alternative imaging methods due to concerns about the toxicity of gadolinium-based contrast agents. The purpose of the study was to synthesize virtual gadolinium contrast-enhanced T1-weighted MR images from noncontrast multiparametric MR images in patients with primary brain tumors by using deep learning.

**MATERIALS AND METHODS:** We trained and validated a deep learning network by using MR images from 335 subjects in the Brain Tumor Segmentation Challenge 2019 training data set. A held out set of 125 subjects from the Brain Tumor Segmentation Challenge 2019 validation data set was used to test the generalization of the model. A residual inception DenseNet network, called T1c-ET, was developed and trained to simultaneously synthesize virtual contrast-enhanced T1-weighted (vT1c) images and segment the enhancing portions of the tumor. Three expert neuroradiologists independently scored the synthesized vT1c images by using a 3-point Likert scale, evaluating image quality and contrast enhancement against ground truth T1c images (1 = poor, 2 = good, 3 = excellent).

**RESULTS:** The synthesized vT1c images achieved structural similarity index, peak signal-to-noise ratio, and normalized mean square error scores of 0.91, 64.35, and 0.03, respectively. There was moderate interobserver agreement between the 3 raters, regarding the algorithm's performance in predicting contrast enhancement, with a Fleiss kappa value of 0.61. Our model was able to accurately predict contrast enhancement in 88.8% of the cases (scores of 2 to 3 on the 3-point scale).

**CONCLUSIONS:** We developed a novel deep learning architecture to synthesize virtual postcontrast enhancement by using only conventional noncontrast brain MR images. Our results demonstrate the potential of deep learning methods to reduce the need for gadolinium contrast in the evaluation of primary brain tumors.

**ABBREVIATIONS:** BraTS = Brain Tumor Segmentation Benchmark; ET = enhancing tumor; GBCA = gadolinium-based contrast agent; MSE = mean squared error; NMSE = normalized mean squared error; PSNR = peak signal-to-noise ratio; RID = Residual Inception DenseNet; SFL = spatial frequency loss; SPL = structural perception loss; SSIM = structural similarity index; T2w = T2-weighted; vT1c = virtual contrast-enhanced T1-weighted; WT = whole tumor

Structural MR imaging offers superior soft tissue contrast compared with other imaging modalities, and plays a crucial role in the evaluation of brain tumors by providing information about lesion location as well as morphologic features such as necrosis, the extent of tumor spread, and the associated mass effect on surrounding brain parenchyma. The administration of

intravenous gadolinium-based contrast agents (GBCAs) shortens T1 relaxation times and increases tissue contrast by accentuating areas where contrast agents have leaked through the blood-brain barrier into the interstitium. This blood-brain barrier breakdown is a feature of certain brain tumors, including high-grade gliomas, and can serve as an important tool for diagnosis and assessment of a treatment response.<sup>1</sup>

GBCAs have been used for decades in MR imaging and have historically been considered safe for patients with normal renal function.<sup>1</sup> It is well-known that there is a risk of nephrogenic systemic fibrosis associated with GBCA administration in patients with renal impairment, particularly when linear conjugates of gadolinium are used.<sup>2</sup> Moreover, recent studies have shown gadolinium deposits in tissues throughout the body, even in the setting of normal renal function, which has raised additional concerns about

Received January 27, 2022; accepted after revision December 1, 2023.

From the Department of Radiology, University of Texas Southwestern Medical Center, Dallas, Texas.

Funding Information: Support for this research was provided by NCI U01CA207091 (A.J.M., J.A.M.) and R01CA260705 (J.A.M.).

Please address correspondence to Fang Frank Yu, MD, UT Southwestern Medical Center, 5323 Harry Hines Blvd, Dallas, TX 75390; e-mail: frankf.yu@utsouthwestern.edu; @FrankFYuMDI



Indicates article with online supplemental data.

<http://dx.doi.org/10.3174/ajnr.A8107>

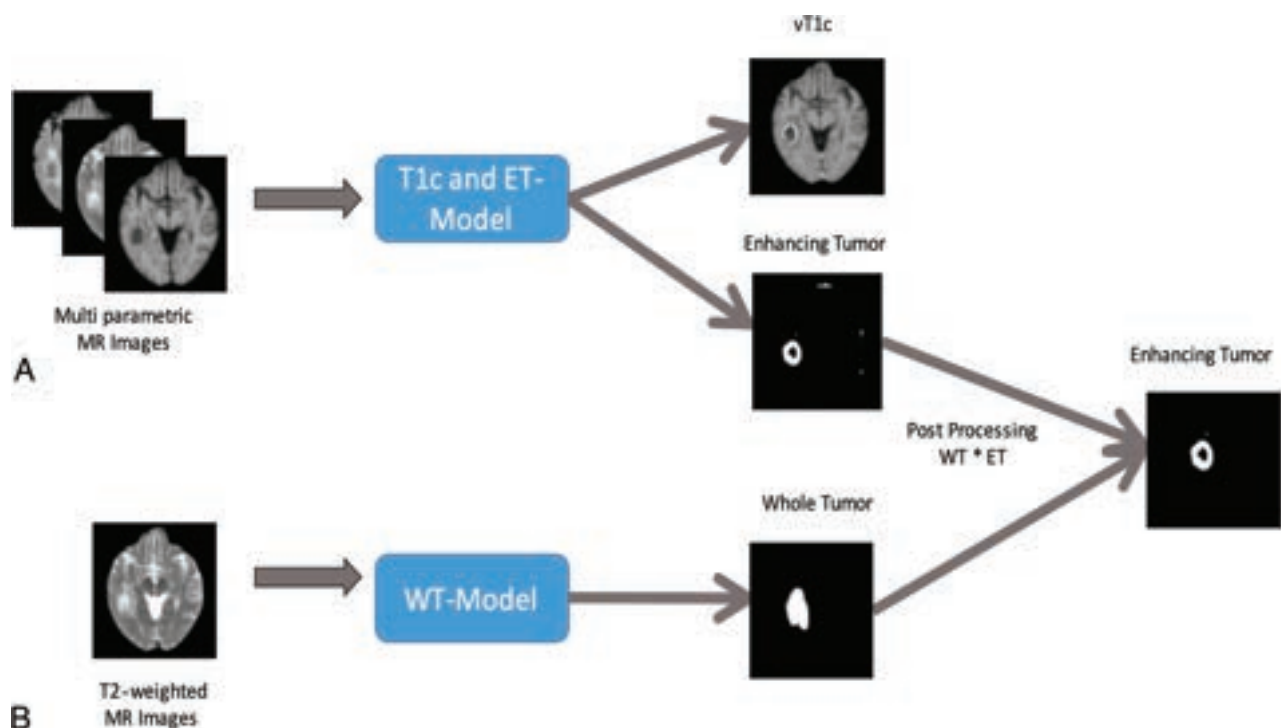


**FIG 1.** Residual inception DenseNet (RID). A, RID model for virtual contrast enhancement (vT1c prediction) and enhancing tumor (ET) segmentation. B, RID model for whole tumor (WT) segmentation.

the long-term safety of these agents.<sup>3</sup> Within the brain, persistent increased signal intensity on T1-weighted (T1w) MR images has been reported within the dentate nucleus and globus pallidus following the prior administration of both linear and macrocyclic GBCAs.

Because of these concerns about the toxicity of gadolinium, there has been growing interest in alternative approaches to contrast-enhanced MR imaging. Examples include manganese-based contrast agents<sup>4</sup> as well as noncontrast techniques, such as arterial spin-labeling<sup>5</sup> and chemical exchange saturation transfer.<sup>6</sup> Recent developments in deep learning algorithms have shown promise in image synthesis and reconstruction. The main goal of this study is to investigate the potential of deep learning methods to simulate contrast enhancement within brain gliomas by using a limited set of standard clinical noncontrast MR images. Our contributions in this work are 3-fold. First, we developed a novel deep learning network to demonstrate the ability of deep learning to synthesize virtual contrast-enhanced T1w images (vT1c) by using only noncontrast FLAIR, T1w, and T2-weighted (T2w) images. Second, we utilized imaging data from different scanners at multiple sites to train the model and evaluated its performance in predicting gadolinium enhancement by using quantitative and qualitative metrics. Third, we analyzed the contribution of each set of input MR images in synthesizing the vT1c image to gain insights regarding the further optimization and streamlining of the MR imaging protocol for clinical application.

## MATERIALS AND METHODS

### Data and Preprocessing

The multimodal Brain Tumor Segmentation Benchmark (BraTS) data set provides a general platform for developing deep learning

models.<sup>7</sup> The BraTS 2019 data set used in our study consists of MR imaging data from 460 patients with gliomas, acquired from multiple institutions,<sup>8</sup> including the University of Pennsylvania; MD Anderson Cancer Center; Washington University School of Medicine in St. Louis; and Tata Memorial Centre in India. The data set has a wide variation in imaging protocols and acquisition parameters. All subjects had precontrast T1w, T2w, and FLAIR as well as postcontrast T1c images. From this set, a single-fold training split of 335 subjects, including 259 high-grade glioma subjects and 76 low-grade glioma subjects, were used for training, while 125 subjects were held out for testing. The training data set was further randomly split into 300 and 35 subjects for the training and in-training validation of the model, respectively.

**Data Preprocessing.** The standard preprocessing steps performed by BraTS included coregistration to an anatomic brain template,<sup>9</sup> resampling to isotropic resolution (1 mm<sup>3</sup>), and skull stripping.<sup>10</sup> Additionally, we performed N4 bias field correction<sup>11</sup> to remove radiofrequency inhomogeneity and normalized to zero mean and unit variance.

### Network Architecture

A schematic of our proposed network architecture is shown in Fig 1. The residual inception DenseNet (RID) network was first proposed and developed by Khenet et al<sup>12</sup> for cardiac segmentation. Our implementation of the RID network incorporated slight modifications in Keras with a TensorFlow backend (Fig 2). In the DenseNet architecture, the GPU memory footprint increases as the feature maps and spatial resolution increases. The skip connections from the down-sampling path to the up-sampling path used elementwise addition, instead of the concatenation operation

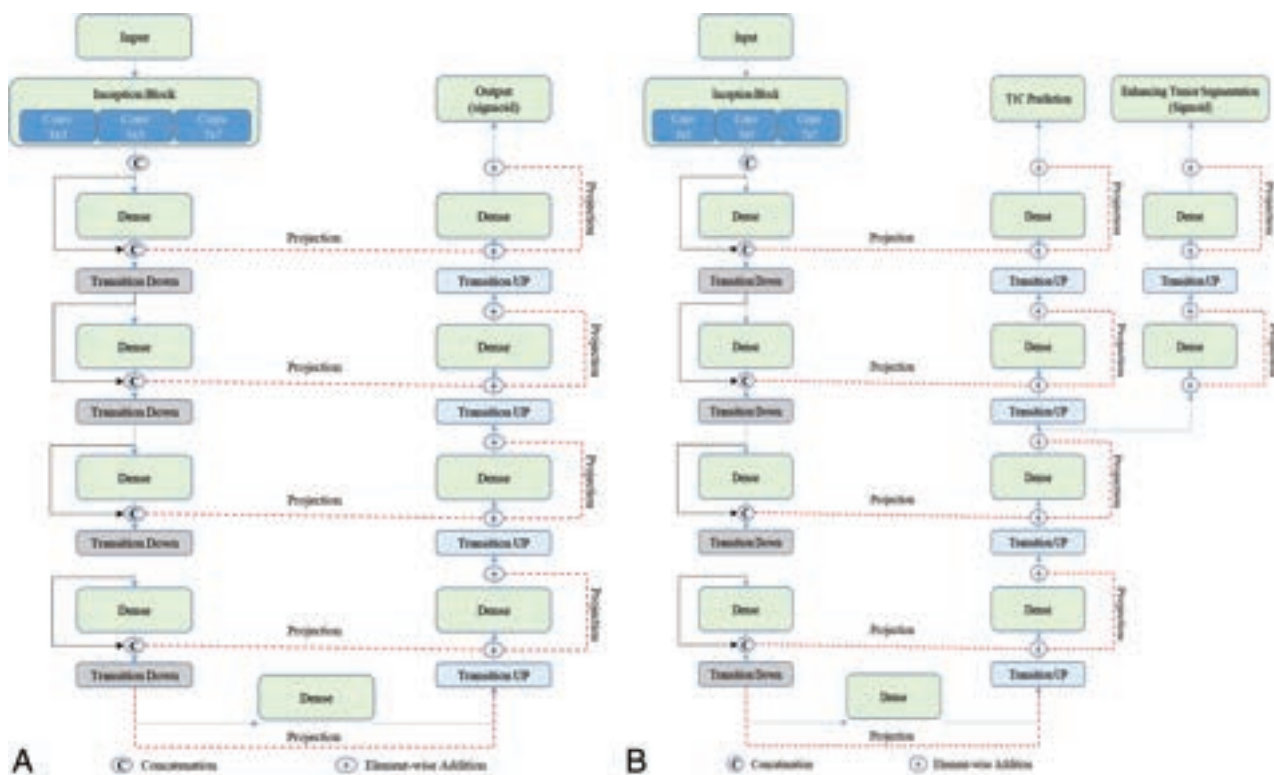


**FIG 2.** Residual inception DenseNet (RID). A, RID model for whole tumor segmentation. B, RID model for virtual contrast enhancement and enhancing tumor segmentation.

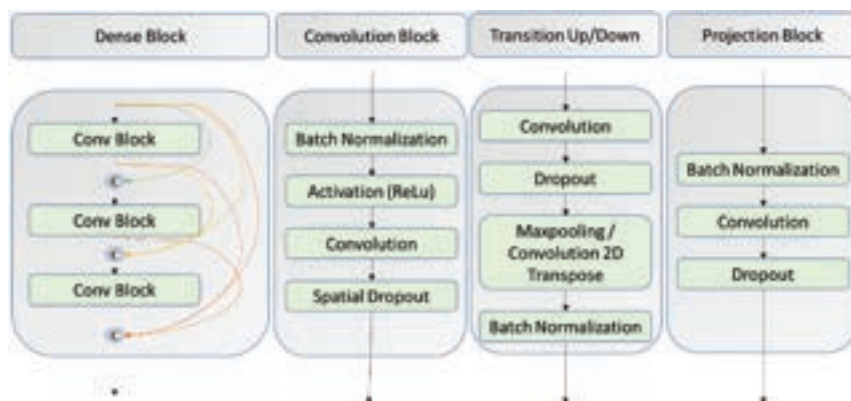


**FIG 3.** Building blocks of residual inception network. From left to right, dense block, convolution block, transition block, and projection block.

in DenseNet, to mitigate feature map explosion in the up-sampling path. For the skip connections, a projection operation was done by using Batch-Norm-1×1-convolution-drop-out to match the dimensions for element-wise addition (Fig 3). These modifications to the DenseNet architecture helped to reduce the parameter space and the GPU memory footprint without affecting the quality of the segmentation output. In addition to performing dimension reduction, the projection operation helped in learning interactions of cross-channel information<sup>13</sup> and accelerated convergence. Furthermore, the initial layer of the RID network included parallel convolutional neural network (CNN) branches that were similar to the inception module with

multiple kernels of varying receptive fields, which helped to capture view-point-dependent object variability and learn relationships between image structures at multiple scales.<sup>14</sup>

### Model Training

The RID model was trained on 2D input patches of size 64×64×3 that were extracted from each image section, with 3 channels (1 for each input image contrast). T1w, T2w, and FLAIR images were concatenated to create the 3 channels of the input. The decoder part of the network was bifurcated to generate 2 outputs: 1) synthesized virtual T1c images (vT1c) and 2) a segmentation

mask of enhancing tumor (ET). Linear and sigmoid activations were utilized for the vT1c generation and ET segmentation, respectively. The mean squared error (L2) loss assumes that the input data set consists of uncorrelated Gaussian signals. This assumption is not always true in real-world data and can result in blurry images. To create sharper output images, we optimized the RID model with the structural perception loss for the vT1c creation and the Dice loss for the ET segmentation. The structural perception loss (SPL), which is further detailed below, is a combination of L2, perception, spatial frequency, and structural similarity loss. Additionally, a separate model, referred to as the whole tumor (WT) model, was trained by using only T2w images to

segment the entire tumor by minimizing Dice loss (Fig 1B). At each stage, the RID model and the WT model were trained until convergence by using Adam optimizers with a learning rate of 0.001 on NVIDIA Tesla P40 GPUs. The tumor grades and manual ground truth annotations for the held out 125 subjects were not made available by BraTS. To facilitate the quantitative analysis and ET segmentations on the held out data set, we derived the annotations by using a model<sup>15</sup> that was trained on the same BraTS 2019 training data set.

### Structural Perception Loss

The loss function based on the mean squared error (MSE) between the pixel values of the original images and the reconstructed images is a common choice for learning. However, only using the MSE (L2 loss) results in blurry image reconstruction<sup>16</sup> with a lack of high spatial frequency components that represent edges. Therefore, in addition to the L2 loss, we used the spatial frequency loss (SFL) to emphasize the high-frequency components. Furthermore, a convolutional layer with a Laplacian filter bank as weights was added to the model to emphasize sharp features, such as edges. Perceptual and structural similarity-based (SSIM) losses were also added to improve the model's performance. We used a pretrained VGG-16 network to define perceptual loss functions that measure perceptual differences between predicted images and ground truth images.<sup>17</sup> The VGG loss network remained fixed during the training process. The model was trained to optimize the combination of all of the above losses, which we refer to as structural perception loss (SPL) for simplicity, and can be determined as follows:

$$\text{SPL} = (1 - \alpha) \cdot \text{L2} + \alpha \cdot \text{SSIM} + \beta \cdot \text{SFL} + \gamma \cdot \text{Perceptual},$$

where  $\alpha$ ,  $\beta$ , and  $\gamma$  represent the normalized contribution of each individual loss. The values were selected to give equal weights for each loss. We combine multiple similarity and error losses to obtain a smooth and realistic virtual contrast synthesis. In this study, we used  $\alpha = .5$ ,  $\beta = .5$ , and  $\gamma = .5$ . The combination of multiple loss functions can be interpreted as a form of regularization, as it constrains the search space for possible candidate solutions for the primary task.<sup>18</sup>

### Evaluation and Statistical Analysis

**Quantitative Evaluation.** Model performance was evaluated by comparing the model predicted output (vT1c) image to the ground truth T1c image. We computed the SSIM, peak signal-to-noise ratio (PSNR), and normalized mean squared error (NMSE). The PSNR measures the voxelwise difference in signal, the NMSE captures the L2 loss, and the SSIM compares the non-local structural similarity. To evaluate the algorithm's performance for a segmenting enhancing tumor, Dice scores were calculated separately for the whole brain, whole tumor, and enhancing tumor regions by using our previously developed brain tumor segmentation ensemble network.<sup>15</sup> The Dice scores of the ET segmentation were calculated without any correction for the whole brain image after skull stripping (whole brain) but with corrections for whole tumor (after removing predictions outside of the whole tumor segmentation) and ET (after

**Table 1: Quantitative evaluation. Analysis of virtual enhancement prediction by using various masks generated by an external model**

Mask	SSIM	NMSE	Dice	PSNR
Whole brain	0.91	0.03	0.32	64.35
Whole tumor	0.90	0.01	0.35	48.99
Enhancing tumor	0.90	0.01	0.62	49.93

removing predictions outside of the ET segmentation) to quantify the performance of the model in segmenting ET.

**Qualitative Evaluation.** To assess the subjective visual quality of the synthesized GBCA enhancement (vT1c), 3 board-certified neuroradiologists (FY [8 years of experience], JD [8 years of experience], and MA [6 years of experience]) rated the synthesized vT1c images by comparing them to the ground truth T1c scans. For each data set, scores were determined by taking into account the general image quality and the degree of visual conformity of the ET region to the ground truth by using a 3-point Likert scale (1 = poor, the algorithm misidentifies the presence or absence of contrast enhancement over the whole tumor volume; 2 = good, the algorithm correctly simulates the signal intensity and the regional extent of enhancement in a portion of the tumor; and 3 = excellent, the algorithm correctly simulates enhancement throughout nearly the full volume of the tumor). The interrater agreement between each rater was computed by using the Fleiss kappa for 3 scale ratings. When discrepancies arose between raters, a consensus rating was obtained through majority voting. The consensus ratings were also dichotomized into low (1) and high (2–3) ratings. The raters also examined the results of the enhancement predictions at a granular level. This included the degree of overestimation or underestimation, the location of enhancement within the tumor (peripheral or lateral), the presence of distant enhancement, the presence of any artifacts, and the overall improvement in image quality.

**Importance of the Input MR Sequences for Prediction.** To determine the contribution of different input MR imaging sequences on the prediction of the vT1c image, we tested the trained model by iteratively replacing all voxels of each input MR image with zeros while retaining the other 2 input noncontrast MR images.

## RESULTS

### Quantitative Evaluation

The T1c-ET RID model was tested on 125 held out test subjects. The average PSNR, NMSE, and SSIM for the whole brain were 64.35, 0.03, and 0.91. The whole tumor and ET regions demonstrated lower SSIM and PSNR values compared with the whole brain (Table 1). The Dice coefficients for ET on 125 validation subjects were .32, .35, and .62 for the uncorrected (whole brain), corrected for whole tumor, and corrected for ET cases, respectively. In most cases, the model was able to synthesize T1c images with well-defined enhancing regions, as shown in Fig 4. Out of the 125 subjects tested, only 13 were labeled as low performance after the consensus rating between 3 raters, resulting in an accuracy of 88.8% in synthesizing vT1c. Table 2 summarizes the quality of enhancement, the location of enhancement in the tumor



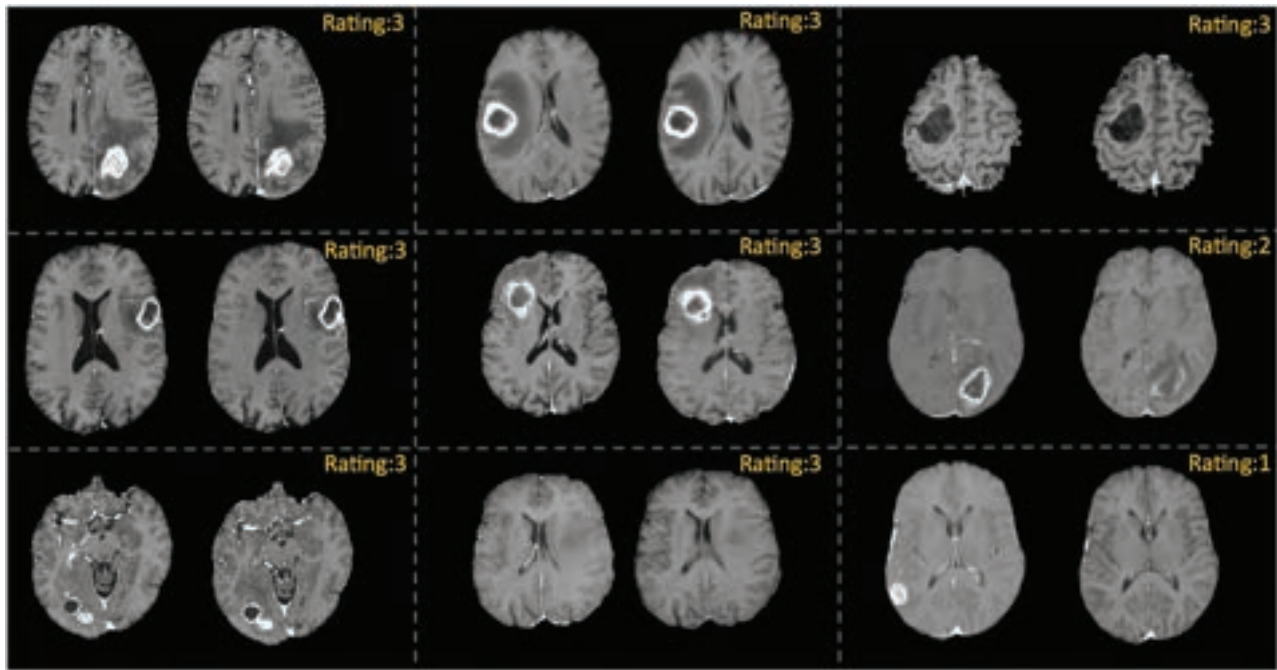


**FIG 4.** Synthesized virtual contrast enhanced T1w (vT1c) images in 3 different subjects. Ground truth (left column) and synthesized vT1c (right column) image pairs for 9 subjects.

**Table 2: Quantitative presence and location of the under/over-estimation of synthetic contrast enhancement, the introduction of artifacts, and the image quality improvement on vT1c**

	Reviewer 1 (FY)	Reviewer 2 (MA)	Reviewer 3 (JD)
Overestimate (O)	26	27	20
Underestimate (U)	71	69	58
Both (O and U)	11	8	34
Central	54	35	64
Peripheral	94	71	97
False distant enhancement	10	9	15
Missed distant enhancement	5	4	2
Artifact	17	22	25
Image quality improved	10	NA	3

**Note:**—NA indicates not applicable.

(peripheral/lateral), the prediction of distant enhancement, the presence of artifacts, and the predicted image quality improvement.

### Qualitative Evaluation

Representative images are shown in Fig 4. Comparing the synthesized vT1c images with the ground truth T1c images, 89.6% of the subjective rater scores after consensus were within the good and excellent range (Supplemental Online Data). The intraclass rater reliability of the 3 neuroradiologists was 0.61, indicating moderate interrater agreement by using the 3-point Likert scale. A consensus rating was obtained through majority voting in situations in which the raters had different scores. In cases where the 3 ratings differed, the lowest rating was taken as the consensus. After consensus, a subset of cases (11.2%, 14 cases) was rated as low, in which enhancing regions were not well-captured or were absent, compared with the ground truth T1c data (Fig 5). An example of a low-rated vT1c image is shown in Fig 4.

### Importance of the Input MR Sequences for Prediction of Contrast Enhancement

By replacing each input sequence with zeros, we were able to determine which sequences are important in the prediction of specific components of the output vT1c images. The T1w image contributes primarily structural brain information in the predicted vT1c image. The FLAIR and T2w images primarily influence the predicted contrast enhancement (Fig 6).

### DISCUSSION

We developed and trained a deep learning model utilizing a diverse multi-institutional data set that was able to synthesize vT1c images for primary brain tumors by using only noncontrast FLAIR, T2w, and T1w images. Qualitative and quantitative evaluations showed the robust performance of the model when predicting tumor enhancement. In most cases, the enhancing and nonenhancing portions of the tumors were correctly predicted.

Gong et al<sup>20</sup> developed a deep learning method to predict full-dose T1w postcontrast (T1c) images by using one-tenth of the standard GBICA dose. With respect to this prior work, our study represents an advancement by using only noncontrast sequences to predict T1c images.<sup>19</sup> Narayana et al<sup>20</sup> evaluated whether deep learning can predict enhancing demyelinating lesions on MR imaging scans that were obtained without the use of contrast material and demonstrated moderate to high accuracy in patients with multiple sclerosis. Kleesiek et al<sup>12</sup> developed a Bayesian network to predict T1c by using noncontrast T1w, T2w, FLAIR, DWI, and SWI as a 10-channel input.<sup>12</sup> Recently, Calabrese et al<sup>21</sup> conducted a study to explore the feasibility of dose-free synthesis by training 3D convolutional networks on an internal data set of 400 subjects with 8 noncontrast MR images as input and evaluating

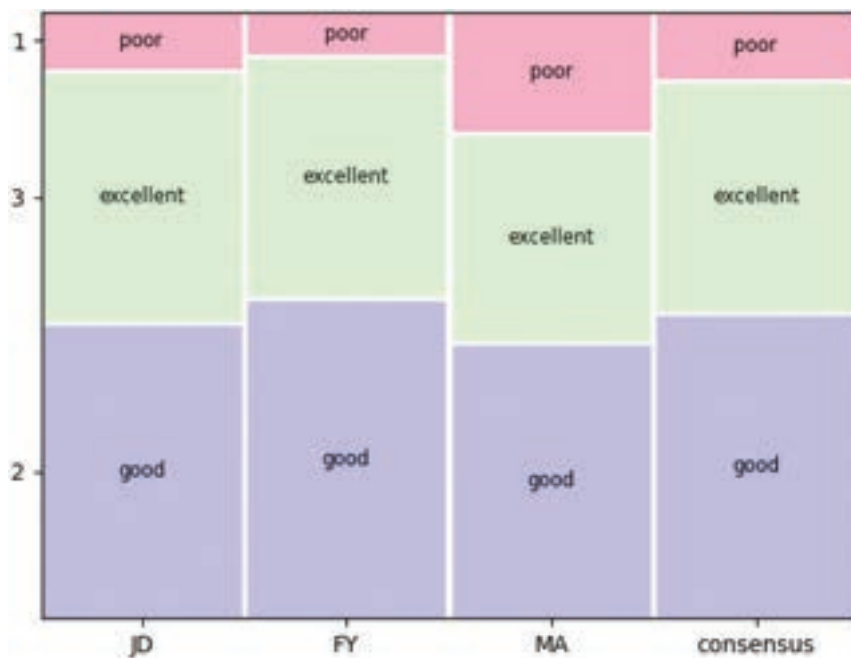


**FIG 5.** Mosaic plot illustrating the distribution of 3 expert radiologists and their consensus along a 3-point Likert scale.

the model on an external BraTS data set of 200 subjects. For quantitative evaluation, the authors employed an external model that was trained on BraTS data to generate enhancing tumor segmentation by incorporating real (T1c) and virtual contrast (vT1c) in addition to other noncontrast multiparametric MR images (T1, T2, and FLAIR). They reported that the synthesized whole brain postcontrast images exhibited both qualitative and quantitative similarity to the real postcontrast images, as indicated by quantitative metrics such as the Dice coefficients of  $0.65 \pm 0.25$  and  $0.62 \pm 0.27$  for the internal and external BraTS data sets, respectively, for the enhancing tumor compartment. In contrast, our method solely utilizes noncontrast multiparametric MR images (T1, T2, and FLAIR) to predict and segment virtual contrast enhancement, which accounts

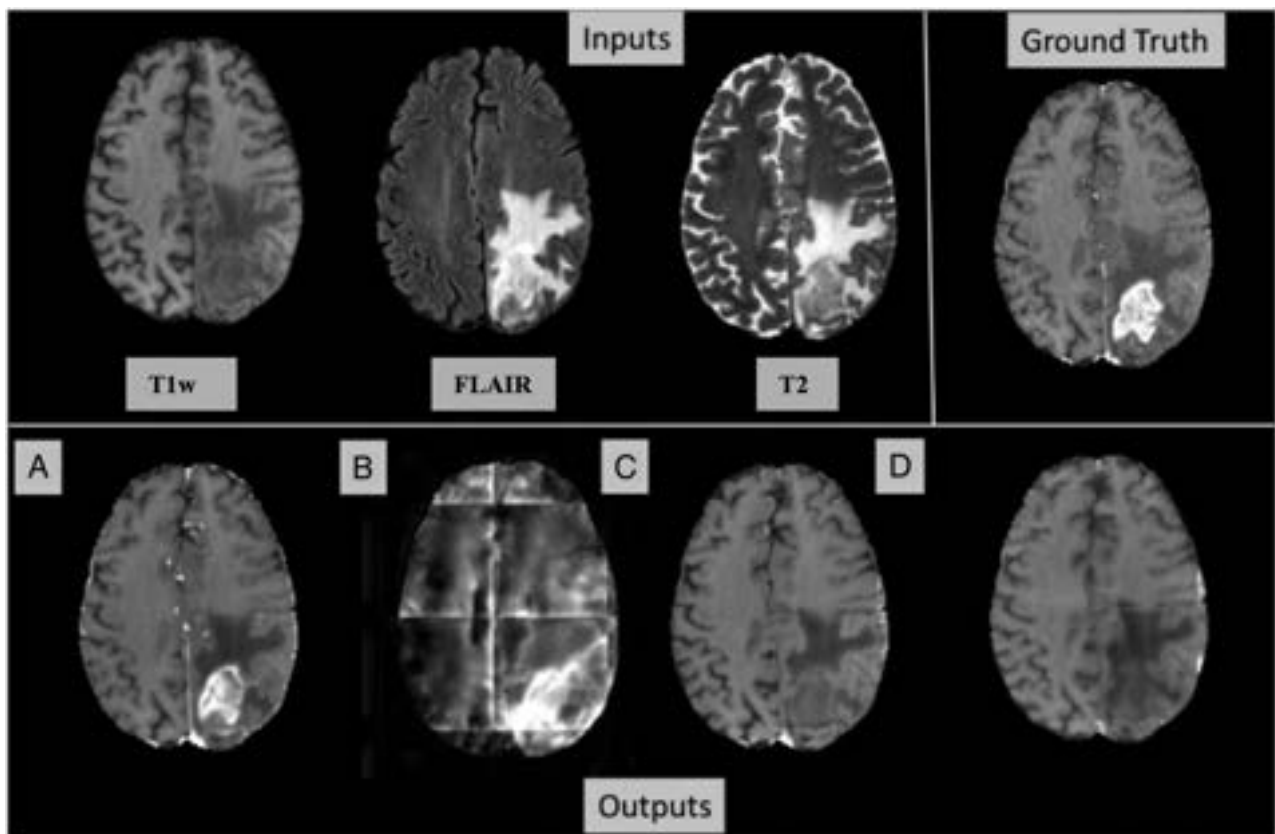


**FIG 6.** Importance of input sequences example. Top row, input images: T1w, FLAIR, T2, and the ground truth T1c. Bottom row, output images with (A) all inputs (T1w, FLAIR, and T2w) given to the model, (B) T1w replaced with zeros in the input, (C) FLAIR replaced with zeros in the input, and (D) T2 replaced with zeros in the input. The T2 and FLAIR inputs together provide contrast enhancement prediction, whereas T1w input provides primarily anatomic detail.

for the comparatively lower enhancing tumor Dice score observed for the whole brain in our study.

Our results further support this approach by demonstrating the successful prediction of enhancement in almost 90% of the testing data set. Moreover, we were able to achieve comparable results (with superior performance in quantitative metrics, including PSNR and SSIM) while utilizing notably fewer sequences (only T1w, T2w, and FLAIR images) that are standard for clinical brain imaging protocols. Furthermore, the need for fewer sequences also facilitates reduced scan times, which is an important consideration for critically ill, claustrophobic, and cognitively impaired patients.

Another advantage of our strategy included the use of a more diverse data set (BraTS) for both training and testing. Whereas prior studies utilized imaging data from a single institution, BraTS comprises data from multiple sites with variations in acquisition parameters, scanner platforms, and imaging protocols.<sup>12,19</sup> Introducing more heterogeneity to the training data set enhances the generalizability of the trained networks. Furthermore, testing on a substantially larger data set quantifies the generalizability of the model more accurately. Taken together, these result in a more generalized approach that is robust to differences in imaging hardware and software and is therefore more amenable to clinical translation.

Our analysis of the relative contributions of the input sequences revealed that the FLAIR and T2w images contributed complementary information in predicting enhancement within the tumor. This is consistent with the results presented by Kleesiek et al<sup>12</sup> who noted that T2w images were the most important for predicting contrast. FLAIR and T2w images are generally thought of as having greater contrast-to-noise for the delineation of pathology, compared with T1w images. Tissue changes that are related to disruption of the blood-brain barrier that led to or are seen in association with contrast enhancement, such as necrosis and edema, may be better delineated with these sequences. The T1w images contributed information primarily toward delineating structural details of the brain. T1w images are generally regarded as anatomic images for their ability to capture the fine anatomic details of the brain.

The T1c-ET model failed to predict gadolinium enhancement in subjects for whom 1 or more of the input sequences had a significant motion artifact and for whom the tumor was isointense to normal brain parenchyma on both T2w and FLAIR sequences (Supplemental Online Data). The failure of the model in the latter scenario may be due to an inadequate representation of tumors with these imaging features in the training set. This could be alleviated through the incorporation of additional, larger data sets for training in the future. The deterioration of image quality due to image artifacts, such as motion, could be separately addressed by either preventing them during acquisition or correcting them retrospectively.<sup>22</sup> Another potential limitation for implementation is that we used only primary brain tumor cases for the training and testing of the model. The application of the algorithm in cases of sub-centimeter brain metastases and its extension to other body parts represent exciting areas to explore in the future.

An in-depth qualitative review of the synthesized vT1c revealed that, though the enhancement accuracy is satisfactory, there is a

tendency to overestimate or underestimate the enhancement, and there is also a potential for distant enhancement. Regarding this approach, the implications of these observations and the effectiveness of radiologic/surgical decisions and survival predictions based on vT1c, compared with those of real T1c images, must be further investigated before the method can be translated into a clinical tool. Taken together, the results of the current study should be regarded as a proof-of-concept study of clinical feasibility. Future directions to augment the performance of our model include the incorporation of larger data sets and different pathologies as well as the potential acquisition of additional sequences, including rapid low-dose, low-resolution echo-planar gadolinium-enhanced images (as are used for dynamic perfusion MR imaging techniques).<sup>19</sup>

## CONCLUSIONS

We developed a novel deep learning architecture to synthesize virtual contrast-enhanced T1w images (vT1c) by using only standard clinical noncontrast multiparametric MR images. The model demonstrated good quantitative and qualitative performance in a larger and more heterogeneous data set than those used in prior studies, and showed the feasibility of gadolinium-free predictions of contrast enhancement in gliomas. FLAIR and T2w images were found to provide complementary information for predicting tumor enhancement. Further studies in larger patient data sets with different neurologic diseases are needed to fully assess the clinical applicability of this novel approach.

**Disclosure forms** provided by the authors are available with the full text and PDF of this article at [www.ajnr.org](http://www.ajnr.org).





## REFERENCES

1. Villanueva-Meyer JE, Mabray MC, Cha SJN. **Current clinical brain tumor imaging.** *Neurosurgery* 2017;81:397–415 CrossRef Medline
2. Weinreb JC, Rodby RA, Yee J, et al. **Use of intravenous gadolinium-based contrast media in patients with kidney disease: consensus statements from the American College of Radiology and the National Kidney Foundation.** *Kidney Med* 2021;3:142–50 CrossRef Medline
3. Hoggard N, Roditi GH. **T<sub>1</sub> hyperintensity on brain imaging subsequent to gadolinium-based contrast agent administration: what do we know about intracranial gadolinium deposition?** *Br J Radiol* 2017;90:20160590 CrossRef Medline
4. Wang J, Wang H, Ramsay IA, et al. **Manganese-based contrast agents for magnetic resonance imaging of liver tumors: structure-activity relationships and lead candidate evaluation.** *J Med Chem* 2018;61:8811–24 CrossRef
5. Greer JS, Wang X, Wang Y, et al. **Robust pCASL perfusion imaging using a 3D Cartesian acquisition with spiral profile reordering (CASPR).** *Magn Reson Med* 2019;82:1713–24 CrossRef Medline
6. Viswanathan S, Kovacs Z, Green KN, et al. **Alternatives to gadolinium-based metal chelates for magnetic resonance imaging.** *Chem Rev* 2010;110:2960–3018 CrossRef Medline
7. Menze BH, Jakab A, Bauer S, et al. **The multimodal brain tumor image segmentation benchmark (BRATS).** *IEEE Trans Med Imaging* 2014;34:1993–2024 CrossRef Medline
8. Bakas S, Akbari H, Sotiras A, et al. **Advancing the cancer genome atlas glioma MRI collections with expert segmentation labels and radiomic features.** *Sci Data* 2017;4:170117
9. Rohlfing T, Zahr NM, Sullivan EV, et al. **The SRI24 multichannel atlas of normal adult human brain structure.** *Hum Brain Mapp* 2010;31:798–819 CrossRef Medline

10. Bakas S, Reyes M, Jakab A, et al. **Identifying the best machine learning algorithms for brain tumor segmentation, progression assessment, and overall survival prediction in the BRATS challenge.** 2018
11. Tustison NJ, Cook PA, Klein A, et al. **Large-scale evaluation of ANTs and FreeSurfer cortical thickness measurements.** *Neuroimage* 2014;99:166–79 CrossRef Medline
12. Kleesiek J, Morshuis JN, Isensee F, et al. **Can virtual contrast enhancement in brain MRI replace gadolinium? A feasibility study.** *Invest Radiology* 2019;54:653–60 CrossRef Medline
13. Lin M, Chen Q, Yan S. **Network in network.** *arXiv preprint arXiv* 2013;1312.4400
14. Szegedy C, Liu W, Jia Y, et al. **Going deeper with convolutions.** In: *Proceedings of the IEEE/CVF Conference on Computer Vision and Pattern Recognition.* Boston, Massachusetts. June 7–12, 2015;1–9
15. Murugesan GK, Nalawade S, Ganesh C, et al. **Multidimensional and multiresolution ensemble networks for brain tumor segmentation.** In: A. Crimi, S. Bakas, eds. *Brainlesion: Glioma, Multiple Sclerosis, Stroke and Traumatic Brain Injuries.* Lecture Notes in Computer Science, vol 12658. Springer; 2021;448–57
16. Ichimura N. **Spatial frequency loss for learning convolutional autoencoders.** *arXiv* 2018;1806.02336
17. Johnson J, Alahi A, Fei-Fei L. **Perceptual losses for real-time style transfer and super-resolution.** In: B. Leibe, J. Matas, N. Sebe, M. Welling, eds. *Computer Vision.* ECCV 2016. Lecture Notes in Computer Science, vol 9906. Springer; 2016;694–711
18. BenTaieb A, Hamarneh G. **Uncertainty driven multi-loss fully convolutional networks for histopathology.** In: M. Cardoso, et al. *Intravascular Imaging and Computer Assisted Stenting, and Large-Scale Annotation of Biomedical Data and Expert Label Synthesis.* Lecture Notes in Computer Science, vol 10552. Springer; 2017;155–63
19. Gong E, Pauly JM, Wintermark M, et al. **Deep learning enables reduced gadolinium dose for contrast-enhanced brain MRI.** *J Magn Reson Imaging* 2018;48:330–40 CrossRef Medline
20. Narayana PA, Coronado I, Sujit SJ, et al. **Deep learning for predicting enhancing lesions in multiple sclerosis from noncontrast MRI.** *Radiology* 2020;294:398–404 CrossRef Medline
21. Calabrese E, Rudie JD, Rauschecker AM, et al. **Feasibility of simulated postcontrast MRI of glioblastomas and lower-grade gliomas by using three-dimensional fully convolutional neural networks.** *Radiology Artif Intell* 2021;3:e200276 CrossRef Medline
22. Duffy BA, Zhao L, Sepehrband F, Alzheimer's Disease Neuroimaging Initiative, et al. **Retrospective motion artifact correction of structural MRI images using deep learning improves the quality of cortical surface reconstructions.** *Neuroimage* 2021;230:117756 CrossRef Medline



# Imaging Biomarker for Early-Stage Alzheimer Disease: Utility of Hippocampal Histogram Analysis of Diffusion Metrics

 Hiroto Takahashi, Yoichi Takami, Shuko Takeda, Naoki Hayakawa, Tsuneo Nakajima, Yasushi Takeya,  Chisato Matsuo-Hagiya,  Atsuko Arisawa, Hiromi Rakugi, and  Noriyuki Tomiyama



## ABSTRACT

**BACKGROUND AND PURPOSE:** Biomarkers have been required for diagnosing early Alzheimer disease. We assessed the utility of hippocampal diffusion parameters for diagnosing Alzheimer disease pathology in mild cognitive impairment.

**MATERIALS AND METHODS:** Sixty-nine patients with mild cognitive impairment underwent both CSF measurement and multi-shell diffusion imaging at 3T. Based on the CSF biomarker level, patients were classified according to the presence (Alzheimer disease group,  $n = 35$ ) or absence (non-Alzheimer disease group,  $n = 34$ ) of Alzheimer disease pathology. Neurite orientation dispersion and density imaging and diffusion tensor imaging parametric maps were generated. Two observers independently created the hippocampal region of interest for calculating histogram features. Interobserver correlations were calculated. The statistical significance of intergroup differences was tested by using the Mann-Whitney U test. Logistic regression analyses, using both the clinical scale and the image data, were used to predict intergroup differences, after which group discriminations were performed.

**RESULTS:** Most intraclass correlation coefficient values were between 0.59 and 0.91. In the regions of interest of both observers, there were statistically significant intergroup differences for the left-side neurite orientation dispersion and density imaging–derived intracellular volume fraction, right-side diffusion tensor imaging–derived mean diffusivity, left-side diffusion tensor imaging–derived mean diffusivity, axial diffusivity, and radial diffusivity ( $P < .05$ ). Logistic regression models revealed that diffusion parameters contributed the most to discriminating between the groups. The areas under the receiver operating characteristic curve for the regions of interest of observers A/B were 0.69/0.68, 0.69/0.68, 0.73/0.68, 0.71/0.68, and 0.68/0.68 for the left-side intracellular volume fraction (mean), right-side mean diffusivity (mean), left-side mean diffusivity (10th percentile), axial diffusivity (10th percentile), and radial diffusivity (mean).

**CONCLUSIONS:** Hippocampal diffusion parameters might be useful for the early diagnosis of Alzheimer disease.

**ABBREVIATIONS:** AD = axial diffusivity; AzD = Alzheimer disease; FA = fractional anisotropy; ICVF = intracellular volume fraction; MCI = mild cognitive impairment; MD = mean diffusivity; NODDI = neurite orientation dispersion and density imaging; ODI = orientation dispersion index; RD = radial diffusivity; Viso = isotropic volume fraction

Identifying Alzheimer disease (AzD) at the earliest stage would offer better disease management and greater therapeutic opportunities. In this regard, great attention has been paid to the evaluation of mild cognitive impairment (MCI).<sup>1</sup> Clinically, it is difficult to exclude the presence of AzD pathologic changes

in cognitively normal subjects and also to discriminate AzD pathology that is associated with a risk of AzD development from non-AzD pathology that is related to other types of dementia in patients with MCI. Therefore, it is desirable to identify quantitative biologic markers that are specific to AzD.

Currently, the most promising biomarkers are CSF tau proteins and  $\beta$ -amyloid 42 ( $A\beta 42$ ) peptides. Of these, a tau pathology model in AzD has been suggested, and the utility of the CSF phosphorylated tau (P-tau) level has been reported as a predictor of disease progression in AzD with hippocampal atrophy.<sup>2</sup> In addition, a decreased  $A\beta 42$  level with amyloid deposition in conjunction with an elevated tau level, especially P-tau, differentiates patients with AzD from normal subjects and from patients with other neurologic conditions with high accuracy.<sup>3</sup> Previous studies have reported these changes in patients with MCI who later developed AzD.<sup>4,5</sup> Accordingly, the CSF P-tau/ $A\beta 42$  ratio might be a useful biomarker of AzD pathologic changes in MCI and

Received June 1, 2023; accepted after revision November 17.

From the Departments of Diagnostic and Interventional Radiology (H.T., C.M.-H., A.A., N.T.), Geriatric and General Medicine (Y. Takami, N.H., T.N., Y. Takeya, H.R.), Clinical Gene Therapy, Graduate School of Medicine (S.T.), Osaka University Graduate School of Medicine, Suita, Osaka, Japan; and Osaka Psychiatric Research Center (S.T.), Osaka Psychiatric Medical Center, Hirakata, Osaka, Japan.

This work was supported by the Japan Society for the Promotion of Science (JSPS) KAKENHI Grant Number JP17K16436.

Please address correspondence to Hiroto Takahashi, MD, PhD, Associate Professor, Department of Diagnostic and Interventional Radiology, Osaka University Graduate School of Medicine, 2-2 Yamadaoka, Suita, Osaka, 565-0871, Japan; e-mail: hiroto.takahashi07@gmail.com



Indicates article with online supplemental data.

<http://dx.doi.org/10.3174/ajnr.A8106>

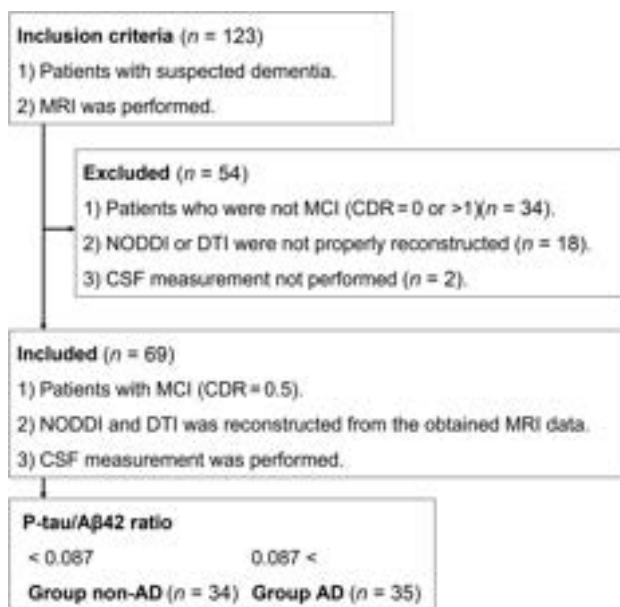


**FIG 1.** Inclusion and exclusion criteria.

might predict both the occurrence and the timing of the conversion of MCI to AzD.<sup>6,7</sup>

Previous diffusion MR imaging studies of AzD-related pathologies have applied a tensor model, termed DTI, to investigate changes in neuronal cytoarchitecture.<sup>8,9</sup> However, the common diffusion tensor model is based on the assumption of a simple underlying Gaussian diffusion process.<sup>10</sup> In contrast, the neurite orientation dispersion and density imaging (NODDI) technique uses a non-Gaussian biophysical model that has a higher sensitivity to non-monoexponential diffusion in microstructural features of the brain, such as neurite density and dendritic structure.<sup>10,11</sup> NODDI assumes a 3-compartment (intracellular, extracellular, and CSF) biophysical tissue model for each voxel, enables the detection of the microstructure of dendrites and axons, and offers greater specificity than that offered by DTI by separating the volume fraction of Gaussian isotropic diffusion, thereby representing the freely diffusing water, such as CSF, from the neural tissue.<sup>12</sup>

The greater focus on the medial temporal lobe of the brain with diffusion MR imaging improves the detection of the presence and progression of cognitive disorders, such as AzD. Functionally related regions in the medial temporal lobe, particularly the entorhinal cortex, perirhinal cortex, and parahippocampal cortex, are tightly interconnected with the hippocampus as parts of the medial temporal memory networks.<sup>13</sup> The perirhinal and entorhinal cortices are among the earliest sites of neurodegeneration in AzD.<sup>13</sup> Similarly, hippocampal subregions are variably affected by AzD pathology.<sup>14</sup> Accordingly, we hypothesized that hippocampal analysis via diffusion MR imaging could provide indirect and highly sensitive measurements of AzD pathology in MCI. Therefore, our aim was to assess the clinical application of hippocampal histogram features of diffusion metrics as imaging biomarkers for the CSF-biomarker-aided diagnosis of early-stage AzD.

## MATERIALS AND METHODS

Our Institutional Review Board approved this study, and all participants provided written informed consent.

## Patients

This study included 123 patients who were referred for an investigation of suspected dementia between February 2019 and November 2021. The patients were evaluated by neurologists by using the *Diagnostic and Statistical Manual of Mental Disorders, Fifth Edition*, and also by using the following clinical scales: the Mini-Mental State Examination, the Alzheimer's Disease Assessment Scale–Cognitive Subscale, the Rivermead Behavioral Memory Test, and the Clinical Dementia Rating.<sup>15</sup> The measurements of Aβ42 and P-tau in CSF and MR imaging examinations were performed within 5 days of the neurologic evaluations. After applying the inclusion and exclusion criteria (Fig 1), 69 patients (34 women, 35 men; age,  $78 \pm 7.90$  years) were diagnosed with MCI (defined as the 0.5 point of the Clinical Dementia Rating scale) and were included in the analysis. Based on a previous report of CSF biomarkers,<sup>6</sup> we adopted a CSF P-tau/Aβ42 ratio value of 0.087 as the cutoff value for discriminating AzD pathology from non-AzD pathology. On this basis, 34 patients were diagnosed with non-AzD pathology ( $< 0.087$ , non-AzD group), and 35 patients were diagnosed with AzD pathology ( $> 0.087$ , AzD group).

## Imaging Studies

All MR imaging studies were performed by using a 3T system (Achieva; Philips Healthcare). We adopted a 2-shell diffusion protocol for a reasonable acquisition time in routine clinical practice. Diffusion-weighted imaging was performed by using a spin-echo EPI sequence with the following parameters: TR, 9810 ms; TE, 100 ms; FOV,  $256 \times 256$  mm; acquisition matrix,  $126 \times 128$ ; section thickness, 2 mm; flip angle,  $90^\circ$ ; 2 b-values (1000 and 2000 seconds/ $\text{mm}^2$ ) with diffusion encoding in 32 isotropic diffusion gradient directions for every b-value and 1 b-value of 0 sec/ $\text{mm}^2$ ; and acquisition time, 10 min.

Three-dimensional sections of a T1-weighted magnetization-prepared rapid acquisition gradient-echo sequence were obtained in the sagittal plane. The sequence parameters were as follows: TR, 6.68 ms; TE, 3.21 ms; FOV,  $240 \times 240$  mm; acquisition matrix,  $256 \times 326$ ; section thickness, 1.2 mm; and flip angle,  $8^\circ$  with no intersection gaps, thereby enabling volumetry. In addition to these imaging approaches, axial T2-weighted imaging was performed via fast spin-echo sequences for all subjects as part of their screening or routine clinical care to confirm that there were no other structural abnormalities. The sequence parameters were as follows: TR, 3000 ms; TE, 80 ms; FOV,  $254 \times 254$  mm; acquisition matrix,  $464 \times 329$ ; section thickness, 5 mm; and flip angle,  $90^\circ$ .

## Diffusion Image Reconstruction

One neuroradiologist with 20 years of experience who was blinded to the clinical details performed all image reconstruction and analysis. All image data were exported to a computer as a DICOM file and were then converted into Neuroimaging Informatics Technology Initiative (NIFTI) format by using dcm2nii with MRICron (<https://www.nitrc.org/projects/mricron>). All image data were corrected for distortions and eddy currents by the respective TOPUP and eddy current correction procedure implemented in FMRIB Software Library 4.1.5 (FSL, [www.fmrib.ox.ac.uk/fsl](http://www.fmrib.ox.ac.uk/fsl)).<sup>16</sup> TOPUP estimates susceptibility-induced distortion

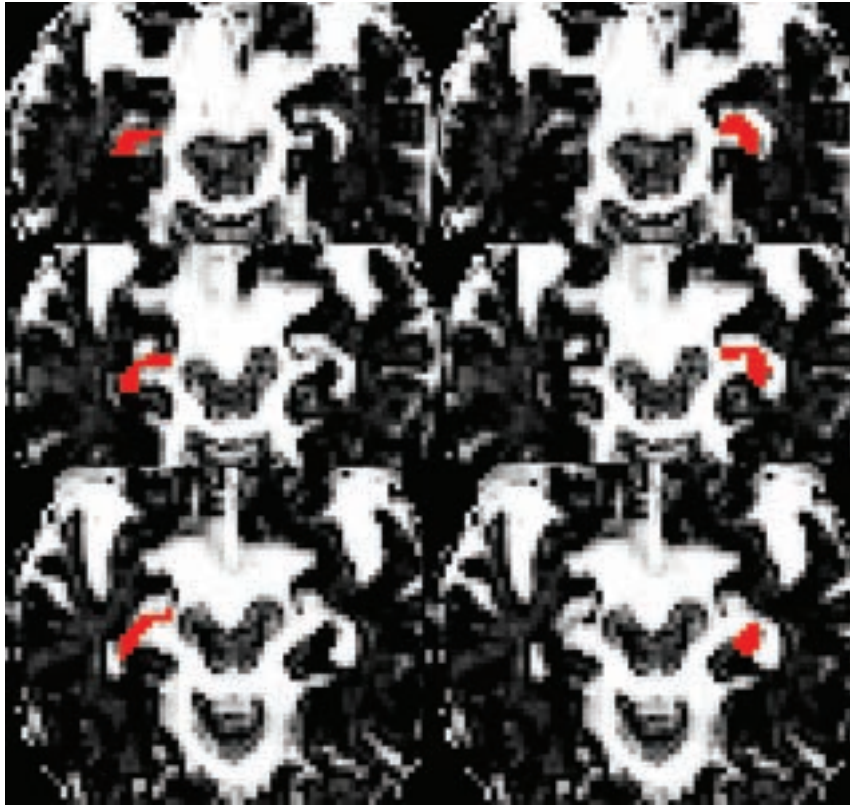


**FIG 2.** A  $b_0$  image showing the 3-section axial ROI that was created manually for each side of the hippocampus.

by extracting 2 nondiffusion-weighted images with opposed phase-encoding polarities (<http://fsl.fmrib.ox.ac.uk/fsl/fslwiki/TOPUP>).<sup>17</sup> The eddy current correction was then applied via the eddy\_correct tool (EDDY) (<http://fsl.fmrib.ox.ac.uk/fsl/fslwiki/EDDY>),<sup>18</sup> using the default settings. The resulting 2-shell diffusion-weighted data with  $b = 0, 1000$ , and  $2000$  seconds/mm<sup>2</sup> were then fitted to the NODDI model<sup>19</sup> by using the NODDI MATLAB Toolbox5 ([http://www.nitrc.org/projects/noddi\\_toolbox](http://www.nitrc.org/projects/noddi_toolbox)). Maps of the intracellular volume fraction (ICVF), orientation dispersion index (ODI), and isotropic volume fraction (Viso) were generated. Only diffusion-weighted images with  $b = 0$  and  $b = 1000$  seconds/mm<sup>2</sup> were used for DTI fitting because each of the DTI parameters of fractional anisotropy (FA), mean diffusivity (MD), axial diffusivity (AD), and radial diffusivity (RD) can be estimated by using a conventional monoexponential model.<sup>12</sup> The maps of all DTI parameters for all subjects were calculated by using the DTIFIT tool ([http://fsl.fmrib.ox.ac.uk/fsl/fsl-4.1.9/fdt/fdt\\_dtfitt.html](http://fsl.fmrib.ox.ac.uk/fsl/fsl-4.1.9/fdt/fdt_dtfitt.html)) implemented in FMRIB Software Library 4.1.5 to fit a tensor model to each voxel of the diffusion-weighted image data.

### ROI Analysis

The hippocampal ROI for each side was created manually as a 3-section axial ROI drawn in the hippocampus on the  $b = 0$  image by 2 neuroradiologist observers (observer A and observer B) with 10 and 15 years of experience, respectively, who were blinded to the research plan (Fig 2). An ROI was set, and diffusion parameter values were measured for both the left and right hippocampus by using commercially available software

(NordicICE v3.3.12; Nordic Imaging Lab). The features from the histogram of the DTI-derived and NODDI-derived diffusion parameters were calculated from the ROI pixel values by using commercially available software (SPSS Statistics for Windows, version 27.0; IBM and Excel for Windows, version 2019, Microsoft). The histogram features were defined as minimum, maximum, mean, standard deviation, distribution, skewness, kurtosis, and the 10th and 90th percentiles.

### Volumetry

The hippocampal volume of each side was calculated from 3D volume T1-weighted image data that were acquired via conventional volumetric imaging techniques. In a preprocessing step, the 3D volume images were exported as a DICOM file and were then converted into NIfTI format by using the dcm2nii tool with MRICron (<https://www.nitrc.org/projects/mricron>). The automated reconstruction and estimation of the volume for the hippocampus were performed on the preprocessed 3D T1 volume image data by using the

FreeSurfer image analysis suite, version 7.1.1 (<http://surfer.nmr.mgh.harvard.edu>).<sup>20</sup>

### Statistical Analysis

All statistical analyses were performed by using commercially available software (SPSS Statistics for Windows, version 27.0). Two-sided  $P$  values of less than .05 were considered to be indicative of a statistically significant result. The statistical significance of intergroup differences in the clinical data was tested by using a 2-tailed Mann-Whitney U test. Correlations between the diffusion parameter values (mean) of the interobservers' ROIs were calculated for the intraclass correlation coefficients. For the histogram features of the diffusion parameter values and volume, the statistical significance of the intergroup differences on each side of the hippocampus was tested by using a 2-tailed Mann-Whitney U test. Additionally, multiple comparisons with an analysis of variance were performed to assess the histogram features of the diffusion parameter values of 4 data sets, including the groups with each 2 observers' ROIs, as an exploratory analysis. The histogram features that showed  $P$  values of less than .05 and that were the lowest among the features of each NODDI and DTI parameter for identifying the statistical significance of the intergroup differences were then selected to set up logistic regression models. The image data, age, sex, and clinical scale were used to assess performance for discriminating between the groups. The logistic regression model aimed to predict a transformation of the logit ( $p$ ) of the response variable that was used. We assumed that  $P$  represented the probability that the diagnosis was AzD pathology and that  $1 - P$



**Table 1: Detailed demographic and clinical data of patients with MCI**

Group	non-AzD	AzD
Number	34	35
Age (Median $\pm$ SD)	78 $\pm$ 9.15	79 $\pm$ 6.58
Sex (M:F)	18:16	17:18
MMSE (Median $\pm$ SD)	26 $\pm$ 5.09	24 $\pm$ 3.81
ADAS-Cog (Median $\pm$ SD)	9.40 $\pm$ 6.91 <sup>a</sup>	11.60 $\pm$ 4.19 <sup>a</sup>
RBMT (Median $\pm$ SD)	11 $\pm$ 6.38 <sup>a</sup>	6.5 $\pm$ 4.99 <sup>a</sup>
P-tau/A $\beta$ 42 ratio	0.05 $\pm$ 0.01	0.18 $\pm$ 0.07
A $\beta$ 42 (pg/mL)	919.38 $\pm$ 323.78 <sup>a</sup>	554.94 $\pm$ 148.24 <sup>a</sup>
P-tau (pg/mL)	46.47 $\pm$ 15.36 <sup>a</sup>	91.37 $\pm$ 28.69 <sup>a</sup>

**Note:**—MMSE indicates Mini-Mental State Examination; ADAS-Cog, Assessment Scale—Cognitive Subscale; RBMT, Rivermead Behavioral Memory Test; A $\beta$ 42,  $\beta$ -amyloid 42; P-tau, phosphorylated tau.

<sup>a</sup>Statistically significant difference between the groups ( $P < .05$ ).

represented the probability that the diagnosis was non-AzD pathology. The logistic regression model enables the prediction of the probability of AzD pathology in relation to the clinical scale and the image data by using the following equation:

$$\text{logit}(p) = \beta_0 + \beta_1 \times \text{the image data} + \beta_2 \times \text{the scale},$$

where  $\beta_0$  is the intercept term and  $\beta_1$  and  $\beta_2$  are the coefficients in the model that are associated with the image data and the clinical scale. We assumed that these data were linearly related to the log odds of the response. The odds ratio for discriminating between the groups can be estimated as the exponentiation of the associated coefficient in the model. The performance of logit ( $p$ ) for the group discrimination was assessed via a receiver operating characteristic analysis. Additionally, in both groups, the correlations between the diffusion parameter values (mean) in each observer's ROIs and the volumes were assessed by using the Pearson correlation coefficient.

## RESULTS

### Participant Demographics

The detailed demographic and clinical data for each group are listed in Table 1. The diagnoses in the non-AzD group were vascular cognitive impairment ( $n = 6$ ), normal pressure hydrocephalus ( $n = 5$ ), frontotemporal degeneration ( $n = 1$ ), and depression ( $n = 1$ ). The diagnoses were not confirmed in 21 cases, including the suspicious cases: argyrophilic grain disease ( $n = 1$ ), dementia with Lewy bodies ( $n = 1$ ), and frontotemporal degeneration ( $n = 1$ ).

There was no significant difference in Mini-Mental State Examination between the groups, whereas the Alzheimer's Disease Assessment Scale—Cognitive Subscale scale was significantly higher in the AzD group than in the non-AzD group, and the Rivermead Behavioral Memory Test scale was significantly lower in the AzD group than in the non-AzD group.

### Hippocampal Values

The intraclass correlation coefficients of the diffusion parameter values (mean) are shown in Table 2. The intraclass correlation coefficients of almost all diffusion parameter values were 0.59–0.91, besides the Viso values (0.12 and 0.07). Table 3 lists the diffusion parameter values that showed significant intergroup differences in both observers' hippocampal ROIs and the volumes of each side of the hippocampus. All results are shown in the Online

**Table 2: ICCs<sup>a</sup> of the left and right hippocampal ROI values**

	Left	Right
	ICC	ICC
NODDI		
ICVF (mean)	0.87 (0.65–0.94)	0.91 (0.86–0.94)
Viso (mean)	0.07 (–0.06–0.23)	0.12 (–0.07–0.31)
ODI (mean)	0.70 (0.36–0.85)	0.74 (0.52–0.85)
DTI		
FA (mean)	0.68 (0.53–0.79)	0.59 (0.41–0.72)
MD (mean)	0.86 (0.40–0.95)	0.84 (0.69–0.91)
AD (mean)	0.82 (0.31–0.93)	0.84 (0.39–0.94)
RD (mean)	0.77 (0.53–0.88)	0.84 (0.65–0.92)

**Note:**—ICCs indicates intraclass correlation coefficient.

<sup>a</sup>The data in parentheses are 95% confidence intervals.

Supplemental Data. Compared with those in the non-AzD group, the ICVF values of the left hippocampus (mean and 90th percentile) were significantly lower, and the MD value of the right hippocampus (mean), the MD and AD values of the left hippocampus (mean, 10th and 90th percentiles), and the RD value of the left hippocampus (minimum, mean, and 90th percentile) were significantly higher in the AzD group. The hippocampal volumes were significantly lower bilaterally in the AzD group than in the non-AzD group. Multiple comparisons showed no statistically significant intergroup differences in both observers' hippocampal ROIs, and the diffusion parameter values that showed statistically significant intergroup differences are shown in the Online Supplemental Data. The Online Supplemental Data lists the raw data of some representative diffusion parameters.

### Performance for the Diagnosis of the AzD Pathology in MCI

The receiver operating characteristic analysis quantified the performance of the logistic regression model, showing the statistically significant intergroup differences with the least  $P$  values among the histogram feature values of each parameter (Fig 3). The respective areas under the receiver operating characteristic curve of logit ( $p$ ) and the odds ratios of the variables in each logistic regression model are listed in Table 4. In the respective ROIs made by observer A and observer B, the areas under the curve for ICVF (mean) of the left hippocampus were 0.69 and 0.68, those for the MD (mean) of the right hippocampus were 0.69 and 0.68, those for the MD (10th percentile) of the left hippocampus were 0.73 and 0.68, those for the AD (10th percentile) of the left hippocampus were 0.71 and 0.68, those for the RD (mean) of the left hippocampus were 0.68 and 0.68, and those for the volume of the left and right hippocampus were 0.67 and 0.68. Among the variables in the entire logistic regression model, the diffusion parameters contributed the most, whereas volume contributed the least, according to the odds ratio.

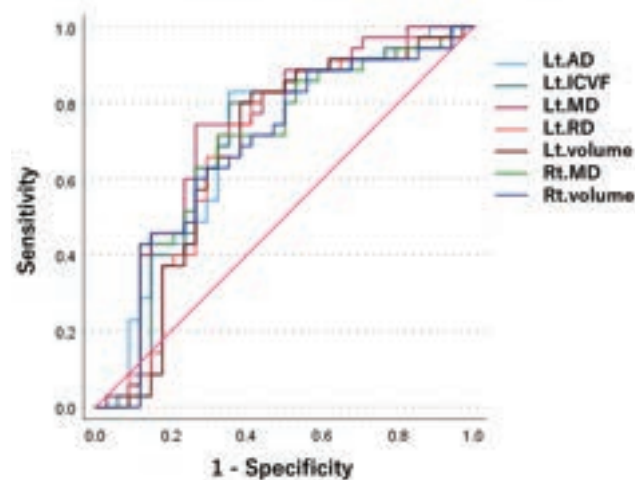
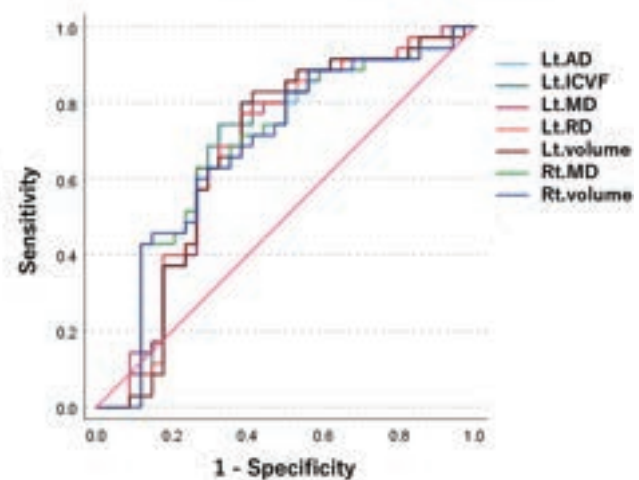
### Correlations between the Hippocampal Values

Heat maps of the correlations among the diffusion parameters and the volume of the left hippocampus in the AzD group are shown in Fig 4. Other heat maps are provided in the Online Supplemental Data. There were many significant correlations among the diffusion parameter values (mean) and volumes in both groups. In detail, the ICVF values were highly correlated with each of the MD, AD, and RD values ( $R$  absolute value greater than 0.55). The ODI value was highly correlated with the FA value ( $R$  absolute value greater than 0.45). Each of the ICVF, MD, AD, and RD



**Table 3: Statistically significant intergroup differences ( $P < .05$ ) in the left and right hippocampal ROI values**

	Hippocampal ROI (Observer A)			Hippocampal ROI (Observer B)		
	Value (Mean $\pm$ Standard Deviation)		P Value	Value (Mean $\pm$ Standard Deviation)		P Value
	non-AzD	AzD		non-AzD	AzD	
NODDI parameter						
Left ICVF (dimensionless)						
Mean	0.377 $\pm$ 0.032	0.358 $\pm$ 0.031	.008	0.366 $\pm$ 0.033	0.349 $\pm$ 0.033	.026
90th percentile	0.474 $\pm$ 0.041	0.452 $\pm$ 0.047	.032	0.469 $\pm$ 0.093	0.438 $\pm$ 0.049	.029
DTI parameter						
Right MD (mm <sup>2</sup> /s)						
Mean	0.699 $\pm$ 0.030	0.715 $\pm$ 0.031	.022	0.707 $\pm$ 0.031	0.723 $\pm$ 0.030	.046
Left MD (mm <sup>2</sup> /s)						
Mean	0.706 $\pm$ 0.033	0.726 $\pm$ 0.034	.004	0.721 $\pm$ 0.038	0.739 $\pm$ 0.039	.014
10th percentile	0.641 $\pm$ 0.032	0.666 $\pm$ 0.032	.001	0.658 $\pm$ 0.035	0.676 $\pm$ 0.039	.011
90th percentile	0.769 $\pm$ 0.042	0.787 $\pm$ 0.040	.029	0.787 $\pm$ 0.058	0.803 $\pm$ 0.047	.026
Left AD (mm <sup>2</sup> /s)						
Mean	0.790 $\pm$ 0.035	0.812 $\pm$ 0.036	.002	0.809 $\pm$ 0.043	0.829 $\pm$ 0.039	.008
10th percentile	0.716 $\pm$ 0.033	0.739 $\pm$ 0.036	.001	0.733 $\pm$ 0.038	0.753 $\pm$ 0.040	.003
90th percentile	0.869 $\pm$ 0.045	0.887 $\pm$ 0.042	.037	0.894 $\pm$ 0.069	0.912 $\pm$ 0.051	.039
Left RD (mm <sup>2</sup> /s)						
Minimum	0.531 $\pm$ 0.053	0.556 $\pm$ 0.053	.028	0.543 $\pm$ 0.076	0.564 $\pm$ 0.066	.044
Mean	0.663 $\pm$ 0.033	0.682 $\pm$ 0.034	.006	0.676 $\pm$ 0.036	0.697 $\pm$ 0.047	.013
90th percentile	0.730 $\pm$ 0.040	0.747 $\pm$ 0.038	.038	0.745 $\pm$ 0.054	0.771 $\pm$ 0.076	.027
Volume (mm <sup>3</sup> )						
Left	3148.913 $\pm$ 519.884	2872.464 $\pm$ 488.542	.006			
Right	3236.159 $\pm$ 438.547	3015.669 $\pm$ 423.202	.017			

**Observer A's ROI-derived diffusion parameter values****Observer B's ROI-derived diffusion parameter values****FIG 3.** Receiver operating characteristic curve of each logistic regression model for each diffusion parameter and volumetry. The diffusion parameter values are from the ROIs of each of observer A and observer B.

values was significantly correlated with the volume (R absolute value greater than 0.35). The Viso value and the volume were weakly correlated (not statistically significant) in the AzD group (R absolute values mostly around 0.30), compared with those of the non-AzD group (R absolute values around 0.01–0.10).

## DISCUSSION

The present findings indicate that, in addition to the clinical scale, quantitative biomarkers are needed for diagnosing AzD pathology in MCI. In terms of cognitive symptoms, the Mini-Mental State Examination score showed no statistically significant difference between the MCI groups, whereas both the Alzheimer's Disease

Assessment Scale–Cognitive Subscale and Rivermead Behavioral Memory Test scores showed statistically significant intergroup differences. However, in both groups, neither the Mini-Mental State Examination score nor the Rivermead Behavioral Memory Test score met the cutoff value for cognitive decline. Alzheimer's Disease Assessment Scale–Cognitive Subscale is commonly used for follow-up studies.<sup>21</sup>

The diffusion metrics showed that hippocampal neurodegeneration was more frequent in patients with MCI with AzD pathology than in patients without AzD pathology. Our results revealed leftward lateralization in hippocampal neurodegeneration. Tau positron emission tomography studies showed leftward

**Table 4: The logistic regression model used in the prediction of the intergroup differences**

	AUC <sup>a</sup>	Odds Ratio				
	Logit (p)	Diffusion Parameter	Volume	Age/Sex	MMSE/ADAs-Cog/RBMT	Intercept Term
NODDI parameter						
Left ICVF (mean)						
Observer A	0.69 (0.56–0.82)	0.00	1.00	0.91/1.71	1.19/1.00/0.81	20682.03
Observer B	0.68 (0.55–0.81)	0.00	1.00	0.91/1.79	1.19/1.02/0.82	3487.07
DTI parameter						
Right MD (mean)						
Observer A	0.69 (0.56–0.82)	159.68	1.00	0.91/1.73	1.19/1.01/0.82	35.23
Observer B	0.68 (0.55–0.81)	31.01	1.00	0.91/1.69	1.17/1.00/0.82	238.04
Left MD (10th percentile)						
Observer A	0.73 (0.61–0.85)	199854741945.31	1.00	0.91/2.08	1.22/1.02/0.79	0.00
Observer B	0.68 (0.55–0.81)	126.30	1.00	0.91/1.91	1.19/1.02/0.82	8.02
Left AD (10th percentile)						
Observer A	0.71 (0.58–0.83)	42437669.81	1.00	0.92/2.05	1.20/1.01/0.80	0.00
Observer B	0.68 (0.55–0.81)	47.98	1.00	0.91/1.93	1.19/1.02/0.82	11.89
Left RD (mean)						
Observer A	0.68 (0.55–0.81)	128.06	1.00	0.91/1.92	1.18/1.01/0.82	11.57
Observer B	0.68 (0.54–0.81)	46.62	1.00	0.91/1.87	1.18/1.01/0.82	26.58
Volume						
Left	0.67 (0.54–0.81)	NA	1.00	0.91/1.95	1.18/1.01/0.82	543.73
Right	0.68 (0.55–0.81)	NA	1.00	0.91/1.72	1.17/1.01/0.82	4849.30

**Note:**—AUC indicates area under the receiver operating characteristic curve; MMSE, Mini-Mental State Examination; ADAS-Cog, Assessment Scale—Cognitive Subscale; RBMT, Rivermead Behavioral Memory Test; NA, not applicable.

<sup>a</sup>The data in parentheses are 95% confidence intervals.

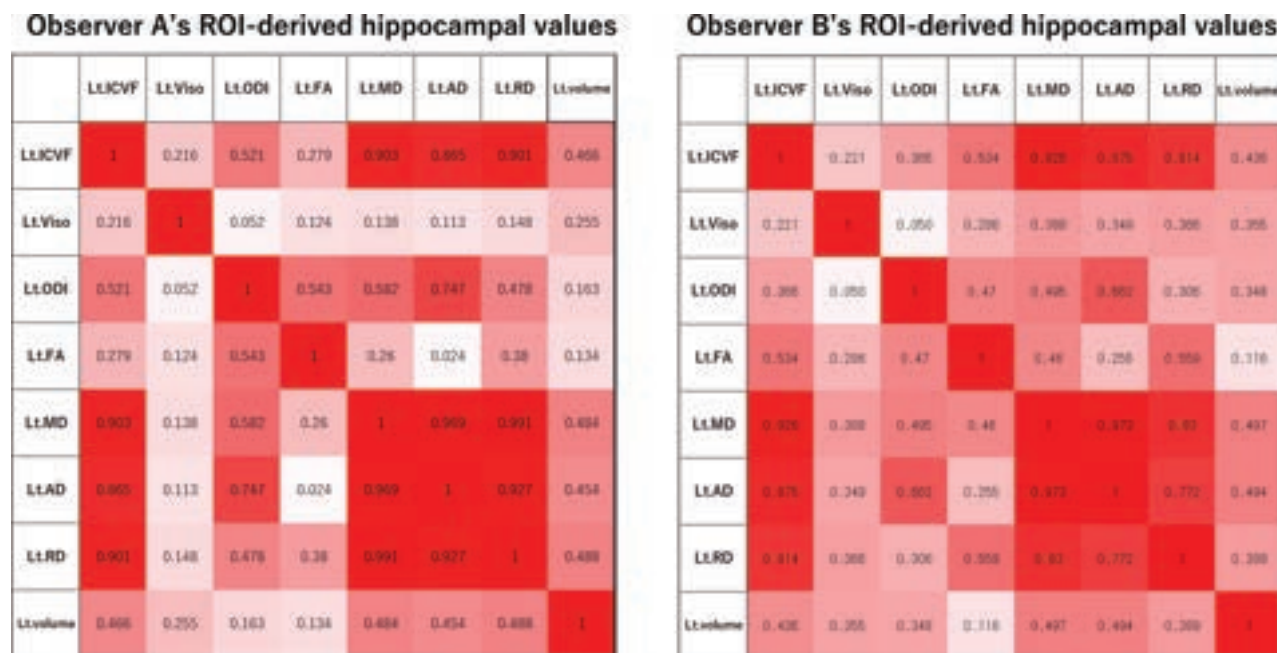


**FIG 4.** R absolute value ( $|R|$ ) of the left hippocampal values in the AzD group. Heat map of the correlations between the diffusion metrics and the volume. Values of  $0.34 < |R| < 0.43$  indicate a statistically significant difference with  $P < .05$ . Values of  $0.43 < |R|$  indicate a statistically significant difference with  $P < .01$ .

uptake in the medial temporal region, which is consistent with the Braak stage.<sup>22,23</sup> However, subject selection bias might have affected our results. Subjects with cognitive symptoms were recruited to the study, and leftward hippocampal neurodegeneration tends to induce cognitive symptoms.<sup>24</sup>

The present findings revealed a statistically significant intergroup difference in hippocampal neuron microstructure. In detail, in the left hippocampus, the ICVF values were statistically

significantly lower, whereas the MD, AD, and RD values were statistically significantly higher, in the AzD group than in the non-AzD group. Only the MD value was statistically significantly higher in the right hippocampus. In contrast, the ODI and FA values showed little intergroup difference in the bilateral hippocampus. A previous diffusion MR imaging study reported that the NODDI model was sensitive to neurodegeneration, displaying higher ODI and lower ICVF values in patients with MCI compared with

healthy controls; however, the DTI model was more sensitive.<sup>25</sup> In the DTI model, FA is limited in estimating pathologic changes because of its nonspecific changes.<sup>26</sup> The NODDI model helps to interpret changes in FA; in particular, it allows for the assessment of neurite density, using the ODI and ICVF values of nerve fibers as 2 key variables.<sup>12</sup> In contrast, our results revealed that ODI highly correlates with FA and that ODI and FA showed almost the same values between the AzD and non-AzD pathologies. These results indicate that there is a greater change in neurite density than in neurite projections in the hippocampi of patients with AzD pathology, compared with patients with non-AzD pathology. As the hippocampal structure atrophies with neurodegeneration, the space generally becomes occupied by CSF. The ability of NODDI to remove the effect of neurodegeneration-derived CSF contamination increases its specificity for cytoarchitecture.<sup>27</sup> The present finding of no statistically significant difference in Viso between the AzD and non-AzD groups indicates only a small effect of hippocampal neurodegeneration-derived CSF contamination on the performance of diffusion metrics. Meanwhile, there was a stronger negative correlation between the hippocampal volume and the Viso value in the AzD group than in the non-AzD group, which indicates that hippocampal neurodegeneration is greater in patients with AzD pathology. Accordingly, we consider that NODDI-derived neuronal density and DTI-derived diffusivity are similar and that both play an important role in the diagnosis of AzD pathology in MCI.

Both amyloid burden with a decreased CSF A $\beta$ 42 level and neurofibrillary tangle burden with an elevated CSF P-tau level might affect the measurements of diffusion metrics in patients with AzD pathology. During the preclinical progression of amyloid deposition, a weaker diffusion restriction at a higher burden has been reported in both gray matter and white matter.<sup>28,29</sup> A previous study using a tau pathology mouse model reported both a positive correlation between increased MD and tau density in gray matter regions, indicating disruption to the cytoarchitecture, and a negative correlation between the hippocampal volume and neurofibrillary tangle density, indicating a strong link between neurofibrillary tangle formation and hippocampal atrophy.<sup>30</sup> Accordingly, measuring neuronal density and volume can be sensitive to neurodegeneration in patients with AzD pathology. Meanwhile, based on the logistic regression model, we consider that diffusion metrics contribute considerably to the diagnostic process for AzD pathology in patients with MCI. Previous studies have reported that hippocampal diffusivity changes were better than the hippocampal volume for diagnosing MCI or predicting conversion from MCI to AzD, which is consistent with our outcome.<sup>31</sup>

There are some limitations to the present study. First, the group of non-AzD pathology included cases of MCI that were not clinically confirmed. However, the group discrimination based on the CSF biomarker level was performed mainly for the diagnosis of AzD pathology in MCI. Second, the hippocampal ROIs were drawn on b0 maps, which are inherently low resolution. Therefore, it is unclear whether the average ROI pixel value was contaminated by adjacent CSF pixel values in the diffusion metrics. According to the high interobserver correlation in the ROI values of the diffusion metrics for quantifying neuronal structures, we believe that the effect of free water diffusion in the

CSF space within each ROI was small. Meanwhile, we consider that the increase of the diffusion image resolution can reduce the CSF contamination in the hippocampal ROI and thereby improve the ability to quantify neuronal structure changes. Finally, given the small sample size, the present study is relatively underpowered to produce strong statistics; therefore, multiple comparisons were performed as an exploratory analysis.

## CONCLUSIONS

Logistic regression analysis, by using both clinical information and the hippocampal image data, revealed that diffusion parameters contributed the most to the CSF-biomarker-aided diagnosis of AzD pathology in MCI, and hippocampal histogram analysis of diffusion metrics might provide additional suitable biomarkers for the diagnosis of early-stage AzD.

**Disclosure forms** provided by the authors are available with the full text and PDF of this article at [www.ajnr.org](http://www.ajnr.org).

## REFERENCES

- Petersen RC. **Clinical practice. Mild cognitive impairment.** *N Engl J Med* 2011;364:2227–34 CrossRef Medline
- Henneman WJP, Vrenken H, Barnes J, et al. **Baseline CSF p-tau levels independently predict progression of hippocampal atrophy in Alzheimer disease.** *Neurology* 2009;73:935–40 CrossRef Medline
- Blennow K, Hampel H. **CSF markers for incipient Alzheimer's disease.** *Lancet Neurol* 2003;2:605–13 CrossRef Medline
- Herukka SK, Hallikainen M, Soininen H, et al. **CSF A $\beta$ 42 and tau or phosphorylated tau and prediction of progressive mild cognitive impairment.** *Neurology* 2005;64:1294–97 CrossRef Medline
- Hansson O, Zetterberg H, Buchhave P, et al. **Association between CSF biomarkers and incipient Alzheimer's disease in patients with mild cognitive impairment: a follow-up study.** *Lancet Neurol* 2006;5:228–34 CrossRef Medline
- Tapiola T, Alafuzoff I, Herukka SK, et al. **Cerebrospinal fluid  $\beta$ -amyloid 42 and tau proteins as biomarkers of Alzheimer-type pathologic changes in the brain.** *Arch Neurol* 2009;66:382–89 CrossRef Medline
- Santangelo R, Masserini F, Agosta F, et al. **CSF p-tau/A $\beta$ 42 ratio and brain FDG-PET may reliably detect MCI "imminent" converters to AD.** *Eur J Nucl Med Mol Imaging* 2020;47:3152–64 CrossRef Medline
- Assaf Y, Pasternak O. **Diffusion tensor imaging (DTI)-based white matter mapping in brain research: a review.** *J Mol Neurosci* 2008;34:51–61 CrossRef Medline
- Horsfield MA, Jones DK. **Applications of diffusion-weighted and diffusion tensor MRI to white matter diseases—a review.** *NMR Biomed* 2002;15:570–77 CrossRef Medline
- Alexander DC, Barker GJ, Arridge SR. **Detection and modeling of non-Gaussian apparent diffusion coefficient profiles in human brain data.** *Magn Reson Med* 2002;48:331–40 CrossRef Medline
- Syková E, Nicholson C. **Diffusion in brain extracellular space.** *Physiol Rev* 2008;88:1277–340 CrossRef Medline
- Zhang H, Schneider T, Wheeler-Kingshott CA, et al. **NODDI: practical in vivo neurite orientation dispersion and density imaging of the human brain.** *Neuroimage* 2012;61:1000–16 CrossRef Medline
- Yushkevich PA, Pluta JB, Wang H, et al. **Automated volumetry and regional thickness analysis of hippocampal subfields and medial temporal cortical structures in mild cognitive impairment.** *Hum Brain Mapp* 2015;36:258–87 CrossRef Medline
- Yassa MA, Stark CEL. **Pattern separation in the hippocampus.** *Trends Neurosci* 2011;34:515–25 CrossRef Medline
- O'Bryant SE, Lacritz LH, Hall J, et al. **Validation of the new interpretive guidelines for the clinical dementia rating scale sum of boxes score in the national Alzheimer's coordinating center database.** *Arch Neurol* 2010;67:746–49 CrossRef Medline

16. Jenkinson M, Beckmann CF, Behrens TE, et al. **FSL**. *Neuroimage* 2012;62:782–90 CrossRef Medline
17. Andersson JL, Skare S, Ashburner J. **How to correct susceptibility distortions in spin-echo echo-planar images: application to diffusion tensor imaging**. *Neuroimage* 2003;20:870–88 CrossRef Medline
18. Smith SM, Jenkinson M, Woolrich MW, et al. **Advances in functional and structural MR image analysis and implementation as FSL**. *Neuroimage* 2004;23 Suppl 1:S208–19 CrossRef Medline
19. Basser PJ, Mattiello J, LeBihan D. **Estimation of the effective self-diffusion tensor from the NMR spin echo**. *J Magn Reson B* 1994;103:247–54 CrossRef Medline
20. Fischl BFS. **FreeSurfer**. *Neuroimage* 2012;62:774–81 CrossRef Medline
21. Rosen WG, Mohs RC, Davis KL. **A new rating scale for Alzheimer's disease**. *Am J Psychiatry* 1984;141:1356–64 CrossRef Medline
22. Johnson KA, Schultz A, Betensky RA, et al. **Tau positron emission tomographic imaging in aging and early Alzheimer disease**. *Ann Neurol* 2016;79:110–19 CrossRef Medline
23. Cho H, Choi JY, Lee HS, et al. **Progressive tau accumulation in Alzheimer disease: 2-year follow-up study**. *J Nucl Med* 2019;60:1611–21 CrossRef Medline
24. Duara R, Loewenstein DA, Potter E, et al. **Pre-MCI and MCI: neuropsychological, clinical, and imaging features and progression rates**. *Am J Geriatr Psychiatry* 2011;19:951–60 CrossRef Medline
25. Wen Q, Mustafi SM, Li J, et al. **White matter alterations in early-stage Alzheimer's disease: a tract-specific study**. *Alzheimers Dement (Amst)* 2019;11:576–87 CrossRef Medline
26. Pierpaoli C, Basser PJ. **Toward a quantitative assessment of diffusion anisotropy**. *Magn Reson Med* 1996;36:893–906 CrossRef Medline
27. Colgan N, Siow B, O'Callaghan JM, et al. **Application of neurite orientation dispersion and density imaging (NODDI) to a tau pathology model of Alzheimer's disease**. *Neuroimage* 2016;125:739–44 CrossRef Medline
28. Montal V, Vilaplana E, Alcolea D, et al. **Cortical microstructural changes along the Alzheimer's disease continuum**. *Alzheimers Dement* 2018;14:340–51 CrossRef Medline
29. Wolf D, Fischer FU, Scheurich A, Alzheimer's Disease Neuroimaging Initiative, et al. **Non-linear association between cerebral amyloid deposition and white matter microstructure in cognitively healthy older adults**. *J Alzheimers Dis* 2015;47:117–27 CrossRef Medline
30. Wells JA, O'Callaghan JM, Holmes HE, et al. **In vivo imaging of tau pathology using multi-parametric quantitative MRI**. *Neuroimage* 2015;111:369–78 CrossRef Medline
31. Weston PS, Simpson IJ, Ryan NS, et al. **Diffusion imaging changes in grey matter in Alzheimer's disease: a potential marker of early neurodegeneration**. *Alzheimers Res Ther* 2015;7:47 CrossRef



# Prediction of Surgical Outcomes in Normal Pressure Hydrocephalus by MR Elastography

Pragalv Karki, Matthew C. Murphy, Petrice M. Cogswell, Matthew L. Senjem, Jonathan Graff-Radford, Benjamin D. Elder, Avital Perry, Christopher S. Graffeo, Fredric B Meyer, Clifford R. Jack, Jr., Richard L. Ehman, and John Huston III



## ABSTRACT

**BACKGROUND AND PURPOSE:** Normal pressure hydrocephalus is a treatable cause of dementia associated with distinct mechanical property signatures in the brain as measured by MR elastography. In this study, we tested the hypothesis that specific anatomic features of normal pressure hydrocephalus are associated with unique mechanical property alterations. Then, we tested the hypothesis that summary measures of these mechanical signatures can be used to predict clinical outcomes.

**MATERIALS AND METHODS:** MR elastography and structural imaging were performed in 128 patients with suspected normal pressure hydrocephalus and 44 control participants. Patients were categorized into 4 subgroups based on their anatomic features. Surgery outcome was acquired for 68 patients. Voxelwise modeling was performed to detect regions with significantly different mechanical properties between each group. Mechanical signatures were summarized using pattern analysis and were used as features to train classification models and predict shunt outcomes for 2 sets of feature spaces: a limited 2D feature space that included the most common features found in normal pressure hydrocephalus and an expanded 20-dimensional (20D) feature space that included features from all 4 morphologic subgroups.

**RESULTS:** Both the 2D and 20D classifiers performed significantly better than chance for predicting clinical outcomes with estimated areas under the receiver operating characteristic curve of 0.66 and 0.77, respectively ( $P < .05$ , permutation test). The 20D classifier significantly improved the diagnostic OR and positive predictive value compared with the 2D classifier ( $P < .05$ , permutation test).

**CONCLUSIONS:** MR elastography provides further insight into mechanical alterations in the normal pressure hydrocephalus brain and is a promising, noninvasive method for predicting surgical outcomes in patients with normal pressure hydrocephalus.

**ABBREVIATIONS:** AUROC = area under the receiver operating curve; DESH = disproportionately enlarged subarachnoid hydrocephalus; DOR = diagnostic OR; FDR = false discovery rate; HCTS = high-convexity tight sulci; MRE = MR elastography; NPH = normal pressure hydrocephalus; NPV = negative predictive value; PPV = positive predictive value; SVM = support vector machine

Normal pressure hydrocephalus (NPH) is a CSF dynamics disorder<sup>1</sup> with imaging features of enlarged ventricles and clinical symptoms of cognitive decline, gait disturbance, and urinary incontinence.<sup>2</sup> NPH has an estimated prevalence of 2.1% for ages 65 and 70 and 8.9%<sup>3</sup> for ages 80 and older. Overlapping symptoms with Alzheimer disease<sup>4</sup> or Parkinson disease<sup>5</sup> could lead to misdiagnosis of NPH. Contrary to these proteinopathies,

NPH may be treated with ventriculoperitoneal shunt surgery<sup>6</sup> with sustained improvement in about 80% of cases.<sup>7,8</sup> Surgery can even reverse the symptoms of progressive dementia.<sup>9-11</sup> However, due to the invasive nature of surgery, improving the predictability of outcomes is imperative.

A spinal tap test is commonly used to predict shunt outcome, with a high positive predictive value (PPV) of 92% but a low negative predictive value (NPV) of 37%.<sup>12</sup> An improved area under the receiver operating curve (AUROC) and diagnostic OR (DOR) can be achieved by extended lumbar drainage and intracranial pressure measurements.<sup>13</sup> These methods, however, have higher rates of infection and complications<sup>14-17</sup> and are less widely available than the tap test. On the basis of a meta-analysis of several radiologic predictors, only callosal angle and periventricular white matter changes could significantly differentiate between shunt responders and nonresponders, though with low DOR values of 1.88 and 1.01, respectively.<sup>18</sup> A machine learning

Received July 24, 2023; accepted after revision November 21.

From the Departments of Radiology (P.K., M.C.M., P.M.C., M.L.S., J.G.-R., C.R.J., R.L.E., J.H.), Neurology (J.G.-R.), and Neurologic Surgery (B.D.E., C.S.G., F.B.M.), Mayo Clinic College of Medicine, Rochester, Minnesota; Department of Neurosurgery (A.P.), Sheba Medical Center, Tel Hashomer, Ramat Gan, Israel; and Department of Neurosurgery (C.S.G.), University of Oklahoma, Oklahoma City, Oklahoma.

Please address correspondence to Pragalv Karki, PhD, Mayo Clinic Rochester, 333 4th Ave SW, Rochester, MN 55905-0002; e-mail: karki.pragalv@mayo.edu

Indicates open access to non-subscribers at www.ajnr.org

Indicates article with online supplemental data.

<http://dx.doi.org/10.3174/ajnr.A8108>

method developed on intracranial pressure and electrocardiogram features during the lumbar infusion test demonstrated excellent accuracy of 82% and an AUROC of 0.89.<sup>19</sup> However, a noninvasive, safe, and practical alternative is still needed. A machine learning approach based on pattern analysis<sup>20</sup> of MR elastography (MRE) data is a promising noninvasive, radiologic method for predicting the outcome of shunt surgeries.

MRE allows noninvasive evaluation of tissue mechanical properties using acoustic waves.<sup>21</sup> Previous studies have demonstrated that the mechanical properties of the brain are altered by NPH.<sup>22–24</sup> These alterations occur in specific patterns, the presence or absence of which can distinguish patients with NPH from healthy controls and those with Alzheimer disease.<sup>20</sup> Past MRE studies evaluated mechanical changes in the brain due to NPH with cases considered as a single group. However, patients with NPH have different morphologic phenotypes that can be assessed with MR imaging.<sup>25–27</sup>

In this study, we first tested the hypothesis that the different morphologic phenotypes of NPH are associated with unique mechanical signatures. Then, we tested the hypothesis that those mechanical features could improve prediction of the clinical response to shunt surgery compared with the use of mechanical features derived from consideration of patients with NPH as a single group.

## MATERIALS AND METHODS

### Patient Recruitment

We retrospectively identified 137 patients who underwent 3T MR imaging for suspected NPH from April 2014 to December 2022. Nine cases were excluded because of comorbidities, including contusions and meningiomas, or technical failure during tissue segmentation caused by exceptionally large ventricles (particularly in congenital cases). From the remaining 128 suspected cases, 68 participants who had normal opening pressure (<25 cm CSF) during lumbar puncture and gait improvement with the spinal tap test underwent treatment with ventriculoperitoneal shunt placement. Of these patients, 54 were shunt responders, and 14 were nonresponders. Shunt responders were defined as patients who had improvement in gait, cognition, or urinary incontinence at >1 month after shunt placement per neurology or neurosurgery clinical notes. The clinician's assessment of improvement was based on patient reports, gait examination/analysis, and/or mental status examinations.

Data from a group of cognitively healthy controls were included from a previously published study.<sup>28</sup> These participants were recruited from the Mayo Clinic Study of Aging and had previously undergone Pittsburgh Compound B-PET imaging to determine that they were free of a significant amyloid load.

### Image Acquisition

Participants were scanned once on either a GE Signa HDx or GE Discovery MR750W or a Siemens Magnetom Prisma scanner. The acquisitions were comparable among the scanners and included MRE and structural imaging. MRE was performed using a flow-compensated, spin-echo, echo-planar imaging pulse sequence. Shear waves were introduced via a pneumatic actuator at a frequency of 60 Hz. Structural imaging included a

whole-brain T1-weighted MPRAGE or 3D inversion-recovery spoiled gradient-recalled acquisition.

The acquisition parameters for the patients with NPH on the 3T GE Healthcare scanner were the following: T1-weighted MPRAGE: TR/TE/TI = 6.3/2.6/900 ms, flip angle = 8°, FOV = 260 × 260 mm, matrix = 256 × 256, section thickness = 1.2 mm; and MRE: TR/TE = 3601.2/57.3 ms, FOV = 240 × 240 mm, matrix = 72 × 72, section thickness = 3 mm. The acquisition parameters for the control participants were the following: T1-weighted 3D inversion-recovery spoiled gradient-recalled: TR/TE = 6.3/2.8 ms, flip angle = 11°, FOV = 270 × 270 mm, matrix = 256 × 256, section thickness = 1.2 mm; and MRE: TR/TE = 3600/62 ms, FOV = 240 × 240 mm, matrix = 72 × 72, section thickness = 3 mm.<sup>28</sup>

The acquisition parameters on the high-performance Compact 3T scanner (GE Healthcare) were the following: T1-weighted MPRAGE: TR/TE/TI = 6.3/2.6/900 ms, flip angle = 8°, FOV = 260 × 260 mm, matrix = 256 × 256, section thickness = 1.2 mm; and MRE: TR/TE = 4001.3/59.3 ms, FOV = 240 × 240 mm, matrix = 80 × 80, section thickness = 3 mm.<sup>29</sup>

The acquisition parameters on the 3T Siemens scanner were the following: T1-weighted MPRAGE: TR/TE/TI = 2300/3.1/945 ms, flip angle = 9°, FOV = 240 × 256 mm, matrix = 320 × 300, section thickness = 0.8 mm; and MRE: TR/TE = 4800/54 ms, FOV = 240 × 240 mm, matrix = 80 × 80, section thickness = 3 mm.

### Evaluation of Morphologic Features

A neuroradiologist classified patients with suspected NPH into 4 subgroups based on their morphologic features assessed on structural imaging. These 4 groups were the following: 1) high-convexity tight sulci (HCTS),<sup>25</sup> 2) congenital hydrocephalus (Congenital), 3) ventriculomegaly alone (Ventric), and 4) neither ventriculomegaly nor HCTS (Neither). HCTS was defined as focal narrowing or effacement of the sulci at the midline/vertex. Most of the cases of HCTS also had enlarged Sylvian fissures and ventriculomegaly, imaging features of disproportionately enlarged subarachnoid hydrocephalus (DESH).<sup>30</sup> The patients with HCTS alone and DESH were considered as 1 group because no significant differences in mechanical properties were detected. Ventriculomegaly was defined by Evans Index > 0.3,<sup>31</sup> which measures the ratio of frontal horn width to internal skull width and the absence of HCTS. Congenital was defined as ventriculomegaly, diffusely narrowed cerebral sulci, and features of impaired aqueductal flow, including aqueductal web, aqueductal stenosis, or triventriculomegaly with a normal fourth ventricle.<sup>26</sup> The Neither group had neither ventriculomegaly nor HCTS.

### Stiffness and Damping Ratio Map Calculation

Stiffness and damping ratio maps were computed using neural network inversion as previously described.<sup>32</sup> After mechanical property estimation, maps were warped into template space for analyses.<sup>33</sup> These methods are further described in the Online Supplemental Data.

### Mapping of Phenotypic Effects on Mechanical Properties

To identify significant differences in the mean stiffness and damping ratios between the groups, we fit a linear model at each voxel with predictors including age, sex, scanner system, and a set

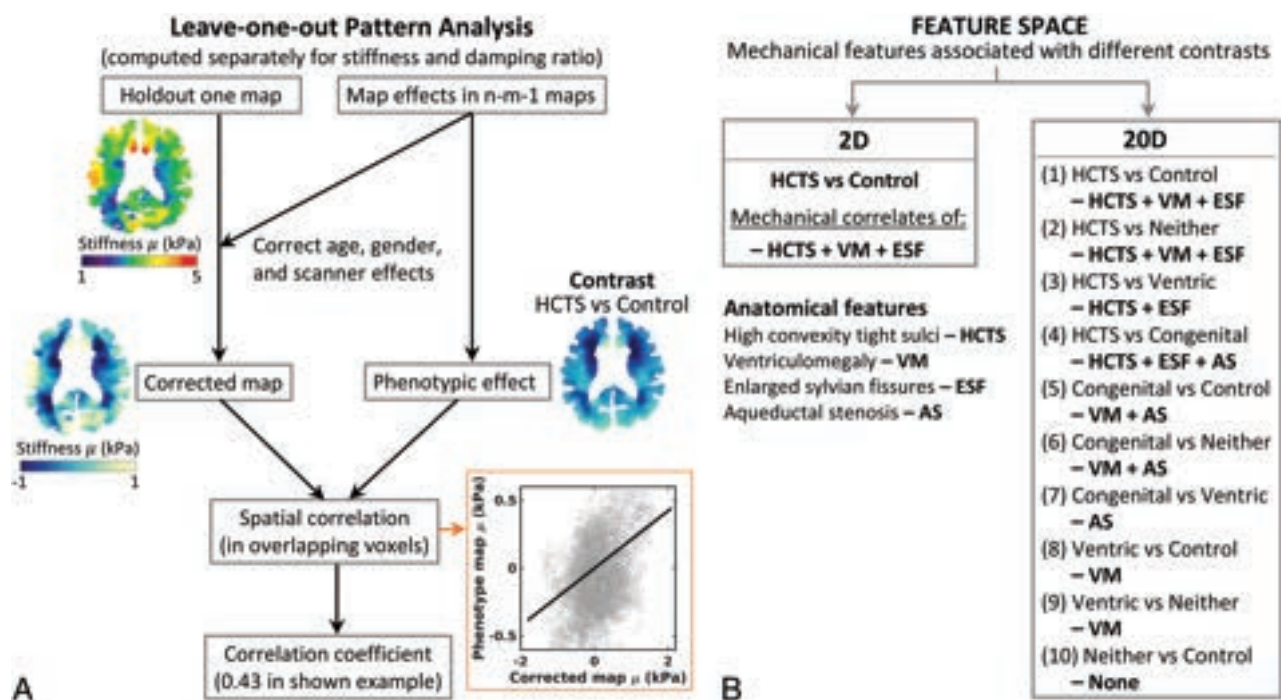


**FIG 1.** Pattern analysis. The pattern analysis procedure is depicted in a flow chart (A) with an example of one of the axial slices of a Ventric case. The procedure is performed for the whole 3D map of an individual. In n-m-1 maps, n represents the total number of cases, and m represents the number of cases from a group that is not included in the correction of the heldout individual map to create the required contrast. For example, in the HCTS-versus-control contrast, m is the number of cases in the control group. In the example shown, a voxelwise spatial correlation of the age, sex, scanner, and the mean corrected heldout individual map was computed in reference to the phenotypic map (HCTS + VM + ESF) of the HCTS versus control contrast. Feature spaces. The flow chart (B) displays the 2 feature spaces with their corresponding mechanical correlates of the anatomic features that would comprise the phenotypic map. In the HCTS-versus-Ventric contrast, mechanical correlates of the HCTS group excluding those common with the Ventric group comprise the phenotypic reference map (HCTS + ESF) for calculating the correlation scores, allowing more distinction in the scores between the HCTS and Ventric cases compared with the scores from the HCTS-versus-control contrast. The expanded feature space of 20D includes all the possible contrasts among the 5 groups, allowing systematic extraction of all possible combinations of the mechanical features that correlate to different anatomic features. ESF indicates enlarged Sylvian fissures; VM, ventriculomegaly.

of categorical variables for group assignment by one-hot encoding. Difference maps and corresponding t-statistics were calculated for stiffness and the damping ratio between HCTS and the other groups. A false discovery rate (FDR) corrected  $Q < 0.05$  as computed by the Storey method<sup>34</sup> was considered significant.

### Pattern Analysis

In this study, we used a previously described pattern analysis method.<sup>20</sup> This method summarizes each person's MRE result by measuring its spatial correlation with the expected mechanical pattern, which is obtained by contrasting 2 groups of interest, while controlling for effects of no interest (ie, age, sex, scanner). Flow charts explaining the procedure are shown in Fig 1. By considering only a single contrast of interest (HCTS versus controls), a 2D feature space is computed (1 pattern score for each of stiffness and damping ratio). By considering all possible contrasts that arise from subtyping the NPH participants, we computed a 20D feature space.

### Machine Learning Classification Model for Shunt Prediction

Support vector machine (SVM) classifiers were trained to predict a successful surgical outcome by using leave-one-out cross-validation to estimate out-of-sample accuracy. Separate SVMs were trained

using either the 2D or 20D feature spaces. We compared the 2 models using the following performance metrics: the AUROC, accuracy, DOR, PPV, and NPV. We first conducted a permutation test to assess whether the AUROC of each model was significantly greater than a random classifier. We then conducted a permutation test to assess whether the performance metrics of the 20D feature space offered improvement compared with the 2D space.

### RESULTS

There were 172 participants in this study, 44 controls, and 128 with suspected NPH. Of the 128 patients with suspected NPH, 91 had morphologic features of HCTS, 12 had congenital hydrocephalus, 20 had ventriculomegaly only, and 5 had neither ventriculomegaly nor HCTS.

A group-wise boxplot of the mean shear stiffness is shown in Fig 2A. There was a statistically significant difference in the mean stiffness of the whole brain between the HCTS and control groups ( $P < .05$ ,  $t$  test). Axial slices of the averaged stiffness maps for each group are shown in Fig 2B. The HCTS group was characterized by stiffening at the midline vertex and softening around the periventricular region. Ventric and congenital groups showed patterns similar to those of HCTS, but the stiffening at the vertex was shifted toward the frontal region of the brain. In the Neither



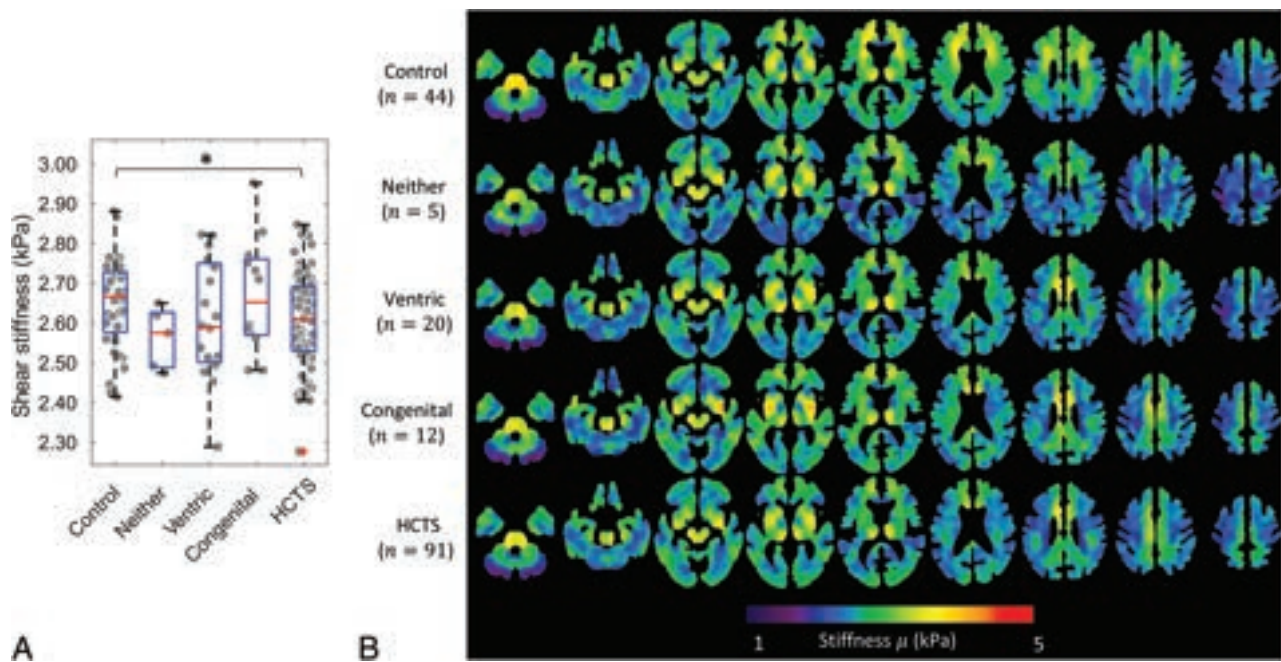


**FIG 2.** Group-wise boxplot overlaid on a jitter plot of mean shear stiffness of the whole brain of each participant (A) and averaged shear stiffness maps (B) of each group. The pair-wise Wilcoxon rank sum test and Welch *t* test results between the groups with  $P < .05$  are indicated with an asterisk in the boxplot.

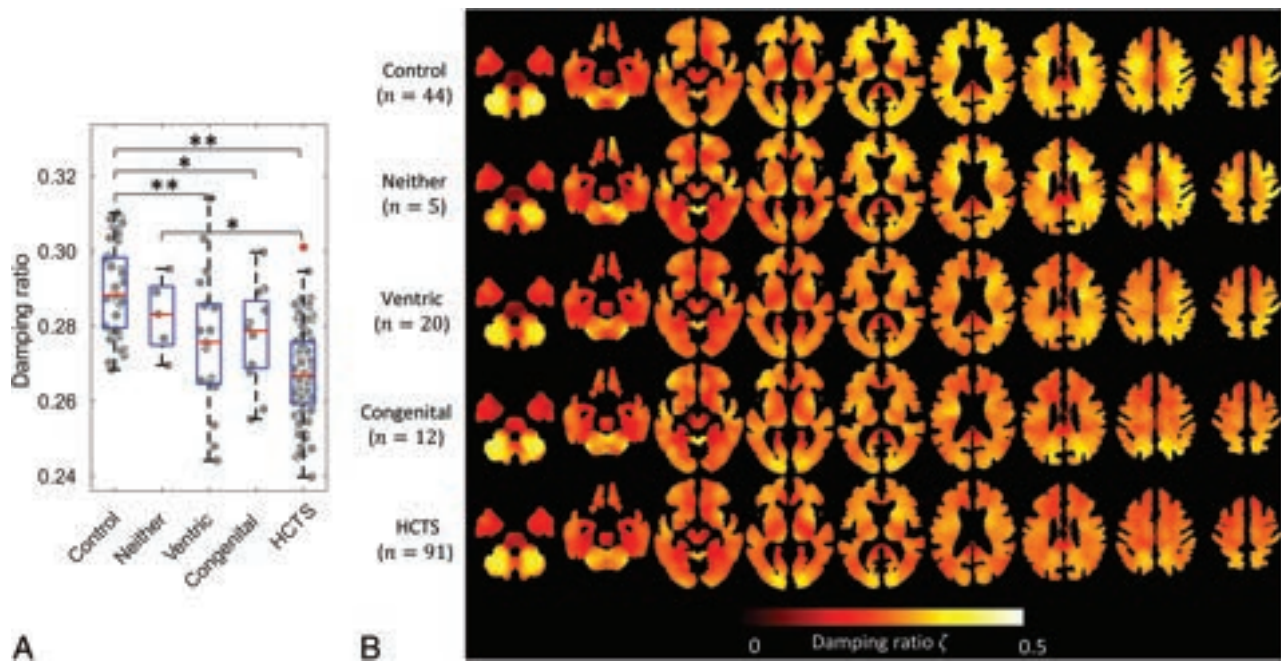


**FIG 3.** Group-wise boxplot overlaid on a jitter plot of the mean damping ratio of the whole brain of each participant (A) and averaged damping ratio maps (B) of each group. The pair-wise Wilcoxon rank sum and Welch *t* test results with  $P < .05$  (asterisk) and  $P < .005$  (double asterisk) are displayed in the boxplot.

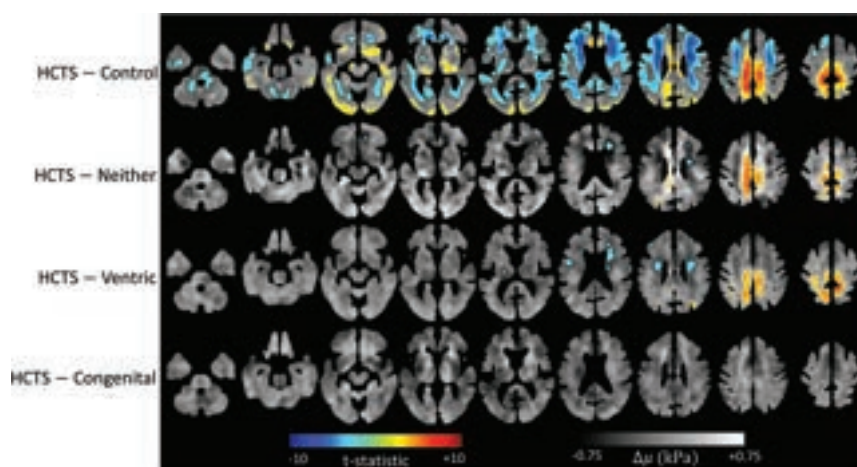
group, softening was evident around the periventricular region, but without stiffening at the vertex.

Figure 3 shows a group-wise boxplot of the mean damping ratio in panel A and damping ratio maps in panel B. The mean damping ratio showed a stepwise decrease as groups exhibited an increasing number of anatomic features. Significant differences in the *t* tests between the groups are labeled in the boxplot. In Fig 3B,

damping ratio patterns demonstrated an overall decline in values in NPH phenotypes compared with controls, with greater differences toward the cranial direction.

The difference maps for the stiffness between HCTS and other groups are shown in Fig 4. A gray-scale map of voxelwise differences is overlaid with a *t*-statistic map thresholded for statistical significance (FDR corrected with  $Q < 0.05$ ). There were 93,254





**FIG 4.** Stiffness difference maps. FDR thresholded ( $Q < 0.05$ )  $t$ -statistic maps overlayed on voxelwise calculated stiffness difference maps between each group and the HCTS group. The number of voxels crossing the FDR threshold was 735 in Congenital, 11,364 in Ventric, 6931 in Neither, and 93,254 in control.

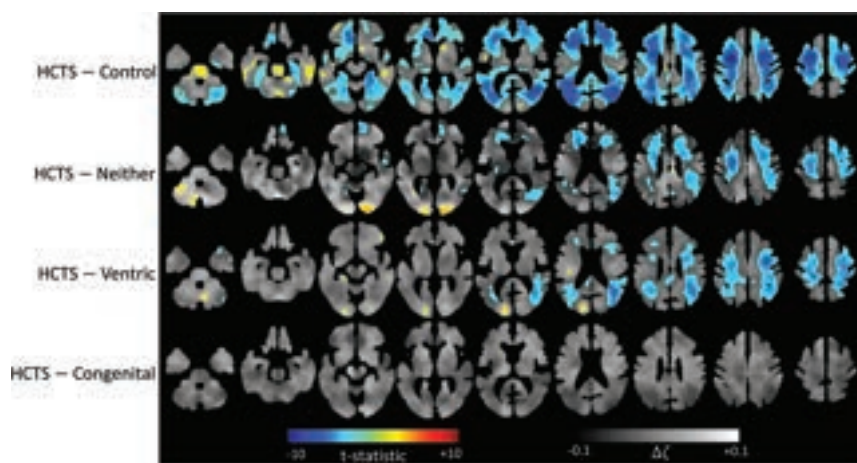


**FIG 5.** Damping ratio difference maps. FDR thresholded ( $Q < 0.05$ )  $t$ -statistic maps overlayed on voxelwise calculated damping ratio difference maps between each group and the HCTS group. Congenital had no voxels crossing the FDR threshold, whereas Ventric had 43,984, Neither had 40,019, and control had 144,233.

voxels that were significantly different between HCTS and controls. The HCTS group had a cluster of voxels with higher stiffness at the midline vertex compared with the Ventric and Neither groups. HCTS had 6931 voxels with a significant difference in comparison with Neither and 11,364 voxels in comparison with Ventric. The HCTS and Congenital groups differed significantly in fewer voxels (735), without any discernible pattern.

Figure 5 illustrates the difference maps for damping ratios of HCTS versus other groups. According to the thresholded  $t$ -statistic maps, damping ratio values were lower overall for the HCTS group. There were significant differences in 144,233 voxels between HCTS and control, 40,019 voxels between HCTS and Neither, 43,984 voxels between HCTS and Ventric, and none between HCTS and Congenital. A globally lower damping ratio of the HCTS group is consistent with the findings in the boxplot of Fig 3A.

In Fig 6, scatterplots of damping ratio and stiffness pattern scores are shown for 4 different contrasts. In the HCTS versus

control contrast (Fig 6A), HCTS and control cases form distinct clusters, demonstrating the separability of these groups based on pattern scores. The remaining NPH subgroup cases were distributed among these clusters with intermediate pattern scores. In the HCTS-versus-Ventric contrast (Fig 6B), Ventric and HCTS cases were further separated than mentioned above because the reference map in this contrast excluded the feature of ventriculomegaly. Figure 6C shows the pattern scores for HCTS-versus-Neither contrast, and Fig 6D shows the pattern scores for HCTS-versus-Congenital contrast. The reference features extracted in these latter contrasts are labeled in Fig 1B. The scatterplots for the remaining 6 contrasts are included in the Online Supplemental Data.

Figure 7 shows the receiver operating characteristic curves with 5 performance metrics for the SVM classification models trained with the limited (2D) or expanded (20D) feature space. The AUROC was 0.66 for the 2D feature space (greater than a random classifier with  $P < .05$ , permutation test) in comparison with 0.77 using the 20D feature space ( $P < .01$ ).

The accuracy of the 20D feature space was 72% compared with 66% for the 2D feature space. The DOR was 6.50 compared with 1.06. PPV was 0.91 compared with 0.80, and NPV was 0.40 compared with 0.21. Though all metrics performed better using the 20D feature space, the difference between the AUROC and NPV was not statistically significant on the basis of a permutation

test. The differences in the DOR and the PPV were statistically significant with  $P < .05$ , and the difference in accuracy approached the level of significance with  $P = .06$ .

## DISCUSSION

This study reproduced the previous finding that HCTS/DESH is associated with characteristic patterns of stiffness and damping ratio alterations.<sup>20</sup> By subclassifying the patients with NPH according to the presence or absence of specific anatomic features, we reported significant differences in brain mechanical properties associated with each phenotype. Furthermore, we showed that the pattern scores computed to summarize these findings at the individual level perform significantly better than chance at predicting the surgical outcomes. Finally, the 20D feature space improved predictions compared with the 2D feature space, indicating that a more detailed summary of the MRE result contains clinically useful information and merits further investigation.

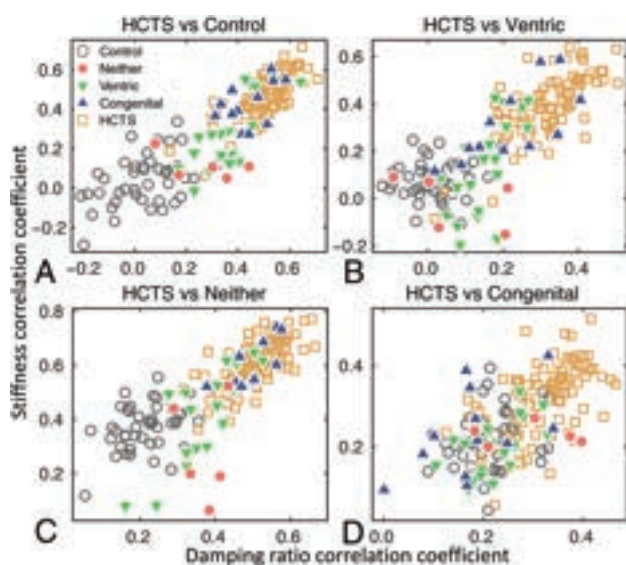


**FIG 6.** Scatterplots of the age, sex, and scanner effect corrected pattern scores of each case for the 4 contrasts of HCTS versus control (A), Ventric (B), Neither (C), and Congenital (D) groups. A, HCTS and control cases are separated into 2 distinct clusters corresponding to the extraction features associated with ventriculomegaly, enlarged ventricles, and tightening of sulci at the vertex of the brain. B, HCTS-versus-Ventric contrast extracted the features associated with the tightening of sulci at the vertex and enlarged Sylvian fissures, excluding the common feature of ventriculomegaly. C, HCTS-versus-Neither contrast further separated cases from the 2 groups. D, Pattern analysis could not distinguish between HCTS and Congenital cases due to similar mechanical patterns demonstrated in Figs 2–5.

Predicting the outcome of shunt surgery is a challenging task. Spinal tap tests are commonly used for prediction with high PPVs but low NPVs. Due to the invasive nature of surgery and the potential for complications, the ability to predict negative outcomes is critical. DESH, which is HCTS along with enlarged Sylvian fissures, is an imaging feature used in the diagnosis of NPH under the widely accepted Japanese criteria.<sup>30</sup> DESH and HCTS have been found to predict clinical improvement after shunt placement in several studies.<sup>35–37</sup> However, studies have indicated that relying only on tight high convexity to predict shunt outcome<sup>38,39</sup> would exclude patients with other NPH phenotypes who could also benefit from surgery, given that HCTS and DESH have even lower performance metrics than the spinal tap test.<sup>12</sup> In this study, we present a noninvasive machine learning approach based on MRE for predicting surgical outcomes in NPH that considers the spectrum of NPH imaging phenotypes and not just DESH.

The results of this study are limited primarily by the number of cases in each NPH subgroup and the number of cases undergoing shunt placement with clinical follow-up. The sample size impacts both the pattern score estimation and the classifier training. Nonetheless, this is the largest MRE study on NPH, to our knowledge. Another limitation of this study is that some of the features in the expanded feature set are likely counterproductive to the classification model. However, we did not use any feature selection because the sample size was not sufficient to add this layer of model tuning. Thus, the presented approach should

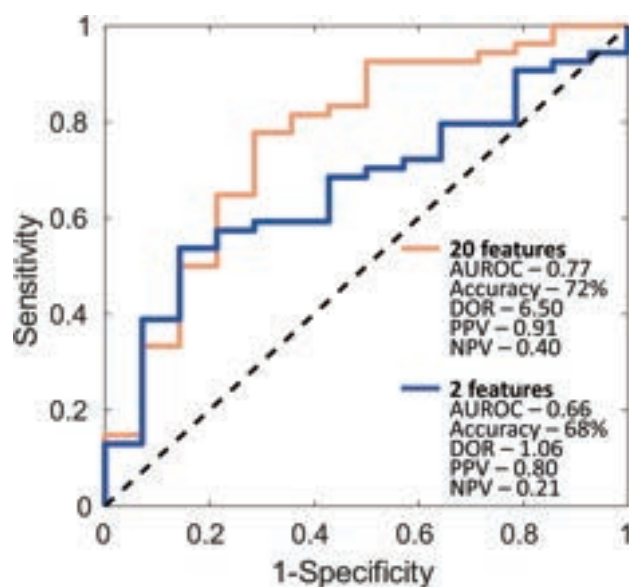


**FIG 7.** SVM receiver operating characteristic curves for the 20D and the 2D feature spaces using a leave-one-out cross-validation procedure. The inset shows the results of 5 performance metrics: AUROC, accuracy, DOR, PPV, and NPV. Random classifier is indicated by the black dashed line.

provide a conservative estimate of model performance and further improvement is expected with additional data.

## CONCLUSIONS

In addition to the clinical importance of predicting shunt efficacy, it is also vital to establish biomarker-derived features for various morphologic phenotypes of NPH to better understand its pathophysiology. The morphologic phenotypes of NPH exhibit distinct mechanical signatures using MRE. Pattern analysis based on MRE presents a promising method for improving diagnosis and prediction of shunt outcomes. In addition, this methodology could be relevant in distinguishing NPH from other neurologic disorders that may have overlapping imaging and/or clinical presentations mimicking NPH, such as Parkinson disease, Alzheimer disease, or progressive supranuclear palsy.<sup>40</sup> The study provides motivation for further research on the underlying mechanical biomarkers of different phenotypes of NPH, in addition to collecting more clinical follow-up after shunt surgery to improve prediction abilities.

Disclosure forms provided by the authors are available with the full text and PDF of this article at [www.ajnr.org](http://www.ajnr.org).

## REFERENCES

- Graff-Radford J, Gunter JL, Jones DT, et al. Cerebrospinal fluid dynamics disorders: relationship to Alzheimer biomarkers and cognition. *Neurology* 2019;93:e2237–46 CrossRef Medline
- Adams RD, Fisher CM, Hakim S, et al. Symptomatic occult hydrocephalus with “normal” cerebrospinal-fluid pressure: a treatable syndrome. *N Engl J Med* 1965;273:117–26 CrossRef Medline
- Andersson J, Rosell M, Kockum K, et al. Prevalence of idiopathic normal pressure hydrocephalus: a prospective, population-based study. *PLoS One* 2019;14:e0217705 CrossRef Medline
- Borzage M, Saunders A, Hughes J, et al. The first examination of diagnostic performance of automated measurement of the callosal angle in 1856 elderly patients and volunteers indicates that 12.4%

- of exams met the criteria for possible normal pressure hydrocephalus. *AJNR Am J Neuroradiol* 2021;42:1942–48 CrossRef Medline
5. Molde K, Söderström L, Laurell K. Parkinsonian symptoms in normal pressure hydrocephalus: a population-based study. *J Neurol* 2017;264:2141–48 CrossRef Medline
  6. Wallenstein MB, McKhann GM. Salomón Hakim and the discovery of normal-pressure hydrocephalus. *Neurosurgery* 2010;67:155–59; discussion 159 CrossRef Medline
  7. Toma AK, Papadopoulos MC, Stapleton S, et al. Systematic review of the outcome of shunt surgery in idiopathic normal-pressure hydrocephalus. *Acta Neurochir (Wien)* 2013;155:1977–80 CrossRef Medline
  8. Wu EM, El Ahmadieh TY, Kafka B, et al. Ventriculoperitoneal shunt outcomes of normal pressure hydrocephalus: a case series of 116 patients. *Cureus* 2019;11:e4170 CrossRef Medline
  9. Kaye JA, Grady CL, Haxby JV, et al. Plasticity in the aging brain: reversibility of anatomic, metabolic, and cognitive deficits in normal-pressure hydrocephalus following shunt surgery. *Arch Neurol* 1990;47:1336–41 CrossRef Medline
  10. Goodman M, Meyer WJ. Dementia reversal in post-shunt normal pressure hydrocephalus predicted by neuropsychological assessment. *J Am Geriatr Soc* 2001;49:685–86 CrossRef Medline
  11. Fisher CM. Reversal of normal pressure hydrocephalus symptoms by subdural collections. *Can J Neurol Sci* 2002;29:171–74 Medline
  12. Mihalj M, Dolić K, Kolić K, et al. CSF tap test: obsolete or appropriate test for predicting shunt responsiveness? A systemic review. *J Neurol Sci* 2016;370:157–84 CrossRef Medline
  13. Thavarajasingam SG, El-Khatib M, Rea M, et al. Clinical predictors of shunt response in the diagnosis and treatment of idiopathic normal pressure hydrocephalus: a systematic review and meta-analysis. *Acta Neurochir (Wien)* 2021;163:2641–72 CrossRef Medline
  14. Haan J, Thomeer RT. Predictive value of temporary external lumbar drainage in normal pressure hydrocephalus. *Neurosurgery* 1988;22:388–91 CrossRef Medline
  15. Walchenbach R, Geiger E, Thomeer RT, et al. The value of temporary external lumbar CSF drainage in predicting the outcome of shunting on normal pressure hydrocephalus. *J Neurol Neurosurg Psychiatry* 2002;72:503–06 CrossRef Medline
  16. El Ahmadieh TY, Wu EM, Kafka B, et al. Lumbar drain trial outcomes of normal pressure hydrocephalus: a single-center experience of 254 patients. *J Neurosurg* 2019;132:306–12 CrossRef Medline
  17. Rebuck JA, Murry KR, Rhoney DH, et al. Infection related to intracranial pressure monitors in adults: analysis of risk factors and antibiotic prophylaxis. *J Neurol Neurosurg Psychiatry* 2000;69:381–84 CrossRef Medline
  18. Thavarajasingam SG, El-Khatib M, Vemulapalli K, et al. Radiological predictors of shunt response in the diagnosis and treatment of idiopathic normal pressure hydrocephalus: a systematic review and meta-analysis. *Acta Neurochir (Wien)* 2023;165:369–419 CrossRef Medline
  19. Mládek A, Gerla V, Skalický P, et al. Prediction of shunt responsiveness in suspected patients with normal pressure hydrocephalus using the lumbar infusion test: a machine learning approach. *Neurosurgery* 2022;90:407–18 CrossRef Medline
  20. Murphy MC, Cogswell PM, Trzasko JD, et al. Identification of normal pressure hydrocephalus by disease-specific patterns of brain stiffness and damping ratio. *Invest Radiol* 2020;55:200–08 CrossRef Medline
  21. Muthupillai R, Lomas DJ, Rossman PJ, et al. Magnetic resonance elastography by direct visualization of propagating acoustic strain waves. *Science* 1995;269:1854–57 CrossRef Medline
  22. Streitberger KJ, Wiener E, Hoffmann J, et al. In vivo viscoelastic properties of the brain in normal pressure hydrocephalus. *NMR Biomed* 2011;24:385–92 CrossRef Medline
  23. Fattahi N, Arani A, Perry A, et al. MR elastography demonstrates increased brain stiffness in normal pressure hydrocephalus. *AJNR Am J Neuroradiol* 2016;37:462–67 CrossRef Medline
  24. Perry A, Graffeo CS, Fattahi N, et al. Clinical correlation of abnormal findings on magnetic resonance elastography in idiopathic normal pressure hydrocephalus. *World Neurosurg* 2017;99:695–700. e691 CrossRef Medline
  25. Kitagaki H, Mori E, Ishii K, et al. CSF spaces in idiopathic normal pressure hydrocephalus: morphology and volumetry. *AJNR Am J Neuroradiol* 1998;19:1277–84 Medline
  26. Oi S, Shimoda M, Shibata M, et al. Pathophysiology of long-standing overt ventriculomegaly in adults. *J Neurosurg* 2000;92:933–40 CrossRef Medline
  27. Kageyama H, Miyajima M, Ogino I, et al. Panventriculomegaly with a wide foramen of Magendie and large cisterna magna. *J Neurosurg* 2016;124:1858–66 CrossRef Medline
  28. Arani A, Murphy MC, Glaser KJ, et al. Measuring the effects of aging and sex on regional brain stiffness with MR elastography in healthy older adults. *Neuroimage* 2015;111:59–64 CrossRef Medline
  29. Foo TKF, Laskaris E, Vermilyea M, et al. Lightweight, compact, and high-performance 3T MR system for imaging the brain and extremities. *Magn Reson Med* 2018;80:2232–45 CrossRef Medline
  30. Mori E, Ishikawa M, Kato T, et al; Japanese Society of Normal Pressure Hydrocephalus. Guidelines for management of idiopathic normal pressure hydrocephalus: second edition. *Neurol Med Chir (Tokyo)* 2012;52:775–809 CrossRef Medline
  31. Miskin N, Patel H, Franceschi AM, et al; Alzheimer's Disease Neuroimaging Initiative. Diagnosis of normal-pressure hydrocephalus: use of traditional measures in the era of volumetric MR imaging. *Radiology* 2017;285:197–205 CrossRef Medline
  32. Scott JM, Pavuluri K, Trzasko JD, et al. Impact of material homogeneity assumption on cortical stiffness estimates by MR elastography. *Magn Reson Med* 2022;88:916–29 CrossRef Medline
  33. Ashburner J, Friston KJ. Unified segmentation. *Neuroimage* 2005;26:839–51 CrossRef Medline
  34. Storey JD. A direct approach to false discovery rates. *J R Stat Soc Series B Stat Methodol* 2002;64:479–98 CrossRef
  35. Narita W, Nishio Y, Baba T, et al. High-convexity tightness predicts the shunt response in idiopathic normal pressure hydrocephalus. *AJNR Am J Neuroradiol* 2016;37:1831–37 CrossRef Medline
  36. Hashimoto M, Ishikawa M, Mori E, et al. Diagnosis of idiopathic normal pressure hydrocephalus is supported by MRI-based scheme: a prospective cohort study. *Cerebrospinal Fluid Res* 2010;7:18 CrossRef Medline
  37. Kazui H, Miyajima M, Mori E, et al; SINPHONI-2 Investigators. Lumboperitoneal shunt surgery for idiopathic normal pressure hydrocephalus (SINPHONI-2): an open-label randomised trial. *Lancet Neurol* 2015;14:585–94 CrossRef Medline
  38. Craven CL, Toma AK, Mostafa T, et al. The predictive value of DESH for shunt responsiveness in idiopathic normal pressure hydrocephalus. *J Clin Neurosci* 2016;34:294–98 CrossRef Medline
  39. Ahmed AK, Luciano M, Moghekar A, et al. Does the presence or absence of DESH predict outcomes in adult hydrocephalus? *AJNR Am J Neuroradiol* 2018;39:2022–26 CrossRef Medline
  40. Quattrone A, Sarica A, La Torre D, et al. Progressive supranuclear palsy with marked ventricular dilatation mimicking normal pressure hydrocephalus. *Neurol Sci* 2022;43:1783–90 CrossRef Medline

# Efficacy of MR Neurography of Peripheral Trigeminal Nerves: Correlation of Sunderland Grade versus Neurosensory Testing

Shuda Xia, Tyler Thornton, Varun Ravi, Yousef Hammad, John R Zuniga, and Avneesh Chhabra

## ABSTRACT

**BACKGROUND AND PURPOSE:** The current reference standard of diagnosis for peripheral trigeminal neuropathies (PTN) is clinical neurosensory testing (NST). MR neurography (MRN) is useful for PTN injury diagnosis, but it has only been studied in small case series. The aim of this study was to evaluate the agreement of Sunderland grades of nerve injury on MRN and NST by using surgical findings and final diagnoses as reference standards.

**MATERIALS AND METHODS:** A total of 297 patient records with a chief complaint of PTN neuralgia were identified from the university database, and 70 patients with confirmed NST and MRN findings who underwent surgical nerve repair were included in the analysis. Cohen weighted kappa was used to calculate the strength of the agreement between the 3 modalities.

**RESULTS:** There were 19 men and 51 women, with a mean age of 39.6 years and a standard deviation of 16.9 years. Most (51/70, 73%) injuries resulted from tooth extractions and implants. MRN injury grades agreed with surgical findings in 84.09% (37/44) of cases, and NST injury grades agreed with surgical findings in 74.19% (23/31) of cases. MRN and NST both showed similar agreement with surgery for grades I to III (70% and 71.43%). However, MRN showed a higher rate of agreement with surgery (88.24%) for injury grades IV and V than did NST (75%).

**CONCLUSIONS:** MRN can objectively improve preoperative planning in patients with higher-grade nerve injuries.

**ABBREVIATIONS:** IAN = inferior alveolar nerve; LN = lingual nerve; MRN = MR neurography; NST = neurosensory testing; PTN = peripheral trigeminal neuropathy

Peripheral trigeminal neuropathy (PTN) can be caused by an injury of the trigeminal nerve or its branches, specifically the inferior alveolar nerve (IAN) and lingual nerve (LN). These injuries can cause a loss of sensation to the lower face and oral cavity, an altered or absent taste sensation of the anterior two-thirds of the tongue due to damage to the chorda tympani fibers that travel with the lingual nerve, and neuropathic pain in the trigeminal nerve distribution.<sup>1-3</sup> Common etiologies of PTN include iatrogenic dentoalveolar surgeries, injection injuries, and trauma, with third molar extraction being the most common cause. With up to 10 million third molar removals occurring each year and an incidence of permanent paresthesia of the lip, tongue, or cheek ranging from 11,500 to 35,000 a year, PTN cause substantial morbidity and can result in significant reductions in quality of life.<sup>4-6</sup>

The current diagnostic reference standard for PTN injuries is clinical neurosensory testing (NST), which compares a patient's pressure and pain sensation in a nerve distribution with that of an expected normal. NST incorporates 3 domains: spatiotemporal sensory perception, monofilament contact detection, and pain tolerance and thresholds.<sup>7</sup> The 5 scores of sensory impairment denote a normal, mild, moderate, severe, or complete loss of function.<sup>8</sup> The results from NST, in combination with clinical history and examination findings, are used to determine proper treatment methods based on the Sunderland classification system. The Sunderland classification system defines the nerve injury in 5 grades, ranging from minor injury to complete nerve transection.<sup>9,10</sup> Higher-grade injuries require timely and accurate interventions to maximize the possibility of the regeneration of axons. However, NST poses various limitations, including decreased test result reliability within the first 3 months following an injury, the subjectivity of patient responses, and substantial intra observer and inter observer variability.<sup>7,11</sup> In addition, being an indirect test, NST cannot show nerve anatomy or lesions. As a result of these limitations, NST may lead to an inaccurate analysis of nerve damage severity and may delay the treatment of more severe

Received June 30, 2023; accepted after revision December 2.

From The University of Texas Southwestern Medical Center (S.X., V.R., Y.H., J.R.Z., A.C.), Dallas, Texas; and The University of North Texas, Health Science Center (T.T.), Fort Worth, Texas.

Please address correspondence to Avneesh Chhabra, MD, MBA, FACR, Chief Musculoskeletal Radiology, Professor of Radiology & Orthopedic Surgery, UT Southwestern Medical Center, Dallas, TX; e-mail: avneesh.chhabra@utsouthwestern.edu

<http://dx.doi.org/10.3174/ajnr.A8120>



**Table 1. Sunderland nerve injury classification with corresponding surgical findings, MRN findings, and surgical indications**

Sunderland Injury Classification	MRN Findings	Recovery Potential	Surgery Indication	Surgical Findings
I	Homogeneous increased T2 signal of nerve with no change in caliber, usually resolve short of surgery	Full	None	Intact with no internal or external fibrosis, normal neuroarchitecture
II	Homogeneous increased T2 signal of nerve and mild to moderate nerve thickening, less than 100% thickening than the adjacent or contralateral nerve	Full	None unless persistent pain for >3 months	Intact with no internal fibrosis, with external fibrosis, restricted mobility with intact neuroarchitecture
III	Homogeneous increased T2 signal of nerve and moderate-marked nerve thickening, more than 100% thickening than the adjacent or contralateral nerve	Slow/incomplete	None or neurolysis	Intact with internal and external fibrosis, restricted mobility, and disturbed neuroarchitecture
IV	Heterogeneous increased T2 signal of nerve and focal enlargement consistent with a neuroma-in-continuity in an otherwise continuous nerve	Poor to none	Nerve repair, graft, or transfer	Partial transected nerve, some amount of distal nerve with or without lateral neuroma
V	Discontinuous nerve with end bulb neuroma and a complete nerve gap	None	Nerve repair, graft, or transfer	Completely transected nerve

**Table 2: NST parameters. Present values exhibit comparable sensitivity within the normative range. Failed values are less than those of the control sites or the normative range. Elevated values are greater than those of the control sites. Absent values are greater than the maximum of the testing device**

Injury Degree	Level A: Spatiotemporal Sensory Perception	Level B: Contact Detection with Monofilament	Level C: Pain, Temperature, and Pressure Threshold and Tolerance
Normal	Present	Present	Present
Mild	Failed	Present	Present
Moderate	Failed	Failed	Present
Severe	Failed	Failed	Elevated
Complete	Failed	Failed	Absent

nerve injuries that require timely surgical repair to improve a patient's prognosis. Thus, the delays can result in otherwise preventable permanent nerve damage with substantial morbidity.

MR neurography (MRN) is an imaging technique that provides a noninvasive method by which to delineate the neuromuscular anatomy and intraneural architecture of peripheral nerves in multiple orthogonal planes.<sup>12-14</sup> Specifically, it has been validated for use in PTN and in the identification of the different Sunderland grades of injuries.<sup>7,10,12</sup> Thus, MRN has the advantage of showing both nerve lesions for presurgical planning and the grade of severity of an injury.

Current literature that evaluates the role of MRN for the diagnosis and management of PTN in patients has been limited to small sample sizes, and its value over NST has not been studied in sufficient detail. The aim of this study was to evaluate the agreement of Sunderland grades of nerve injury on MRN and NST by using surgical findings and the final clinical diagnosis as the reference standards in a larger, consecutive patient cohort. We hypothesized that the reported MRN injury grade agreed with surgical findings in a higher percentage of cases than did NST. As a secondary aim, we also evaluated the agreement between MRN-assigned and NST-assigned nerve injury grades.

## MATERIALS AND METHODS

An Institutional Review Board approved this retrospective cross-sectional study, and informed consent was waived.

## Patient Demographics and Injury Classification

A consecutive group of 297 adults of all genders with a suspected injury of PTN were queried from an institutional database over a 6-year period (July 2015 to November 2021). All patients were referred from the institutional oral and maxillofacial surgery clinic. These patients were all seen at the institution by an experienced maxillofacial surgeon and had trigeminal MRN imaging that was interpreted by an experienced radiologist. Seventy patients from the initial cohort had surgery, NST, and MRN, and these patients were included in the final sample.

## Clinical and Surgical Classification

The NST was performed by the same oral and maxillofacial surgeon (J.R.Z., with 30 years of experience) and the Sunderland class grades were reported in the medical charts based on clinical findings and NST. The 70 patients who underwent surgery were also graded intraoperatively by using the Sunderland classification criteria in Table 1. The NST parameters are described in Table 2. The final diagnoses with injury grades, based on surgical and histopathology findings, were reported in the patients' charts and served as the reference standards for both MRN and NST.

## MRN Imaging and Reports

Seventy patients underwent MRN imaging by using a standardized institutional protocol (Table 3). Sixty-two patients had MRN on 3T scanners, and 8 patients had MRN on 1.5T scanners.

**Table 3: Institutional protocol for MRN imaging**

Plane	Sequence	Coverage	Slice Thickness/ Gap (mm)	Pixel Size (mm)	FOV (mm)	TR (ms)	TE (ms)	Comments
3 plane	Scout	Axial: Cover from						
Axial	2D T2W TSE	skin to skin for	4/0.4	0.3 × 0.4	170 × 180	3500–4500	50–65	Base of skull to C5 level
Axial	2D TIW TSE	FOV	4/0.4	0.3 × 0.4	171 × 180	400–600	6–9	Base of skull to C5 level
Coronal	3D DW-PSIF	Coronal: Cover from anterior	0.9 ISO/0	Acquired ISO	172 × 180	12	3–4	Midskull to C5 level; b-value = 60/70
Axial	3D BFFE	nasal skin to back of the ear; R-L skin to skin	0.9 ISO/0	Acquired ISO	173 × 180	5.2	3	Midskull to C2 level
Axial	DTI	Sagittal: Cover both sides even if unilateral pain	4/0	1.5 × 1.5	174 × 180	5000–10,000	60–75	b-value = 0–600; 12 directions; echo spacing ≤ 0.7 ms

**Note:**—T2W indicates T2-weighted; TIW, T1-weighted; BFFE, balanced fast field echo; R-L, right-left; A-P, anterior-posterior; DW, diffusion-weighted; PSIF, reversed fast imaging in steady state free precession.

The same imaging sequences and similar parameters were used on both types of scanners (Ingenia, Achieva, Philips; Avanto, Siemens). Most scans were noncontrast scans (90%, 63/70). 1.5T was used in the setting of dental hardware in a small minority of cases. The protocol was longer on the 1.5T scanners than on the 3T scanners by 15 minutes, overall. Otherwise, the image quality was similar, except for less-than-optimal fat suppression on 3D MR imaging and a less ideal demonstration of the lingual nerve on 1.5T. We prefer 3T scanners for most cases because of the time efficiency and better fat suppression on 3D imaging. Contrast scans do not make any difference in nerve evaluation, as the injured nerves do not enhance in our experience. It was a referring doctor's preference to obtain a few scans with contrast imaging. The MRN reports were generated by an experienced radiologist (A.C., 15 years of postfellowship experience and 14 years of MRN-reading experience) as the standard of care, and injury grades were placed in the reports prospectively, based on imaging and a review of patient history (duration after injury, distribution of pain to cheek or tongue, paresthesia, taste changes, etc), independent of the NST score.

### Data Analysis

The medical charts were reviewed by 3 medical students. All charts were data mined to identify the Sunderland injury class on NST and MRN, previous surgeries, surgical findings, whether surgery was performed after the MRN, and surgical pathology results. The Sunderland classification system of nerve injury is described in detail in Table 1. Of the cohort, 70 patients had surgery. In the surgical cohort, not all patients had definitive MRN and NST injury grades in their charts. For example, inconclusive results included patients whose injury grades could not be definitively classified into a single grade. Thus, when doing the statistical analysis, inconclusive results were not included (Fig 1).

### Statistical Analysis

Descriptive statistics were used for the demographic data and nerve injury classifications on NST and MRN. The agreement of NST and MR imaging was obtained, using surgical and histopathology findings as reference standards. Cohen weighted kappa

was also calculated. The distribution of injury classes by NST, MRN, and surgical findings can be found in Figure 2. The agreement coefficient interpretations used were as follows: Excellent Agreement: 0.75–1.00, Good Agreement: 0.60–0.75, Fair Agreement: 0.40–0.60, Poor Agreement: < 0.40.<sup>15</sup>

## RESULTS

### Patients

Seventy patients underwent surgical repair. The study cohort consisted of 19 (27%) men and 51 (73%) women with a mean age of 39.6 years and a standard deviation of 16.9 years. Most (51/70, 73%) injuries resulted from tooth extractions and implants, with other injuries including motor vehicle crashes, sinus surgery, and mandibular bone grafting. Table 4 contains the breakdown of injury grades for NST, MRN, and surgical findings among the 70 patients. Of the 70 patients, 44 had LN injuries, 15 had IAN injuries, 5 had both IAN and LN injuries, and 6 had maxillary nerve injuries. The mean time from MRN to surgery was 87 days, with a standard deviation of 141 days.

### NST, MRN, and Surgical Correlations

The study found that NST showed fair agreement with surgical findings, whereas MRN exhibited good to excellent agreement with surgical findings. Overall, NST and MRN had excellent agreement with each other.

The study found that the MRN Sunderland injury grades agreed with surgical findings 84% (37/44 cases) of the time, whereas NST injury grades agreed with surgical findings 74% (23/31 cases) of the time. The weighted kappa values with 95% CI for the comparisons of each pair of techniques can be seen in Table 5. Figure 3 shows a case in which the NST did not agree with surgical findings but the MRN did. Figure 4 shows a case in which the NST was inconclusive, but the MRN agreed with surgical findings. Figure 5 shows a case in which all 3 modalities agreed. The MRN and NST injury grades agreed 81% of the time (17/21 cases).

Sunderland injury grades of I through III have better prognoses and may not be treated surgically unless either persistent pain exists or extensive surrounding scarring causes nerve entrapment. Sunderland injury grades of IV and V show worse prognoses

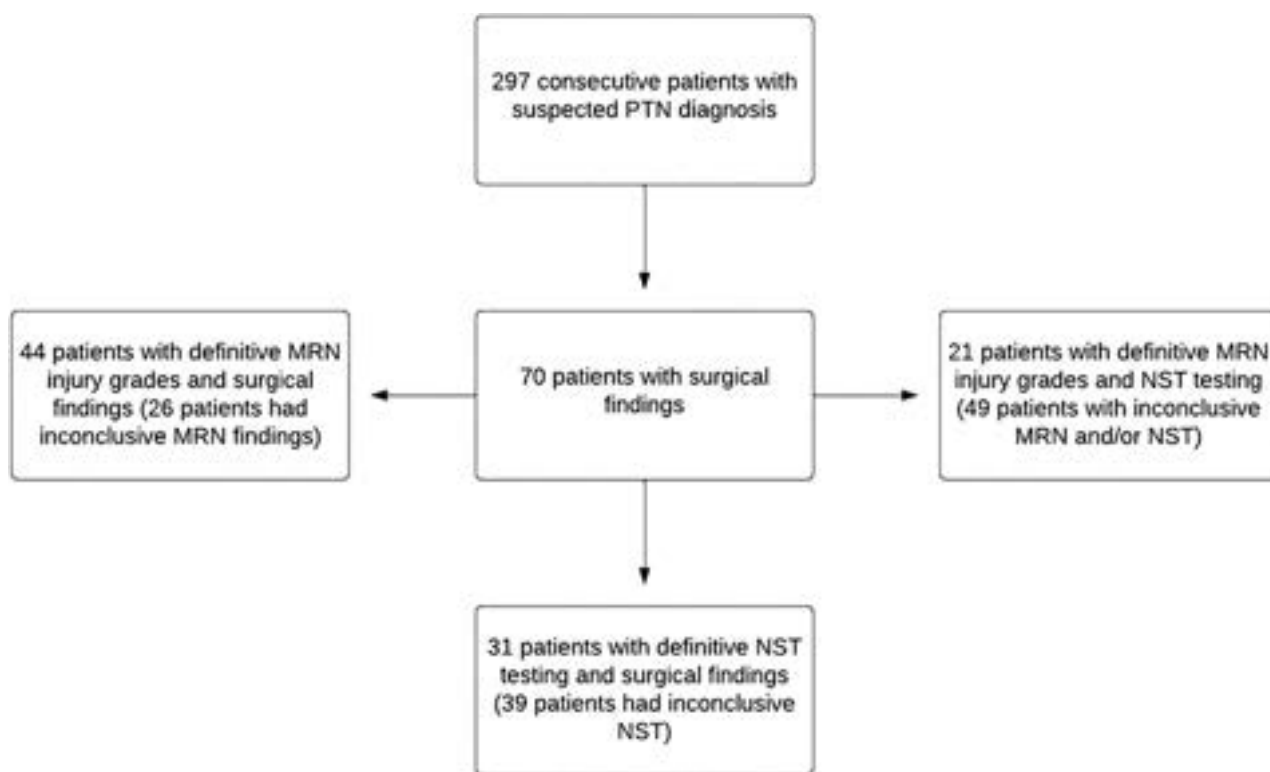


**FIG 1.** The 3 groups from the main cohort of 70 surgical patients were included in the statistical analysis. Because patients had inconclusive results in different modalities, the 3 groups had different sizes. For example, the 44 patients in the MRN versus surgical findings cohort were derived from the original 70 patients because 26 patients in the 70-patient surgical cohort had inconclusive MRN findings.

unless treated timely with surgery.<sup>9</sup> Thus, the study also analyzed the rates of agreement for NST and MRN in these 2 overarching injury categories. MRN and NST had similar rates of agreement with surgical findings for Sunderland injury classes I to III (70% for MRN, 71.43% for NST). However, MRN showed a moderately higher rate of agreement with surgical findings (88.24%) for Sunderland injury grades IV and V, compared with NST findings (75%). Detailed statistics can be found in Table 6. Table 1 contains a more detailed explanation of the Sunderland injury classifications as well as their respective surgical indications and radiologic findings.

## DISCUSSION

Peripheral nerve injury is one of the most common causes of chronic neuropathic pain, contributing to significant disease burden.<sup>16</sup> The most common cause of PTN results from molar tooth extractions, resulting in facial and jaw pain or paresthesia.<sup>17</sup> In PTN, early diagnosis and timely management are essential for improved patient outcomes and prognosis, with outcomes deteriorating due to older age, delayed treatment, and a larger nerve gap.<sup>18</sup>

The current standard for diagnosing PTN by using NST is limited, as the subjectivity of the results delays the treatment of higher-class injuries, resulting in potentially irreversible nerve damage. MRN provides an alternative method for the diagnosis and staging of patients with PTN because of its ability to delineate anatomy and the exact location of injury for preoperative planning.<sup>8</sup>

Similar to previous studies, this study establishes that MRN can accurately diagnose patients with PTN, with localization of

the nerve lesion. Though previous literature has demonstrated the viability of MRN in the diagnosis of patients with PTN, sample sizes were small, and surgical findings were not systematically examined. This study expands on current literature by examining the correlations between injury grading based on NST and MRN, using surgical and histopathology findings as reference standards. This study found that though NST and MRN had similar rates of agreement with surgical findings in lower-grade injuries, MRN had higher rates of agreement with surgical findings than did NST in higher-grade injuries. MRN also yielded smaller confidence intervals than did NST. Because NST is subjective, responses can be similar in different grades of nerve injury due to various factors, such as delayed or exaggerated sensory responses, psychological issues, and secondary gain. However, MRN displays a more objective anatomy of the nerve and injury. Thus, MRN can be a useful tool for the staging of patients with PTN, especially patients with higher-grade injuries for whom timely intervention is crucial in lowering the risk of irreversible nerve damage. It should also be noted that the NST was performed by the same surgeon, who had extensive experience with NST. While it takes years of experience and clinical skills to establish such acumen, MRN is more widely available and is not dependent on subjective patient information about pain and pressure sensitivity. Though a strength of the study was having MRN interpretations done by an experienced reader who prospectively assigned the injury grades, this may limit generalizability. However, MRN is increasingly becoming widely available, as higher Tesla strengths are being incorporated into clinical practices and 3D MR imaging protocols have been standardized.

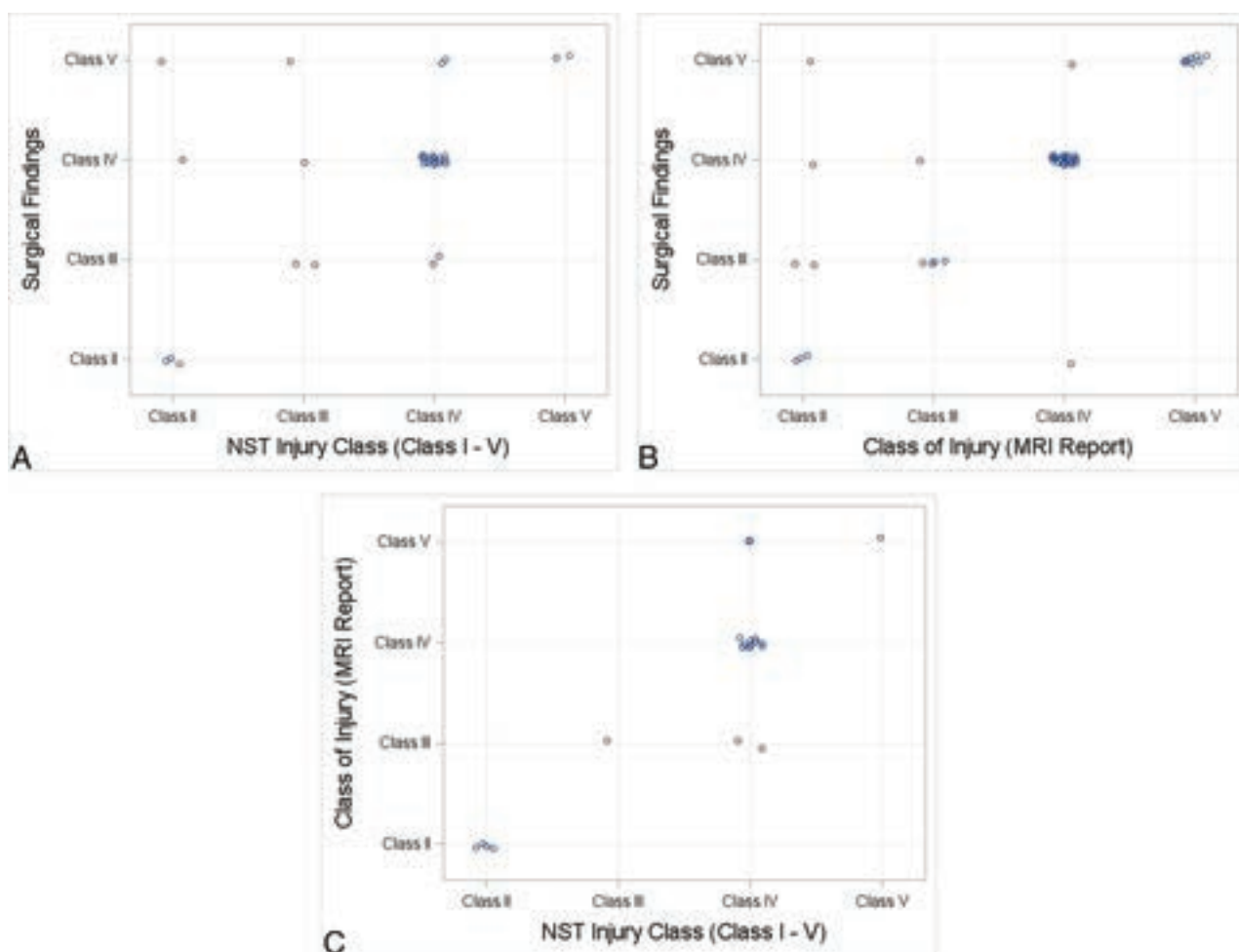


**FIG 2.** Jitter plots showing injury class distributions for (A) NST versus surgery, (B) MRN versus surgery, and (C) NST versus MRN.

**Table 4: Distribution of injury grades for NST, MRN, and surgical findings among the 70 patients. Inconclusive results mean that the injury grade was unable to be narrowed down to just 1 class. For example, a grade of II/III being reported in the patient chart is recorded as inconclusive**

Injury Grade	NST	MRN	Surgery
I	0	0	0
II	5	7	12
III	4	5	12
IV	20	24	33
V	2	8	13
Inconclusive	39	26	0

**Table 5: Weighted Cohens kappa with 95% CIs for the NST grade versus MRN, surgical findings versus MRN, and surgical findings versus NST**

Comparison	Cohen Weighted Kappa Coefficient (quadratic)	95% CI
NST versus surgical findings	0.51	(0.1–0.92)
MRN versus surgical findings	0.7	(0.44–0.97)
MRN versus NST	0.88	(0.76–1)

This study has some limitations. The patients in the cohort had symptomatic PTN that warranted referral to the university maxillofacial clinic, resulting in a cohort that had higher degrees

of nerve injuries, overall. However, there were 24/70 class II and III injuries available, as well. Additionally, not all patients underwent surgery, and the same surgeon who documented the NST results performed the final surgeries. Furthermore, some patients had inconclusive results on MRN and NST such that a definitive injury class could not be determined between class II or III. This decreased the size of the cohort that could be examined. It was also a learning experience for the MRN reader, as the imaging knowledge from other, larger peripheral nerves was being transferred to the smaller jaw nerves. It is expected that future correlations might even be improved with consistent and improved imaging on the newer scanners. We also did not reevaluate the MRN scans, as doing so would have led to results that differed from the prospectively determined MRN grades of injury and would have compromised the first approximation that we wanted to derive about the MRN-NST-surgery correlation data that was intended with this institutional audit of the utility of MRN. The full utility of MRN would be best demonstrated in future prospective studies with the possible randomization of patient groups. Furthermore, there was possible bias in the evaluation of the NST grades, as only 1 surgeon evaluated the NST gradings. Likewise, because only 1 radiologist read the MRN and generated the final reports, there could be bias and errors on the assignment of the Sunderland grading scale on the MRN. However, the



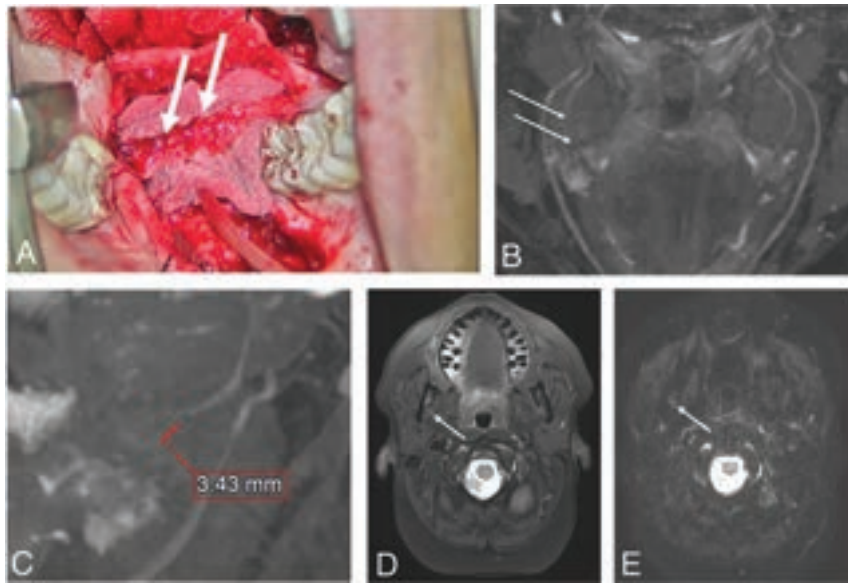


**FIG 3.** A 46-year-old woman with an injury to the right lingual nerve from molar teeth extraction. The NST yielded an injury grade of IV, but MRN yielded an injury grade of V, consistent with the surgical findings of a class V injury with amputation neuroma and a fibrous connection to the distal end. *A*, Intraoperative picture with amputation neuroma and foreign material highlighted by arrows. *B*, Coronal 3D PSIF MRN image of the lower face with arrows pointing to a gap in the right lingual nerve. *C*, Sagittal 3D PSIF MRN image reconstruction showing the neural gap in more detail, measuring 3.43 mm. *D*, Axial T2 SPAIR and (*E*) axial DTI showing the abnormal right lingual nerve (arrows). The nerve gap is best seen on 3D MRN images. PSIF indicates reversed fast imaging in steady state free precession; SPAIR, spectral attenuated inversion recovery.

radiologist is experienced with reading MRN (14 years), and the possibility of misclassifying injuries on MRN is slim.

Because the MR imaging and NST grades agreed well, the noninferiority of results may encourage surgeons to use MRN more in their practices. Future related studies could examine the utilization of MRN in the evaluation of PTN in the preoperative and postoperative periods as well as whether the utilization of MRN led to better patient outcomes in patients who underwent surgery.

## CONCLUSIONS

This study demonstrates that MRN-derived peripheral trigeminal nerve injury grades correlate with intraoperative findings in patients with higher-grade nerve injuries better than do NST-derived grades. This finding supports MRN as an important tool for the diagnosis and clinical management of patients with PTN. With a timely diagnosis of higher-grade injuries,

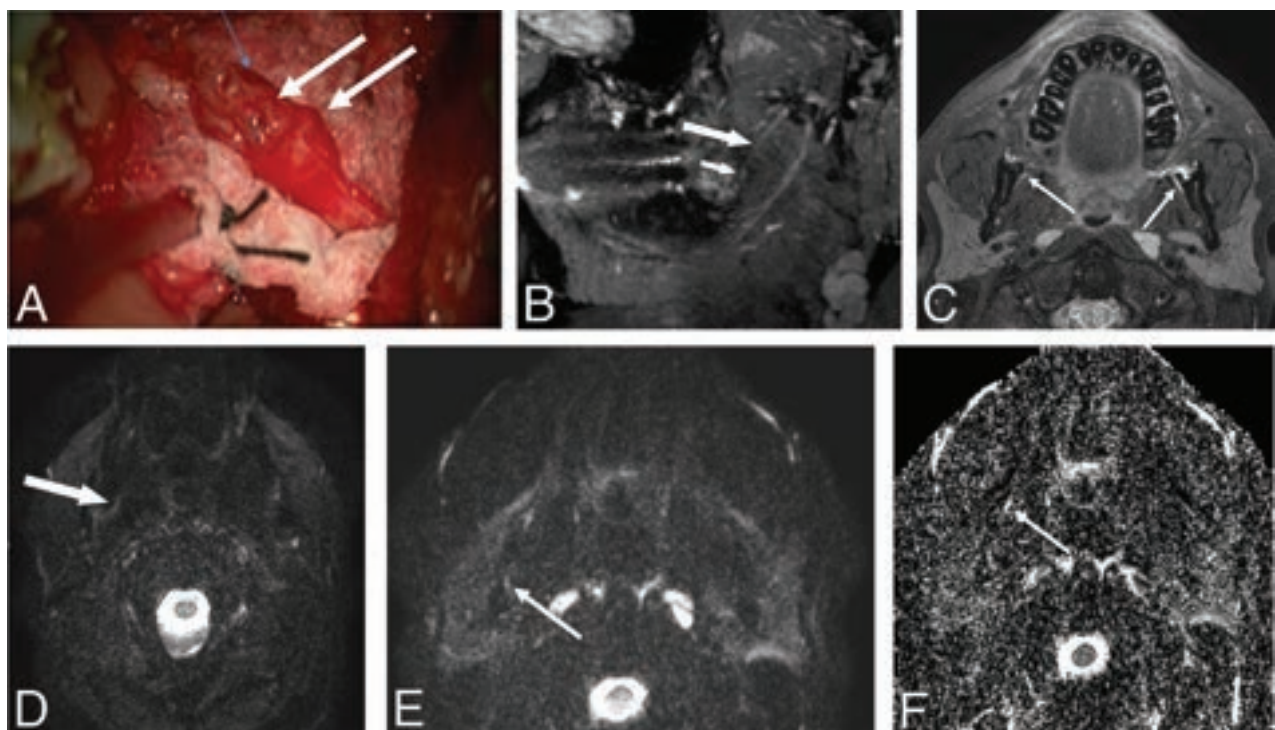


**FIG 4.** A 33-year-old man with bilateral injuries to the lingual nerves caused by a third molar extraction. The NST was inconclusive, but MRN revealed a Sunderland grade IV injury, consistent with surgical findings. *A*, Intraoperative picture of the left lingual nerve showing a neuroma in continuity. *B*, 3D PSIF sagittal reconstructed 3D MRN image showing the focal nerve swelling (*small arrow*) in the abnormal nerve (*large arrow*) as a neuroma in continuity. *C*, Corresponding axial T2 SPAIR image showing abnormally hyperintense and enlarged lingual nerves bilaterally (arrows). *D* and *E*, Axial DTI and (*F*) axial ADC images showing the abnormally hyperintense right lingual nerve (arrows) with nonvisualization of the left lingual nerve on DTI and ADC images. PSIF indicates reversed fast imaging in steady state free precession; SPAIR, spectral attenuated inversion recovery.

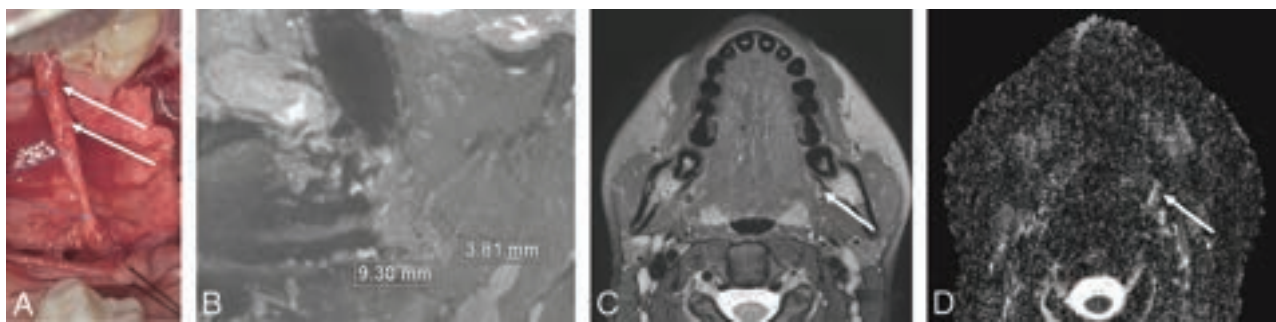


**FIG 5.** A 23-year-old woman with an injury to the right lingual nerve caused by a third molar extraction. Both MRN and NST revealed a Sunderland grade IV injury, consistent with surgical findings. A, Intraoperative picture showing neuroma in continuity. B, 3D PSIF sagittal reconstructed MRN image of the lower face showing a neuroma in continuity of 3.81 mm with a 9.3 mm overall abnormal hyperintense nerve. C, Focal nerve swelling can be appreciated in an axial T2-weighted SPAIR image and (D) the corresponding DTI, as outlined by the arrows. PSIF indicates reversed fast imaging in steady state free precession; SPAIR, spectral attenuated inversion recovery.

**Table 6: Agreement percentages for all modalities**

Comparison	Class	Agreement Percentage
NST versus surgical findings	I to III	71.43%
	IV and V	75%
	Overall	74.19%
MRN versus surgical findings	I to III	70%
	IV and V	88.24%
	Overall	84.09%
MRN versus NST	Overall	80.95%

it can result in potentially lower times to intervention and can thereby impact patient outcomes.

Disclosure forms provided by the authors are available with the full text and PDF of this article at [www.ajnr.org](http://www.ajnr.org).

## REFERENCES

- Joo W, Yoshioka F, Funaki T, et al. Microsurgical anatomy of the trigeminal nerve. *Clin Anat* 2014;27:61–88 CrossRef Medline
- Al-Amery SM, Nambiar P, Naidu M, et al. Variation in lingual nerve course: a human cadaveric study. *PLoS One* 2016;11:e0162773 CrossRef Medline
- Kikuta S, Iwanaga J, Kusakawa J, et al. An anatomical study of the lingual nerve in the lower third molar area. *Anat Cell Biol* 2019;52:140–42 CrossRef Medline
- Valmaseda-Castellón E, Berini-Aytés L, Gay-Escoda C. Inferior alveolar nerve damage after lower third molar surgical extraction: a prospective study of 1117 surgical extractions. *Oral Surg Oral Med Oral Pathol Oral Radiol Endod* 2001;92:377–83 CrossRef Medline
- Osborn TP, Frederickson G, Jr., Small IA, et al. A prospective study of complications related to mandibular third molar surgery. *J Oral Maxillofac Surg* 1985;43:767–69 CrossRef Medline
- Friedman JW. The prophylactic extraction of third molars: a public health hazard. *Am J Public Health* 2007;97:1554–59 CrossRef Medline
- Zuniga JR, Meyer RA, Gregg JM, et al. The accuracy of clinical neurosensory testing for nerve injury diagnosis. *J Oral Maxillofac Surg* 1998;56:2–8 CrossRef Medline
- Dessouky R, Xi Y, Zuniga J, et al. Role of MR neurography for the diagnosis of peripheral trigeminal nerve injuries in patients with prior molar tooth extraction. *AJNR Am J Neuroradiol* 2018;39:162–69 CrossRef Medline
- Robinson PP. Observations on the recovery of sensation following inferior alveolar nerve injuries. *Br J Oral Maxillofac Surg* 1988;26:177–89 CrossRef Medline
- Chhabra A, Ahlawat S, Belzberg A, et al. Peripheral nerve injury grading simplified on MR neurography: as referenced to Seddon and Sunderland classifications. *Indian J Radiol Imaging* 2014;24:217–24 CrossRef Medline
- Manoliu A, Ho M, Nanz D, et al. MR neurographic orthopantomogram: ultrashort echo-time imaging of mandibular bone and teeth complemented with high-resolution morphological and functional MR neurography. *J Magn Reson Imaging* 2016;44:393–400 CrossRef Medline
- Zuniga JR, Mistry C, Tikhonov I, et al. Magnetic resonance neurography of traumatic and nontraumatic peripheral trigeminal neuropathies. *J Oral Maxillofac Surg* 2018;76:725–36 CrossRef Medline
- Wu W, Wu F, Liu D, et al. Visualization of the morphology and pathology of the peripheral branches of the cranial nerves using three-dimensional high-resolution high-contrast magnetic resonance neurography. *Eur J Radiology* 2020;132:109137 CrossRef Medline
- Zuniga JR, AbdelBaky O, Alian A, et al. Does presurgical magnetic resonance neurography predict surgical gap size in trigeminal class IV and V injuries? *J Oral Maxillofac Surg* 2021;79:2574–81 CrossRef Medline
- Cicchetti D. Guidelines, criteria, and rules of thumb for evaluating normed and standardized assessment instrument in psychology. *Psychol Assess* 1994;6:284–90 CrossRef
- Scholz J, Finnerup NB, Attal N, Classification Committee of the Neuropathic Pain Special Interest Group (NeuPSIG), et al. The IASP classification of chronic pain for ICD-11: chronic neuropathic pain. *Pain* 2019;160:53–59 CrossRef Medline
- Bouloux GF, Steed MB, Perciaccante VJ. Complications of third molar surgery. *Oral Maxillofac Surg Clin North Am* 2007;19:117–28, vii CrossRef Medline
- Bagheri SC, Meyer RA, Cho SH, et al. Microsurgical repair of the inferior alveolar nerve: success rate and factors that adversely affect outcome. *J Oral Maxillofac Surg* 2012;70:1978–90 CrossRef Medline

# Diagnostic Performance of Dynamic Contrast-Enhanced 3T MR Imaging for Characterization of Orbital Lesions: Validation in a Large Prospective Study

Emma O'Shaughnessy, Chloé Le Cossec, Natasha Mambour, Adrien Lecoeuvre, Julien Savatovsky, Mathieu Zmuda, Loïc Duron, and Augustin Leclerc



## ABSTRACT

**BACKGROUND AND PURPOSE:** Orbital lesions are rare but serious. Their characterization remains challenging. Diagnosis is based on biopsy or surgery, which implies functional risks. It is necessary to develop noninvasive diagnostic tools. The goal of this study was to evaluate the diagnostic performance of dynamic contrast-enhanced MR imaging at 3T when distinguishing malignant from benign orbital tumors on a large prospective cohort.

**MATERIALS AND METHODS:** This institutional review board–approved prospective single-center study enrolled participants presenting with an orbital lesion undergoing a 3T MR imaging before surgery from December 2015 to May 2021. Morphologic, diffusion-weighted, and dynamic contrast-enhanced MR images were assessed by 2 readers blinded to all data. Univariable and multivariable analyses were performed. To assess diagnostic performance, we used the following metrics: area under the curve, sensitivity, and specificity. Histologic analysis, obtained through biopsy or surgery, served as the criterion standard for determining the benign or malignant status of the tumor.

**RESULTS:** One hundred thirty-one subjects (66/131 [50%] women and 65/131 [50%] men; mean age, 52 [SD, 17.1] years; range, 19–88 years) were enrolled. Ninety of 131 (69%) had a benign lesion, and 41/131 (31%) had a malignant lesion. Univariable analysis showed a higher median of volume transfer constant ( $K^{trans}$ ) and constant of transfer from the interstitial environment to the blood plasma ( $kep$ ) and a higher interquartile range of  $K^{trans}$  in malignant-versus-benign lesions (1.1 minute<sup>-1</sup> versus 0.65 minute<sup>-1</sup>,  $P = .03$ ; 2.1 minute<sup>-1</sup> versus 1.1 minute<sup>-1</sup>,  $P = .01$ ; 0.81 minute<sup>-1</sup> versus 0.65 minute<sup>-1</sup>,  $P = .009$ , respectively). The best-performing multivariable model in distinguishing malignant-versus-benign lesions included parameters from dynamic contrast-enhanced imaging, ADC, and morphology and reached an area under the curve of 0.81 (95% CI, 0.67–0.96), a sensitivity of 0.82 (95% CI, 0.55–1), and a specificity of 0.81 (95% CI, 0.65–0.96).

**CONCLUSIONS:** Dynamic contrast-enhanced MR imaging at 3T appears valuable when characterizing orbital lesions and provides complementary information to morphologic imaging and DWI.

**ABBREVIATIONS:** AUC = area under the curve; DCE = dynamic contrast-enhanced; ICC = intraclass correlation coefficient; IQR = interquartile range;  $kep$  = constant of transfer from the interstitial environment to the blood plasma (minute<sup>-1</sup>);  $K^{trans}$  = Constant of transfer from blood plasma to the interstitial environment (minute<sup>-1</sup>); OCVM = orbital cavernous venous malformation; ROC = receiver operating characteristic; TIC = time-intensity curve;  $Ve$  = extravascular-extracellular volume per unit of volume of tissue (mL/100mL of tissue; %);  $Vp$  = plasmatic volume per unit of volume of tissue (mL/100mL of tissue; %);  $WI$  = weighted imaging

Orbital lesions constitute a heterogeneous group, with various histopathologies, which are difficult to characterize solely by clinical examination and imaging. Among the most common benign orbital lesions, vascular malformations are prominent, with cavernous orbital malformation being by far the most frequent benign tumor in adults. Additionally, there is a group of orbital

inflammations that encompasses both idiopathic and specific inflammations, involving a wide range of causes. Among the most common malignant orbital lesions, lymphoma is the most frequent tumor, especially in the elderly. Carcinomas are also relatively common lesions. A particular diagnostic challenge lies in distinguishing orbital inflammation from lymphomas because they often exhibit similar morphologic features on imaging.<sup>1,2</sup> Histologic evidence obtained by biopsy or surgery remains the milestone for characterizing orbital lesions. However, biopsy or complete removal of an orbital lesion might be challenging and even dangerous. Indeed, all orbital surgery is complex due to the numerous vascular, nervous, and muscular structures within the orbit, which entail a non-negligible risk to both aesthetic and functional outcomes.<sup>3,4</sup>

Received October 6, 2023; accepted after revision December 5.

From the Departments of Neuroradiology (E.O., J.S., L.D., A.L.), Clinical Research (C.L.C., A.L.), and Ophthalmology (N.M., M.Z.), Rothschild Foundation Hospital, Paris, France.

Please address correspondence to Emma O'Shaughnessy, MD, MPH, Department of Neuroradiology, Rothschild Foundation Hospital, 25 rue Manin, 75019 Paris, France; e-mail: eoshaughnessy@for.paris



Indicates article with online supplemental data.

<http://dx.doi.org/10.3174/ajnr.A8131>



Developing noninvasive techniques for characterization, such as imaging, is therefore crucial and valuable to avoid unnecessary surgery in patients with benign lesions. A few imaging techniques proved useful to characterize orbital lesions. Color Doppler ultrasound measures the resistance index in lesion vessels. MR imaging gives specific imaging findings such as an enlarged infraorbital nerve, the ADC, or the intravoxel incoherent motion.<sup>5-13</sup>

Dynamic contrast-enhanced (DCE) imaging is another advanced MR imaging technique, allowing direct quantification of the perfusion volumes as well as an estimation of the capillary permeability, reflecting the tumor microcirculation.<sup>14</sup> It is, therefore, a valuable technique for the characterization of orbital lesions. DCE showed valuable results for assessing aggressiveness in optic pathway gliomas, lymphoproliferative disorders, and lacrimal gland tumors.<sup>15-17</sup> However, only a few studies have evaluated this technique in the orbit so far. Most evaluated small series of patients or were retrospective. Various approaches have been documented in the literature, encompassing qualitative, semiquantitative, or quantitative methods to evaluate DCE, along with the use of complex pharmacodynamic models. Consequently, a range of metrics has been suggested. Among these, the most promising ones for characterizing orbital lesions were the area under the curve  $AUC_{DCE}$  (millimol.liter<sup>-1</sup>.minute), the constant of transfer from the interstitial environment to the blood plasma (minute<sup>-1</sup>) (Kep), and the constant of transfer from blood plasma to the interstitial environment (minute<sup>-1</sup>) ( $K^{trans}$ ).<sup>15,16,18-26</sup>  $K^{trans}$  represents the rate constant for the transfer of substances from the blood plasma to the interstitial environment, while Kep (minute<sup>-1</sup>) signifies the rate constant for the reverse transfer from the interstitial environment back to the blood plasma. By means of the extended Tofts pharmacokinetic model, one can obtain 2 other parameters:  $V_e$  (milliliter/100mL of tissue; %) (the extravascular-extracellular volume within a given volume of tissue) and  $V_p$ ; the plasmatic volume within the same unit of tissue volume).

The goal of this study was to evaluate the diagnostic performance of DCE MR imaging at 3T when distinguishing malignant from benign orbital tumors on a large prospective cohort. This work is involved in the validation process of a new diagnostic imaging tool and biomarkers. It contributes to improving the level of evidence on the value of DCE MR for the diagnostic management of orbital tumors.

## MATERIALS AND METHODS

### Research Design

A prospective single-center study was conducted in a tertiary center specializing in ophthalmic diseases (NCT02434120). This study was approved by an Institutional Research Ethics Board and adhered to the tenets of the Declaration of Helsinki. Our study follows the Standards for Reporting of Diagnostic Accuracy Studies guidelines. Signed informed consent was obtained from all subjects.

### Population

A total of 345 participants were enrolled from December 2015 to May 2021.

Inclusion criteria were the following: 1) older than 18 years of age, 2) the presence of an orbital mass for which a biopsy or a

complete removal was planned, and 3) MR imaging completed before surgery.

Primary exclusion criteria were the following: 1) absolute or relative contraindication to MR imaging or to an injection of gadolinium, 2) opposition of the patient to participating in the study, and 3) absence of an affiliation to the social welfare system.

Secondary exclusion criteria were the following: 1) artifacts preventing analysis of the area of interest, 2) biopsy or surgery not performed, and 3) MR image analysis allowing a diagnosis considered as certain.

For all patients, no treatment that may alter imaging, such as steroids, and no surgery or biopsy was undertaken before MR imaging.

The final study cohort enrolled 131 participants. A flow chart is given in Fig 1.

### Clinical and Ophthalmologic Data

The clinical examination and management of patients was performed by a team of ophthalmologists specialized in orbital surgery at our institution. Medical history (cancer, autoimmune disease, HIV seropositivity, diabetes, hypertension, smoking) and clinical symptoms (diplopia, vision loss, exophthalmos, palpebral inflammation, ptosis) were noted. Fundoscopy was performed to detect optic disc edema and optic nerve atrophy. Oculomotricity testing was performed.

### Reference Standard

Histopathology was assessed, by an experienced pathologist, blinded to imaging data, who specialized in orbital pathology with 30 years of experience and was considered the reference standard. Orbital lesions were classified as malignant or benign. For further analysis, subgroups of lymphomas and orbital inflammations were extracted from malignant and benign lesions, respectively.

### MR Imaging Protocol

All orbital MR images were obtained on the same 3T Ingenia system (Philips Healthcare). The MR imaging protocol is shown in the Online Supplemental Data. DCE MR imaging acquisitions were based on a 3D T1 fast-field echo sequence with a temporal resolution of 2.9 seconds and a total duration of 6 minutes 23 seconds after an injection of a 0.1-mmol/kg bolus of gadobutrol (Gadovist; Bayer) at a speed of 4 mL/s. Participants were asked to look at a fixed point during the acquisitions to prevent kinetic artifacts generated by eye movement.

### Imaging Analysis

The morphologic analysis was performed by a senior neuroradiologist (A.L.) with >10 years of experience in orbital imaging, blinded to all data.

The reader assessed the following characteristics of each orbital lesion:

- Center of the lesion: lacrymal gland, orbital fat, eyelid, muscle, bone
- Boundaries, defined as regular or irregular
- Shape, defined as regular or irregular
- Type, defined as infiltrative with ill-defined margins or well-delineated with sharply defined margins



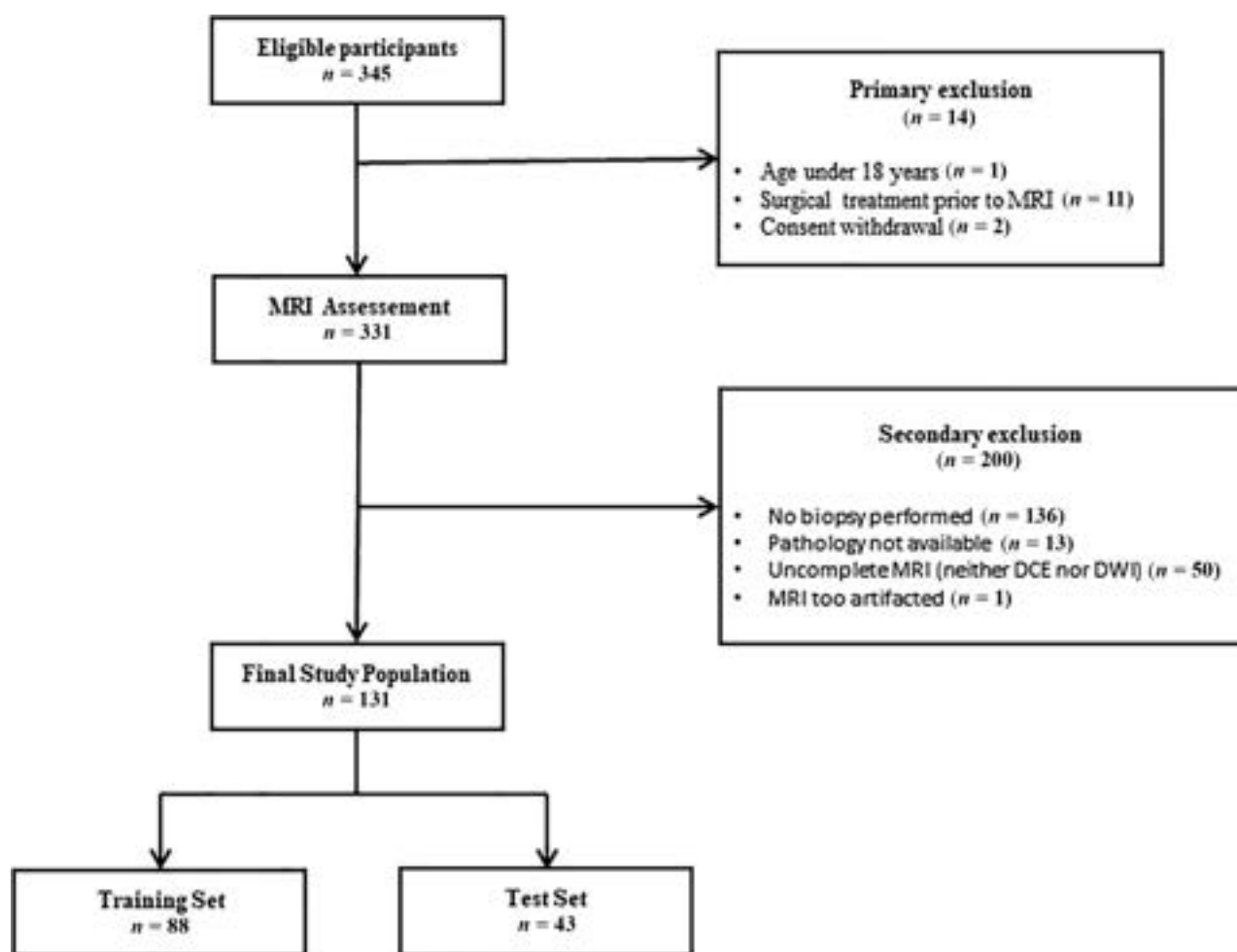


**FIG 1.** Flow chart.

- Signal intensity on T1WI and T2WI, defined as hypointense, isointense, or hyperintense in comparison with the signal intensity of a healthy ipsilateral or contralateral extraocular muscle (defined by normal morphology and signal)
- Signal intensity on DWI defined as hypointense, isointense, or hyperintense in comparison with the signal intensity of a healthy ipsilateral or contralateral extraocular muscle
- Signal intensity on the ADC map, defined as hypointense, isointense, or hyperintense in comparison with the signal intensity of a healthy ipsilateral or contralateral extraocular muscle
- Type of enhancement, defined as homogeneous or heterogeneous
- Enhancement intensity on contrast-enhanced T1WI, defined as absent, lower than that of the extraocular muscle, equal to that of the extraocular muscle, or higher than that of the extraocular muscle.

#### **DCE MR Imaging Postprocessing and Analysis**

All the postprocessing steps were performed using Olea Sphere software (Version 3.0; Olea Medical). Postprocessing was performed by a radiologist in training with 3 years of experience (E.O.). It lasted <1 minute. A 2D single-section ROI, encompassing the maximum area of the lesion, was manually drawn on each lesion on the AUC<sub>DCE</sub> colored map by the same radiologist

in training, as recommended by Qian et al.<sup>27</sup> A second ROI was manually drawn on the same lesion and at the same level on the ADC colored map. A second reading was done by the senior neuroradiologist (L.D.) to evaluate the interreader reproducibility.

A qualitative assessment of the DCE time-intensity curve (TIC) was made, classified into 3 types, according to Yuan et al.<sup>18</sup> type 1, defined as the persistent pattern with straight or curved lines and continuous enhancement over the entire dynamic study; type 2, defined as the plateau pattern with a relatively prominent increase of slope and a final intensity of 90%–100% of the peak grade; and type 3, defined as the washout pattern with a rapid increase of slope and a final intensity lower than 90% of the peak grade.

The AUC<sub>DCE</sub> (millimol.liter<sup>-1</sup>.minute), which is a semiquantitative parameter reflecting the relative quantity of contrast agent with time, was obtained by a model-free analysis of the TIC.

An extended Tofts pharmacokinetic model was then used, on the basis of Bayesian probabilities performing a biexponential modeling of diffusion, providing the 4 following quantitative parameters:  $K^{\text{trans}}$ ,  $K_{\text{ep}}$ ,  $V_e$ , and  $V_p$ .<sup>28</sup>

Both the median and interquartile range (IQR) were obtained for each DCE parameter. The median, which is a positional parameter less affected by extreme values than the mean, and the IQR, which gives information about the statistical dispersion,

**Table 1: Participant characteristics and lesion histopathologies**

Mean (SD) or No. (%)	Whole Sample ( <i>n</i> = 131)
Age	52 (17.1) (range, 19–88)
Sex	
Female	66/131 (50.4%)
Male	65/131 (49.6%)
Histopathology	
Benign lesion	
Overall	90/131 (68.7%)
Orbital inflammation	43/131 (32.8%)
Orbital cavernous venous malformation	9/131 (6.9%)
Other benign lesion	38/131 (29.0%)
Malignant lesion	
Overall	41/131 (31.3%)
Lymphoma	20/131 (15.3%)
Primary solid malignant tumor	12/131 (6.9%)
Solid tumor metastasis	9/131 (9.2%)
Bilateral lesion	22/131 (16.8%)

provide distinct information and thus are not considered redundant. Colored maps were displayed for all parameters.

### Statistical Methods

For all quantitative variables, the mean and standard deviation (SD) were provided. For all qualitative variables, both the number and percentage were given.

A univariable analysis was performed. For quantitative variables, a *t* test with a Welch correction if necessary or a Wilcoxon test was used. For qualitative variables,  $\chi^2$  or Fisher tests were used. Given the exploratory approach of this step, we did not correct for the  $\alpha$  inflation risk. The analysis was conducted for 2 comparisons: malignant-versus-benign lesions and lymphoma-versus-orbital inflammation.

A multivariable analysis was then performed using logistic regressions. The whole data set of patients was divided randomly into a training and a test set, with a respective proportion of two-thirds and one-third. We considered 4 models: model A with DCE parameters; model B with DCE parameters and ADC; model C with DCE and morphologic imaging parameters; and model D with DCE, ADC, and morphologic imaging parameters. Three additional models were also considered without DCE: model E with morphologic imaging parameters alone, model F with ADC alone, and model G with morphologic imaging parameters and ADC.

For each model, variables with a *P* value < 20% in univariable analysis were considered. A stepwise procedure based on the Akaike criterion was used to select the relevant parameters.

For each parameter of DCE and each model, a receiver operating characteristic (ROC) curve with a 95% confidence interval was drawn, and the AUC was computed. Sensitivity and specificity were calculated when AUCs were >0.80. The Youden method was used for threshold identification. Confidence intervals for the model ROC curves and AUC were obtained by a bootstrap technique. The *P* value for the AUC was obtained using the DeLong test, at 5%  $\alpha$  risk.

The interobserver agreement was evaluated using the Bland-Altman limits of agreement and an intraclass correlation coefficient

(ICC) with 95% confidence intervals for quantitative variables<sup>29</sup> and the Cohen  $\kappa$  for qualitative variables.

Analyses were performed using the R statistical and computing software, Version 4.2.0 (<http://www.r-project.org/>) by a methodologist statistician (C.L.C.) with 8 years of experience.

## RESULTS

### Study Population

A total of 131 patients (66/131 [50%] women and 65/131 [50%] men (mean age, 52 [SD, 17.1] years; range, 19–88 years) were enrolled, among whom 41/131 (31%) had malignant lesions. Participant characteristics and lesion histopathologies are available in Table 1. More details on histopathologies can be found in the Online Supplemental Data.

### Distinction between Malignant and Benign Orbital Lesions

**Univariable Analysis.** Patients with a malignant lesion were significantly older than those with a benign one: 62.4 (SD, 15.4) versus 47.3 (SD, 15.8) years, *P* < .001.

Regarding the morphologic features, there was a significant difference in DWI and ADC signal, enhancement intensity, and the type of TIC between patients with a malignant lesion compared with those with a benign lesion (*P* < .001).

Among all DCE parameters, the medians of  $K^{trans}$  and  $K_{ep}$  and the IQR of  $K^{trans}$  were significantly higher in malignant lesions compared with benign lesions: 1.1 minute<sup>-1</sup> versus 0.65 minute<sup>-1</sup>, *P* = .03; 2.1 minute<sup>-1</sup> versus 1.1 minute<sup>-1</sup>, *P* = .01; and 0.81 minute<sup>-1</sup> versus 0.37 minute<sup>-1</sup>, *P* = .009, respectively. The median of the AUC<sub>DCE</sub> was significantly lower in malignant lesions compared with benign ones:  $3.8 \times 10^4$  versus  $5.4 \times 10^4$ , *P* = .01. The median of the ADC was significantly lower in malignant lesions compared with benign ones: 0.86 versus 1.2 mm<sup>2</sup>/s, *P* = .001. The detailed data for both groups are given in the Online Supplemental Data.

**ROC Curves for Each DCE Parameter and ADC.** The parameters with the highest AUC were the median of  $K_{ep}$ , the IQR of  $K_{ep}$ , and the IQR of  $K^{trans}$  with AUCs of 0.74 (95% CI, 0.65–0.83), 0.73 (95% CI, 0.64–0.82), and 0.71 (95% CI, 0.61–0.80), respectively. The AUC of the median and the IQR of the ADC were, respectively, 0.74 (95% CI, 0.63–0.85) and 0.6 (95% CI, 0.48–0.72). The ROC curves of each DCE parameter and ADC are shown in Fig 2.

**Multivariable Analysis.** The training set included 88 patients, and the test set, 43 patients, with 26 and 15 malignant lesions, respectively. The model with the highest diagnostic performance was model D (DCE, ADC, and morphologic imaging features), with an AUC = 0.81 (95% CI, 0.67–0.96) (*P* value =  $1.6 \times 10^{-5}$ , in comparison with an AUC of 0.5), sensitivity = 0.82 (95% CI, 0.55–1), and specificity = 0.81 (95% CI, 0.65–0.96). The Online Supplemental Data show the diagnostic performance of models evaluated, and ROC curves are available in Fig 3.

Model D had a sensitivity of 0.82 (95% CI, 0.55–1) and a specificity of 0.81 (95% CI, 0.65–0.96), with 2 false-negatives and 5 false-positives. Model E had a specificity of 0.48 (95% CI, 0.3–0.67) with 14 false-positives. Model F showed a sensitivity of 0.5 (95% CI,

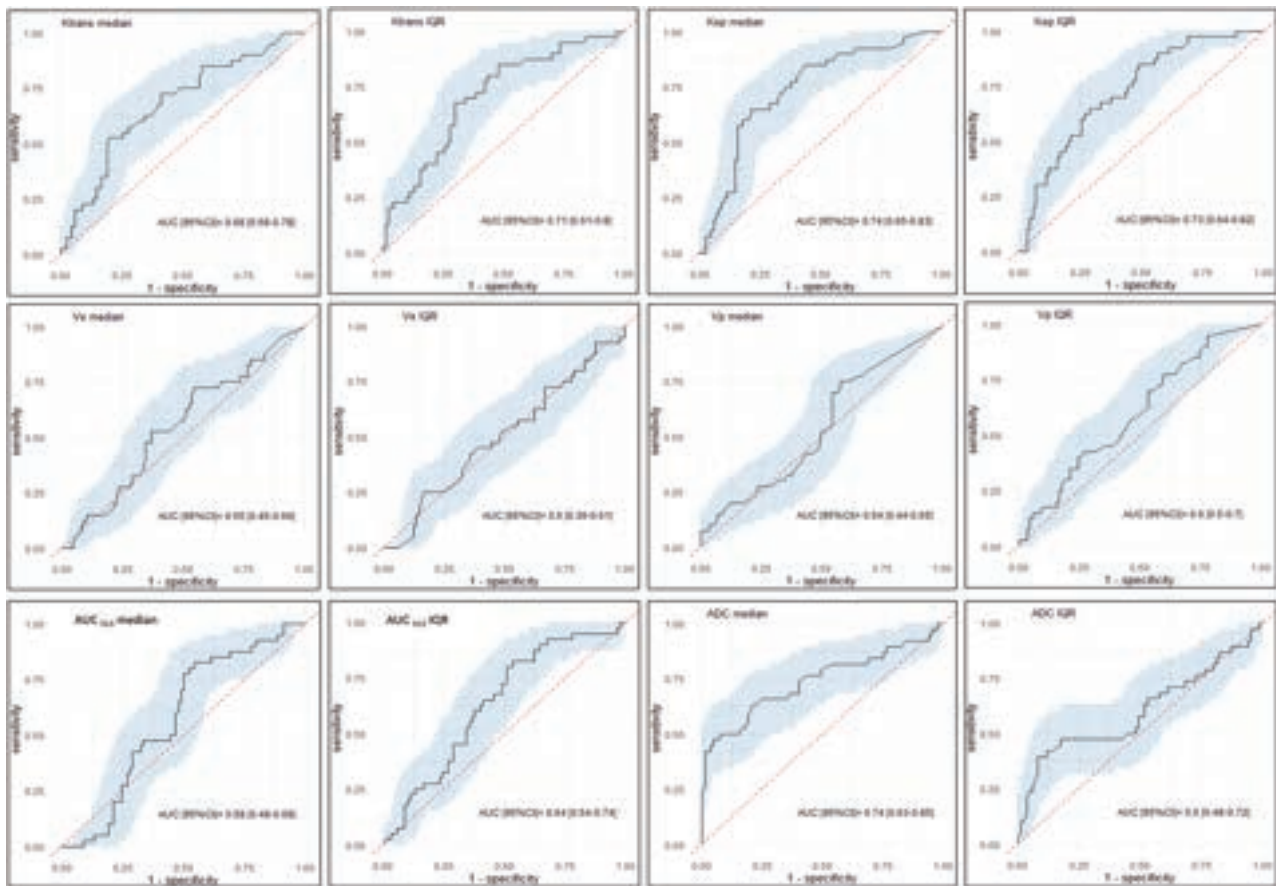


**FIG 2.** ROC curves of each DCE and ADC parameter when distinguishing malignant from benign lesions. The x-axis refers to 1-specificity, and the y-axis refers to the sensitivity. The *black line* represents the AUC; the *blue area*, the 95% confidence interval; and the *dotted red line*, the diagonal, ie, an AUC of 0.5.

0.25–0.75) with 6 false-negatives. Model G demonstrated a specificity of 0.58 (95% CI, 0.38–0.77) with 11 false-positives.

**Interreader Reproducibility.** Interreader reproducibility, performed on the distinction between malignant and benign lesions, was good for the IQR of Ve and the median of Vp with an ICC of 0.73 and 0.87, respectively. Interreader reproducibility was excellent for all other quantitative DCE parameters, with an ICC higher than 0.90 (Table 2).

### Distinction between Lymphomas and Orbital Inflammations

**Univariable Analysis.** Among all DCE parameters, the medians of  $K^{trans}$  and Kep and the IQR of  $K^{trans}$  and Kep were significantly higher in lymphomas compared with orbital inflammations: 1.2 versus 0.6  $\text{minute}^{-1}$ ,  $P = .001$ ; 2.3 versus 1.1  $\text{minute}^{-1}$ ,  $P < .001$ ; 1 versus 0.3  $\text{minute}^{-1}$ ,  $P < .001$ ; and 1.8 versus 0.6  $\text{minute}^{-1}$ ,  $P < .001$ , respectively. The detailed data for both groups are given in the Online Supplemental Data.

**ROC Curves for Each DCE Parameter.** The parameters with the highest AUC were the median of Kep and the IQR of Kep, with AUCs of 0.83 (95% CI, 0.73–0.93) and 0.81 (95% CI, 0.71–0.92), respectively (Online Supplemental Data).

**Multivariable Analysis.** The training set included 43 patients, and the test set, 20 patients, with 14 and 6 lymphomas, respectively. The model with the highest diagnostic performance was the model D, with an AUC = 0.84 (95% CI, 0.65–0.1), sensitivity = 0.83 (95% CI, 0.5–1), and specificity = 0.85 (95% CI, 0.62–1). The Online Supplemental Data show the diagnostic performance of models evaluated, and the ROC curves are in the Online Supplemental Data.

An example of orbital tumor is provided as Fig 4. Additional examples are also provided in the Online Supplemental Data.

### DISCUSSION

Our study showed that DCE is a valuable tool when characterizing orbital lesions, either alone or in combination with morphologic imaging and DWI.

This large prospective work involves the validation process of a new diagnostic imaging tool and biomarkers. Indeed, a few studies already showed the promising results of DCE when characterizing orbital lesions, but most were retrospective, with inherent methodologic bias, and the rare prospective ones included only a small number of patients.<sup>23,30</sup> By confirming the previous results in the literature, our study improves the level of evidence of this technique, facilitating its use in clinical practice. This work suggests that DCE can help distinguish malignant

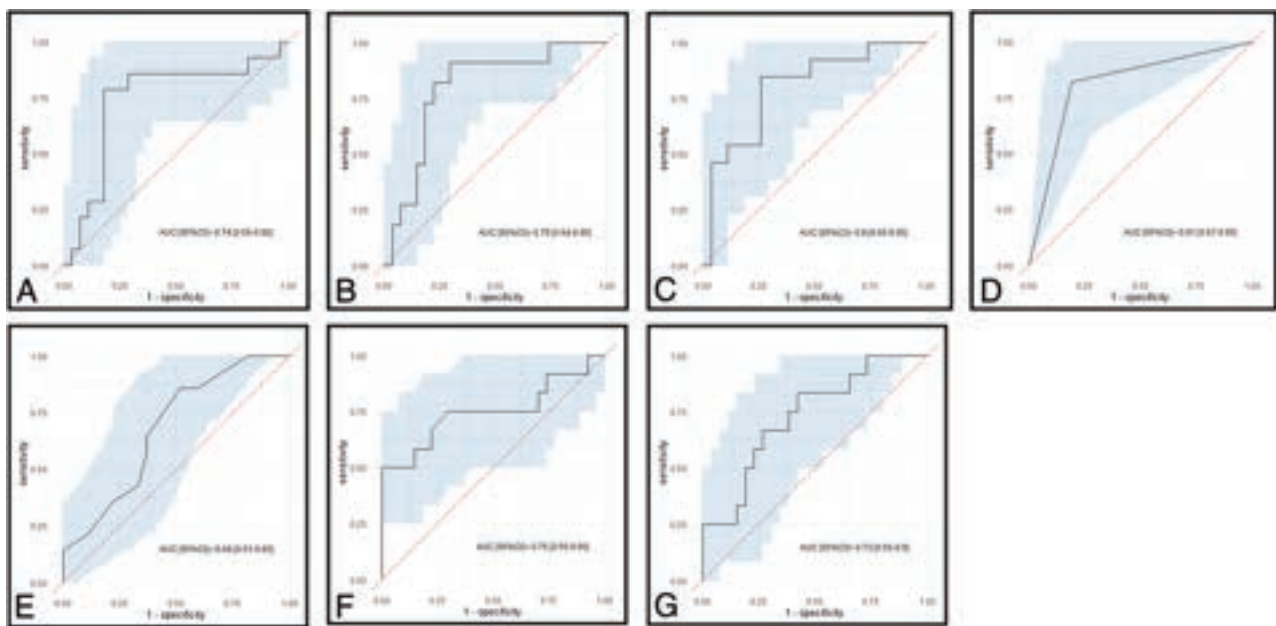


**FIG 3.** ROC curves of each model when distinguishing malignant from benign lesions. The x-axis refers to 1-specificity; the y-axis, to the sensitivity. The *black line* represents the AUC; the *blue area*, the 95% confidence interval; and the *dotted red line*, the diagonal, ie, an AUC of 0.5. A indicates model A with DCE parameters only; B, model B with DCE and ADC parameters combined; C, model C with DCE and morphologic imaging parameters combined; D, model D with DCE, ADC, and morphologic imaging parameters combined; E, model E with morphologic imaging parameters only; F, model F with ADC only; and G, model G with ADC and morphologic imaging parameters.

**Table 2: Interobserver reproducibility**

$K^{\text{trans}}$ (minute <sup>-1</sup> )	
Median (ICC)	0.99
IQR (ICC)	0.96
Kep (minute <sup>-1</sup> )	
Median (ICC)	0.99
IQR (ICC)	0.99
Ve (mL/100 mL of tissue; %)	
Median (ICC)	0.94
IQR (ICC)	0.73
Vp (mL/100 mL of tissue; %)	
Median (ICC)	0.87
IQR (ICC)	0.94
AUC <sub>DCE</sub> (mmol.min/L)	
Median (ICC)	0.98
IQR (ICC)	0.96
Type of the DCE TIC	
Cohen $\kappa$	0.67

from benign lesions, which is in line with findings in previous articles.<sup>19,21,24</sup> Some studies have also suggested that DCE could improve characterization of orbital cavernous venous malformations, schwannomas, or optic pathway gliomas.<sup>15,22,31</sup>

In this study, we decided to distinguish orbital cavernous venous malformation (OCVM) from other venous malformations, defined according the 2018 International Society for the Study of Vascular Anomalies.<sup>32</sup> Indeed, because slow-flow venous malformations of the orbit encompass several distinct diseases including OCVM, the International Society for the Study of Vascular Anomalies classification might be inaccurate in the orbit.<sup>33,34</sup> To avoid any confusion, we used the term OCVM.<sup>35</sup>

Among DCE parameters, Kep was higher in malignant lesions compared with benign ones, in line with previous

studies.<sup>19,21,23,25,27</sup> The ROC curve for Kep yielded an AUC of 0.74 versus an AUC of 0.84 reported by Hu et al.<sup>21</sup>

We showed that the constant of transfer from blood plasma to the interstitial environment ( $K^{\text{trans}}$ ) was higher in malignant lesions compared with benign ones and in lymphomas compared with orbital inflammations, also in line with previous studies.<sup>23-25</sup> The ROC curve for  $K^{\text{trans}}$  yielded an AUC of 0.68, which is a little lower than that of the Kep. Physiopathologically, the  $K^{\text{trans}}$  reflects both the perfusion and permeability processes. It might be influenced by several vascular factors, making its physiopathologic interpretation challenging. Nevertheless,  $K^{\text{trans}}$  is one of the most widely used DCE parameters in head and neck diseases for both diagnosis and prognosis.

Most interesting, we showed that the AUC<sub>DCE</sub> was lower in malignant lesions compared with benign ones and in lymphomas compared with orbital inflammations. The AUC<sub>DCE</sub> has already shown its usefulness when distinguishing orbital lesions in the literature.<sup>19,23,24</sup> The AUC<sub>DCE</sub> can be obtained without using any pharmacokinetic models, making it easier to use in clinical practice than the Kep or the  $K^{\text{trans}}$ . Jittapiromsak et al<sup>19</sup> concluded that the AUC<sub>DCE</sub> was the best diagnostic criterion and that there was no need for using more complex pharmacokinetic models. However, the ROC curve for the AUC<sub>DCE</sub> yielded an AUC of 0.58, which is substantially less than that of Kep and  $K^{\text{trans}}$ . In addition, the AUC<sub>DCE</sub> is derived from a semiquantitative approach that has limitations, not always having a physical meaning and being mixed measures. The AUC<sub>DCE</sub> is a combination of the vascular permeability of tissue blood flow and fractional interstitial space.<sup>28</sup> Therefore, we believe that it is probably better to use a pharmacokinetic model. Most postprocessing software is now able to compute DCE data very quickly.



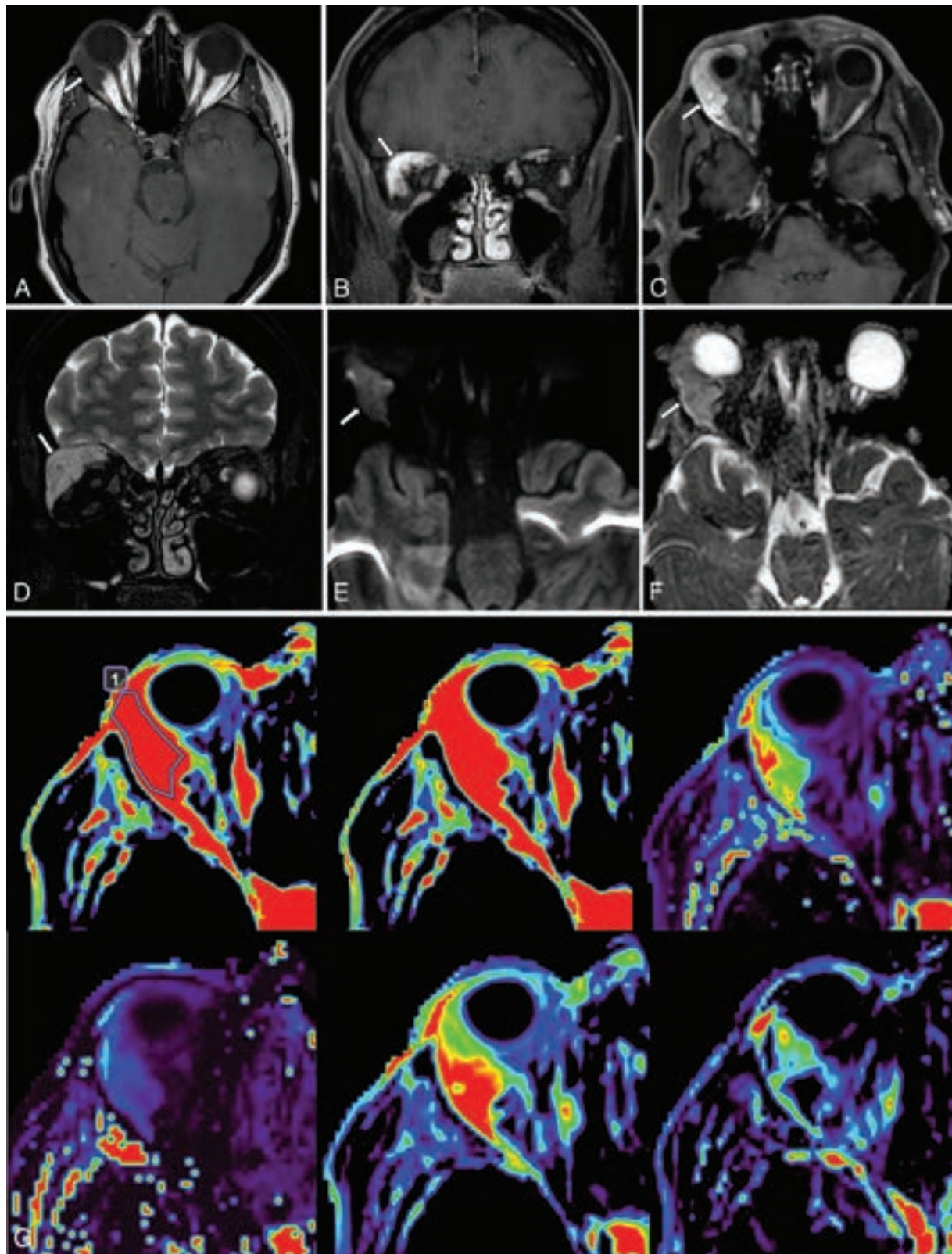


**FIG 4.** 3T MR imaging in a 45-year-old female patient presenting with vertical diplopia. Axial T1WI (A), contrast-enhanced coronal (B) and axial (C) Dixon T1WI, coronal Dixon T2WI (D), axial DWI (E), axial ADC (F), and DCE MR imaging (G) show a right orbital mass (arrow). DCE colorimetric maps are presented as follows from left to right and from top to bottom: AUC<sub>DCE</sub>, K<sup>trans</sup>, V<sub>e</sub>, V<sub>p</sub>. On the basis of morphologic and DWI features alone, the lesion was considered benign. DCE shows high K<sup>trans</sup> and K<sup>ep</sup>, suggesting malignancy. Postsurgery, the final diagnosis was a carcinoma.

In this study the DCE TIC was significantly different in malignant lesions compared with benign ones and in lymphomas compared with orbital inflammations, in line with the literature.<sup>17-19,23</sup>

However, the overlap among the different types of TICs is substantial, making this tool hazardous to use on its own. Indeed, the 3 types of curves are found in each of the groups, not allowing a clinically relevant discrimination. Furthermore, its interobserver reproducibility is limited compared with other DCE parameters, both in this work and in the literature.<sup>36</sup>

Beyond using a single DCE parameter, we showed that a combination of DCE and ADC yielded higher diagnostic performance compared with DCE or ADC alone, which is similar to previous data reported.<sup>16,17,20,23,25</sup> The ADC has proved extremely useful when characterizing orbital lesions, especially for diagnosing orbital lymphomas.<sup>6-9</sup> However, DWI alone failed to correctly classify all malignant lesions such as orbital carcinomas in our study, whereas the combination of DCE and ADC managed to do so. This specific example shows that DCE might translate into a change of management in clinical practice. Moreover, combining DCE and ADC and morphologic imaging features yielded the highest sensitivity among all models when distinguishing malignant from benign lesions and the highest sensitivity and specificity when distinguishing lymphomas from orbital inflammations. Conversely, we showed that models without DCE (morphology alone, ADC alone, or morphology combined with ADC) yielded lower accuracy compared with models with DCE. These results support the importance of performing a comprehensive analysis of all MR imaging data, including a DCE sequence, despite the time cost, when characterizing orbital lesions. This comprehensive approach is in line with 2 radiomics studies showing that all MR imaging sequences provided original and nonredundant features when characterizing orbital lesions and showing that a bag-of-features-based radiomics including DCE data was more effective than without DCE when differentiating ocular adnexal lymphoma and idiopathic orbital inflammation.<sup>26,37</sup>

The duration of our protocol was <20 minutes, which is acceptable. There are no current guidelines regarding the MR imaging protocol when characterizing orbital lesions. On the basis of our study and on the literature data, we suggest that a minimum protocol might include both precontrast and fat-suppressed or Dixon contrast-enhanced T1WI, T2WI, DWI, and DCE imaging, with calculation of the ADC and of at least 1 quantitative parameter such as the  $K_{ep}$  or  $K^{trans}$ . Postprocessing of both DWI and DCE is now relatively easy and fast, making them usable in clinical practice. It was <1 minute in our study and might be shortened with automatization of the process, which is available on most clinically available postprocessing software. Moreover, this postprocessing might easily be conducted by a technician rather than a radiologist to alleviate the radiologist's workload. We showed that the interobserver reproducibility was high for quantitative DCE parameters and substantially higher than a visual analysis of the type of DCE TIC, in line with the literature.<sup>21</sup> Integrating DCE into clinical practice might help achieve more reliable and reproducible characterization of orbital lesions among various centers worldwide.

Our study has some limitations. First, this is a single-center study including a relatively small number of patients. However, orbital lesions remain rare, thus enrolling patients is challenging. Our study remains a large prospective one evaluating DCE when characterizing orbital lesions. Multicentric prospective studies would be valuable to evaluate the reproducibility of our results. Second, a substantial number of patients initially enrolled in the study and scheduled for surgery did not ultimately undergo surgery after MR imaging but underwent a simple follow-up. Among them, a substantial number of patients had a well-delineated intraconal lesion with typical high signal intensity on T2WI and a progressive centripetal pattern of enhancement easily visible on native DCE MR images, making the diagnosis of orbital cavernous venous malformation almost pathognomonic. Third, the DCE model we used was an extended Tofts model, whereas a study evaluating various DCE models in the orbit showed that the 2CX model was the best-performing one.<sup>24</sup> However, the 2CX model is not available on most postprocessing software, including the Olea Sphere software we used. Fourth, all MR imaging examinations were performed on an optimized 3T MR imaging machine with a 32-channel head coil in a tertiary center specializing in ophthalmology, which might limit the generalization of our results. DCE parameters might vary depending on the type of MR imaging scanner and the type of DCE sequence, so it was not reasonable to provide DCE parameter thresholds for the management of patients with an orbital lesion. Fifth, we performed a DCE sequence with both high spatial and time resolution, which might not be possible on all MR imaging. Further research is needed to evaluate whether a DCE 1.5T MR imaging or one performed with a lower time resolution might achieve equivalent accuracy. Conversely, 7T might help to characterize orbital lesions.<sup>38</sup> Finally, we did not integrate a radiomics analysis into our study, whereas radiomics studies showed high diagnostic performance.<sup>26,39,40</sup>

## CONCLUSIONS

This large prospective study confirms that DCE MR imaging is a valuable tool when characterizing orbital lesions. It can be a complementary source of information and can improve the diagnostic capabilities of 3T MR imaging when characterizing orbital lesions, in particular in combination with DWI. DCE should be considered in clinical practice to improve the diagnosis of orbital lesions. This work participates in the validation process of a new diagnostic imaging tool and biomarkers. It contributes to improving the level of evidence of this technique, and it might help accelerate the adoption of DCE in imaging protocols in all centers worldwide when characterizing orbital lesions.

## ACKNOWLEDGMENTS

We acknowledge Souhila Silem and Bahia Abdat, clinical research technicians in the Department of Clinical Research, Rothschild Foundation Hospital, Paris, France, for actively contributing to this study.

**Disclosure forms** provided by the authors are available with the full text and PDF of this article at [www.ajnr.org](http://www.ajnr.org).



## REFERENCES

- Shields JA, Shields CL, Scartozzi R. **Survey of 1264 patients with orbital tumors and simulating lesions.** *Ophthalmology* 2004;111:997–1008 CrossRef Medline
- Demirci H, Shields CL, Shields JA, et al. **Orbital tumors in the older adult population.** *Ophthalmology* 2002;109:243–48 CrossRef Medline
- Kansakar P, Sundar G. **Vision loss associated with orbital surgery: a major review.** *Orbit* 2020;39:197–208 CrossRef Medline
- Purgason PA, Hornblass A. **Complications of surgery for orbital tumors.** *Ophthalmic Plast Reconstr Surg* 1992;8:88–93 CrossRef Medline
- Lecler A, Boucenna M, Lafitte F, et al. **Usefulness of colour Doppler flow imaging in the management of lacrimal gland lesions.** *Eur Radiol* 2017;27:779–89 CrossRef Medline
- Jaju A, Rychlik K, Ryan ME. **MRI of pediatric orbital masses: role of quantitative diffusion-weighted imaging in differentiating benign from malignant lesions.** *Clin Neuroradiol* 2020;30:615–24 CrossRef Medline
- Eissa L, Abdel Razek AA, Helmy E. **Arterial spin labeling and diffusion-weighted MR imaging: utility in differentiating idiopathic orbital inflammatory pseudotumor from orbital lymphoma.** *Clin Imaging* 2021;71:63–68 CrossRef Medline
- Elkhamary SM, Galindo-Ferreiro A, AlGhafri L, et al. **Characterization of diffuse orbital mass using apparent diffusion coefficient in 3-Tesla MRI.** *Eur J Radiol Open* 2018;5:52–57 CrossRef Medline
- Phuttharak W, Boonrod A, Patjanasontorn N, et al. **The roles of the diffusion-weighted imaging in orbital masses.** *J Med Imaging Radiat Oncol* 2017;61:753–58 CrossRef Medline
- Lecler A, Duron L, Zmuda M, et al. **Intravoxel incoherent motion (IVIM) 3T MRI for orbital lesion characterization.** *Eur Radiol* 2021;31:14–23 CrossRef Medline
- Soussan JB, Deschamps R, Sadik JC, et al. **Infraorbital nerve involvement on magnetic resonance imaging in European patients with IgG4-related ophthalmic disease: a specific sign.** *Eur Radiol* 2017;27:1335–43 CrossRef Medline
- Sepahdari AR, Aakalu VK, Setabutr P, et al. **Indeterminate orbital masses: restricted diffusion at MR imaging with echo-planar diffusion-weighted imaging predicts malignancy.** *Radiology* 2010;256:554–64 CrossRef Medline
- Shor N, Sené T, Zuber K, et al. **Discriminating between IgG4-related orbital disease and other causes of orbital inflammation with intra voxel incoherent motion (IVIM) MR imaging at 3T.** *Diagn Interv Imaging* 2021;102:727–34 CrossRef Medline
- Cuenod CA, Balvay D. **Perfusion and vascular permeability: basic concepts and measurement in DCE-CT and DCE-MRI.** *Diagn Interv Imaging* 2013;94:1187–204 CrossRef Medline
- Jost SC, Ackerman JW, Garbow JR, et al. **Diffusion-weighted and dynamic contrast-enhanced imaging as markers of clinical behavior in children with optic pathway glioma.** *Pediatr Radiol* 2008;38:1293–99 CrossRef Medline
- Xu XQ, Hu H, Liu H, et al. **Benign and malignant orbital lymphoproliferative disorders: differentiating using multiparametric MRI at 3.0T.** *J Magn Reson Imaging* 2016;45:167–76 CrossRef Medline
- Li X, Wu X, Qian J, et al. **Differentiation of lacrimal gland tumors using the multi-model MRI: classification and regression tree (CART)-based analysis.** *Acta Radiol* 2022;63:923–32 CrossRef Medline
- Yuan Y, Kuai XP, Chen XS, et al. **Assessment of dynamic contrast-enhanced magnetic resonance imaging in the differentiation of malignant from benign orbital masses.** *Eur J Radiol* 2013;82:1506–11 CrossRef Medline
- Jittapiromsak N, Hou P, Liu HL, et al. **Dynamic contrast-enhanced MRI of orbital and anterior visual pathway lesions.** *Magn Reson Imaging* 2018;51:44–50 CrossRef Medline
- Haradome K, Haradome H, Usui Y, et al. **Orbital lymphoproliferative disorders (OLPDs): value of MR imaging for differentiating orbital lymphoma from benign OPLDs.** *AJNR Am J Neuroradiol* 2014;35:1976–82 CrossRef Medline
- Hu H, Xu XQ, Liu H, et al. **Orbital benign and malignant lymphoproliferative disorders: differentiation using semi-quantitative and quantitative analysis of dynamic contrast-enhanced magnetic resonance imaging.** *Eur J Radiol* 2017;88:88–94 CrossRef Medline
- Xian J, Zhang Z, Wang Z, et al. **Evaluation of MR imaging findings differentiating cavernous haemangiomas from schwannomas in the orbit.** *Eur Radiol* 2010;20:2221–28 CrossRef Medline
- Ro SR, Asbach P, Siebert E, et al. **Characterization of orbital masses by multiparametric MRI.** *Eur J Radiol* 2016;85:324–36 CrossRef Medline
- Lecler A, Balvay D, Cuenod CA, et al. **Quality-based pharmacokinetic model selection on DCE-MRI for characterizing orbital lesions.** *J Magn Reson Imaging* 2019;50:1514–25 CrossRef Medline
- Wang Y, Song L, Guo J, et al. **Value of quantitative multiparametric MRI in differentiating pleomorphic adenomas from malignant epithelial tumors in lacrimal gland.** *Neuroradiology* 2020;62:1141–47 CrossRef Medline
- Hou Y, Xie X, Chen J, et al. **Bag-of-features-based radiomics for differentiation of ocular adnexal lymphoma and idiopathic orbital inflammation from contrast-enhanced MRI.** *Eur Radiol* 2021;31:24–33 CrossRef Medline
- Qian W, Xu XQ, Hu H, et al. **Dynamic contrast-enhanced MRI in orbital lymphoproliferative disorders: effects of region of interest selection methods on time efficiency, measurement reproducibility, and diagnostic ability.** *J Magn Reson Imaging* 2018;47:1298–305 CrossRef Medline
- Gaddikeri S, Gaddikeri RS, Tailor T, et al. **Dynamic contrast-enhanced MR imaging in head and neck cancer: techniques and clinical applications.** *AJNR Am J Neuroradiol* 2016;37:588–95 CrossRef Medline
- Benchoufi M, Matzner-Lober E, Molinari N, et al. **Interobserver agreement issues in radiology.** *Diagn Interv Imaging* 2020;101:639–41 CrossRef Medline
- Russo C, Strianese D, Perrotta M, et al. **Multi-parametric magnetic resonance imaging characterization of orbital lesions: a triple blind study.** *Semin Ophthalmol* 2020;35:95–102 CrossRef Medline
- Tanaka A, Mihara F, Yoshiura T, et al. **Differentiation of cavernous hemangioma from schwannoma of the orbit: a dynamic MRI study.** *AJR Am J Roentgenol* 2004;183:1799–804 CrossRef Medline
- International Society for the Study of Vascular Anomalies. **Classification.** <https://www.issva.org/classification>. Accessed August 26, 2023
- Tawfik HA, Dutton JJ. **Orbital vascular anomalies: a nomenclatorial, etiologic, and nosologic conundrum.** *Ophthalmic Plast Reconstr Surg* 2022;38:108–21 CrossRef Medline
- Steele L, Zbeidy S, Thomson J, et al. **How is the term haemangioma used in the literature? An evaluation against the revised ISSVA classification.** *Pediatr Dermatol* 2019;36:628–33 CrossRef Medline
- Elbaze S, Duron L, Mambour N, et al. **A signature of structural MRI features at 3 Tesla allows an accurate characterization of orbital cavernous venous malformation.** *Eur Radiol* 2023;33:2149–59 CrossRef Medline
- Xian J, Zhang Z, Wang Z, et al. **Value of MR imaging in the differentiation of benign and malignant orbital tumors in adults.** *Eur Radiol* 2010;20:1692–702 CrossRef Medline
- Lecler A, Duron L, Balvay D, et al. **Combining multiple magnetic resonance imaging sequences provides independent reproducible radiomics features.** *Sci Rep* 2019;9:2068 CrossRef Medline
- Lecler A, Duron L, Charlon E, et al. **Comparison between 7 Tesla and 3 Tesla MRI for characterizing orbital lesions.** *Diagn Interv Imaging* 2022;103:433–39 CrossRef Medline
- Duron L, Heraud A, Charbonneau F, et al. **A magnetic resonance imaging radiomics signature to distinguish benign from malignant orbital lesions.** *Invest Radiol* 2021;56:173–80 CrossRef Medline
- Duron L, Savatovsky J, Fournier L, et al. **Can we use radiomics in ultrasound imaging? Impact of preprocessing on feature repeatability.** *Diagn Interv Imaging* 2021;102:659–67 CrossRef Medline

# Application of Spinal Subtraction and Bone Background Fusion CTA in the Accurate Diagnosis and Evaluation of Spinal Vascular Malformations

Xuehan Hu, Zhidong Yuan, Kaiyin Liang, Min Chen, Zhen Zhang, Hairong Zheng, and Guanxun Cheng



## ABSTRACT

**BACKGROUND AND PURPOSE:** Accurate pretreatment diagnosis and assessment of spinal vascular malformations using spinal CTA are crucial for patient prognosis, but the postprocessing reconstruction may not be able to fully depict the lesions due to the complexity inherent in spinal anatomy. Our purpose was to explore the application value of the spinal subtraction and bone background fusion CTA (SSBBF-CTA) technique in precisely depicting and localizing spinal vascular malformation lesions.

**MATERIALS AND METHODS:** In this retrospective study, patients (between November 2017 and November 2022) with symptoms similar to those of spinal vascular malformations were divided into diseased (group A) and nondiseased (group B) groups. All patients underwent spinal CTA using Siemens dual-source CT. Multiplanar reconstruction; routine bone subtraction, and SSBBF-CTA images were obtained using the snygo.via and ADW4.6 postprocessing reconstruction workstations. Multiple observers researched the following 3 aspects: 1) preliminary screening capability using original images with multiplanar reconstruction CTA, 2) the accuracy and stability of the SSBBF-CTA postprocessing technique, and 3) diagnostic evaluation of spinal vascular malformations using the 3 types of postprocessing images. Diagnostic performance was analyzed using receiver operating characteristic analysis, while reader or image differences were analyzed using the Wilcoxon signed-rank test or the Kruskal-Wallis rank sum test.

**RESULTS:** Forty-nine patients (groups A and B: 22 and 27 patients; mean ages, 44.0 [SD, 14.3] years and 44.6 [SD, 15.2] years; 13 and 16 men) were evaluated. Junior physicians showed lower diagnostic accuracy and sensitivity using multiplanar reconstruction CTA (85.7% and 77.3%) than senior physicians (93.9% and 90.9%, 98% and 95.5%). Short-term trained juniors achieved SSBBF-CTA image accuracy similar to that of experienced physicians ( $P > .05$ ). In terms of the visualization and localization of spinal vascular malformation lesions (nidus/fistula, feeding artery, and drainage vein), both multiplanar reconstruction and SSBBF-CTA outperformed routine bone subtraction CTA ( $P = .000$ ). Compared with multiplanar reconstruction, SSBBF-CTA allowed less experienced physicians to achieve superior diagnostic capabilities (comparable with those of experienced radiologists) more rapidly ( $P < .05$ ).

**CONCLUSIONS:** The SSBBF-CTA technique exhibited excellent reproducibility and enabled accurate pretreatment diagnosis and assessment of spinal vascular malformations with high diagnostic efficiency, particularly for junior radiologists.

**ABBREVIATIONS:** AP = arterial phase; AUC = area under the curve; CE-MRA = contrast-enhanced MRA; MPR-CTA = multiplanar reconstruction CTA; RBS-CTA = routine bone subtraction CTA; ROC = receiver operating characteristic; SSBBF-CTA = spinal subtraction and bone background fusion CTA; SVM = spinal vascular malformation; 3D-VR = 3D volume-rendering

Spinal vascular malformations (SVMs) are rare CNS vascular lesions, with spinal AVFs (arteriovenous directly shunting with a fistula) and AVMs (arteriovenous connection with a true nidus) being the most common types (95%).<sup>1</sup> Their clinical presentations

are variable and nonspecific, including progressive motor, sensory, and urogenital disturbances, similar to chronic myelitis, demyelinating lesions, disc lesions, and so forth.<sup>2,3</sup> However, the treatments and prognoses differ completely. Delayed or incorrect diagnosis and treatment can lead to serious complications, permanent disability, and even fatality.<sup>4-6</sup> Therefore, accurate

Received August 26, 2023; accepted after revision December 2.

From the Department of Radiology (X.H., Z.Y., K.L., Z.Z., G.C.), Peking University Shenzhen Hospital, Shenzhen, China; Paul C. Lauterbur Research Center for Biomedical Imaging (X.H., H.Z.), Shenzhen Institutes of Advanced Technology, Chinese Academy of Sciences; and Department of Radiology (M.C.), Southern University of Science and Technology Hospital, Shenzhen, China.

Xuehan Hu and Zhidong Yuan contributed equally to this work and should be considered co-first authors.

This work was supported by the China Postdoctoral Science Foundation (No. 2021M703373) and the Shenzhen High-Level Hospital Construction Fund.

Please address correspondence to Guanxun Cheng, MD, PhD, Peking University Shenzhen Hospital, 1120#, Lianhua Rd, Futian District, Shenzhen, 518036 Guangdong, China; e-mail: chengguanxun@outlook.com



Indicates article with online supplemental data.



Indicates article with supplemental online video.

<http://dx.doi.org/10.3174/ajnr.A8112>



diagnosis and evaluation before treatment are crucial for developing an appropriate treatment plan and improving neurologic function.

Spinal DSA is the criterion standard for diagnosing SVMs.<sup>7,8</sup> However, selective level-by-level radicular spinal DSA is technically difficult, particularly in patients with atherosclerosis or vascular variations. This not only consumes time with an increased incidence rate of neurologic complications but also results in a high burden of iodinated contrast and radiation exposure.<sup>7,9,10</sup> Therefore, pre-DSA noninvasive vascular imaging examinations, such as CTA or contrast-enhanced MRA (CE-MRA), are crucial for the preliminary diagnosis and angioarchitecture evaluation of SVMs.<sup>11-13</sup> These insights can aid clinicians in optimal preoperative preparation, potentially reducing the operative duration and elevating surgical outcomes.<sup>14,15</sup>

Despite being radiation-free and having high tissue resolution, the use of CE-MRA for preoperative assessment is still limited because of the long scanning time, small scanning range per scan, and large contrast agent dosage, which can make it difficult for patients to remain motionless for protracted periods.<sup>9,16</sup> However, CTA can effectively address these issues, on the basis of its advantages of fast scanning speed for obtaining the entire range of the spine in a short time and high spatial resolution for displaying smaller subcortical blood vessels.<sup>12</sup> The advantages of CTA are yet to be explored further, especially in the area of vascular image postprocessing. Difficulty in simultaneous and clear display of the vertebral body and abnormal small blood vessels within the vertebral canal is the limitation of routine 3D volume rendering (3D-VR) reconstruction for SVMs.<sup>12</sup> On the basis of extensive clinical experience, even with meticulous bone subtraction techniques, the 3D-VR reconstruction images still have difficulty presenting the core lesions of SVMs, much less achieving a comprehensive representation of the extensively draining venous network.

This study proposes an improved 3D-VR technique, the spinal subtraction and bone background fusion CTA (SSBBF-CTA) technique, which obviates the requirement for third-party software integration. It optimizes the display of angioarchitectures of lesions and their relationship with the bones. The use of SSBBF-CTA for the accurate diagnosis and localization of SVMs can substantially assist in preoperative evaluation and clinical treatment decisions.

## MATERIALS AND METHODS

### Patients

Forty-nine patients, including 22 patients diagnosed with SVMs (group A) and 27 patients without SVMs (group B), between November 2017 and November 2022, were retrospectively enrolled in our study. The inclusion criteria were as follows: 1) clinical manifestations of motor/sensory disturbances; 2) all patients having undergone spinal CTA examinations, including precontrast and arterial phase (AP) imaging; 3) group A: DSA examination conducted within 1 week that confirmed the diagnosis of SVMs; and 4) group B: DSA, MR imaging, and other sufficient evidence that confirmed the absence of SVMs by clinical physicians and radiologists with >10 years of experience. The exclusion criteria were as follows: 1) insufficient or incomplete clinical

data, 2) intramedullary tumors or after aortic replacement surgery, and 3) severe motion artifacts on images. The patient screening process is illustrated in the flow chart shown in Fig 1. This retrospective study received approval from the institutional review board and was granted an exemption from the requirement for informed consent.

### CT Protocol

All patients underwent multiphasic CT consisting of precontrast and AP images using a Somatom Definition Flash CT scanner (Siemens). The scan parameters were as follows: 100-kV tube voltage, tube current determined by the Automatic Tube Current Modulation system (Care Dose4D, Siemens; 100-mAs reference tube current, and 120- to 350-mAs effective tube current), 0.28-second gantry rotation time, 1.2 pitch,  $64 \times 0.6$  mm collimation. All data sets were reconstructed with a slice thickness of 0.75 mm and an increment of 0.5 mm. The contrast agent (iomeprol, Iomeron, 400 mgI/mL; Shanghai Bracco Sine Pharmaceutical) was injected at a flow rate of 0.075 mL/kg/s, 14-second injection duration, and 10-second same flow of saline. The AP determined by the bolus-tracking technique started 8 seconds after the threshold of the ascending aorta reached 120 HU. The scanning ranges of the 2 phases were identical.

### Image Postprocessing

First, all the original images, including the precontrast and AP images, were transferred to a postprocessing workstation (syngo.via VB20; Siemens), and the multiplanar reconstruction images were obtained. Routine bone subtraction CTA (RBS-CTA) 3D-VR images were obtained by subtracting the precontrast images from the AP images on the basis of the currently more precise bone subtraction algorithm of Siemens. Second, all original and RBS-CTA images were transferred to the ADW4.6 workstation (GE Healthcare), which is more proficient in the reconstruction of microvascular structures. Bone background images were obtained by reconstructing precontrast images. The aortic trunk and branches were obtained from the RBS-CTA images. Abnormal vascular structures were identified by processing the original AP images. The fusion of the 3 aforementioned types of images produced SSBBF-CTA images. The MPR images were postprocessed in real-time following patient scanning, whereas the RBS and SSBBF-CTA images were processed retrospectively.

### Image Analysis and Evaluation Criteria

Three major steps were involved in image analysis. Patients were randomly assigned to each reading session. All readers read the images independently and blinded to the final diagnosis. Postprocessing image reconstruction and diagnostic accuracy were evaluated against DSA as the criterion standard, which was verified by seasoned vascular interventionalists (Online Supplemental Data).

1) Preliminary screening capability using original images with MPR-CTA to evaluate the actual diagnostic accuracy of SVMs when radiologists first read radiographs using only general images. The patients in groups A and B were randomized, and 3 types of readers 1-3 participated in this step. Reader 1 was a junior undergoing radiologist training with 1 year of experience.

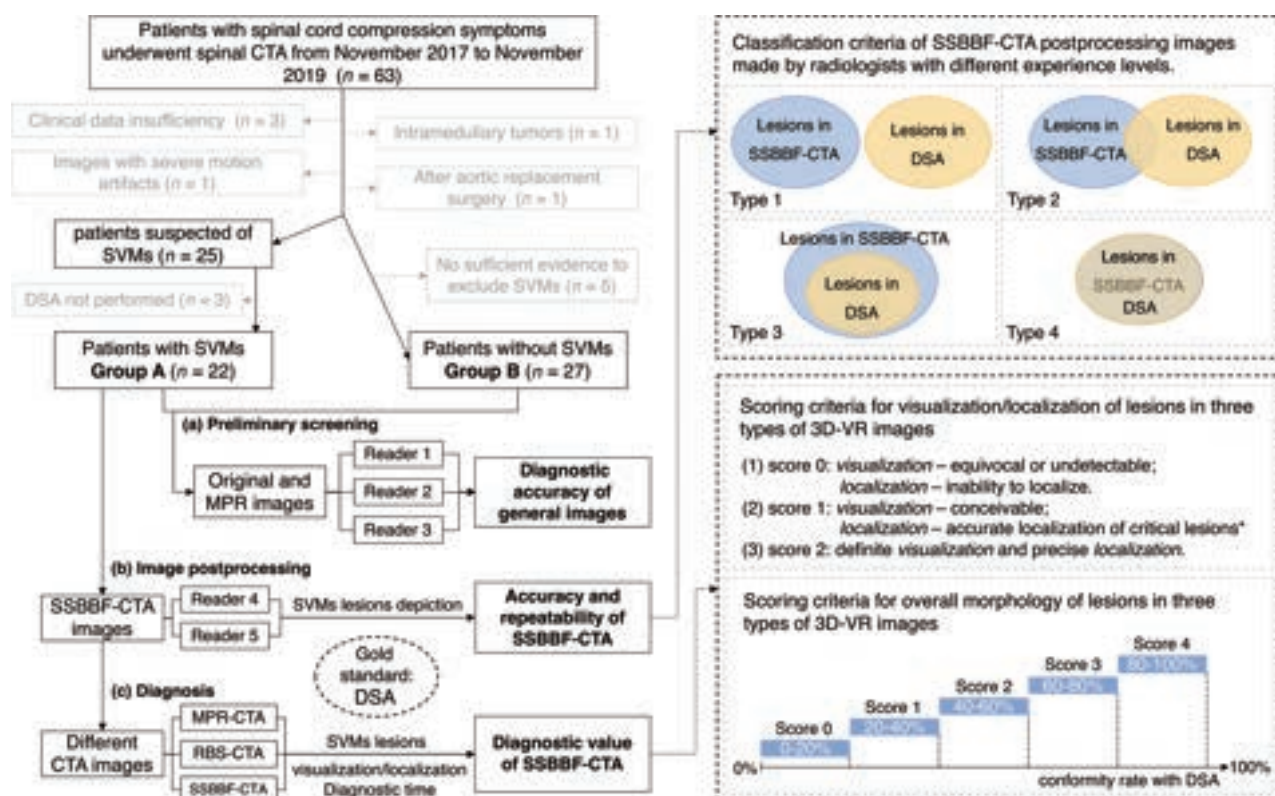


**FIG 1.** Flow chart of the patient enrollment process and workflow of this study. Asterisk indicates accurate localization of critical lesions which defined as mostly correct when multiple feeding arteries are present, and the identification of drainage veins covering over 70% of the range.

Reader 2 was a type of junior practicing radiologist with 3–8 years of experience, who submitted the original diagnostic report for the first time. Reader 3 was a type of senior radiologist with >10 years of experience who signed the report.

2) The accuracy and stability of the SSBBF-CTA postprocessing technique to evaluate whether the postprocessing method of SSBBF-CTA performed by radiologists with different experience levels was accurate and repeatable. Images of group A were used. The SSBBF-CTA image postprocessing was performed by 2 practicing radiologists with 4 and 20 years of experience (readers 4 and 5, respectively), and the differences between the 2 were assessed. The classification criteria (types 1–4) of SSBBF-CTA images are shown in Fig 1, including the localization and number of nidus/fistulas and feeding arteries, the extent of the drainage vein, and overall morphology.

3) Diagnostic value of lesion details of SVMs using 3 types of postprocessing images to analyze the lesion details (visualization and localization of feeding arteries, nidus/fistula, and draining veins) by different 3D-VR images and compare the differences among the 3. Reader 1 (same as above) and reader 4 evaluated and scored the lesions of SVMs in the MPR-CTA, RBS-CTA, and SSBBF-CTA images, respectively. All final scores were confirmed by discussion in cases of disagreement and supervised by reader 5. Finally, a comparison of the diagnostic time was made between reader 1 and reader 4 in terms of evaluating all SVM lesions using MPR-CTA and SSBBF-CTA. The scoring criteria for the visualization/localization of lesions (evaluating feeding arteries, nidus, and draining veins separately) and overall morphology in MPR, RBS, and SSBBF-CTA images are shown in Fig 1.

## Statistical Analysis

Demographic and clinical variables were compared between patients in groups A and B. The Mann-Whitney *U* test was used for non-normally distributed quantitative data. For normally distributed data, the independent samples *t* test was used.  $\chi^2$  tests were performed on categorical data. Receiver operating characteristic (ROC) analysis was performed to evaluate the diagnostic performance of readers 1–3, using DSA diagnosis as the criterion standard. Comparison of the areas under the ROC curves was performed using the DeLong test. The Wilcoxon signed-rank test was used to compare the differences between the postprocessed images of readers 4 and 5, as well as the differences in diagnostic evaluation and time between readers 1 and 4. The Kruskal-Wallis rank sum test was used to compare the differences in lesion identification and localization among the different postprocessing images.

All continuous variables were expressed as mean (SD) when normally distributed and median (interquartile range) if not. Statistical significance was set at  $P < .05$ . Statistical analyses were performed using SPSS (Version 25.0; IBM) and MedCalc (Version 18.21.1; MedCalc Software).

## RESULTS

### Patient Characteristics

Of 63 patients with similar symptoms of spinal cord compression who underwent preoperative spinal CTA, 14 were excluded from this study for the following reasons: 1) insufficient clinical data

(*n* = 3); 2) patients with intramedullary tumors (*n* = 1) or aortic replacement surgery (*n* = 1); 3) images with severe motion artifacts (*n* = 1); 4) patients suspected of having SVMs without confirmed DSA (*n* = 3); and 5) no sufficient evidence to exclude patients with SVMs (*n* = 5). Accordingly, 49 patients (group A: 22 patients; mean age, 44.0 [SD, 14.3] years; and group B: 27 patients; mean age 44.6 [SD, 15.2] years) comprised the final study sample, and their demographic and clinical variables are summarized in Table 1. Only urogenital disturbances showed statistically significant differences between patients with and without SVMs (*P* = .005).

**Preliminary Screening of SVMs**

The diagnostic efficacies of the original images with MPR for the primary screening of SVMs by different readers are shown in Table 2. As radiologic experience increased, the area under the curve (AUC) values for readers 1, 2, and 3 were 0.849, 0.936, and 0.977, respectively. Among all diagnostic indicators, sensitivity was the least effective, with reader 1 demonstrating a sensitivity of only 77.3%. Moreover, the DeLong test demonstrated a statistically significant difference between the ROC curves of reader 1 and reader 3 (*P* = .031).

**SSBBF-CTA Postprocessing Images**

The SSBBF-CTA images processed by readers 4 and 5 were classified into 4 types: types 1–4. The higher the classification level, the greater was the clinical utility, with types 3 and 4 being considered particularly beneficial in aiding clinical diagnosis and treatment. Nearly all lesion characteristics, including localization and the number of nidi/fistulas, drainage veins, and overall morphology, were classified as either type 3 or 4, with the majority falling into the type 4 category (Fig 2). Only 2 cases had

deviations in the feeding artery, characterized by the presence of multiple supplying vessels or the involvement of complex scenarios involving the extracranial arteries and intracranial collateral circulation (Online Videos 1 and 2). In addition, no statistically significant difference was observed between readers 4 and 5 (*P* > .05).

**Diagnosis and Evaluation of SVMs Using Different CTA Postprocessing Images**

We compared the diagnostic capabilities of SVM lesions using 3 postprocessing methods (MPR-CTA, RBS-CTA, and SSBBF-CTA, Figs 3 and 4, Online Videos 3 and 4), using scores that were discussed by readers 1 and 4 and subsequently corrected under the supervision of reader 5. In terms of accuracy in visualization and localization of lesions (nidus/fistula, feeding artery, and drainage vein) and the overall morphology of SVMs, RBS-CTA demonstrated significantly inferior performance (*P* = .000) compared with MPR-CTA and SSBBF-CTA, whereas no significant difference (*P* > .05) was observed between MPR and SSBBF (Table 3). Additionally, reader 1 performed worse than reader 4 in the assessment of lesions using MPR-CTA (*P* < .05), whereas no difference (*P* > .05) was observed between the 2 when using SSBBF-CTA (Table 4 and Online Supplemental Data). Moreover, both readers 1 and 4 required significantly less diagnostic time when using SSBBF-CTA for lesion assessment than when using MPR-CTA (*P* = .000, Table 4).

**DISCUSSION**

This study used clinically prevalent postprocessing workstations to optimize postprocessing techniques for spinal artery CTA, achieving precise visualization and localization of SVM lesions using 3D-VR, thereby enhancing the diagnostic ability and efficiency of radiologists. This advancement allows clear visualization of tertiary and higher-order arterial branches within 3D-VR images, potentially having considerable importance for the diagnostic utility of CTA in vasculopathy.

The accuracy of SVM diagnosis using the original and MPR-CTA images was lower for junior physicians than for more experienced physicians, particularly in terms of diagnostic sensitivity. The incidence rate of SVMs was quite low, making it impractical to reach an occurrence rate of approximately 50% in this study. Therefore, in the practical field of radiology, the likelihood of diagnostic errors or missed diagnoses is even higher.<sup>17</sup> However, the consequences of a missed diagnosis or misdiagnosis can be very serious for patients with SVMs.<sup>4</sup> Impairment of spinal cord venous drainage can result in progressive neurologic deficit symptoms, such as sensory, motor, and even urogenital disturbances, which lead to disability and significantly impact the patient’s

**Table 1: Patient characteristics<sup>a</sup>**

	Group A	Group B	P Value
Age (yr) <sup>b</sup>	44.0 (SD, 14.3)	44.6 (SD, 15.2)	.898
Sex <sup>c</sup>			.990
Female	9	11	
Male	13	16	
Sensory disturbance	100% (22/22)	88.9% (24/27)	.242
Motor disturbance	90.9% (20/22)	77.8% (21/27)	.269
Reflex abnormality	68.2% (15/22)	66.7% (18/27)	.910
Urogenital disturbance	72.7% (16/22)	33.3% (9/27)	.005 <sup>d</sup>
Back pain	9.1% (2/22)	11.1% (3/27)	1.000

<sup>a</sup> Unless otherwise indicated, data are percentages, with numbers of patients in parentheses.

<sup>b</sup> Age is presented as the mean.

<sup>c</sup> Data are numbers of patients.

<sup>d</sup> The clinical features of groups A and B showed statistically significant differences (*P* < .05).

**Table 2: Diagnostic efficacy of original images with MPR for primary screening of SVMs by different readers<sup>a</sup>**

Reader	Sensitivity (%)	Specificity (%)	Accuracy (%)	PPV (%)	NPV (%)	AUC [95% CI]	Youden
Reader 1 <sup>b</sup>	77.3 (17/22)	92.6 (25/27)	85.7 (42/49)	89.5 (17/19)	83.3 (25/30)	0.849 (0.718–0.935)	0.699
Reader 2	90.9 (20/22)	96.3 (26/27)	93.9 (46/49)	95.2 (20/21)	92.9 (26/28)	0.936 (0.828–0.986)	0.872
Reader 3	95.5 (21/22)	100 (27/27)	98.0 (48/49)	100 (21/21)	96.4 (27/28)	0.977 (0.888–0.999)	0.955

**Note:**—PPV indicates positive predictive value; NPV, negative predictive value; Reader 1, a radiologist with one year of experience; Reader 2, a junior physician who submitted the original report for the first time; Reader 3, a reviewing physician who also submitted the original report for the first time.

<sup>a</sup> Data in brackets are 95% CIs, and data in parentheses are numbers of patients.

<sup>b</sup> Readers 1 and 3 showed statistically significant differences (*P* < .05).



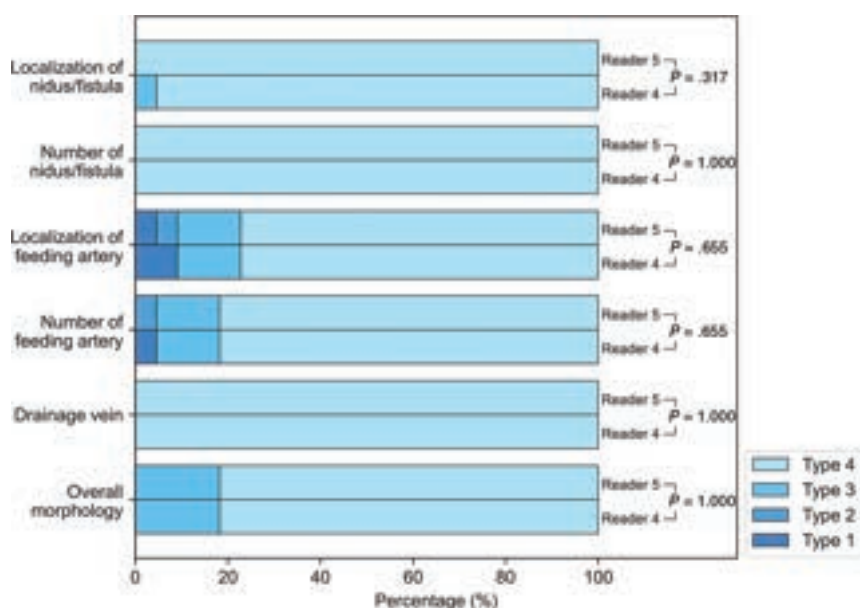


**FIG 2.** Percentage of stacked bar chart of categorization of postprocessing SSBBF reconstruction accuracy. Types 3 and 4 are considered particularly beneficial in aiding clinical diagnosis and treatment.

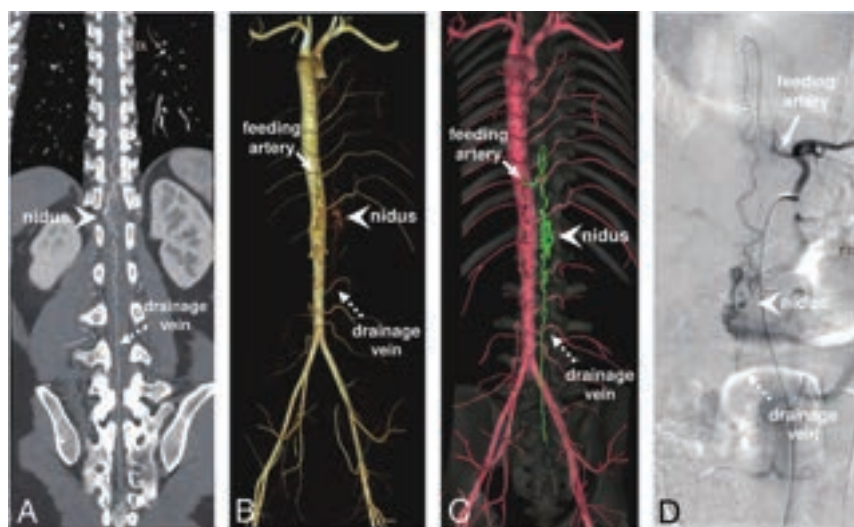


**FIG 3.** Spinal CTA images in a 28-year-old man with a spinal AVM. The crucial lesions, including nidus (arrowhead), feeding artery (solid arrow), and drainage vein (dotted arrow), are shown in MPR-CTA (A), RBS-CTA (B), SSBBF-CTA (C), and DSA images (D).

quality of life.<sup>18-20</sup> If misdiagnosed as a demyelinating disease, treatment with hormone shock therapy may lead to hematomyelia, which can be fatal.<sup>21,22</sup> Therefore, improving the diagnostic sensitivity of pretreatment patient screening can reduce potentially serious medical risks. We recommend that the following patients should undergo CTA examination with our SSBBF-CTA method before treatment after balancing radiation and clinical needs: 1) those presenting with special neurologic symptoms, 2) those with an initial MRI suggesting evident flow void signals adjacent to the spinal cord, 3) those with existing examinations that could not definitively rule out vascular anomalies, and 4) those with contraindications for MR imaging and no contraindications for CTA.

This study achieved clear visualization and localization of SVM lesions by innovatively combining the advantages of Siemens and GE Healthcare postprocessing workstations for image postprocessing without the need for third party software. The spinal artery, a third-order or higher branch with a small diameter, runs through the intervertebral foramen and spinal canal and is closely related to the vertebrae.<sup>23</sup> These unique anatomic features make it challenging to maintain vessel continuity while accurately subtracting the bones. According to our clinical experience, the bone subtraction algorithm of the Siemens workstation is more precise,<sup>24</sup> but it falls short of displaying the small vessels of SVMs. The GE Healthcare workstation can display complete SVMs lesion details by tracking small vessels; however, it cannot obtain clean aorta and intercostal artery 3D-VR images using its bone subtraction algorithm. Thus, a combination of the advantages of both workstations provided clear and unobstructed 3D-VR reconstruction images of the SVMs. The fusion of a reduced-opacity bone background with clear vessels was implemented to achieve accurate localization of the SVM lesion without obstructing their visibility. A spinal CTA acquisition (from the beginning of the noncontrast scan to the completion of the CTA) rarely exceeds 1 minute and, therefore, rarely produces motion artifacts. Because the positioning coordinates of the images in the plain scan and APs are consistent and the image superposition is based on the coordinates, no additional artifacts will affect the image quality. Furthermore, junior physicians can achieve a level of accuracy in SSBBF-CTA images comparable with that of experienced physicians through short-term training, and the difference in the amount of time required to perform postprocessing was minimal. However, in complex cases, it is advisable to perform these procedures under the supervision of experienced physicians.

Preoperative information regarding the nidi/fistulas, feeding arteries, and drainage veins of SVMs is crucial for guiding the selection of clinical treatment plans. When using MPR-CTA, the less experienced physicians tended to have a lower accuracy than the physicians with more extensive experience, and both physicians demonstrated high accuracy in evaluating SVM lesions when using SSBBF-CTA. This finding indicates that the use of the



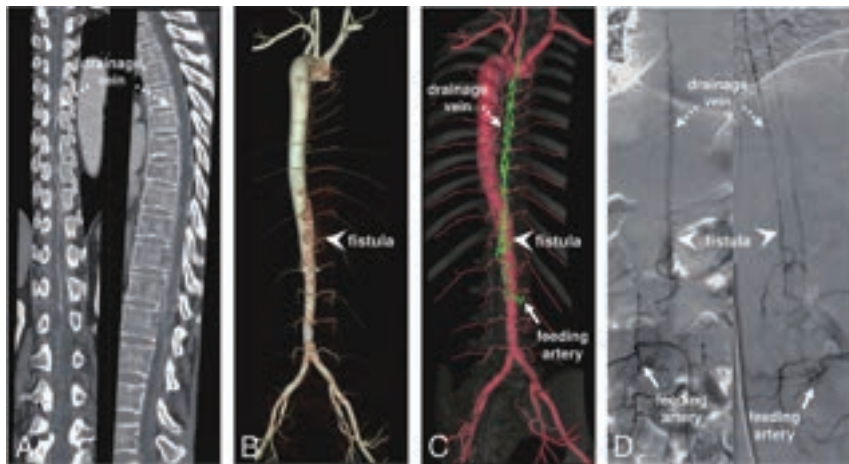


**FIG 4.** Spinal CTA images in a 55-year-old woman with a spinal AVF. The crucial lesions, including the fistula (arrowhead), feeding artery (solid arrow), and drainage vein (dotted arrow), are shown in an MPR-CTA image (A), a RBS-CTA image (B), SSBBF-CTA image (C), and a DSA image (D).

**Table 3: Scoring of lesion localization and visualization of SVMs using different postprocessing techniques of CTA images<sup>a</sup>**

	MPR-CTA	RBS-CTA <sup>b</sup>	SSBBF-CTA	P Value <sup>c</sup>
Visualization of lesions (total points)	6.00 (1.00)	4.00 (2.75)	6.00 (0.63)	.000
Nidus/fistula	2.00 (0.00)	1.50 (1.00)	2.00 (1.25)	.000
Feeding artery	2.00 (0.63)	1.00 (1.50)	2.00 (0.00)	.000
Drainage vein	2.00 (0.00)	1.00 (1.00)	2.00 (0.00)	.000
Localization of lesions (total points)	6.00 (0.00)	3.25 (3.00)	6.00 (1.00)	.000
Nidus/fistula	2.00 (0.00)	1.00 (1.00)	2.00 (0.00)	.000
Feeding artery	2.00 (0.00)	1.00 (2.00)	2.00 (0.00)	.000
Drainage vein	2.00 (0.00)	1.00 (1.13)	2.00 (0.00)	.00
Overall morphology	4.00 (0.00)	2.75 (2.63)	4.00 (0.50)	.000

<sup>a</sup> The data are presented as median (interquartile range).

<sup>b</sup> There is a statistically significant difference between RBS-CTA and the other 2 groups ( $P < .05$ ).

<sup>c</sup> There is a significant statistical difference among the 3 groups ( $P < .05$ ).

**Table 4: Assessment of lesions of SVMs and diagnostic time using different postprocessing CTA techniques by different readers<sup>a</sup>**

	Reader 1	Reader 4	P Value
MPR-CTA			
Visualization of lesions	4.00 (1.25)	6.00 (1.00)	.001 <sup>b</sup>
Localization of lesions	4.50 (2.00)	6.00 (0.00)	.003 <sup>b</sup>
Overall morphology	4.00 (1.00)	4.00 (0.00)	.025 <sup>b</sup>
Diagnostic time	9.00 (6.75)	7.00 (3.00)	.017 <sup>b</sup>
RBS-CTA			
Visualization of lesions	3.50 (3.00)	3.50 (3.00)	.353
Localization of lesions	2.25 (3.00)	3.00 (2.50)	.178
Overall morphology	2.50 (1.25)	3.00 (2.00)	.070
Diagnostic time	NA	NA	NA
SSBBF-CTA			
Visualization of lesions	6.00 (1.00)	6.00 (1.00)	.705
Localization of lesions	6.00 (1.00)	6.00 (1.00)	.206
Overall morphology	4.00 (0.25)	4.00 (0.13)	.655
Diagnostic time	3.00 (2.00) <sup>c</sup>	3.00 (1.25) <sup>c</sup>	.943

**Note:**—NA indicates not applicable; Reader 1, a radiologist with one year of experience; Reader 4, a radiologist with 4 years of experience.

<sup>a</sup> The data are presented as median (interquartile range). The visualization and localization of lesions represent the total score of the nidus/fistula, feeding artery, and drainage vein.

<sup>b</sup> There is a significant statistical difference between readers 1 and 4 ( $P < .05$ ).

<sup>c</sup> There is a statistically significant difference in diagnostic time between the use of MPR-CTA and SSBBF-CTA ( $P = .000$ ).

SSBBF-CTA 3D-VR reconstruction technique enables the accurate identification of the key lesions of SVMs by less-experienced radiologists and clinical physicians with limited radiologic experience. Furthermore, SSBBF-CTA can significantly shorten the diagnostic time without compromising diagnostic accuracy for both junior and senior radiologists. These aspects contribute to the establishment of effective communication between the clinical and radiology departments, thereby improving diagnostic efficiency.

The advantages of CTA have yet to be fully explored and improved. Several studies have reported that 320-layer and 640-layer spiral CTA can achieve an accuracy rate of 62.5%–85.7% in locating the fistula of spinal AVFs.<sup>12,13,25</sup> Our research aimed to update the postprocessing image quality on the basis of standard CTA, producing a more intuitive and clearer visualization of lesions and allowing a detailed and efficient analysis of lesion features of SVMs. 3D-VR images of types 3 and 4 were considered clinically acceptable diagnostic results, accounting for nearly 100% of the cases. The current research indicates that the accuracy of CE-MRA in locating fistulas for AVFs is higher than 80%,<sup>26</sup> while time-resolved CE-MRA has an even higher accuracy rate of up to 91%.<sup>11</sup> Therefore, in clinical practice, a reasonable selection should be made on the basis of the individual patient and hardware conditions of different hospitals, considering the respective advantages of CTA and MRA.

In addition, the classification of SVMs is complex, and at least 5 classification methods are currently known.<sup>27</sup> Regardless of the classification standard, there are great advantages for extramedullary high-flow lesions, such as lesions classified as type I (dural AVF) and type IV (perimedullary AVF). For intramedullary lesions (type II, intramedullary glomus AVM and type III, intramedullary juvenile AVM), CTA can also provide useful information on vascular lesions, but it is limited in the evaluation of the spinal cord. For type V, extradural AVF, it may be difficult to visualize a fistula (too closely related to the bones). Challenges remain for lesions with slow flow; however, some abnormal vascular manifestations can suggest the diagnosis of SVMs.<sup>28</sup> A second, late arterial CTA scan can also solve a part of this problem; however, the radiation dose issue needs to be considered.

This study has some limitations. By using SSBBF-CTA for comprehensive preoperative assessment of SVMs, clinicians can obtain more lesion details to develop appropriate surgical strategies, which can potentially shorten the surgical duration, reduce contrast agent use, and limit radiation exposure. However, the

assumption that CTA might indirectly enhance surgical outcomes remains speculative and warrants further longitudinal observation. Although the SSBBF-CTA postprocessing technology itself does not add additional radiation, CTA examinations still need to be reasonably selected by balancing radiation and patient conditions. In addition, because of the low incidence rate of the disease, the number of included patients was relatively insufficient, and this study explored only the universal applicability of SSBBF-CTA for SVMs. Our team is continuing to collect cases for a more detailed classification to further explore the practicality of SSBBF-CTA. This research methodology has been integrated into the general work of our hospital and has already helped avoid many medical risks. A one-stop image postprocessing reconstruction software that can combine the advantages of algorithms from 2 different postprocessing workstations will make clinical work more convenient. The rapid advancement of artificial intelligence technology holds great potential for achieving simplified and increasingly accurate CTA reconstruction images in the future.

## CONCLUSIONS

The SSBBF-CTA technique demonstrated excellent reproducibility, significantly enhancing both the accuracy and efficiency of the diagnosis and assessment of SVMs, with particular benefits for junior radiologists. It has the potential for substantial clinical benefits in the preoperative evaluation and selection of appropriate treatment strategies.

Disclosure forms provided by the authors are available with the full text and PDF of this article at [www.ajnr.org](http://www.ajnr.org).

## REFERENCES

- Clarencon F, Di Maria F, Sourour NA, et al. **Evaluation of intra-aortic CT angiography performances for the visualisation of spinal vascular malformations' angioarchitecture.** *Eur Radiol* 2016;26:3336–44 CrossRef Medline
- Zalewski NL, Rabinstein AA, Brinjikji W, et al. **Unique gadolinium enhancement pattern in spinal dural arteriovenous fistulas.** *JAMA Neurol* 2018;75:1542–45 CrossRef Medline
- Jeng Y, Chen DY, Hsu HL, et al. **Spinal dural arteriovenous fistula: imaging features and its mimics.** *Korean J Radiol* 2015;16:1119–31 CrossRef Medline
- Yu JX, Hong T, Krings T, et al. **Natural history of spinal cord arteriovenous shunts: an observational study.** *Brain* 2019;142:2265–75 CrossRef Medline
- Hunt R, Roberts RM, Mortimer AM. **Spinal dural arteriovenous fistula: delay to radiological diagnosis and sources of radiological error.** *Clin Radiol* 2018;73:835.e811–e816 CrossRef Medline
- Jablawi F, Schubert GA, Dafotakis M, et al. **Long-term outcome of patients with spinal dural arteriovenous fistula: the dilemma of delayed diagnosis.** *AJNR Am J Neuroradiol* 2020;41:357–63 CrossRef Medline
- Orru E, Mekabaty AE, Millan DS, et al. **Removal of antiscatter grids for spinal digital subtraction angiography: dose reduction without loss of diagnostic value.** *Radiology* 2020;295:390–96 CrossRef Medline
- Barreras P, Heck D, Greenberg B, et al. **Analysis of 30 spinal angiograms falsely reported as normal in 18 patients with subsequently documented spinal vascular malformations.** *AJNR Am J Neuroradiol* 2017;38:1814–19 CrossRef Medline
- Tarabishy AR, Boo S, Rai A. **Spinal dural fistula evaluation using 4-dimensional intra-aortic spinal CT angiography in a hybrid angiography suite.** *J Neuroradiol* 2021;48:492–94 CrossRef Medline
- Lee CW, Huang A, Wang YH, et al. **Intracranial dural arteriovenous fistulas: diagnosis and evaluation with 64-detector row CT angiography.** *Radiology* 2010;256:219–28 CrossRef Medline
- Grossberg JA, Howard BM, Saindane AM. **The use of contrast-enhanced, time-resolved magnetic resonance angiography in cerebrovascular pathology.** *Neurosurg Focus* 2019;47:E3 CrossRef Medline
- Kim AY, Khil EK, Choi I, et al. **Spinal extradural arteriovenous fistula after lumbar epidural injection: CT angiographic diagnosis using 3D-volume rendering.** *Skeletal Radiol* 2020;49:2073–79 CrossRef Medline
- Brinjikji W, Colombo E, Cloft HJ, et al. **Clinical and imaging characteristics of spinal dural arteriovenous fistulas and spinal epidural arteriovenous fistulas.** *Neurosurgery* 2021;88:666–73 CrossRef Medline
- Lai PH, Weng MJ, Lee KW, et al. **Multidetector CT angiography in diagnosing type I and type IVA spinal vascular malformations.** *AJNR Am J Neuroradiol* 2006;27:813–17 Medline
- Yamamoto S, Kanaya H, Kim P. **Spinal intraarterial computed tomography angiography as an effective adjunct for spinal angiography.** *J Neurosurg Spine* 2015;23:360–67 CrossRef Medline
- Kannath SK, Rajendran A, Thomas B, et al. **Volumetric T2-weighted MRI improves the diagnostic accuracy of spinal vascular malformations: comparative analysis with a conventional MR study.** *J Neurointerv Surg* 2019;11:1019–23 CrossRef Medline
- Ronald AA, Yao B, Winkelman RD, et al. **Spinal dural arteriovenous fistula: diagnosis, outcomes, and prognostic factors.** *World Neurosurg* 2020;144:e306–15 CrossRef Medline
- Zhang HB, Zhai XL, Li L, et al. **Imaging characteristics, misdiagnosis and microsurgical outcomes of patients with spinal dural arteriovenous fistula: a retrospective study of 32 patients.** *Ann Transl Med* 2022;10:832 CrossRef Medline
- Naylor RM, Topinka B, Rinaldo L, et al. **Progressive myelopathy from a craniocervical junction dural arteriovenous fistula.** *Stroke* 2021;52:e278–81 CrossRef Medline
- Jablawi F, Mull M. **The clinical value of venous drainage in patients with spinal dural arteriovenous fistula.** *J Neurol Sci* 2019;397:50–54 CrossRef Medline
- Donghai W, Ning Y, Peng Z, et al. **The diagnosis of spinal dural arteriovenous fistulas.** *Spine (Phila Pa 1976)* 2013;38:E546–53 CrossRef Medline
- Ma Y, Hong T, Chen S, et al. **Steroid-associated acute clinical worsening and poor outcome in patients with spinal dural arteriovenous fistulas: a prospective cohort study.** *Spine (Phila Pa 1976)* 2020;45:E656–62 CrossRef Medline
- Hsu JL, Cheng MY, Liao MF, et al. **The etiologies and prognosis associated with spinal cord infarction.** *Ann Clin Transl Neurol* 2019;6:1456–64 CrossRef Medline
- Aulbach P, Mucha D, Engellandt K, et al. **Diagnostic impact of bone-subtraction ct angiography for patients with acute subarachnoid hemorrhage.** *AJNR Am J Neuroradiol* 2016;37:236–43 CrossRef Medline
- Shimoyama S, Nishii T, Watanabe Y, et al. **Advantages of 70-kV CT angiography for the visualization of the Adamkiewicz artery: comparison with 120-kV imaging.** *AJNR Am J Neuroradiol* 2017;38:2399–405 CrossRef Medline
- Lindenholz A, Terbrugge KG, van Dijk JM, et al. **The accuracy and utility of contrast-enhanced MR angiography for localization of spinal dural arteriovenous fistulas: the Toronto experience.** *Eur Radiol* 2014;24:2885–94 CrossRef Medline
- Deng F, Knipe H. **Spinal vascular malformations.** 2016. *Radiopaedia* Radiopaedia.org. Accessed October 18, 2023
- Kona MP, Buch K, Singh J, et al. **Spinal vascular shunts: a patterned approach.** *AJNR Am J Neuroradiol* 2021;42:2110–18 CrossRef Medline

# Multinodular and Vacuolating Neuronal Tumor–like Lesion of the Spinal Cord: Two Case Reports

Joris Schollaert, David Van der Planken, Sam Mampaey, Matthew Breen, Farn-Yang Foo, Rajan Jain, and Johan W.M. Van Goethem

## ABSTRACT

**SUMMARY:** We describe 2 cases of a spinal cord lesion with imaging features closely resembling those described in supratentorial multinodular and vacuolating neuronal tumor (MVNT) or infratentorial multinodular and vacuolating posterior fossa lesions of unknown significance. Multiple well-delineated nonenhancing T2-hyperintense intramedullary cystic ovoid nodules were visualized within the white matter of the spinal cord, including some immediately abutting the gray matter. No alterations in signal intensity or morphology were detected in a follow-up. Moreover, no relevant clinical symptoms attributable to the lesions were present. We describe these lesions as presumed MVNT, and we therefore use the term MVNT-like spinal cord lesions.

**ABBREVIATIONS:** MVNT = multinodular and vacuolating neuronal tumor; MV-PLUS = multinodular and vacuolating posterior fossa lesions of unknown significance; UC = ulcerative colitis

A multinodular and vacuolating neuronal tumor (MVNT) is a fairly new and distinctive entity in the 5<sup>th</sup> edition of the World Health Organization classification of central nervous system tumors.<sup>1</sup> It was first described in 2013 by Huse et al<sup>2</sup>, who showed a case series of benign seizure-associated intra-axial lesions. Imaging features on MR imaging include clusters of multiple well-delineated T2-hyperintense millimetric ovoid nodules subcortically in the white matter (ie, a “bubbly appearance”), which can also be found juxtacortically. The gray matter is generally not affected. Classically, there is no contrast enhancement, no diffusion restriction, and no signal loss on FLAIR sequences. Cerebral MVNT is described as a “leave me alone” lesion. The microscopic appearance of a MVNT consists of immature neuroepithelial cells organized in nodules with a prominent vacuolating matrix<sup>3</sup> that is almost pathognomonic.

## CASE SERIES

### Case 1

A 45-year-old woman presented with right-sided cervicobrachialgia for several weeks. Except for discrete paresthesias in the right

thumb and index finger, no neurologic symptoms were present. There was no relevant medical history.

Alongside a disk extrusion and degenerative uncovertebral changes on the right, MR imaging showed a large multilobar intradural intramedullary lesion, consisting of multiple well-defined homogeneous T2-hyperintense and T1-hypointense cystic-like changes, at the cervicothoracic junction (C5–T2) (Fig 1). These cystic-like changes were located in the white matter of the spinal cord, including some immediately abutting the gray matter. There was no contrast enhancement and no diffusion restriction. No perilesional signal changes were detected. Follow-up MR imaging after 12 months showed no volume and/or signal intensity changes of the lesion. To exclude intracranial pathology, an MR imaging examination of the brain was performed, and it showed no abnormalities. All lab values, including infectious serology, were normal.

### Case 2

A 37-year-old woman with a history of *BRCA1* carrier status and ulcerative colitis (UC) presented with approximately 9 months of chronic headache. She reported that the headaches began following an intrauterine fetal demise in the setting of a UC flare, complicated by retained products of conception, requiring dilatation and curettage. She reported a dull, nonlocalizable headache that was a 2/10 in severity but denied other neurologic symptoms.

For a work-up of her headaches, she was referred for MR imaging of the head, which revealed numerous well-demarcated, nonenhancing T2-hyperintense cystic-like lesions in the medulla and visualized upper cervical spinal cord. Subsequent dedicated spine MR imaging revealed the extent of these intramedullary

Received October 18, 2023; accepted after revision December 5.

From the Departments of Radiology (J.S., S.M., J.W.M.V.G.) and Neurosurgery (D.V.d.P.), VITAZ General Hospital, Sint-Niklaas, Belgium; Department of Radiology (J.W.M.V.G.), University Hospital of Antwerp (UZA), Antwerp, Belgium; Departments of Radiology (M.B., R.J.), Neurology (F.-Y.F.), and Neurosurgery (R.J.), New York University Grossman School of Medicine, New York, New York.

Please address correspondence to Joris Schollaert, VITAZ General hospital, Medical and Molecular Imaging, Moerlandstraat 1, Sint-Niklaas, 9100, Belgium; e-mail: schollaert.joris@gmail.com

<https://dx.doi.org/10.3174/ajnr.A8133>





**FIG 1.** Case 1; 45-year-old woman A, Sagittal T2-weighted image shows a multilobar intradural intramedullary lesion. There are multiple cystic-like changes within the spinal cord at different levels of the cervicothoracic junction. Note that there is neither syringomyelia nor T2-hypointense changes within the medulla. A cervical disk extrusion at C6–C7 can also be seen. B, Sagittal T1-weighted image after the intravenous administration of gadolinium. No contrast enhancement can be seen. C, Sagittal echo-planar diffusion-weighted image shows no diffusion restriction within the lesion. D, Para-axial gradient recalled-echo T2-weighted image depicts the cystic-like intra-axial lesion. Note the sharp delineation of the lesions without perilesional edema. These lesions are located within the white matter of the spinal cord, without affecting the gray matter. E, Sagittal FLAIR T2-weighted image shows the T2-hyperintense lesion. Unlike perivascular spaces (also called Virchow-Robin spaces), there is no signal loss on FLAIR. F, Sagittal short tau inversion recovery T2-weighted image from a 12-month follow-up. No alterations in signal intensity or morphology were detected. Stable lesion.

lesions within the cervical spinal cord, down to the C4 level (Fig 2). Follow-up imaging over the next 4 years remained stable, without the development of clinical symptoms. The laboratory values and infectious work-up were unrevealing. CSF sampling revealed mildly elevated protein but was otherwise normal.

## DISCUSSION

In our cases, we see lesions that include a cluster of multiple well-delineated T2-hyperintense millimetric ovoid nodules in the spinal cord white matter, some immediately next to the gray matter. All imaging characteristics are exactly as described in MVNT. Moreover, the lesions did not present any clinical symptoms and did not change on follow-up. Therefore, we describe these lesions as MVNT-like spinal cord lesions.

We present 2 cases of cervical multilobar intradural intramedullary lesions. The differential diagnosis includes neoplastic, inflammatory, vascular, or infectious lesions. Neoplasms,

such as glioma, ependymoma, hemangioblastoma, metastasis, and diffuse leptomeningeal glioneuronal tumors have a different morphology and generally show contrast enhancement. Because of its similar T1-signal and T2-signal characteristics, spinal cord subependymoma should also be considered. Spinal subependymomas tend to present as diffuse T2-hyperintense lesions with cord enlargement and possibly some enhancement. As they arise from subependymal glial cells, these lesions are typically centrally located in the spinal cord, rather than being peripheral. The lesions are larger than the typical “cysts” seen in MVNT, and they have a lower signal intensity compared with CSF. In MVNT and in our cases, cystic portions are isointense on T1-weighted and T2-weighted images. Various neurologic symptoms have been described in patients with spinal cord subependymoma, but they can also be asymptomatic. Infectious diseases, such as cryptococcosis and echinococcosis may also be considered; however, all lab values were negative. Further, there were no clinical signs of infection and the lesions did not show any enhancement. Inflammatory disorders of the cervical spinal cord with T2-hyperintense lesions mainly consist of multiple sclerosis, neuromyelitis optica, and acute disseminated encephalomyelitis. Neither lesion showed any change on follow-up examinations, and there were no clinical symptoms or laboratory findings attributable to either of

the lesions. Vascular pathology (eg, vasculitis) may mimic this imaging presentation. However, lesions associated with vasculitis usually show contrast enhancement and may be irregularly delineated. Perivascular spaces, also called Virchow-Robin spaces, are also included in the differential diagnosis of a cerebral MVNT, but dilated perivascular spaces in the spinal cord have only been reported on microscopy and not on MR imaging.

In the literature, MVNT was originally exclusively described within the cerebrum. Early case series reported that MVNT occurs supratentorially in all lobes,<sup>3</sup> and a recent publication has shown that these benign lesions do not change over long-term follow-ups.<sup>4</sup> Lesions, although originally associated with seizures, are often asymptomatic, incidental findings.<sup>5,6</sup> Recent publications have also demonstrated cystic multinodular lesions infratentorially in the posterior fossa, with imaging characteristics compatible with MVNT.<sup>7–9</sup> These were reported within the cerebellar hemispheres and vermis. None were histologically proved.



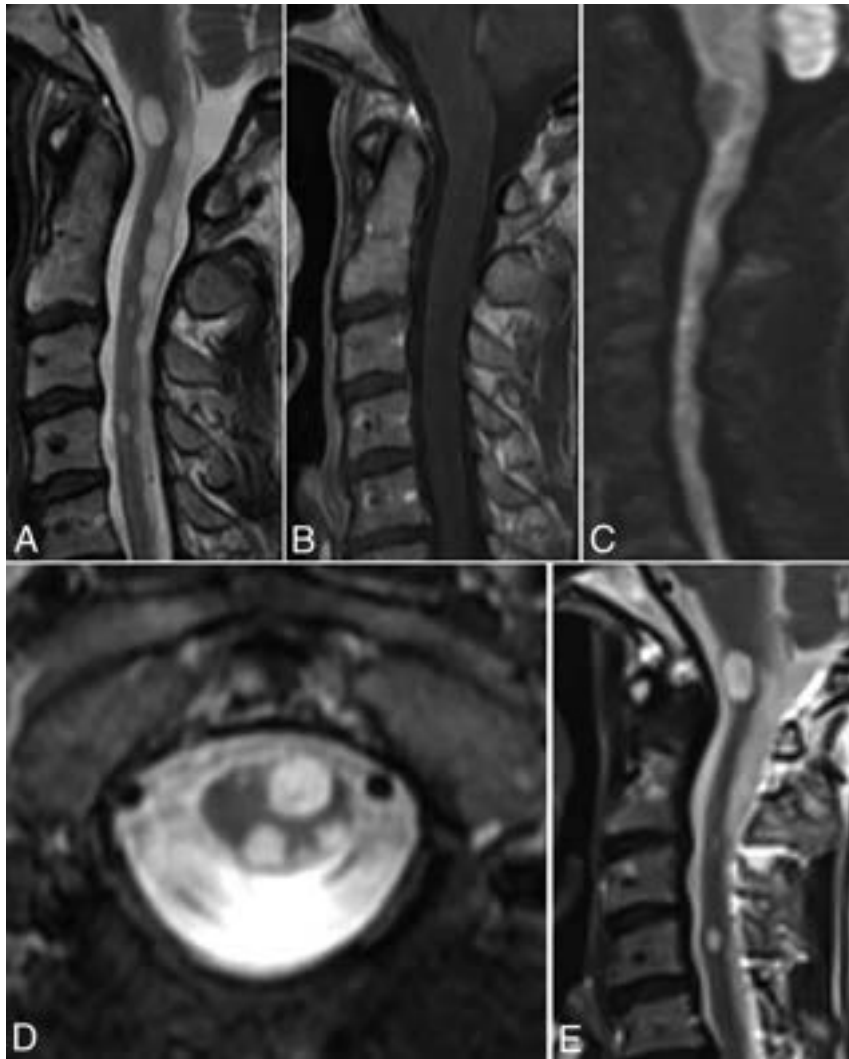


**FIG 2.** Case 2; 37-year-old woman A, Sagittal T2-weighted image shows multilobar intradural intramedullary lesions. Similar to case 1, there was neither syringomyelia nor any T2-hypointense changes within the medulla. B, Sagittal T1-weighted image after the intravenous administration of gadolinium. No contrast enhancement can be seen. C, Sagittal echo-planar diffusion-weighted image shows no diffusion restriction within the lesions. D, Para-axial T2-weighted image depicts the cystic-like intra-axial lesions. Note the sharp delineation of the lesions. These lesions are located within the white matter of the spinal cord, without affecting the gray matter. E, Sagittal T2-weighted image from a 4-year follow-up MR-examination. No volume changes and/or signal intensity changes could be detected, allowing for differences in the field of view.

The term multinodular and vacuolating posterior fossa lesions of unknown significance (MV-PLUS) was proposed.<sup>7</sup>

No case reports were found describing MVNT in the spinal cord. However, the imaging features of these lesions in our patients and the stable findings on follow-up MR imaging were MVNT-like lesions. It is reasonable to hypothesize that MVNTs can also occur within the spinal cord, as they may also occur in the posterior fossa. Short-term follow-up is a limitation of this case report. There was a follow-up period of 12 months in case 1 and a 4-year

follow-up in case 2. Also, because of the asymptomatic characteristics of the lesions in combination with their locations in the spinal cord, no histopathologic confirmation was obtained. However, other publications regarding MV-PLUS also have no histopathological confirmation.

Disclosure forms provided by the authors are available with the full text and PDF of this article at [www.ajnr.org](http://www.ajnr.org).

## REFERENCES

1. Louis DN, Perry A, Wesseling P, et al. **The 2021 WHO classification of tumors of the central nervous system: a summary.** *Neuro Oncol* 2021;23:1231–51 CrossRef Medline
2. Huse JT, Edgar M, Halliday J, et al. **Multinodular and vacuolating neuronal tumors of the cerebrum: 10 cases of a distinctive seizure-associated lesion.** *Brain Pathol* 2013;23:515–24 CrossRef Medline
3. Nunes RH, Hsu CC, da Rocha AJ, et al. **Multinodular and vacuolating neuronal tumor of the cerebrum: a new “leave me alone” lesion with a characteristic imaging pattern.** *AJNR Am J Neuroradiol* 2017;38:1899–904 CrossRef Medline
4. Dogra S, Zagzag D, Young M, et al. **Long-term follow-up of multinodular and vacuolating neuronal tumors and implications for surveillance imaging.** *AJNR Am J Neuroradiol* 2023;44:1032–38 CrossRef Medline
5. Arbuiso S, Roster K, Gill A, et al. **Multinodular and vacuolating neuronal tumor: incidental diagnosis of a rare brain lesion.** *Cureus* 2021;13:e20674 CrossRef Medline
6. Makrakis D, Veneris S, Papadaki E. **Multinodular and vacuolating neuronal tumor incidentally discovered in a young man: conventional and advanced MRI features.** *Radiology Case Rep* 2018;13:960–64 CrossRef Medline
7. Lecler A, Bailleux J, Carsin B, ENIGMA Investigation Group (European Interdisciplinary Group for MVNT Analysis), et al. **Multinodular and vacuolating posterior fossa lesions of unknown significance.** *AJNR Am J Neuroradiol* 2019;40:1689–94 CrossRef Medline
8. Morassi M, Bagatto D. **Infratentorial multinodular and vacuolating neuronal tumor or multinodular and vacuolating posterior fossa lesions of unknown significance? Clinico-radiologic findings from 2 cases.** *World Neurosurg* 2020;136:58–61 CrossRef Medline
9. Múnera V, Vargas S, Herrera Jaramillo DA. **Lesión multinodular y vacuolar de fosa posterior. Presentación de caso en Colombia.** *Rev Colomb Radiology* 2020;31:5339–41 CrossRef